

POLITECNICO DI MILANO

Department of Civil and Environmental Engineering

Doctoral School in Structural, Seismic and Geotechnical Engineering

XXV Cycle



Ph.D. Thesis

**INTRINSIC DAMAGE AND SPALLING SENSITIVITY OF
CONCRETE SUBJECTED TO HIGH TEMPERATURE**

Politecnico Supervisor:

Prof. Pietro G. GAMBAROVA

Ph.D. Candidate:

Chiara ROSSINO

CTG-Italcementi Group Co-Supervisor:

Eng. Stefano CANGIANO

Doctoral School in Structural, Seismic and
Geotechnical Engineering Coordinator:

Prof. Roberto PAOLUCCI

Chiara Rossino

Intrinsic damage and spalling sensitivity of concrete subjected to high temperature

© March 2014

Doctoral School in Structural, Seismic and Geotechnical Engineering
Department of Civil and Environmental Engineering
Politecnico di Milano

XXV Cycle

Faculty Members

Prof. Roberto Paolucci (Coordinator)

Dott. Raffaele Ardito

Prof. Fabio Biondini

Prof. Gabriella Bolzon

Prof. Claudia Comi

Prof. Alberto Corigliano

Dott. Dario Coronelli

Prof. Claudio di Prisco

Prof. Marco di Prisco

Dott. Liberato Ferrara

Prof. Attilio Frangi

Prof. Elsa Garavaglia

Prof. Cristina Jommi

Prof. Pier Giorgio Malerba

Prof. Anna Pandolfi

Prof. Umberto Perego

Prof. Federico Perotti

Prof. Lorenza Petrini

Prof. Gianpaolo Rosati

Prof. Luigi Zanzi

To my family

SUMMARY

The great efforts devoted in the last decades to investigate the effects of thermal actions on concrete mechanical properties and their microstructural changes have not been accompanied so far by as many studies on the interactions between the chemo-physical reactions at high temperature occurring in concrete basic constituents (microstructural level) and concrete heat-affected mechanical properties (macro level), according to the information arising from the comprehensive literature review carried out in the first part of this Ph. D. thesis. Knowing the micro-macro interactions and establishing appropriate relationships may be the basis for optimizing concrete mixes able to effectively resist to thermal actions. In this context, an extensive collaboration between CTG-Italcementi Group and Politecnico di Milano (Department of Civil and Environmental Engineering) has been activated to perform a joint research project whose results are shown in this Ph. D. thesis. The main objectives regard the investigation of the relationships between the intrinsic damage, due to chemo-physical reactions and thermal incompatibility between cementitious matrix and aggregates, and the consequent mechanical properties, as well as the study of the thermo-mechanical damage deriving from vapour pressure build-ups in concrete, attributable to the onset of temperature gradients with time and space.

The experimental campaign was performed on eleven concrete mixes ($f_{cm,cube} \geq 45, 70, 95$ MPa), formulated under the restraints of maintaining constant the slump class, the type of cement and the volume fraction of the cement paste. The considered parameters are the mineralogical nature of the aggregate, the type of the fibers (polymer, either monofilament and fibrillated, and steel) and their content. Mechanical and microstructural characterizations have been carried out on the eleven concrete mixes. The first foresaw the measurements of compressive strength, the secant elastic modulus, as well as the acquisition of constitutive law in compression. The chemo-physical characterization was focused on both the chemical composition (by means of X-Ray Diffraction and Thermogravimetric Analysis) and the microstructure (by means of Mercury Intrusion Porosimetry and Scanning Electron Microscopy). Maximum pressure build-up (P_{lim}) and temperature at failure (T_{lim}) and the thermal diffusivity, both during monotonic heating, were evaluated as well, by using the specific test procedures developed by Department of Civil and Environmental Engineering of Politecnico di Milano. Before being characterized, the concrete specimens were subjected to a

single thermal cycle at different “reference” temperatures (105, 250, 500 and 750°C). The residual properties were compared with those obtained at 20°C.

In the context of the experimental results, X-Ray Diffraction and Thermogravimetric Analysis confirm the chemical evolution of the main hydrated constituents of the cementitious matrix, under increasing temperature, as well as the transformations concerning the aggregates. Scanning Electron Microscopy observations indicate that, after thermal exposure, cracking usually started at the aggregate-cement paste interface, propagated into the cementitious matrix and finally bridged the aggregates. In the case of intermediate grade basalt concrete, this evolution was strongly limited, even after exposure at 750°C, and only few thin cracks were observed. The Mercury Intrusion Porosimetry tests indicate that the higher the temperature exposure, the higher the total porosity. In the concrete mixes containing polymeric fibers, after heating to 250 and 500°C, some peaks appear in the zone of macropores, as a consequence of melting/degradation of the fibers. The compressive strength and elastic modulus exhibit a downward trend at increasing temperature, confirming values found by other Researchers. Thermal diffusivity data ranges basalt, silico-clacareos and calcareous intermediate grade concretes.

Considering all the experimental results, both microstructural and mechanical ones, it has been observed that the Mercury Intrusion Porosimetry results allow justify the exponential decay in maximum pressure build-up (P_{lim}) by identifying a critical range of pore radius responsible for the sizable differences in P_{lim} values of mixes having almost the same total porosity, after thermal exposure, but different compressive strength. Coupling Mercury Intrusion Porosimetry and Scanning Electron Microscopy results allow identify the appearance of microcracks, whose size is similar to that of macro pores ($>10\mu m$). This microstructural behavior is in some way reflected by the different post-peak behaviors of the constitutive law in compression. In fact, very thin microcracks for basalt concrete can be associated to the steeper post-peak branch than in both silico-calcareous and calcareous mixes. Concerning spalling-related phenomena during monotonic heating, porosimetric results are used to determine the water released into the pore system after heating and the moisture specific volume. In this way the pressure values ($P_w(T)$) corresponding to the measured temperatures at failure (T_{lim}) are identified in Clapeyron’s plane. A satisfactory agreement is found between the pressure and temperature experimental values and those derivable from Clapeyron’s plane. Once the thermodynamic state of the moisture is known, at any given temperature value, the ratio between the pressure identified in the Clapeyron’s plane ($P_w(T)$) and

the maximum pressure (P_{lim}), experimentally measured, is defined as a spalling sensitivity index ($S_{s,o}$) allowing to predict the failure occurrence in heat-exposed concrete.

In conclusion, all the microstructural and mechanical observations turn out to be instrumental in understanding, in a generalized way, the decay phenomena occurring in the concrete during heating, describable by exponential laws, and the mechanism that induce the pressure build-ups in heat-exposed concrete, introducing a spalling sensitivity index allowing to predict the material behaviour.

ACKNOWLEDGMENT

*“Do not say to the world what you are able to do,
just do it”
- Riccardo Oda -*

I would like to express my deepest gratitude to CTG-Italcementi Group, in the person of Dr. Enrico Borgarello, whose support and effort have been essential in allow me to attend the Executive Ph. D. program. A very special and particularly felt thanks to my Supervisor in CTG, Eng. Stefano Cangiano, for his indispensable and invaluable technical and moral support during the four Ph.D. years and during the Ph.D. thesis drawing up.

I also wish to thanks my Supervisor in Politecnico di Milano, Prof. Pietro G. Gambarova, which, together with the Faculty Members, welcomed me in the Department, despite my non-engineering background. Thanks to Prof. Gambarova also for the support during my educational activity and for the final dissertation of my Ph.D. thesis. A special thanks also to Prof. Roberto Felicetti, Technical Responsible of the joint project between CTG-Italcementi Group and the Civil and Environmental Engineering Department of Politecnico di Milano, as well as Eng. Francesco Lo Monte, which collaboration was fundamental in order to carry out a significant part of the experimental activity collected in this thesis.

A grateful thanks to all my colleagues of the Research and Development Department of CTG in Bergamo that have collaborate with me in the entire experimental campaign foreseen for the Ph. D. thesis, starting from the specimens casting to all the microstructural analysis needed to characterize the concrete materials. In this context, a special thanks goes to my manager Eng. Massimo Borsa, and to all the colleagues of the Aggregate and Concrete Team, in particular Adalberto Schiavi and Massimo Facchinetti. I'd like also the say thank you to all my colleagues of the CTG Material Validation Center in Calusco d'Adda, in the person of Eng. Alessandro Morbi, and to all my colleagues of Chemical Laboratories, in particular to Dr. Emanuele Gotti e Dr. Maurizio Marchi.

A sincere thank you to all the people that support me during my educational activity and exams in Politecnico di Milano, thus my Ph. D. colleagues, in particular Eng. Giada Colasante, and my

classmates during the first years in Bachelor and Master Degree courses, in particular Chiara Zanetti and Keti Parapani.

A grateful and endless thanks to my family, in a particular way to my parents, whose support encouragement and care have been always present and essential in these years. I could never forget my boyfriend and my dearest friends and colleagues, which have shared with me all the moments and moods that have accompanied this unique and unforgettable period of my life.

Last but not least, a heartfelt thanks to all those who believed in me.

March 2014

Chiara Rossino

CONTENTS

CONTENTS

List of Figures	5
List of Tables.....	13
List of Abbreviations.....	17
1. INTRODUCTION (GENERAL OVERVIEW)	19
1.1 High temperature exposure scenarios	20
1.2 Specific case histories of fire scenarios	23
1.2.1 Fire: economical and social aspects.....	23
1.2.2 Fire: some real cases.....	26
1.2.3 Temperature-time curves for different fire scenarios	29
1.2.4 The concept of construction robustness.....	31
1.3 Type of Damage in Concrete Structures Subjected To High Temperatures/Fires.....	31
1.3.1 Intrinsic damage.....	32
1.3.2 Mechanical damage and spalling.....	33
1.4 Introduction (General Overview): conclusive remarks.....	34
2. LITERATURE REVIEW.....	35
2.1 Intrinsic Damage	35
2.1.1 Main constituents of concrete	35
2.1.1.1 Thermal degradation of cementitious paste	35
2.1.1.1.1 Portland cement paste	36
2.1.1.1.2 Effect of mineral constituents on thermal behaviour of cement pastes	38
2.1.1.1.3 Thermodynamic and kinetic aspects of thermal degradation reactions	41
2.1.1.1.4 Heating rate effect on intrinsic damage of cement pastes.....	49
2.1.1.1.5 Volume fraction evolution of cement paste constituents, before and after thermal exposure	51
2.1.1.2 Thermal Stability of Aggregates	55

CONTENTS

2.1.1.2.1 Calcite decarbonation reaction.....	56
2.1.1.2.2 Mass loss of Aggregates	57
2.1.1.2.3 Micro-cracking distribution	60
2.1.1.2.4 Dimensional stability of aggregates	61
2.1.2 Concrete system.....	63
2.1.2.1 Heating rate effect on intrinsic damage of concrete	63
2.1.2.2 Microstructural changes in concrete after thermal exposure	66
2.1.2.2.1 Concrete microstructure after thermal exposure	66
2.1.2.2.2 Concrete microstructure: the mode of action of PP fibers	72
2.2 Mechanical damage and Spalling	76
2.2.1 Mechanical damage of concrete after thermal exposure	76
2.2.1.1 Compressive strength.....	76
2.2.1.2 Stress-strain curves and modulus of elasticity	82
2.2.1.3 Splitting tensile strength.....	85
2.2.1.4 Effect of heating rate on mechanical properties.....	86
2.2.2 Explosive spalling in concrete	88
2.2.2.1 Pore pressure build-up	89
2.2.2.2 Thermal gradients in heated concrete	93
2.2.2.3 Mass transport in concrete after thermal exposure	95
2.2.2.4 Permeability determination in HPC at high temperatures	97
2.3 Literature review: concluding remarks	102
3. OBJECTIVE OF THE THESIS WORK	105
4. EXPERIMENTAL PROCEDURES.....	107
4.1 General planning of tests.....	107
4.1.1 Characterization of starting materials	108
4.1.1.1 Cement, filler and pozzolanic addition	108
4.1.1.2 Aggregates	113

CONTENTS

4.1.1.3 Polypropylene and Steel fibers	116
4.1.1.4 Admixtures.....	118
4.1.3 Intrinsic and mechanical damage evaluation.....	122
4.1.3.1 Thermal cycle design	122
4.1.3.2 Microstructural characterization: testing procedures	124
4.1.3.3 Mechanical characterization: testing procedure.....	128
4.1.4 Spalling sensitivity.....	130
4.1.4.1 Diffusivity determination.....	130
4.1.4.2 Pore pressure measurement and splitting test procedure	131
4.1.4.3 Permeability determination.....	133
5. EXPERIMENTAL RESULTS.....	135
5.1 Intrinsic damage evaluation: microstructural characterization	135
5.1.1 Thermogravimetric Analysis (TGA) results.....	135
5.1.2 X-Ray Diffraction (XRD) results	140
5.1.3 Mercury Intrusion Porosimetry (MIP) results	144
5.1.4 Scanning Electron Microscopy (SEM) results	160
5.2 Mechanical characterization	172
5.2.1 Stress-strain curves	172
5.2.2 Compressive strength.....	176
5.2.3 Elastic modulus.....	180
5.3 Spalling sensitivity.....	182
5.3.1 Spalling due to thermal stresses: diffusivity determination results	183
5.3.2 Spalling due to pressure build-up	184
5.3.2.1 Pore pressure measurement results	184
5.3.2.2 Splitting test results.....	187
5.3.2.3 Permeability results.....	189
5.4 Experimental results: concluding remarks.....	191

CONTENTS

6. DISCUSSION ON THE EXPERIMENTAL RESULTS.....	195
6.1 Intrinsic and mechanical damage evaluation	195
6.2 Spalling sensitivity assessment	205
6.2.1 Spalling due to pressure build-up	205
6.2.2 Generalization of the problem of pressure build-up taking into account the mass transport processes	216
6.3 Spalling due to thermal gradients.....	221
7. CONCLUDING REMARKS.....	223
8. OUTLOOK	227
References	229
Annex A	239
Annex B	243
Annex C	249
Annex D	261
Annex E	273

LIST OF FIGURES

List of Figures

Figure 1: Oil well cementing scheme.	20
Figure 2: Concrete storage tanks.....	21
Figure 3: Nuclear concrete vessels.....	22
Figure 4: Concrete airport runways.	23
Figure 5: Graphic economic-statistical evaluation of "costs" of fire (average for 2006-2008) [Brushlinsky et al., 2012].	24
Figure 6: Trends in fire deaths in the countries of the world in 2006-2010.	25
Figure 7: Trends in fire injuries in the countries of the world in 2007-2010.....	25
Figure 8: Fire in Mont Blanc (a) and Gotthard tunnels (b).....	26
Figure 9: Windsor Tower Fire during and after fire.	27
Figure 10: CESP 2 Core Collapse in Sao Paulo, Brazil.....	28
Figure 11: Fukushima fires after earthquake and tsunami.	28
Figure 12: Temperature-time curves for fire scenario evaluation.....	30
Figure 13: Evolution of the normalised intensity during heating for the different compounds in cement paste (high C ₃ A amount) [Castellote et al., 2004].	37
Figure 14: Evolution of the normalised intensity during heating for the different compounds in cement paste (low C ₃ A amount) [Castellote et al., 2004].	37
Figure 15: SEM micrographs of fracture surfaces of hardened QP0 and QP20 at different temperatures [Rashad and Zeedan, 2012].	40
Figure 16: Equilibrium relationship between temperature and pressure for portlandite dehydration [Schaube et al., 2012].	42
Figure 17: Conversion rate of CH as a function of conversion degree at heating rate of 20°C/min [Zelić et al., 2002, graphic elaboration by Zhao, 2012].	44
Figure 18: Conversion rate of CH as a function of temperature at different conversion degrees [Zelić et al., 2002, graphic elaboration by Zhao, 2012].	45
Figure 19: Dehydration of CH in N ₂ atmosphere [Schaube et al., 2012].	46
Figure 20: Conversion rate of AFt as a function of temperature at different conversion degrees [Zhao, 2012].	47

LIST OF FIGURES

Figure 21: Relative C-S-H amount as a function of exposure duration under different temperatures [Peng and Huang, 2008].....	48
Figure 22: Decomposition of CH under different heating rates [Zhao, 2012].....	50
Figure 23: Decomposition of C-S-H under different heating rates [Zhao, 2012].....	50
Figure 24: Decomposition of hydrated aluminates under different heating rates [Zhao, 2012].....	51
Figure 25: Capillary porosity evolution under different heating rates [Zhao, 2012].....	54
Figure 26 : Thermal degradation curves of CaCO ₃ at 1–3, 2–6, 3–9, and 4–12 K/min heating rate [Georgieva et al., 2013].....	56
Figure 27 : TGA of different flints and quartzite aggregates [Xing, Hèbert et al. 2011].	57
Figure 28: TGA of different calcareous aggregates [Xing, Hèbert et al. 2011].	58
Figure 29: Weight loss (by TGA) of siliceous aggregates [Niry et al., 2013].	59
Figure 30: Evolution of the porosity of calcareous, silico-calcareous and siliceous aggregates [Xing, Beaucour et al., 2011].	59
Figure 31: Flint’s cracking by SEM as function of temperature [Niry et al., 2013].....	61
Figure 32: Dilatometric curves for ten rocks: AN=Anorthosite, BA=Basalt, DO=Dolomite, GD=Granodiorite, GR=Granite, LI=Limestone, QM=Quartz Monzonite, QR=Quartz, RH=Rhyolite, SY=Syenite [Harmathy, 1993].....	62
Figure 33: Thermal expansion coefficient of aggregates in function of thermal expansion coefficient of concrete [Harmathy, 1993].	63
Figure 34: Evolution of the mass loss kinetics at 110, 150, 200 and 250°C with heating rate [Gallè et al., 2003].....	64
Figure 35: Evolution of the mass loss with temperature and heating rate [Gallè et al., 2003].	65
Figure 36: DSC curves of both strength concretes [Noumowe, 2005].	67
Figure 37: PP fibers in HSC, before thermal exposure [Noumowe, 2005].	68
Figure 38: Traces of melted fibers in HSC [Noumowe, 2005].....	68
Figure 39: SEM analysis of HSC without fibers, after 750°C [Guerrini et al., 2004].....	70
Figure 40: SEM analysis of a hybrid HSC concrete, at different temperatures [Guerrini et al., 2004].	70
Figure 41: Porosity before and after high temperature exposure [Chan et al., 2000].....	71
Figure 42: Pore size distribution before and after exposure to high temperature for NSC and HPC-1 [Chan et al., 2000].....	71

LIST OF FIGURES

Figure 43: Micropores size distribution in initial mortar with and without PP fibers [Alonso et al., 2013].	73
Figure 44: SEM microstructure of PP fibers distribution in the bulk of initial mortar (before heating) a) Microcracks, b) Gap at ITZ PP fiber/cement paste and aggregate/cement paste [Alonso et al., 2013].	74
Figure 45: Pore size distribution of capillary pores after heating of mortars (200°C) [Alonso et al., 2013].	75
Figure 46: SEM microstructure of PP fibers in the bulk of mortar after heating a) after 170°C, b) after 300°C [Alonso et al., 2013].	75
Figure 47: Compressive strength for calcareous concrete in function of temperature obtained by means of stressed and unstressed tests at high temperature and unstressed residual test, after heating [Koury, 1992].	77
Figure 48 : Compressive strength-temperature trends for NSC and NWA Concretes by unstressed residual-strength test [Phan and Carino, 1998].	78
Figure 49: Compressive Strength-Temperature trends for NSC and LWA Concretes by unstressed residual-strength test [Phan and Carino, 1998].	79
Figure 50: Residual compressive strength values for HSC containing pozzolanic additions [Poon et al, 2001].	80
Figure 51: Relative residual compressive strength of limestone (on the left) and siliceous (on the right) aggregates [Savva et al., 2005].	81
Figure 52: Stress-strain curves for lower (on the left) and higher (on the right) grade HSC at different exposure temperatures [Felicetti and Gambarova, 1998].	83
Figure 53: Modulus of elasticity curves for lower (on the left) and higher (on the right) grade HSC at different exposure temperatures [Felicetti and Gambarova, 1998].	83
Figure 54: Modulus of elasticity curves for HSC, with different aggregates and presence/absence of steel fibers, at different exposure temperatures [Cheng et al., 2004].	84
Figure 55: Modulus of elasticity-temperature trends for LWA, NWA and NSC concretes by unstressed residual-strength test [Phan and Carino, 1998].	85
Figure 56: Evolution of the compressive strength with temperature and heating rate [Gallè et al., 2003].	86
Figure 57: Evolution of the tensile strength with temperature and heating rate [Gallè et al., 2003].	87
Figure 58: Evolution of the elastic modulus with temperature and heating rate [Gallè et al., 2003].	88

LIST OF FIGURES

Figure 59: Pressure, specific volume and temperature diagram for water [Moran and Shapiro, 2008].	90
Figure 60: Possible mechanisms of explosive thermal spalling: (a) pressure shear model, (b) buckling model, and.....	93
Figure 61: New test setup for the permeability measurements at elevated temperatures [Ožbolt and Bošnjak, 2013].	98
Figure 62: Intrinsic permeability of HPC with and without PP fibers in function of temperature [Ožbolt and Bošnjak, 2013].	99
Figure 63: Test apparatus for permeability measurements at elevated temperatures [Schneider, 2010].	100
Figure 64: Permeability of HPC during heating and cooling ($p_1 = 5$ bar) [Schneider, 2010].	101
Figure 65: Schematic program of the experimental activity.....	107
Figure 66: Laser granulometric distribution for CEM I, 42.5 R.	109
Figure 67: Granulometric analysis (laser distribution) for LF.	111
Figure 68: Granulometric analysis (laser distribution) for GGBS.....	112
Figure 69: Granulometric distribution for silico-calcareous aggregates fractions.....	114
Figure 70: Granulometric distributions for calcareous aggregate fractions.....	115
Figure 71: Granulometric distributions for basalt aggregates fractions.....	115
Figure 72: DSC thermograms for PP monofilament fibers.....	117
Figure 73: DSC thermograms for PP fibrillated fibers.	117
Figure 74: Hooked steel fibers added to HPC mixes [La Matassina].....	118
Figure 75: Time exposure as a function of temperature at different conversion degrees.	123
Figure 76 : Thermal cycle in electric furnace.	124
Figure 77: TGA apparatus.....	125
Figure 78: XRD apparatus.	126
Figure 79: MIP apparatus.....	127
Figure 80: SEM apparatus.....	128
Figure 81: Instrumented specimen tested in compression (controlled displacement).	129
Figure 82: Test specimen for thermal diffusivity inside the oven (1: thermocouple in the center of the specimen, 2: thermocouple near the external specimen surface).	131
Figure 83: Insulated specimen during heating.	132
Figure 84: Cubic molds for pore pressure specimens, instrumented with curved pipes.....	133

LIST OF FIGURES

Figure 85: TGA experimental trends for 70-S after all exposure temperatures.....	136
Figure 86: TGA experimental trends for two different concrete grades.....	137
Figure 87: TGA experimental trends for concretes with different aggregate types.....	138
Figure 88: TGA experimental trends for concretes with different PP fibers types and contents. ...	139
Figure 89: TGA experimental trends for concretes with different steel fibers contents.....	139
Figure 90: TGA experimental trends for concretes with different fibers types (PP and steel fibers).	140
Figure 91: XRD patterns for 70-S after all exposure temperatures.	141
Figure 92: XRD patterns for different concrete grades and different PP fibers contents at 20°C...	142
Figure 93: XRD patterns for 70-S, 70-C and 70-B at 20°C.....	143
Figure 94: XRD patterns for 70-S, 70-C and 70-B at 750°C.....	143
Figure 95: Cumulative distributions for 95-S after heating (different exposure temperatures).....	145
Figure 96: Differential distributions for 95-S after heating (different exposure temperatures).....	145
Figure 97: Concrete total porosity as a function of the temperature for different concrete grades and aggregate types.....	147
Figure 98: Cumulative distributions for different concrete grades at 20°C.....	148
Figure 99: Cumulative distributions for different aggregate types at 20°C.....	149
Figure 100: Differential distributions for different concrete grades at 20°C.....	149
Figure 101: Differential distributions for different aggregate types at 20°C.....	150
Figure 102: Cumulative distributions for different concrete grades at 20 and 500°C.....	151
Figure 103: Differential distributions for different concrete grades at 20 and 500°C.....	151
Figure 104: Cumulative distributions for different aggregate types at 20 and 500°C.....	152
Figure 105: Differential distributions for different aggregate types at 20 and 500°C.....	153
Figure 106: Concrete total porosity as a function of the temperature for different types and contents of PP fibers.....	154
Figure 107: Differential distributions for 70-S-Pm 1 after heating (different exposure temperatures).	155
Figure 108: Cumulative distributions for 70-S-Pm 1 after heating (different exposure temperatures).	156
Figure 109: Differential distributions for different PP mnf fibers contents concretes at 20 and 500°C.	156
Figure 110: Cumulative distributions for 70-S, 70-S-Pm 2 and 70-S-Pf 2 at 20 and 500°C.....	157

LIST OF FIGURES

Figure 111: Relative distributions for 70-S, 70-S-Pm 2 and 70-S-Pf 2 at 20 and 500°C.	158
Figure 112: Concrete total porosity as a function of temperature for different steel fibers contents.	159
Figure 113: Relative distributions for 70-S, 70-S-Sf 40 and 70-S-Sf 60 at 20 and 500°C.	159
Figure 114 : A) PP monofilament fiber in 70-S-Pm 1 not exposed concrete; B) typical void left free by a fiber after heating at 250°C (70-S-Pm 1).	169
Figure 115: Steel fiber in 70-S-Sf 40 mix after 500°C exposure 100 X (A) and 250 X (B).	170
Figure 116: SEM microanalysis of the interfare between steel fiber and cementitous matrix.	171
Figure 117: Residual stress-strain curves for different concrete grades after all exposure temperatures.	172
Figure 118: Residual stress-strain curves for concretes with different aggregate types after all exposure temperatures.....	173
Figure 119: Residual stress-strain curves for concretes with different contents and types of PP fibers and different contents of steel fibers after all exposure temperatures.....	175
Figure 120: Residual compressive strength as a function of the temperature for different concrete grades.	177
Figure 121: Residual compressive strength as a function of temperature for different aggregate types.	178
Figure 122: Residual compressive strength as a function of temperature for concrete with different types and contents of PP fibers.	179
Figure 123: Residual compressive strength as a function of temperature for concretes with different contents of steel fibers.....	179
Figure 124: Residual compressive strength as a function of temperature for concretes with highest contents of PP and steel fibers.	180
Figure 125: Residual elastic modulus as a function of temperature for different concrete grades and aggregate types.....	181
Figure 126: Residual elastic modulus as a function of temperature for concretes with different types and contents of PP and steel fibers.....	182
Figure 127: Thermal diffusivity tests for different concrete grades and different aggregate types.	183
Figure 128: Thermal diffusivity tests for concretes with different types and contents of PP and steel fibers.....	184

LIST OF FIGURES

Figure 129: Pore pressure versus temperature trends for each concrete mixes (except the steel fiber mixes).....	185
Figure 130: Pore pressure as a function of temperature for concrete mixes.....	186
Figure 131: Characterization performed on the concrete mixes.	196
Figure 132: Compressive strength ($f_{cm,cyl}$) as a function of total porosity at 20°C and after heating for different concrete grades.	198
Figure 133: Elastic modulus (E_c) as a function of total porosity at 20°C and after heating for different concrete grades.	198
Figure 134: σ - ϵ curves and SEM images for 70-S and 70-B at 20°C and after thermal exposure at 500°C.	199
Figure 135: Maximum pore pressure (P_{lim}) versus total porosity (f_p) at 250°C for silico-calcareous mixes.	201
Figure 136 : Differential distributions at 250°C for different concrete grades.	202
Figure 137: Cumulative distribution at 250°C for 70-S and 95-S mixes.....	202
Figure 138: Cumulative distribution at 250°C for silico-calcareous mixes with and without PP monofilament fibers.	203
Figure 139: Concrete control unit volume totally insulated from the external environment.....	205
Figure 140: Clapeyorn's diagram for water (P - V_{sp} water phase diagram).	206
Figure 141: Specific volume V_{sp} versus P_{lim} and $P_w(T_{lim})$ of silico-calcareous concrete mixes, comprising the saturated liquid and vapour curves.....	211
Figure 142: Close-up of specific volume V_{sp} versus P_{lim} and $P_w(T_{lim})$ of silico-calcareous concrete mixes, comprising the saturated liquid curve.....	211
Figure 143: Main phases of concrete spalling assessment (from experimental results discussion).215	
Figure 144: Reference Pressure-Temperature curve and Pressure-Temperature values obtained by experimental set-up for pore pressure measurement.....	216
Figure 145: Sealed and insulated specimen ready for pore pressure determination.	217
Figure 146: Concrete unit volume in which the water-proof barriers are removed.....	218
Figure 147: Permeability versus total porosity for different concrete grades at 20°C.....	221

LIST OF TABLES

List of Tables

Table 1: Summary of materials and related compressive strength data reviewed by Phan and Carino (1998).	78
Table 2: Chemical and physico-mechanical analysis for CEM I, 42.5 R.	108
Table 3: Chemical and granulometric analysis for LF and GGBS.	110
Table 4: Chemical analysis for silico-calcareous aggregate.	113
Table 5: Specific gravity for silico-calcareous aggregate fractions.	113
Table 6: Chemical analysis for calcareous and basalt aggregates.	114
Table 7: Specific gravity for calcareous aggregate fractions.	115
Table 8: Specific gravity for basalt aggregate fractions.	115
Table 9: Mix design and mechanical properties of concretes with different compressive strength grades and different aggregates.	120
Table 10: Mix design and mechanical properties of concrete at intermediate grade with and without PP and steel fibers.	121
Table 11: Total porosity values for different compressive strength grades and different type of aggregate concretes at 20°C.	146
Table 12: Total porosity values for different compressive strength grades and different type of aggregate concretes at 105°C.	146
Table 13: Total porosity values for different compressive strength grades and different type of aggregate concretes at 250°C.	146
Table 14: Total porosity values for different compressive strength grades and different type of aggregate concretes at 500°C.	146
Table 15: Total porosity values for different compressive strength grades and different type of aggregate concretes at 750°C.	147
Table 16: Total porosity values for different type and content of PP fibers concretes at 20°C.	153
Table 17: Total porosity values for different type and content of PP fibers concretes at 105°C.	154
Table 18: Total porosity values for different type and content of PP fibers concretes at 250°C.	154
Table 19: Total porosity values for different type and content of PP fibers concretes at 500°C.	154
Table 20: SEM images for 70-S at 100X and 1000X magnitude after all exposure temperatures. .	161
Table 21: SEM images for different concrete grades at 100X and 1000X magnitude at 250°C.	162

LIST OF TABLES

Table 22: SEM images for different concrete grades at 100X and 1000X magnitude at 500°C.....	163
Table 23: SEM images for different concrete grades at 100X and 1000X magnitude at 750°C.....	164
Table 24: SEM images for different aggregate types at 100X and 1000X magnitude at 250°C.....	165
Table 25: SEM images for different aggregate types at 100X and 1000X magnitude at 500°C.....	166
Table 26: SEM images for different aggregate types at 100X and 1000X magnitude at 750°C.....	167
Table 27: SEM images for concrete with different types and contents of PP fibers at 100X and 1000X magnitude at 500°C.....	168
Table 28: SEM images for concretes with and without steel fibers at 100X and 1000X magnitude at 500°C.	170
Table 29: Compressive strength values at 20°C for different cylindrical specimens at different ages.	176
Table 30: Compressive strength values for all concrete mixes after all temperatures.....	177
Table 31: Splitting tensile strength values at 20°C for all concretes.	187
Table 32: Splitting test values for 45-S mix and related T_{sp}	188
Table 33: Splitting test values for 70-S, 95-S, 70-B and 70-C mixes and related T_{sp}	188
Table 34: Splitting test values for 70-S mix containing different types and contents of PP fibers and related T_{sp} values.....	189
Table 35: Permeability data for all concrete mixes at 20°C.	189
Table 36: Pore radius corresponding to the maximum of the peak of the three different concrete grades from MIP differential distributions.....	196
Table 37: Total porosity data detected between the pore radius corresponding to peak maximum and the higher one detected by MIP for the three different concrete grades.	197
Table 38: Maximum pressure (P_{lim}) and temperature (T_{lim}) and total porosity (f_p) at 250°C for 70-S and 95-S mixes.....	201
Table 39: P_{lim} and T_{lim} values for silico-calcareous mixes with and without PP monofilament fibers.	204
Table 40 : Available pore volume ($f_p(250^\circ\text{C}) \cdot V_{o,c}$), porosity increase ($\Delta f_p(\%)$) between 20 and 250°C and bound water amount ($m_{w,bound}$) for silico-calcareous concrete mixes (considered totally dried).	209
Table 41: Specific volume at 250°C values for silico-calcareous concrete mixes (considered totally dried).	209
Table 42: T_{lim} , $V_l(T_{lim})$ and $V_v(T_{lim})$ values for silico-calcareous concrete mixes.....	210

LIST OF TABLES

Table 43: $P_w(T_{lim})$, P_{lim} and F values for silico-calcareous concrete mixes.....	210
Table 44: V_{sp} calculated and from reference saturated liquid curve and their difference for silico-calcareous concrete mixes.....	212

LIST OF ABBREVIATIONS

List of Abbreviations

BSE	Back Scattered Electrons
C ₂ S	Belite, (CaO) ₂ ·SiO ₄ (Dicalcium Silicate)
C ₃ S	Alite, (CaO) ₃ ·SiO ₄ (Tricalcium Silicate)
C ₃ A	(CaO) ₃ ·Al ₂ O ₃ (Tricalcium Aluminate)
C ₄ AF	(CaO) ₄ ·Al ₂ O ₃ ·Fe ₂ O ₃ (Tricalcium Alumino Ferrite)
CH	Portlandite, Ca(OH) ₂ (Calcium Hydroxide)
C-S-H	Calcium Silicate Hydrate, (CaO) _{3.4} ·(SiO ₄) ₂ ·(H ₂ O) ₃
AFt	Ettringite, (CaO) ₃ ·Al ₂ O ₃ ·(CaSO ₄) ₃ ·(H ₂ O) ₃₂
FA	Fly Ash
GGBS	Ground Granulated Blast Furnace Slag
HC	Hydrocarbon curve
HCM	Hydrocarbon Modified curve
HPC	High Performance Concrete
HSC	High Strength Concrete
ITZ	Interfacial Transition Zone
LWA	LightWeight Aggregate
MIP	Mercury Intrusion Porosimetry
MK	Metakaolin
NSC	Normal Strength Concrete
NWA	Normal-Weight Aggregate
OPC	Ordinary Portland Cement
PP	PolyPropylene
SE	Secondary Electrons
SEM	Scanning Electron Microscopy
SF	Silica Fume
TGA	Thermogravimetric Analysis
VF	Volumetric Fraction
XRD	X-Ray Diffraction

1. INTRODUCTION (GENERAL OVERVIEW)

Concrete, and in general cementitious materials, are one of the most diffused construction products and they can be found in many applications, starting from civil buildings structures. It is well-known that concrete is a heterogeneous material composed by coarse granular materials (aggregate and filler) embedded in a hardened matrix, the hydrated cement paste, that fills the space between the aggregate particles, holding them together.

Concrete is a material that can be exposed to several aggressive conditions, and one of them is thermal exposure. The severity of this physical action depends on the temperature level, the heating rate and the number of thermal cycles applied to the material. In any case, the thermal exposure can activate degradation phenomena, leading to changes in microstructure, mechanical properties and durability.

Most concrete structures are commonly subjected to a range of temperature not more severe than that imposed by ambient environmental conditions. However, there are important cases where these structures may be exposed to much higher temperatures, either in case of high temperature service state or accidental events, such as fire scenarios (Naus, 2010).

First of all, it is fundamental to discriminate the two mentioned cases of thermal exposure.

High temperature exposure takes place when the target temperature is reached at low heating rate, such as some unit of °C/min, and then maintained for a brief or long period. This thermal action on the material can be repeated in thermal cycles that can last for months or years. In the field of high temperatures, some regions in which the material is subjected to different levels of degradation can be defined, also considering the damaged material already able to withstand the service loadings and to maintain its mechanical properties.

Fire scenario is an exceptional event in which the heating rate acting on the material is significantly faster in comparison with the previous one and it is normally about tens of °C per minute, with a duration that does not exceed a few hours. Differing from the previous situation, this action has been standardized in many countries during the last decades.

The following Paragraphs are focused on a general overview of most common concrete applications where high temperature exposure and fire scenario can take place.

INTRODUCTION (GENERAL OVERVIEW)

1.1 High temperature exposure scenarios

Concrete can be employed in structures designed for some special uses, such as oil and geothermal wells, storage tanks, nuclear vessels, airport runways, in which the material is or can be subjected to high temperature services state.

Historically, the first example of thermal exposure of cementitious materials is represented by the use of special slurries in **oil and geothermal wells** in order to bond and support the steel casing. Cement slurry is pumped through it to the bottom of the well and then up through the annulus between the casing and the surrounding rock (Figure 1). As cement descends into the well, the slurry is hydrating under elevated temperature and pressure (Zang 2010). Moreover, the hardened cement paste is required to sustain these critical conditions during its life-service time. The maximum temperature reached **in service conditions** can be higher than 260°C, both in oil (DeBrujin et al., 2008) and geothermal wells (Iverson, Maxson and Bour, 2010).

In these types of applications, the cement paste must withstand also extreme downhole conditions including hard and corrosive formations, lost-circulation zones, CO₂ and other toxic-gas intrusion. For these reasons, specific cement types are used, characterized by Tricalcium Silicate (C₃S) as principal phase and sulfate-resistant action.

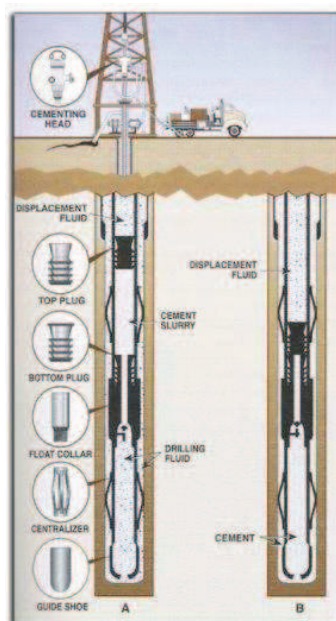


Figure 1: Oil well cementing scheme.

INTRODUCTION (GENERAL OVERVIEW)

The high temperature exposure in service state is an issue also for concrete used in massive structures for nuclear waste long-term storage facilities or other type of waste **storage tanks** (Figure 2).

Over several decades, vitrified waste and spent fuel have generated an important quantity of heat which may affect the long-term behaviour of surrounding structures. In standard conditions, ambient temperature should not exceed 60°C but in case of failure of a cooling system, concretes, in particular High Strength Concrete (HSC), could be temporarily exposed to temperatures up to 250°C (Gallè et al., 2003).

In certain applications, the concrete vaults of the high-level waste storage tanks can be exposed to high temperatures for a long period due to decay heating of the waste materials stored in the tanks. These materials can be also produced as a result of chemical processing of nuclear materials. The wastes in many tanks are reported to have achieved a temperature range of 150-180°C; the waste temperatures in a few tanks are suspected of having attained a higher range of 200-315°C (Kassir, 1996).



Figure 2: Concrete storage tanks.

Portland cement concrete possesses many of the physical qualities of an ideal radiation shield so it can be used as **nuclear vessels** material (Figure 3). In fact, gamma rays are absorbed by the high-density aggregate materials and neutrons are attenuated by hydrogen atoms in the cement paste. A concrete shield is exposed to two sources of heat: heat transferred from hot parts of the reactor system and heat produced internally by the attenuation of neutrons and gamma rays (Etherington, 1958). Energy captured from slowed down fast neutrons and gamma rays entering the shield from the reactor core is deposited within the shield material and radiated as heat. The total amount of heat generated can be considerable. Temperatures reached by concrete can be almost 300°C, but also

INTRODUCTION (GENERAL OVERVIEW)

higher depending on the type of nuclear reactor (Crispino, 1972). The heat generated may have detrimental effects on the physical, mechanical, and nuclear properties of the concrete.

Different types of concrete perform differently under radiation exposure, although if heated to relatively high temperatures, they all will become somewhat weaker and less effective in neutron attenuation (Glasstone and Sesonske, 1967).

From a practical point of view, concrete for radiation shielding typically uses ordinary normal weight aggregates, however, special types of aggregate have been used to improve the attenuation properties of concrete or to reduce the thickness of concrete shields. Typically this involves incorporation of heavyweight aggregate materials. Compared to normal weight aggregate concrete having a typical unit weight of 2400 kg/m^3 , heavyweight concretes weigh from 2900 to 6100 kg/m^3 .

One of the most diffused is the barytic aggregate that retain mechanical properties after elevated temperature exposure better than the limestone aggregate concrete (Crispino 1972).



Figure 3: Nuclear concrete vessels.

Plain and reinforced concrete plates are also widely used in transportation engineering, to construct highway and airport pavements and bridge decks due to their mechanical strength, good surface finish, durability and economy. The service life of a concrete pavement depends on many factors including mechanical and rheological material properties, applied loads, environment conditions and eventually de-icing salt application (Giussani and Mola, 2012).

In the case of **airport runways** (Figure 4), during the take-off and landing of advanced aircraft, concrete airfield pavement is subjected to extremely rapid transient high-temperature loadings as

INTRODUCTION (GENERAL OVERVIEW)

well as thermal cycles of heating and cooling due to very hot exhaust gas emanating from modern vectored thrust engines (VTE) or auxiliary power units. In some cases, the exhaust gas temperature of a VTE could rapidly reach over 800°C, and the corresponding exhaust velocity could go beyond 600 m/s (Ju and Zang, 1998).

Damage to airfield concrete pavement could be in the form of thermomechanical "spalling" of concrete runways and launch pads due to transient (monotonic or cyclic) high temperature loadings.



Figure 4: Concrete airport runways.

1.2 Specific case histories of fire scenarios

1.2.1 Fire: economical and social aspects

Next to the service state conditions involving high temperature exposure, the fire scenario is an exceptional condition more severe and more aggressive for concrete. When it occurs, the consequences fall down in different economical and social aspects. From the economical point of view, the implications are related to structural damage, which leads to the loss of properties and necessity of repairing, as well as the interruption of activities conducted in the damaged structure. The evaluation of economical costs between 2006 and 2008 in a world group of countries is reported in Figure 5 (see Annex A for tabulated values) (Brushlinsky et al., 2012). Different parameters have been considered:

- Direct losses, traceable to fire as the proximate cause (loss that is caused by smoke or by water used in extinguishing a fire);

INTRODUCTION (GENERAL OVERVIEW)

- Indirect losses, comprising all the aspects not directly occurring with the fire;
- Cost of fire service;
- Fire protection in buildings;
- Fire insurance administration.

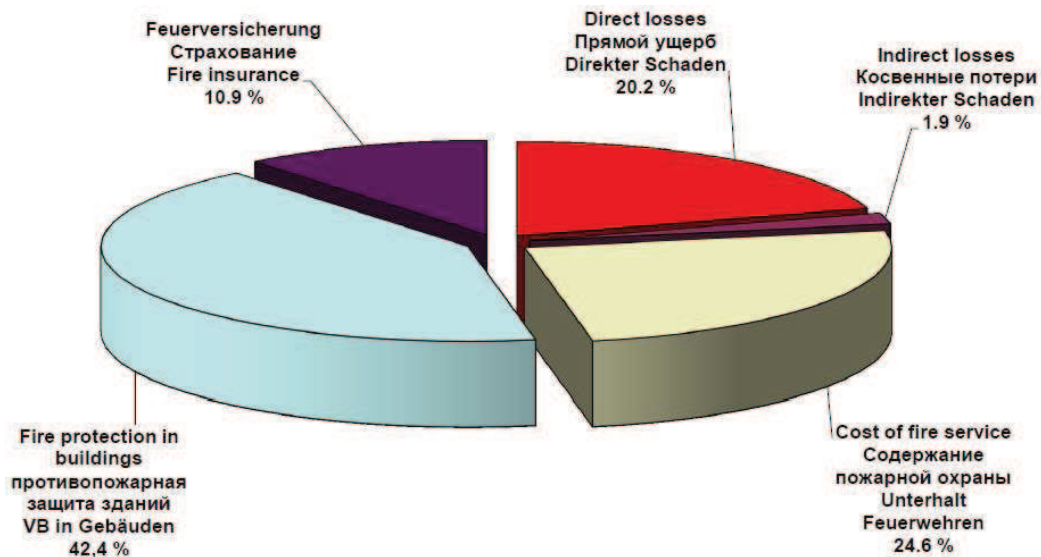


Figure 5: Graphic economic-statistical evaluation of "costs" of fire (average for 2006-2008) [Brushlinsky et al., 2012].

From Figure 5 it arises that between 2006 and 2008 the most relevant impact on costs is that of fire protection in buildings and cost of fire service, indicating a particular attention and effort in preventing fire events.

Social implications are important at the same time because of people injuries and deaths caused by fire (see Figure 6 and Figure 7 about the elaborations carried out by the writer concerning number of deaths and injuries, respectively, between 2006 and 2010, and Annex A for consulting the complete tabulated data) (Brushlinsky et al., 2012).

INTRODUCTION (GENERAL OVERVIEW)

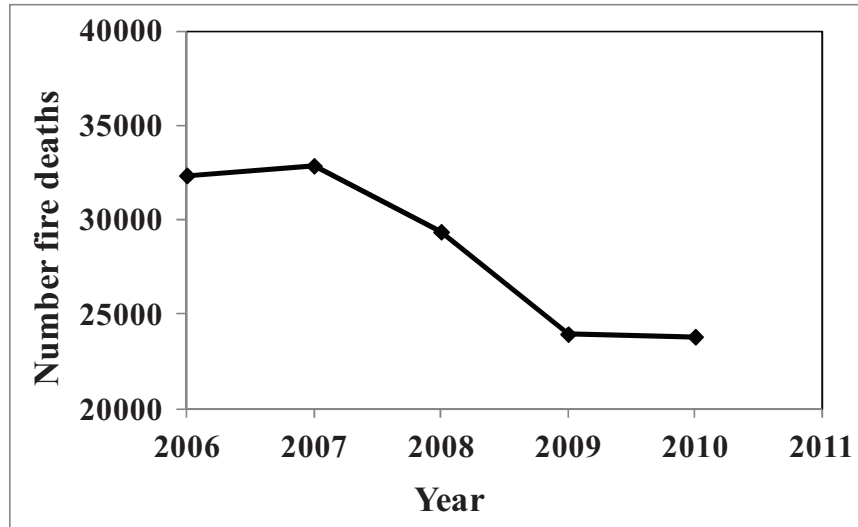


Figure 6: Trends in fire deaths in the countries of the world in 2006-2010.

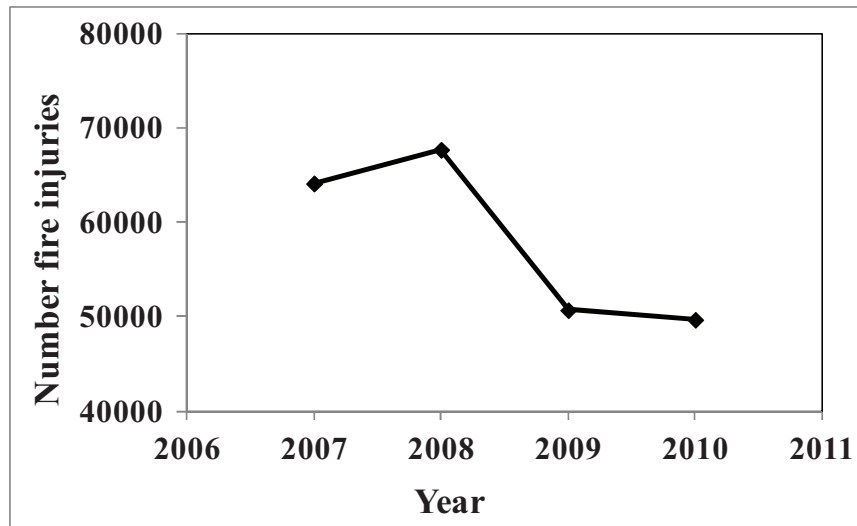


Figure 7: Trends in fire injuries in the countries of the world in 2007-2010.

In Figure 6 and Figure 7 it is possible to appreciate a significant decrease in the number of deaths and injuries, respectively after the year 2007 and 2008. These numbers mean that in the last years important progress has been made but many future initiatives for improvement in fire safety have to be carried out in order to minimize the social and economical impact of fire.

INTRODUCTION (GENERAL OVERVIEW)

1.2.2 Fire: some real cases

In the last decades, severe fire episodes took place in Europe and all around the world; in general they can develop both in confined and non-confined environments.

In case of confined fire scenarios, some of the most serious cases took place in tunnels. A number of unwanted events, combination of events and various faults can lead to a fire in a tunnel. Up to about 95% of all fires are caused by electrical and mechanical defects in the vehicles, i.e. motor and brake overheating. Less frequent causes are collisions, technical defects of tunnel equipments and maintenance works in tunnels. The duration of recorded serious fires in road tunnels ranges from 20 minutes to 4 days.

Most of the serious fires are in the magnitude of 2-3 hours; however, 4 fires in road tunnels stand out as particularly serious (European Thematic Networks of Fire in Tunnels):

- **Nihonzaka**, Japan, 1979, collision, duration 4 days (7 deaths and 2 injuries);
- **Mont Blanc**, France/Italy, 1999, self-ignition of a Heavy Goods Vehicle (HGV), duration 53 hours (39 deaths);
- **Tauern**, Austria, 1999, collision, duration 15 hours (12 deaths and 40 injuries);
- **Gotthard**, Switzerland, 2001, collision, duration 20 hours (11 deaths).

Some pictures of the above-mentioned events are shown in Figure 8.



Figure 8: Fire in Mont Blanc (a) and Gotthard tunnels (b).

Most of the fire scenarios in non-confined environments are related mainly to large concrete structures, that normally present good behaviour in fire. A very large number of reinforced concrete buildings which have experienced severe fires have been repaired and put back into use. Concrete

INTRODUCTION (GENERAL OVERVIEW)

resistance to fire is due to its non-combustible characteristic, as well as its low thermal conductivity. In fact, catastrophic failures of reinforced concrete structures in fire are rare, even if occasionally they may occur. In these cases, the structural failure is mainly caused by the inability of the other parts of the structures to absorb the large imposed thermal deformations, and seldom to the loss of strength of the materials (Buchanan, 2001).

Some examples of real fire in structures are reported as follow:

- **The Windsor Tower Fire** (Madrid, Spain, 2005): 32-story tower made of steel-reinforced concrete. The fire, which lasted for almost a day, spread quickly throughout the entire building, leading to the collapse of the outermost steel parts of the upper floors (Figure 9). While seven firefighters were injured, nobody was killed in the fire, which was the worst in Madrid's history.



Figure 9: Windsor Tower Fire during and after fire.

- **CESP Building 2 Fire** (Sao Paulo, Brazil, 1987): one of the biggest fires in Brazil took place on 21th May 1987, in which a substantial partial collapse of the central core of the CESP Building 2 occurred (Figure 10). This was a 21-story office building, headquarters of

INTRODUCTION (GENERAL OVERVIEW)

the Sao Paulo Power Company (CESP). Buildings 1 and 2 of this office complex were both constructed of reinforced concrete framing, with ribbed slab floors (Beitel and Iwankiw, 2010).



Figure 10: CESP 2 Core Collapse in Sao Paulo, Brazil.

- **Fukushima Daiichi nuclear disaster** (Japan, 2011): was an energy accident at the Fukushima Nuclear Power Plant, initiated by the tsunami of the Tōhoku earthquake and tsunami on 11th March 2011. The damage caused by the tsunami produced equipment failures, and without this equipment a loss-of-coolant accident followed with nuclear meltdowns and releases of radioactive materials beginning on March 12th. It is the largest nuclear disaster since the Chernobyl disaster of 1986. On this occasion, 4 severe fires took place after the earthquake and tsunami. The numbers of deaths for the disaster are almost 15000 and 3000 missing persons (Figure 11).



Figure 11: Fukushima fires after earthquake and tsunami.

INTRODUCTION (GENERAL OVERVIEW)

1.2.3 Temperature-time curves for different fire scenarios

In order to study the impact of fire on concrete materials, temperature-time curves have been defined from experience in real fires for testing, analysis and design fire scenarios. They differ on the basis of maximum temperature (T_{\max}), the time needed to reach T_{\max} and the heating rate in the initial phase (the first 20 minutes); they are divided in three main categories, depending upon the applications (buildings, offshore/petrochemical structures, tunnels)(Koury, 2000):

- **ISO 834:** this curve is applied to various elements in construction for determining their fire resistance when subjected to standard fire exposure conditions (according to ISO 834-1, 1999). The standard furnace curve represents a typical building fire based upon a cellulosic fire in which the fuel source is wood, paper, fabric, etc. The related equation of T (average furnace temperature in °C) in function of time is:

$$T = 345 \log (8t + 1) + T_0$$

where t is the time (minutes) and T_0 is the ambient temperature (°C).

By comparison, real fires can have a slower or longer growth phase, and once they are established, temperatures can be higher than the furnace temperatures, though they are rarely sustained because they are subject to pronounced fluctuations. The standard temperature-time curve, therefore, corresponds to a severe fire, but not the severest possible fire.

- **Hydrocarbon (HC) curve:** this curve is used to carry out tests on structures and materials used within the petrochemical industry. The hydrocarbon curve is applicable where small petroleum fires might occur, i.e. car fuel tanks, petrol or oil tankers, certain chemical tankers etc. In fact, although the hydrocarbon curve is based on a standardised type fire, there are numerous types of fire associated with petrochemical fuels. The temperature development of the Hydrocarbon (HC) fire curve is described by the following equations:

$$T = 20 + 1080 (1 - 0,325 e^{-0,167 t} - 0,675 e^{-2,5 t})$$

where t is the time (minutes) and T is the temperature in °C.

Derived from the above-mentioned Hydrocarbon curve, the French regulation considers an increased version of the same curve, named Hydrocarbon Modified (HCM) curve. The maximum temperature of the HCM curve is 1300°C instead of the 1100°C related standard HC curve. However, the temperature gradient in the first few minutes of the HCM fire is as

INTRODUCTION (GENERAL OVERVIEW)

severe as all Hydrocarbon based fires (RWS, HCM, HC), possibly causing a temperature shock to the surrounding concrete structure and concrete spalling as a result of it.

- **RWS AND RABT:** recently, most of major tunnel fires has indicated that an even more severe fire scenario needs to be considered. In the Netherlands, the Ministry of Public Works, the Rijswaterstaat (RWS), and the TNO Centre for Fire Research have established a fire curve for the evaluation of passive protecting materials in tunnels. This RWS Dutch fire curve models a most severe hydrocarbon fire, rapidly exceeding 1200°C and peaking at 1350°C after 60 min and then falling gradually to 1200°C at 120 min, the end of the curve. However, the maximum temperatures attained in recent major fires did not reach RWS levels, e.g. Channel (1100°C), Great Belt (800°C), Mont Blanc (1000°C), Tauern (1000 3C). The RWS fire curve, therefore, represents the severest form of tunnel fire in terms of initial heating rates and maximum temperatures.

The RABT German fire curve, with a descending branch, represents a less severe fire scenario in tunnels than the RWS curve, reaching a maximum temperature of 1200°C sustained up to 1 h before decaying to ambient.

The graphic comparison among all the above-mentioned curves is reported in Figure 12.

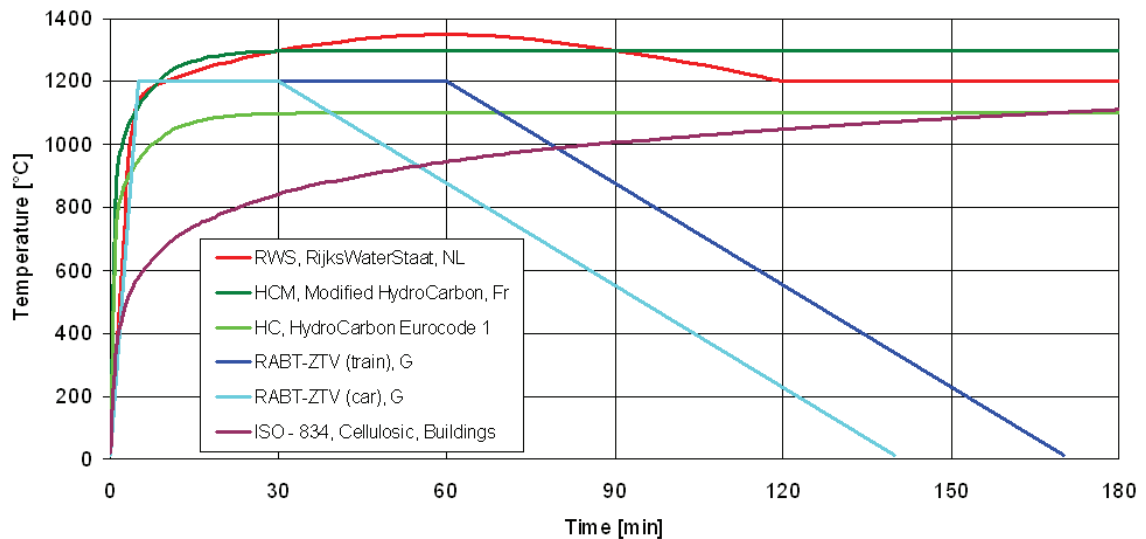


Figure 12: Temperature-time curves for fire scenario evaluation.

From the comparison among all the above-mentioned curves, the RWS reaches the highest temperature in the longest time; instead, the most severe in the first part of the fire scenario is the

INTRODUCTION (GENERAL OVERVIEW)

HC as well HCM. The ISO 834 curve presents the lowest T_{\max} , reached after 180 minutes of fire exposure, thus it is the less severe among all those considered.

1.2.4 The concept of construction robustness

Considering all these aspects related to fire behaviour of concrete structures and elements, it can be interesting to introduce the concept of robustness. It has to be evaluated in case of contemporary unfavorable events, consisting not only in fire, but also earthquake, explosive loading or impacts, as occurring in the exceptional real case of Fukushima disaster. Hence, the most important aspect characterizing the material could be the evaluation of robustness in concrete structures in order to contrast severe events, first of all real fire, that can also take place as consequence, for example, of earthquake phenomena.

The Italian Code (Technical Italian Law on Construction, 2008) introduces the concept of combined actions for ultimate state structural design, in Paragraph 2.5.3. In the same document, fire is considered as an exceptional action as well as explosions and shocks. Thus, it could be important to evaluate the construction robustness following technical legislations that take into account the effect of combined severe actions.

1.3 Type of Damage in Concrete Structures Subjected To High Temperatures/Fires

The performances of concrete at high temperature and fire exposure have often been taken for granted because of its non-combustible nature as well as its capacity to prevent the thermal diffusion and the fire spread through structural elements. On the other hand, it has to be considered that concrete and fire have a complex interaction, due to the composition of concrete and the extreme thermal conditions often found in fire. Concrete is already defined as a non homogeneous material, where each of its components has a different reaction to thermal exposure in itself, and the behaviour of this composite system in high temperature and fire is not easy to define or model (Khoury, 2000).

Moreover, the fire behaviour of concrete is linked to the temperature-dependant material properties. Since the thermal diffusivity is rather low, compared to steel, strong temperature

INTRODUCTION (GENERAL OVERVIEW)

gradients are usually generated within fire-exposed concrete elements. Together with the high thermal inertia, this means that the core region may take a long time to heat up. Thus, whilst the compressive strength of concrete is rapidly lost beyond a critical temperature, which is not too dissimilar to the equivalent temperature for loss of steel strength, structural effectiveness is not diminished until the bulk of the material reaches the same temperature. This requires an analysis of the thermal response of the entire structural element (Fletcher et al., 2007).

Considering the heterogeneous nature of concrete and its constituents, it arises that thermal exposure causes significant effects on the material, especially on:

- Microstructure, which reaches an evolution due to chemical and crystallographic changes induced by thermal exposure;
- Mechanical properties, which undergo a significant decrease after specific values of temperature exposure, as well as after fire scenario;
- Macroscopic behaviour, principally linked to concrete explosive spalling taking place in a concrete element.

For all the exposed reasons, it is necessary to distinguish the damage types occurring in concrete and its constituents, when exposed to high temperature and/or fire. In the next paragraphs, these aspects, intimately linked between them, will be presented, concerning the material intrinsic damage, its mechanical behaviour and the occurring of spalling phenomenon after thermal exposure.

1.3.1 Intrinsic damage

When concrete is exposed to high temperature and fire, some chemical transformations take place at micro-level. At specific temperature ranges, degradation reactions of different type of chemical compounds occur, in particular related to the hydrated phases in cementitious matrix, as well as the aggregates. These phenomena can be considered as intrinsic damage, which influences the microstructure evolution during the thermal exposure.

The chemical changes due to thermal exposure will be distinguished in the next literature review paragraphs on the basis on those occurring in cement paste, also in case of blended cements, and

INTRODUCTION (GENERAL OVERVIEW)

aggregates. Their differences can also appear as different microcracks patterns and damage both at micro- and macro-levels.

In order to complete the basis collection of information regarding this topic, the evolution of the microstructure of the whole concrete system will be explained, considering also the effect that Polypropylene fibers, commonly added to mixes in order to reduce explosive spalling, carry out on concrete material. The PP fiber mode of action (up to now not completely understood) will be discussed as well.

1.3.2 Mechanical damage and spalling

When concrete is exposed to high temperature and/or fire, it is well-known that it undergoes decay in mechanical properties.

In this context, the two different types of macroscopic effect that occur in concrete exposed to thermal actions will be considered: the modification in mechanical properties (such as compressive strength, stress-strain curves, modulus of elasticity and splitting tensile strength) and spalling phenomenon.

Explosive spalling which takes place in concrete elements presents structural implications, because as a consequence the rebars will be directly exposed to the surroundings and the structural integrity can be significantly affected. If spalling does not take place, the material may maintain its integrity characteristics and its elastic properties for probably a hundred °C more than the temperature in which the material and element result damaged. For this reason, the spalling phenomenon must be treated in a specific way, including it in a more general context regarding thermal degradation of concrete constituents. The latter context is linked to heating rate, impacting on degradation reactions kinetics, and material type.

The causes generating explosive spalling will be deepened in the literature review, as well as the mass transport equation, considering the fundamental role that permeability plays on this phenomenon. For this reason, some experimental set-up for measuring the permeability of concrete at high temperatures will be presented.

INTRODUCTION (GENERAL OVERVIEW)

1.4 Introduction (General Overview): conclusive remarks

From the previous paragraphs, it arises that high temperature and especially fire exposure lead to severe economical direct and indirect damages as well as serious social implications, related to significant number of deaths and injuries. More specifically, one of the components in economical fire impact is surely caused by structure damage, sometimes accompanied by significant failure, which means that not only the whole structures, but also the material, play an important role in thermal exposure behaviour.

It is also introduced the concept of structure robustness (Technical Italian Law on Construction, 2008) which regards the risk of combine actions. In the mentioned document, the fire is considered as exceptional action as well as explosions and shocks, which should be taken into account as combine in order to evaluate the effect on structural characteristics.

In the previous last Paragraph, the principal types of concrete damages due to thermal actions (on material and structures) are also defined. More specifically, the concept of intrinsic damage is introduced, concerning the nano, micro and meso scale, as well as the mechanical damage, considering also spalling phenomena, both occurring at macroscale.

2. LITERATURE REVIEW

2. LITERATURE REVIEW

2.1 Intrinsic Damage

Intrinsic damage of concrete exposed to high temperature or fire can derive from:

- a combination of chemo-physical reactions taking place within the cementitious matrix or aggregates, at micro-nano level;
- at meso level, thermal incompatibility between the cementitious matrix and aggregate that can initially lead to triggering of debonding and microcracking phenomena localized at the interface zone (ITZ) between these components; considering that the ITZ is the weakest zone in concrete, these occurrences can lead to an onset of interfacial microcracks that can propagate into the matrix and bridge between aggregates with a consequent progressive collapse of concrete structure.

Moreover, depending on the temperature reached during the thermal exposure, different chemical and physical changes occur in concrete, leading to variations both in microstructure and physico-mechanical properties. In particular, the main chemical process responsible for the internal damage of concrete is the alteration of hydrates.

In the next Paragraphs, the chemical degradation in the cement paste and aggregates will be presented, as well as the microstructural changes occurring in concrete after high temperature exposure.

2.1.1 Main constituents of concrete

In the following, the thermal behaviour of the main constituents of concrete will be considered, in particular cementitious pastes (either pure or blended) and aggregates.

2.1.1.1 Thermal degradation of cementitious paste

2. LITERATURE REVIEW

2.1.1.1.1 Portland cement paste

Cement pastes, when exposed to high temperature, are subjected to a series of chemical transformations, each of them occurring in a specific temperature range. The most relevant cement paste degradation reactions are the following, proved by Thermogravimetric Analysis (TGA) carried out on cement pastes heated at different temperatures, from 100 to 750°C (Alonso and Fernandez, 2004):

- Below 100°C, ettringite disappears;
- The water supposed free present in the samples is removed up to about 105°C;
- From 105 and 300°C, the most part of bound water mainly from the C-S-H gel is expelled from the cement paste. This process is concluded at about 350°C (see Figure 13 and Figure 14);
- Portlandite, Ca(OH)_2 (CH), dehydration occur between 400 and 500°C, producing CaO;
- Between 650 and 800°C, the calcite (CaCO_3) decarbonation takes place, converting to CaO;
- At 750°C the C-S-H gel completely disappears and is mainly replaced by new nesosilicate phase (similar to a structure of C_2S but with less crystalline structure).

Figure 13 represents the evolution quantity of chemical compounds (indicated as normalized intensity of the signal), experimentally detected in cement paste by Neutron Diffraction, during thermal exposure up to 700°C. It concerns the thermal behaviour of a Portland cement paste containing a high Tricalcium Aluminate (C_3A) content and high alkaline content (Castellote et al., 2004).

From Figure 13, the disappearance of ettringite is confirmed below 100°C, as well as the portlandite dehydration, in this case occurring between 500 and 600°C, with the contemporary increase in CaO content beyond 500°C. An increase of larnite (known in Cement Chemistry as Belite, C_2S) is detected when the crystalline fraction of the C-S-H gel disappears, which undergoes dehydration up to 400°C. An increase in anhydrous silicate content has been also observed by other Authors, considering the sum of C_2S and C_3S , detected by means of X-Ray Diffraction (XRD) (Piasta, Sawicz and Rudzinski, 1984).

2. LITERATURE REVIEW

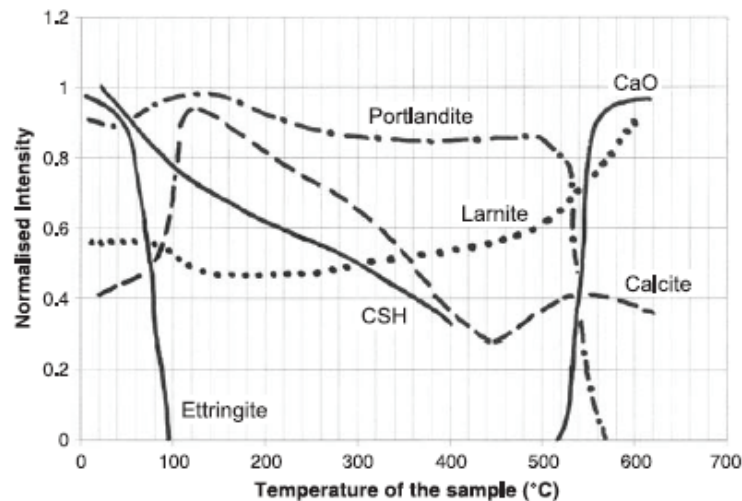


Figure 13: Evolution of the normalised intensity during heating for the different compounds in cement paste (high C₃A amount) [Castellote et al., 2004].

Regarding calcite, a content increase is detected up to 120°C, due to precipitation caused by the loss of the free water in the pores of the paste. Furthermore, there is an additional release of Ca²⁺ coming from the decomposition of ettringite, which certainly contributes to the precipitation of calcite, besides portlandite. A further increase in calcite content is shown between 450 and 550°C, due to the carbonation of CaO caused by the CO₂ gas existing in the cementitious matrix pores (Alonso and Fernandez, 2004).

As a comparison, the same graph as the previous is reported in Figure 14 regarding a cement paste prepared with a Portland cement type containing low C₃A and low alkaline content.

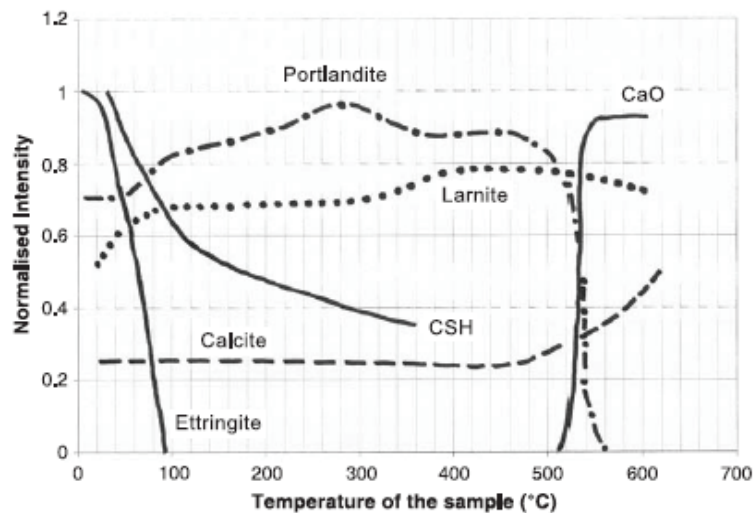


Figure 14: Evolution of the normalised intensity during heating for the different compounds in cement paste (low C₃A amount) [Castellote et al., 2004].

2. LITERATURE REVIEW

Comparing Figure 13 and Figure 14 the most significant difference is related to the calcite trend, which in the second case remains constant before starting to increase at almost 500°C. Another important difference is the change of temperature of portlandite dehydration (in the second case, this reaction starts at lower temperature, almost 450°C) as well as the C-S-H dehydration trend, which is faster up to 150°C in case of low C₃A cement paste. It is important to underline that in the literature different decomposition reactions of C-S-H have been mentioned, so it is confirmed that different trends can be detected (Shaw, Henderson and Komanschek, 2000).

From the microstructural point of view, experimental observations with Scanning Electron Microscopy (SEM) have been conducted on Ordinary Portland cement pastes, exposed to temperature from 105 and 1000°C (Zang and Ye, 2011). The microstructural development process can be divided in three steps:

- From 30°C to 400°C, the microstructure of cement paste didn't change too much. The C-S-H kept gel-like morphology;
- From 500°C to 800°C, due to the volume change of hydrate, cracks occur in the cement paste matrix. The isolated pores in the cement paste matrix became connected with each others. C-S-H gel and portlandite is converted to their dehydration products. The gel-like C-S-H shrunk gradually and became more and more dense.
- At about 1000°C, the hydrates including C-S-H were transferred into crystalline-like phase completely and the pore system seriously expanded.

From the experimental results shown, the above-mentioned chemical changes have an impact also on the porosity and connectivity of pore and they increase in value with increasing temperatures (Zang and Ye, 2011).

2.1.1.1.2 Effect of mineral constituents on thermal behaviour of cement pastes

Different Authors conducted experimental studies on blended cement pastes containing different types and contents of mineral constituents, including pozzolanic materials, in order to characterize their microstructure and physico-mechanical behavior after exposure to elevated temperatures.

More in detail, the addition of 15% of metakaolin MK (a pozzolanic material obtained by controlled calcinations of caolin) and silica fume SF (obtained as a byproduct of industrial

2. LITERATURE REVIEW

production of silica and iron-silica alloys) after thermal exposure at 200, 400 and 800°C causes a relatively compact microstructure and a low porosity in comparison with those related to cement pastes. These effects lead to relatively high compressive strength values as compared with those of cement paste at 800°C (Morsy, Shebl and Rashad, 2008).

The addition of fly ash FA (obtained by electro-precipitation of ashes produced during combustion of coal), in different amount of substitution, has also been studied and it has been detected that even a 10% fly ash replacement completely eliminates all visible surface cracking due to post-cooled exposure to air for specimens heated-up at 600°C. The rapid degradation of mechanical properties beyond 300°C is probably due to the onset of increasing porosity and microcracking above that temperature. The disintegration of specimens on post-cooled exposure after thermal treatment at 400°C can be connected to the portlandite dissociation and its subsequent expansive rehydration on post-cooling phase (Dias, Khoury and Sullivan, 1990).

Another main constituent of cement can be the Ground Granulated Blast Furnace Slag (GGBS) thanks to its latent hydraulicity. GGBS is a byproduct of blast furnace industrial production. It was found that cement pastes, in which cement has been partially replaced by slag, achieved a significant and beneficial reduction of the amount of CH₂ in fact an increase in the proportion of slag in the cement paste, in general, led to an improvement in the mechanical properties following exposure to temperatures beyond 400°C (Mendes, Sanjayan and Collins, 2008).

As a mineral addition also quartz powder has been considered (even if this is not complied with EN 197-1, 2011) in substitution of cement. SEM investigations show, in Figure 15, the microstructure of cement paste (QP0, a) after 28 days at room temperature appears to have less density with open microstructure and limited amount of C-S-H compared to the microstructure containing quartz powder (QP20, b). The latter shows, after exposure to elevated temperature of 600°C, more compact and defined structures than those of cement pastes (QP20, d). After 1000°C exposure, all the hydrated phases including C-S-H appear as amorphous structures by losing their characteristic crystal structure. In the present work, the Authors didn't study the α - β quartz transition. Further, a more significant increase in porosity due to the CaCO₃ decomposition was accompanied by microstructural damage. In particular the blended cement paste containing quartz powder (QP20, f), presents a microstructure similar to the microstructure observed for cement paste (QP0, e), but seemed to be denser and with lower porosity. From the current described paper, it arises that the quartz addition enhances the mechanical properties and thermal shock resistance of this type of blended cement pastes; moreover, the improved fire-resistant properties can be

2. LITERATURE REVIEW

attributed to two aspects, one is that addition of quartz powder can help to form dense structure of the paste and the other is the lower amount of CH contained in the system (Rashad and Zeedan, 2012).

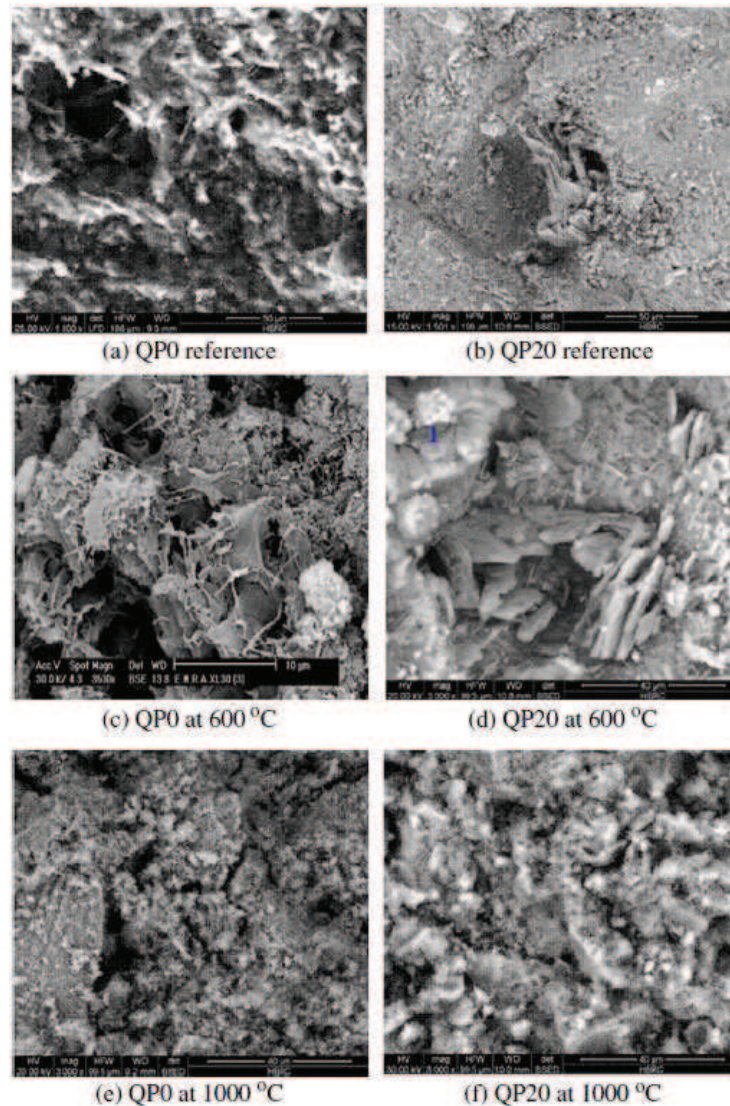


Figure 15: SEM micrographs of fracture surfaces of hardened QP0 and QP20 at different temperatures [Rashad and Zeedan, 2012].

From the above-mentioned papers, it was found that the replacement with pozzolanic materials or mineral additions (such as metakaolin, silica fume, fly ash, slag and quartz) allows to enhance the residual compressive strength and thermal shock resistance, and to decrease damage phenomena. These properties are due to a denser microstructure, with lower porosity, which enhances the mechanical behaviour of the material.

2. LITERATURE REVIEW

2.1.1.1.3 Thermodynamic and kinetic aspects of thermal degradation reactions

The thermal degradation phenomena due to chemical reactions are conditioned by thermodynamic and kinetic factors, influencing the rate with which they occur. The relations regulating these factors are complex if multi-components systems are considered. In fact, the dehydration reaction of each compound present in the system contributes to the kinetic of global degradation reaction, as well as to thermodynamic, in particular to equilibrium. Because of the reaction reversibility, all these considerations are valid also for the rehydration phenomenon taking place during the cooling phase.

These aspects have been considered to evaluate the effect of heating rate on dehydration reactions in order to design the thermal cycle to be applied on concrete specimens. Hence, these considerations will be explained in Paragraph 4.1.3.1, regarding the thermal cycle design.

The above-mentioned complexity of the system leads to consider, in this discussion, only the degradation reactions of the main components, and in particular the dehydration of portlandite (**case A**), ettringite (**case B**) and C-S-H (**case C**).

First of all, a brief general introduction regarding the thermodynamic equilibrium of a chemical reaction is presented in order to explain the concept of equilibrium constant K and degree of conversion X .

Considering a generic reaction:



where:

- $\alpha_1, \alpha_2, \alpha_n$ are the reaction coefficients of reagents;
- $\beta_1, \beta_2, \beta_n$ are the reaction coefficients of products;
- R_1, R_2, R_n are the different species of reagents;
- P_1, P_2, P_n are the different species of the products.

The equilibrium constant K is defined as:

$$K = P_1^{\beta_1} \cdot P_2^{\beta_2} \cdot \dots \cdot P_n^{\beta_n} / R_1^{\alpha_1} \cdot R_2^{\alpha_2} \cdot \dots \cdot R_n^{\alpha_n} = \prod_{i=1}^n P_i^{\beta_i} / \prod_{i=1}^n R_i^{\alpha_i} \quad [1]$$

2. LITERATURE REVIEW

The reaction degree of conversion X , indicating the quantity of product obtained at time t in relation to total conversion of reagents, is expressed as:

$$X = (m_i - m_t) / (m_i - m_f) \quad [2]$$

where:

- m_i is the initial sample mass;
- m_f is the final sample mass;
- m_t is the current sample mass at time t .

The equilibrium conditions are influenced by pressure and temperature of the system. For example, the effect of these parameters on equilibrium constant K related to portlandite dehydration can be represented schematically in Figure 16 (Schaube et al., 2012).

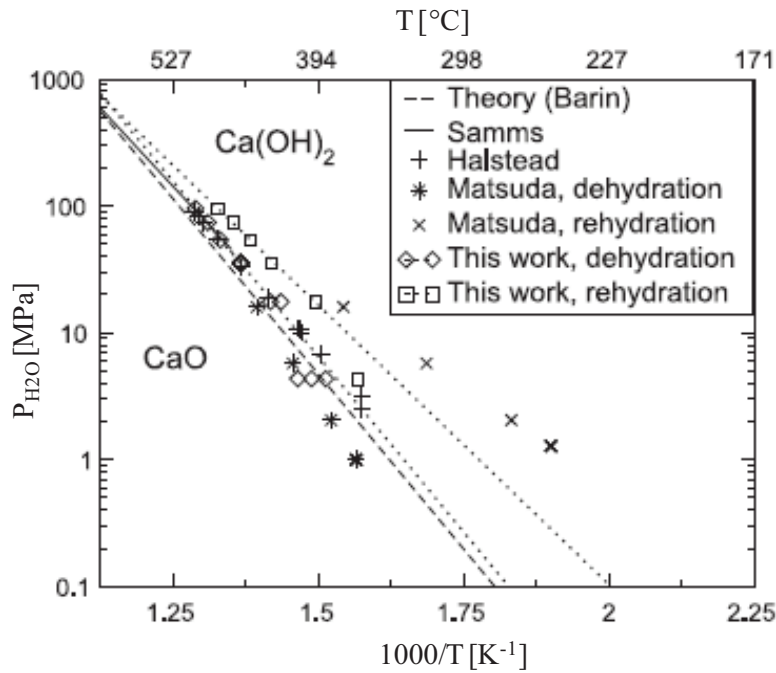


Figure 16: Equilibrium relationship between temperature and pressure for portlandite dehydration [Schaube et al., 2012].

From Figure 16 it can be drawn that as the equilibrium temperature of thermal dehydration of CH increases, the partial pressure of H_2O at equilibrium (P_{H_2O}) increases.

The degree of conversion, because of its dependency by time, can be used to define the conversion rate (dX/dt) and its direct link to reaction kinetic constant k by the following relation (considering that $f(X)$ is a tabulated function depending on conversion degree):

2. LITERATURE REVIEW

$$dX/dt = k(T) \cdot f(X) \quad [3]$$

The kinetic constant k (indicating the quantity of reagent consumed or product formed in the time unit due to a chemical reaction) is function of temperature by the well-known Arrhenius Equation (Atkins, 2006) [4]:

$$k(T) = A \cdot \exp\left(\frac{-E_a}{RT}\right) \quad [4]$$

where :

- A defines the pre-exponential factor;
- E_a the activation energy (tabulated);
- R is the molar gas constant.

Substituting the Arrhenius Equation in relation [3], the following expression for conversion rate is obtained:

$$dX/dt = k(T) \cdot f(X) = A \cdot \exp\left(\frac{-E_a}{RT}\right) \cdot f(X) \quad [5]$$

where the direct relation between the rate of conversion and kinetic constant, dependant by temperature, is highlighted.

Three special cases of dehydration kinetics are presented below.

CASE A: Portlandite dehydration

The de- and rehydration of CH has been considered on the basis of some experimental papers regarding the related thermodynamic and kinetic aspects. This is reversible gas-solid reaction:



According to Zelić et al., CH starts to decompose at 430°C, the activation energy is $E_a=127$ kJ/mol, the pre-exponential factor is $A=7.58 \times 10^6 \text{ s}^{-1}$, and the kinetic expression follows a power law (Zelić et al., 2002):

$$f(X) = 2 \cdot X^{1/2} \quad [6]$$

2. LITERATURE REVIEW

The conversion rate equation, valid for conversion degrees between 0.004 and 0.554, can be expressed as follows:

$$dX/dt = 1.516 \times 10^7 \exp(-1.528 \times 10^4/T) \cdot X^{1/2} \quad [7]$$

It was also found from the Authors that the conversion rate against the conversion degree is mirror-symmetric with respect to the conversion degree of 0.5, in which the rate of conversion is the highest, as shown in Figure 17 (Zelić et al., 2002).

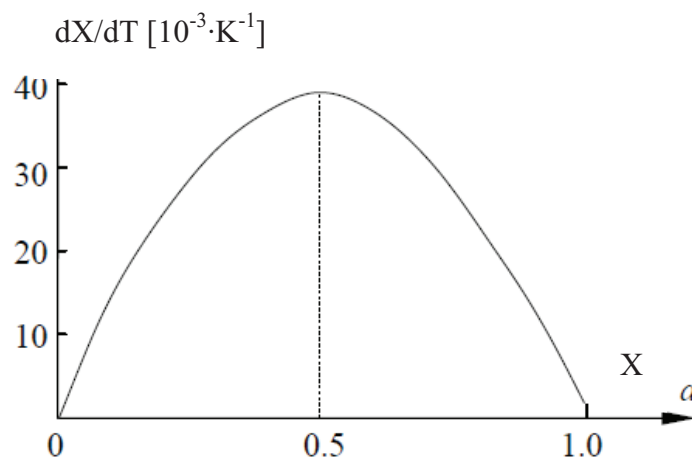


Figure 17: Conversion rate of CH as a function of conversion degree at heating rate of 20°C/min [Zelić et al., 2002, graphic elaboration by Zhao, 2012].

The Authors have also indicated the dependence of rate of conversion in function of temperature, at different conversion degrees, and it is plotted in Figure 18.

2. LITERATURE REVIEW

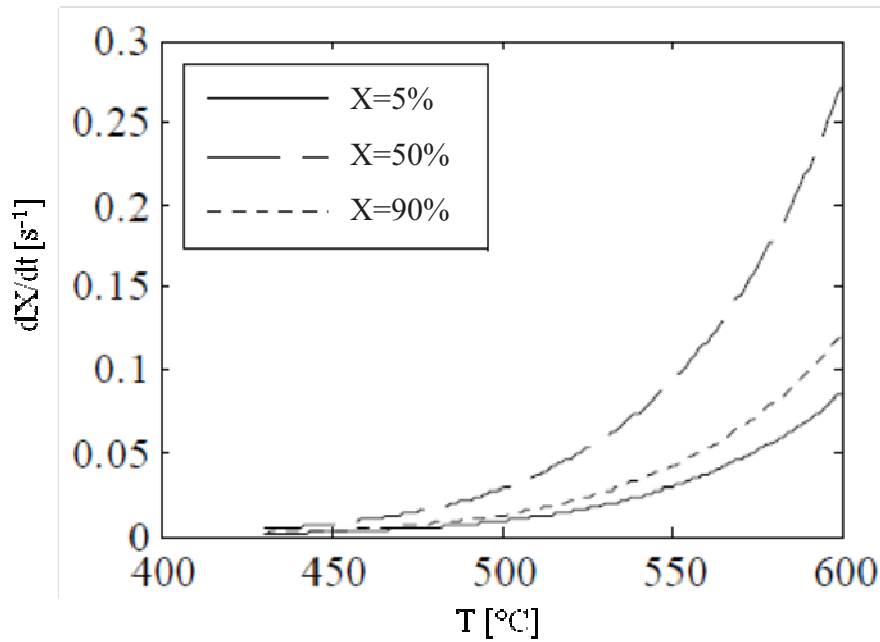


Figure 18: Conversion rate of CH as a function of temperature at different conversion degrees [Zelić et al., 2002, graphic elaboration by Zhao, 2012].

In Figure 18, it arises that the rate of conversion is the highest in case of $X = 0.5$, at constant temperature, confirming the previous data in Figure 17. Then, comparing the curves related to X equals to 0.05 and 0.9, it can be observed that the conversion rate is higher in the second case, at constant temperature.

Moreover, the variation of degree of conversion in function of temperature, with different heating rate, has been detected also in N_2 atmosphere and reported in Figure 19 (Schaube et al., 2012).

From Figure 19 the curves reach different maximum peak depending on heating rate, thus it is possible to correlate the degree of conversion with the heating rate parameter. The higher the heating rate, the higher the temperature corresponding to maximum peak and the lower the peak value of degree of conversion in function of temperature.

It arises that fixed a value of degree of conversion, the higher the heating rate, the higher the temperature needed to reach that value. In Figure 19 for X value of 0.2, it has shown that for reaching the considered X value, a higher temperature for higher heating rate is needed.

2. LITERATURE REVIEW

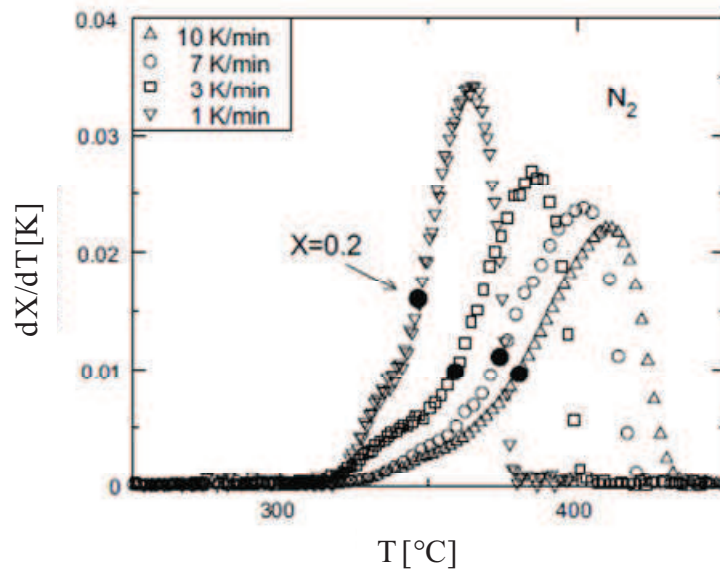


Figure 19: Dehydration of CH in N₂ atmosphere [Schaube et al., 2012].

CASE B: Ettringite dehydration

Ettringite (AFt) is one of the hydrated phase of Portland cement and it presents expansive behaviour when it is formed. As for CH, AFt undergoes degradation reaction when exposed to high temperatures.

Some Authors have studied the AFt degradation reaction kinetic, obtaining that the activation energy is $E_a = 59$ kJ/mol, the pre-exponential factor is $A = 1.0 \times 10^{-6} \text{ min}^{-1}$ ($1.66 \times 10^4 \text{ s}^{-1}$), and the kinetic expression is the following (Pourchez et al., 2006):

$$f(X) = (1 - X)^{1/2} \quad [8]$$

The Authors detected that AFt started to decompose at 70°C; the conversion rate can be expressed in the next equation, while the conversion rate in function of temperature, at constant rate of conversion, is indicated in Figure 20:

$$dX/dt = 1.66 \times 10^4 \exp(-7.096 \times 10^3/T) \cdot (1-X)^{1/2} \quad [9]$$

2. LITERATURE REVIEW

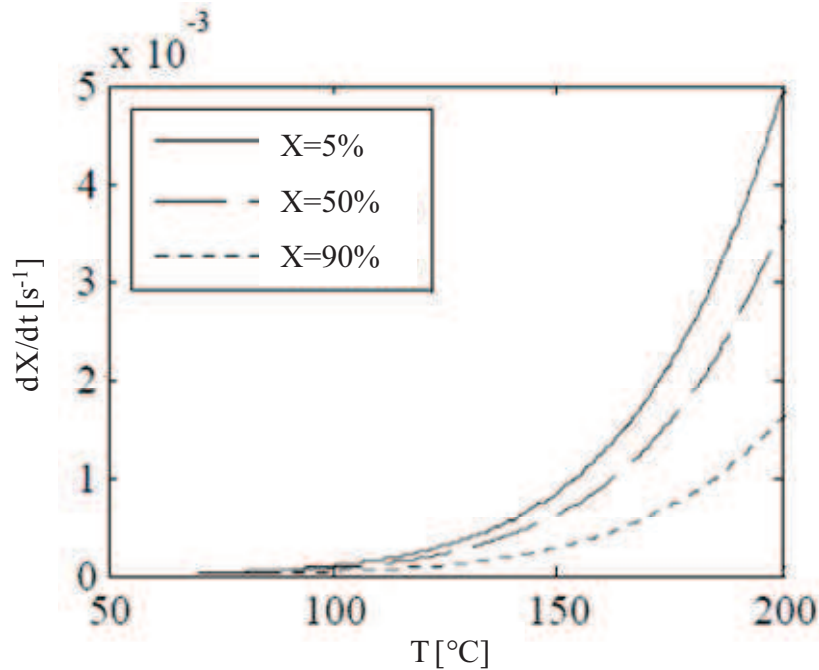


Figure 20: Conversion rate of AFt as a function of temperature at different conversion degrees [Zhao, 2012].

In Figure 20 it can be observed that the highest rate of conversion is reached for the lower conversion degree of 0.05, while the lowest for a conversion degree of 0.9, at constant temperature. It arises that the highest is the conversion degree, the highest the conversion rate at increasing temperatures.

By integrating the equation [9], the time as a function of temperature for a given X value can be expressed, in a similar way as for CH dehydration.

CASE C: C-S-H dehydration

C-S-H is the hydrated amorphous phase deriving from Portland cement silicate. The chemical formula of conventional solid C-S-H is $(\text{CaO})_{3.4}(\text{SiO}_4)_2(\text{H}_2\text{O})_3$ (Tennis and Jennings, 2000). Its thermal degradation has been experimentally studied by some Authors, which considered three temperatures of exposure and for each of them, they have detected the rate of conversion (Peng and Huang, 2008). The equation [3] explicitated at $T= 600, 700$ and 800°C , after substitution of Arrhenius equation and $f(X)$ expression, becomes as follows according to Peng et al.:

2. LITERATURE REVIEW

$$\frac{dX}{dt} = \begin{cases} 3 \times 10^{-6} t^2 - 0.0026t + 0.36, & \text{for } T = 600 \text{ }^\circ\text{C} \\ 6.0 \times 10^{-6} t^2 - 0.004t + 0.67, & \text{for } T = 700 \text{ }^\circ\text{C} \\ 1.0 \times 10^{-7} t^4 - 3.2 \times 10^{-5} t^3 + 0.0045t^2 - 0.26t + 5.47, & \text{for } T = 800 \text{ }^\circ\text{C} \end{cases} \quad [10]$$

Starting from these equations, the relative C-S-H amount in function of heating duration have been plotted, at the three different temperatures, and reported in Figure 21:

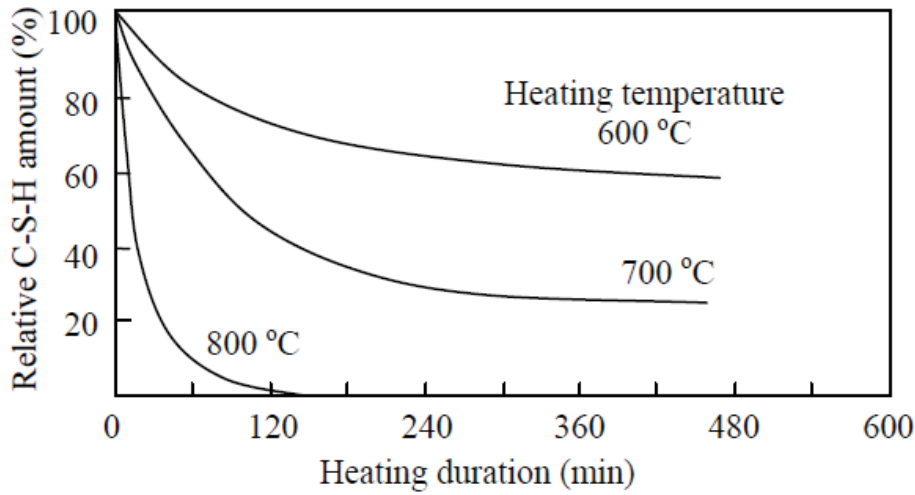


Figure 21: Relative C-S-H amount as a function of exposure duration under different temperatures [Peng and Huang, 2008].

From Figure 21 it can be observed that the dehydration occurs causing a decreasing content of C-S-H, more pronounced and rapid at higher temperature exposure. This decrease takes place up to the achievement of a plateau, with an asymptotic trend, indicating that the thermodynamic equilibrium, expressed by the constant K, has been reached. This plateau level changes with different temperatures, indicating that the conversion degree is influenced not only by temperature exposure, but also by the heating duration. In fact, if the equilibrium is reached, further exposure time is not useful in order to increase the conversion degree.

By integrating the equation [10], the time vs. temperature for an assigned X value can be expressed, in a similar way as for CH and AFt dehydration.

Moreover, the important experimental indication is that increasing temperature exposure, different heating duration time are necessary to reach a certain conversion, thus the exposure time is dependant on the test temperature exposure.

2. LITERATURE REVIEW

2.1.1.1.4 Heating rate effect on intrinsic damage of cement pastes

In Paragraph 2.1.1.1.3, thermodynamic equilibrium conditions have been considered, subjecting the hydrated phases to a theoretical condition of constant temperature exposure. In the current Paragraph, the objective is to collect information regarding dynamic reaction conditions, in which the kinetic effect is prevalent. In particular, it results important to evaluate the influence of temperature on $k(T)$ (see equation [4]), considering that temperature usually increases with time during the thermal exposure.

In order to show the numerical approach applied to study the dependence of conversion degree in function of temperature (depending in turn on time), the CH dehydration has been considered. Starting from [7] equation expressing the rate of conversion in function of temperature:

$$dX/dt = 1.516 \times 10^7 \exp(-1.528 \times 10^4/T) \cdot X^{1/2} \quad [11]$$

and considering that temperature changes in function of time depending on heating rate as $T = \alpha \cdot t$, (linear or non linear correspondence), the previous expression can be written as:

$$dX/dt = 1.516 \times 10^7 \exp(-1.528 \times 10^4/(\alpha \cdot t)) \cdot X^{1/2} \quad [12]$$

Integrating this equation by variables separation and solving it, it is possible to obtain the conversion degree relationships in function of any type of variation of temperature in function of time (linear or not).

In order to observe graphically this effect, Zhao considered four heating rates, 1°C/min, 5°C/min, 10 °C/min (linear), and the standard heating curve recommended in ISO 834 (not linear); the conversion degree of principal hydrated phases, CH, C-S-H and hydrated aluminates are reported in Figure 22, Figure 23 and Figure 24 respectively.

2. LITERATURE REVIEW

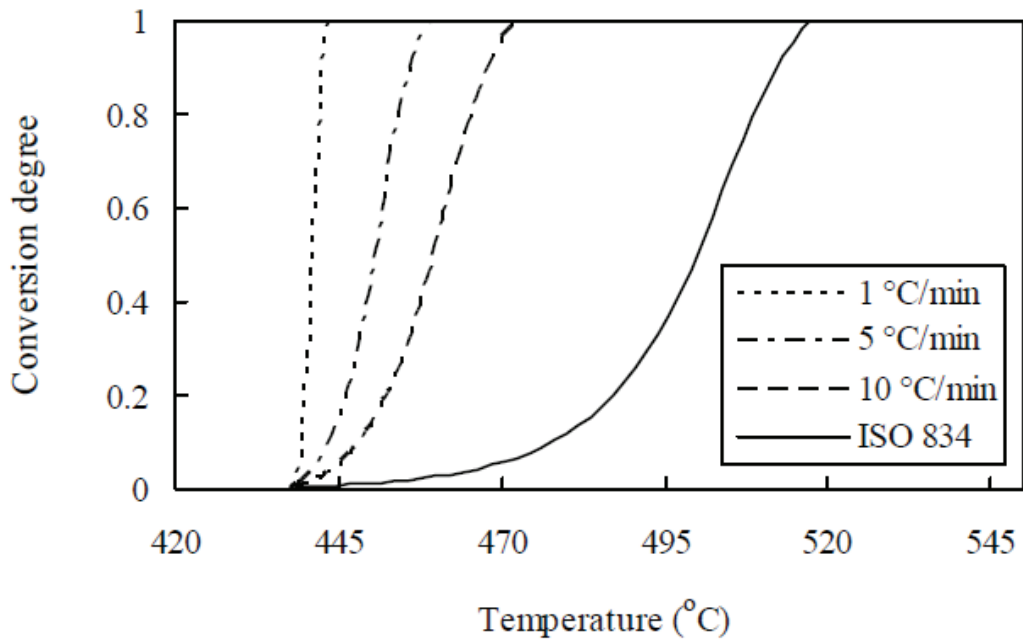


Figure 22: Decomposition of CH under different heating rates [Zhao, 2012].

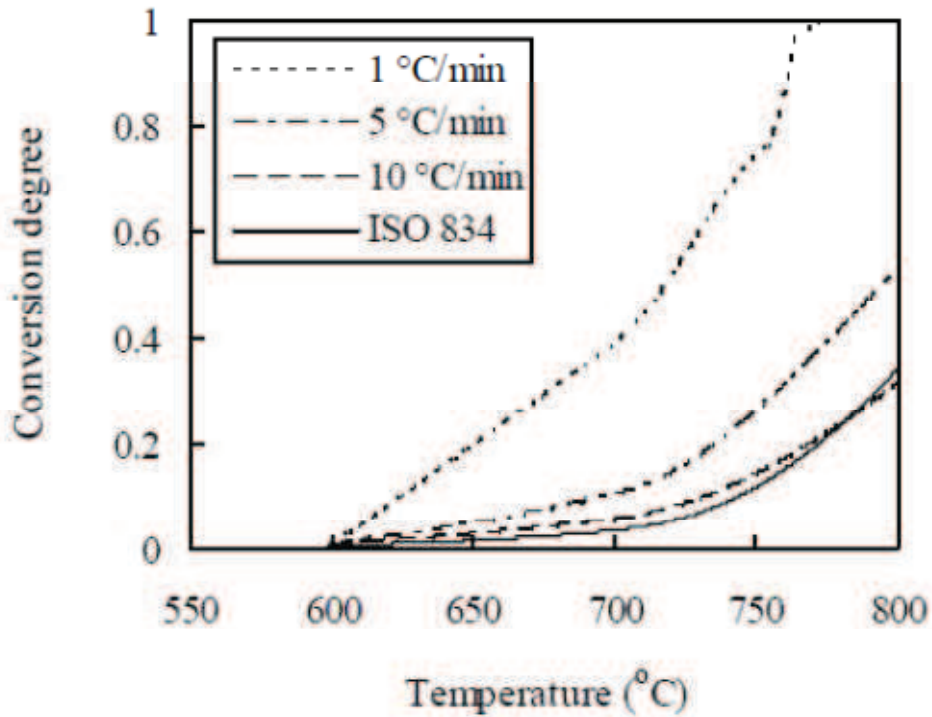


Figure 23: Decomposition of C-S-H under different heating rates [Zhao, 2012].

2. LITERATURE REVIEW

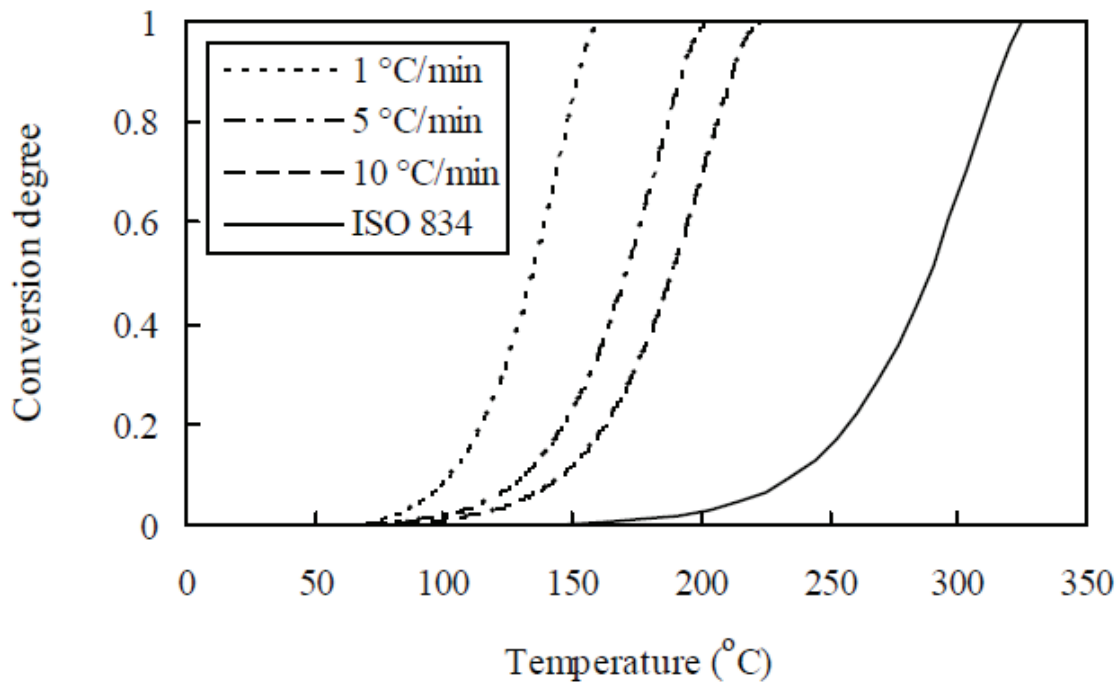


Figure 24: Decomposition of hydrated aluminates under different heating rates [Zhao, 2012].

From the last three Figures, it can be seen that the heating rate exerts a remarkable influence on the hardened cement paste degradation. When the heating rate increases, the temperature of complete decomposition of hydrated aluminates and CH increase (from 162 325°C for aluminates and from 443 to 519°C for CH). At 800°C, C-S-H decomposes completely under the heating rate of 1°C/min. Under the heating rate of 10°C/min or exposed to ISO 834 fire, however, the conversion degree is only about 33%.

It arises also that, at constant temperature value, the higher the heating rate the lower the degree of conversion.

2.1.1.1.5 Volume fraction evolution of cement paste constituents, before and after thermal exposure

As mentioned in the previous paragraphs, the cement paste constituents undergo a thermal degradation when exposed to high temperature, which induces a modification in internal porosity of the material. In this context, it can be significant to predict how the volume fraction related to capillary pores changes, because to the initial water contained in the capillary pores, an additional

2. LITERATURE REVIEW

part deriving from the dehydration reactions has to be considered (Zhao, 2012). Capillary pores are conventionally comprised between tens of nanometers to unit of micrometers (Colleparidi, 1991).

The volume of water, derived from dehydration process, can be regarded as an increase of porosity, given by:

$$f_i^w = f_i^0 a_i n_i^w \frac{\rho_i / M_i}{\rho_w / M_w} \quad [13]$$

where:

- f_i^0 is the initial volume fraction of reactant i ($i=CH, Aft$ and $C-S-H$);
- a_i is the degree of conversion for the reactant i ;
- n_i^w is the amount of water, in mole, decomposed per mole of reactant i ;
- ρ_i is the density of reactant i ;
- ρ_w is the density of water;
- M_i is the molar mass of reactant i ;
- M_w is the molar mass of water;

The increase in porosity due to dehydration process can be calculated by the following way:

- **CH**: $n_{CH}^w = 1.0$, $\rho_{CH} = 2.24 \text{ g/cm}^3$, $M_{CH} = 74 \text{ g/mol}$;
- **Aft**: its degradation leads to meta-ettringite, which contains 10-13 H_2O molecules per formula unit (Pourchez et al., 2006). Thus, $n_{Aft}^w = 20$, $\rho_{Aft} = 1.8 \text{ g/cm}^3$, $M_{Aft} = 1255 \text{ g/mol}$;
- **C-S-H**: since conventional cement gel contains 28% gel pores (Bentz et al., 2000), f_i^0 ($i = C-S-H$) in the last equation should be replaced with the volume fraction of solid C-S-H, f_{C-S-H}^s . According to the experimental results (Peng and Huang, 2008), the main product of C-S-H decomposition is C_nS , thus $n_{C-S-H}^w = 3.0$. In addition, for solid C-S-H, $\rho_{C-S-H} = 1.75 \text{ g/cm}^3$, $M_{C-S-H} = 365 \text{ g/mol}$ (Tennis and Jennings, 2000).

The initial volume fraction of the solid part in conventional C-S-H, f_{C-S-H}^s , equals to:

$$f_{CSH}^s = (1 - f_{CSH}^{gelp}) f_{CSH}^0 \quad [14]$$

2. LITERATURE REVIEW

where:

- f_{C-S-H}^{gelp} is the volume fraction of gel pores in conventional C-S-H, given by

$$f_{CSH}^{gelp} = 0.28 / f_{gel}^{CSH} \quad [14.b]$$

Thus, the total initial volume fraction of solid C-S-H is to be considered as:

$$f_{CSH}^{0s} = f_{CSH}^s \quad [14.c]$$

By converting gel pores into capillary pores with the decomposition of C-S-H, the volume fraction of additional capillary pores due to the decomposition of C-S-H is equal to:

$$f_{CSH}^{cap} = f_{CSH}^w + f_{CSH}^s a_{CSH} \frac{f_{CSH}^{gelp}}{1 - f_{CSH}^{gelp}} \quad [15]$$

Considering all these relations, the total volume fraction of capillary pores is given by:

$$f_{cap} = f_{cap}^0 + f_{CH}^w + f_{AFt}^w + f_{CSH}^{cap} \quad [16]$$

At this point, the residual volume of the considered hydrates can be determined as follows (where AL is related to aluminated hydrates and r is indicating the residual conditions):

$$f_{CH}^r = (1 - a_{CH}) f_{CH}^0 \quad [17]$$

$$f_{AL}^r = (1 - a_{AFt}) f_{AL}^0 \quad [18]$$

$$f_{CSH}^r = (1 - a_{CSH}) f_{CSH}^s / (1 - f_{CSH}^{gelp}) \quad [19]$$

Moreover, the porosity of the decomposition products of hydrated aluminates, CH and conventional C-S-H can be calculated as:

2. LITERATURE REVIEW

$$f_{AL}^{pp} = n_{AL}^w \frac{\rho_{AL} / M_{AL}}{\rho_w / M_w} = 0.52 \quad [20]$$

$$f_{CH}^{pp} = n_{CH}^w \frac{\rho_{CH} / M_{CH}}{\rho_w / M_w} = 0.54 \quad [21]$$

$$f_{CSH}^{pp} = n_{CSH}^w \frac{\rho_{CSH} / M_{CSH}}{\rho_w / M_w} + 0.28 / f_{gel}^{CSH} = 0.58 \quad (\text{if } f_{gel}^{CSH} = 0.65) \quad [22]$$

In these last expressions, the total porosity in function of conversion degree can be determined considering the dehydration reaction for the principal cement paste hydrates.

The evolution of capillary pores in function of increasing heating rate has been also considered and the experimental trends are collected in Figure 25 (Zhao, 2012).

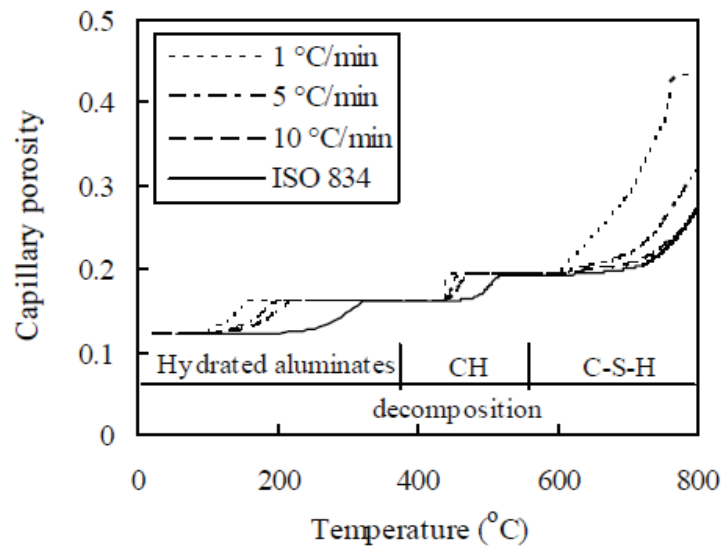


Figure 25: Capillary porosity evolution under different heating rates [Zhao, 2012].

From Figure 25 it arises that also in case of this parameter, the heating rate influences in a significant way the evolution of capillary porosity. The higher the heating rate, the slower the development of the capillary porosity with respect to the exposure temperature, because a lower amount of free spaces are generated for the vapor expulsion. As consequence, the corresponding

2. LITERATURE REVIEW

material properties, the release of water from decomposition, the escape of water vapor, and the development of vapor pressure will be significantly different.

2.1.1.2 Thermal Stability of Aggregates

Concrete mixes are generally composed in volume by almost 70% by aggregates, having different composition, origin and shape. Some Authors have studied the high temperature exposure behaviour of these materials considering several aspects, such as physical and chemical properties as well as micro-cracking investigation, in order to characterize their thermal stability. In fact, this parameter can be studied with reference to mass loss, micro-cracking distribution inside the material and dimensional stability after thermal exposure.

Thermal stability determination is fundamental to understand the thermal behaviour of concrete system. In this case, two aspects have to be considered: the thermal compatibility between cementitious matrix and aggregates and the aggregate-matrix interface. This zone can be considered as weaker because the accumulation of water in this zone creates a more porous zone in which cracking will be initiated (Xing, Beaucour et al., 2011).

For the above-mentioned reasons, some experimental campaigns have been carried out in order to improve the knowledge of the deterioration of different types of aggregates subjected to high temperature phenomena, and to characterize the physical and chemical transformations they undergo (Niry et al. 2013; Xing, Hèbert et al. 2011).

According to Part 1-2 of Eurocode 2, the aggregates are distinguished between siliceous and calcareous, but in one of the considered experimental studies, they have been differentiate on the basis of a petrographic study performed according to EN 932-3, 1996 (Niry et al., 2013). In particular, they are organized in the following categories:

- Igneous rocks: granite, basalts and rhyolite;
- Sedimentary rocks: limestones and flints;
- A third category corresponding to igneous or sedimentary rocks: quartz vein or quartzite, quartzo-feldspatic rock.

After thermal exposure, aggregates can be studied in order to detect their changes in chemical and mineralogical compositions, as well as micro-cracking investigation. In the following sub-paragraphs, these parameters characterizing thermal stability will be treated.

2. LITERATURE REVIEW

2.1.1.2.1 Calcite decarbonation reaction

The calcite decarbonation has been considered due to the fact that this compound represents an important constituent of common silico-calcareous and calcareous aggregates.

Some Authors focused their experimental work on the detection of thermodynamic and kinetic parameters related to the degradation of CaCO_3 (Georgieva et al., 2013). This is a high temperature reversible and strongly endothermic decomposition reaction involving a relatively large mass-loss associated with the evolution of carbon dioxide (CO_2):



As for portlandite dehydration, it is possible to follow the trend of degree of conversion in function of heating rate, by means of TGA, as reported in Figure 26, in terms of mass loss (%) (Georgieva et al., 2013).

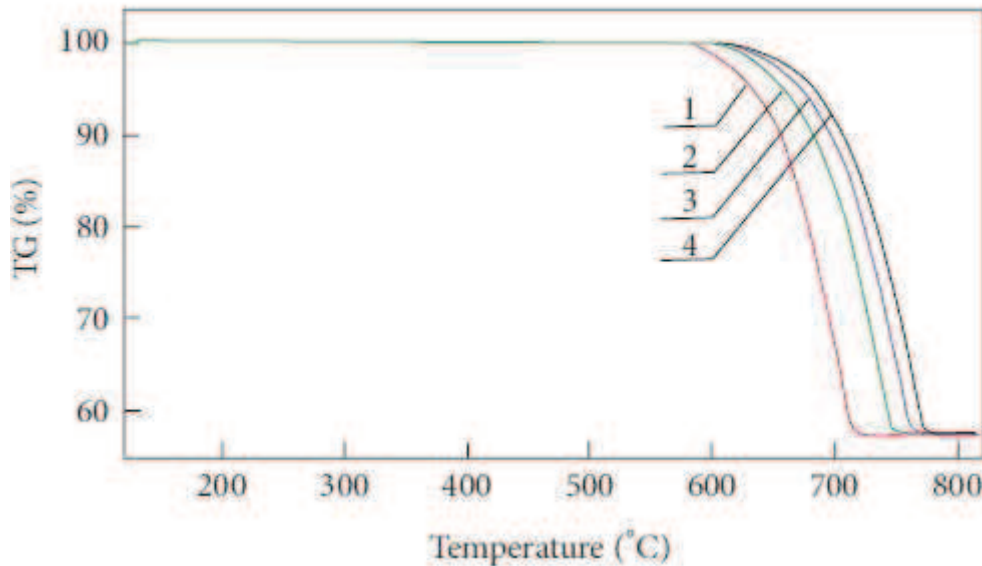


Figure 26 : Thermal degradation curves of CaCO_3 at 1–3, 2–6, 3–9, and 4–12 K/min heating rate [Georgieva et al., 2013].

In Figure 26 considering a fixed mass loss, it has been detected at higher temperature with increasing heating rate. As for the previous reactions, the higher the heating rate, the higher the temperature at which a fixed degree of conversion is reached.

2. LITERATURE REVIEW

These experimental results, collected for two single reactions occurring in the cementitious system, show that if the thermal exposure is carried out with lower heating rate, a fixed degree of conversion is reached at lower temperature. This proves that the heating rate plays an important role on the kinetics and thermodynamic aspects linked to chemical reaction taking place during high temperature and/or fire exposure.

2.1.1.2.2 Mass loss of Aggregates

This first aspect linked to thermal stability of aggregates can be monitored by means of TGA. In Figure 27 and Figure 28 the thermograms of different quartzites are collected, as well as flints (siliceous) and calcareous aggregates (Xing, Hèbert et al. 2011).

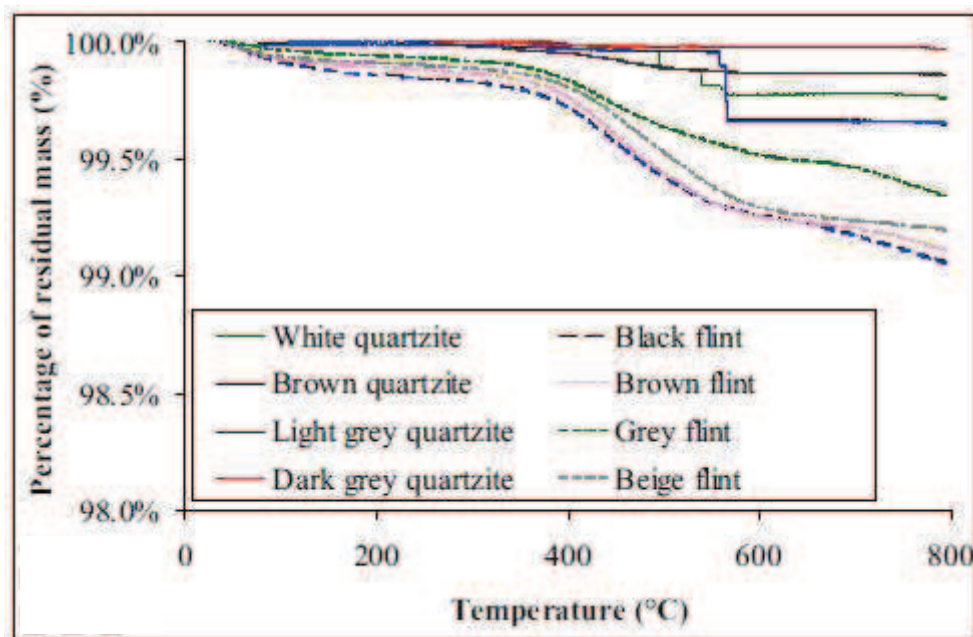


Figure 27 : TGA of different flints and quartzite aggregates [Xing, Hèbert et al. 2011].

2. LITERATURE REVIEW

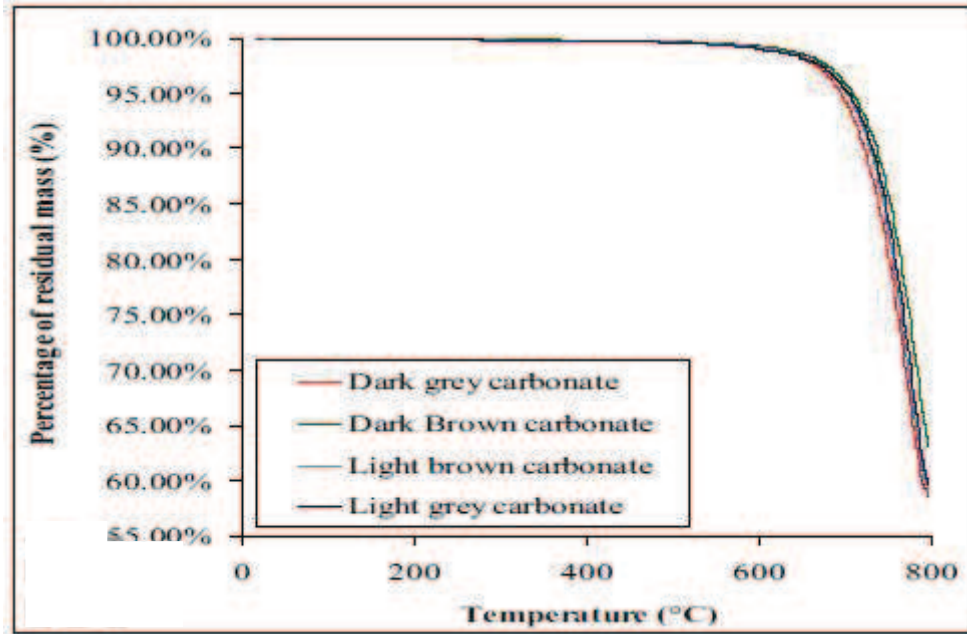


Figure 28: TGA of different calcareous aggregates [Xing, Hèbert et al. 2011].

Regarding TGA of flints aggregates, mass losses correspond to a release of water in two stages. Firstly, the complete expulsion of bond water up to $190^{\circ}\text{C}\pm 10^{\circ}\text{C}$. Over this temperature, the silanols in the siliceous phases undergo a dehydroxylation that produces water. The departure of water from the system occurs between 400°C and 570°C , linked to a significant mass loss.

The mass loss of quartzite aggregate is twice lower than that of flint because the content of silanols in the quartzite (macrocrystalline quartz) is lower. Regarding this, Xing refers that according to Verstraete, the molar fraction of silanol is 5.3% for flint and 1.3% for quartz. The TGA analysis curves of quartzite aggregates show that their physical behaviour is relatively stable with the imposed temperature.

For calcareous aggregates, the mass loss (almost 40%) is caused by the decarbonation of CaCO_3 which begins between 600 and 700°C . The degradation of this type of aggregate is strong after a few days of cooling because of the rehydration of the free lime with ambient humidity, which is transformed to CH with a increasing volume that generates cracking and consequent crumbling of concrete.

Mass loss of almost 2.5% has been detected on specific types of aggregates (multiphasic siliceous aggregates, such as quartzo-feldspathic rocks, granites, basalts and rhyolite, which contains other minerals in addition to quartz) as reported in Figure 29. The light blue curve is

2. LITERATURE REVIEW

related to a quartzo-feldspathic rock, which presents the most significant mass loss among the considered siliceous aggregates (Niry et al., 2013).

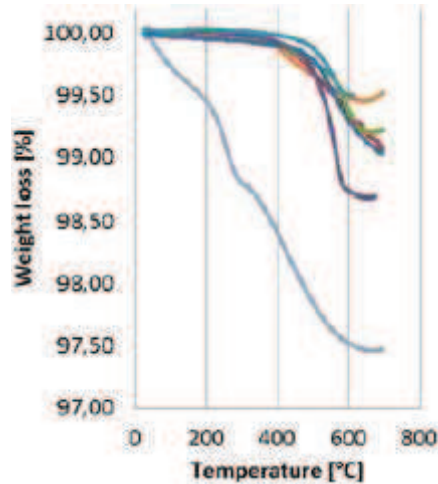


Figure 29: Weight loss (by TGA) of siliceous aggregates [Niry et al., 2013].

These experimental data can be linked to those obtained as variation of porosity with increasing temperature, after heating-cooling cycles, as reported in Figure 30 (Xing, Beaucour et al., 2011).

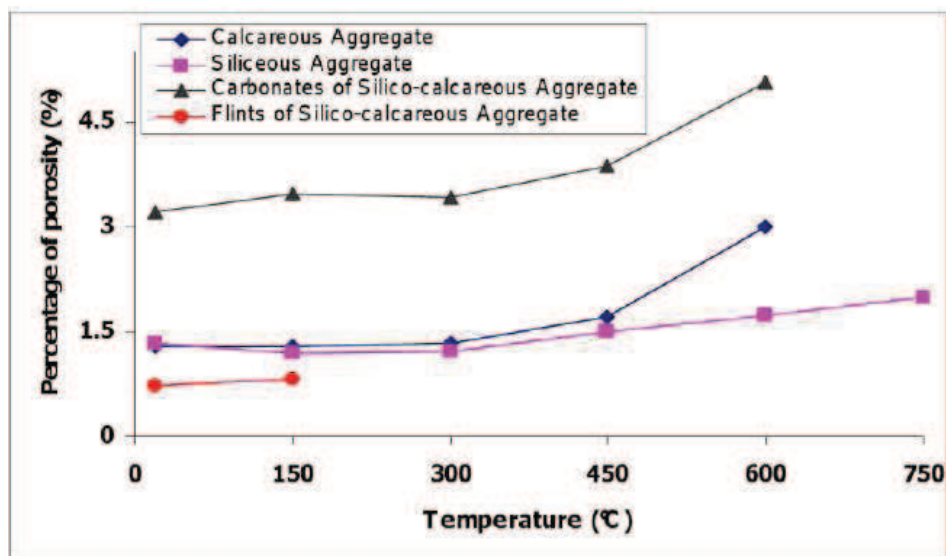


Figure 30: Evolution of the porosity of calcareous, silico-calcareous and siliceous aggregates [Xing, Beaucour et al., 2011].

The porosity of flints could not be measured after 150°C because they broke into multiple fragments. For silico-calcareous aggregates, the porosity study was then only carried out on carbonates. Figure 30 that flint aggregates have a very low porosity, less than 1%. The carbonates

2. LITERATURE REVIEW

from silico-calcareous aggregates are more porous than those from calcareous aggregates. Porosities of both calcareous and siliceous aggregates are similar and do not vary up to 300 °C. Beyond 300 °C, the porosity of the carbonates increases more significantly.

2.1.1.2.3 Micro-cracking distribution

By means of SEM, the micro-cracking investigation after thermal exposure can be carried out and the different types of aggregates can be classified by the occurrence of micro-cracks as follows:

- No significant cracks is observed up to 600°C for calcareous and quartz aggregates;
- Small-scale cracks are observed in basalts, rhyolite, granites and sedimentary quartzo-feldspathic rock;
- Widespread development of cracks observed in flints, especially from 500 to 750°C. The related SEM images are reported in Figure 31. In image **a** is represented flint after heating/cooling at 500 °C, where primary cracking develops and cracks meet at right angles; in image **b**, after heating/cooling at 600°C, secondary orthogonal cracking develops dividing the flint surface into spalled blocks, while in image **c**, after heating/cooling at 750°C, spalled blocks are subdivided by tertiary cracking (Niry et al., 2013).

The micro-cracking distribution is attributable to the rock heterogeneity: the higher the heterogeneity the more distributed are the microcracks. In fact, calcareous and quartz aggregates are more homogeneous, at petrographic level, so they are significantly less affected by microcracks at high temperature (up to 600°C) in comparison with flints and granites, that are more heterogeneous materials, thus more thermal instable.

2. LITERATURE REVIEW

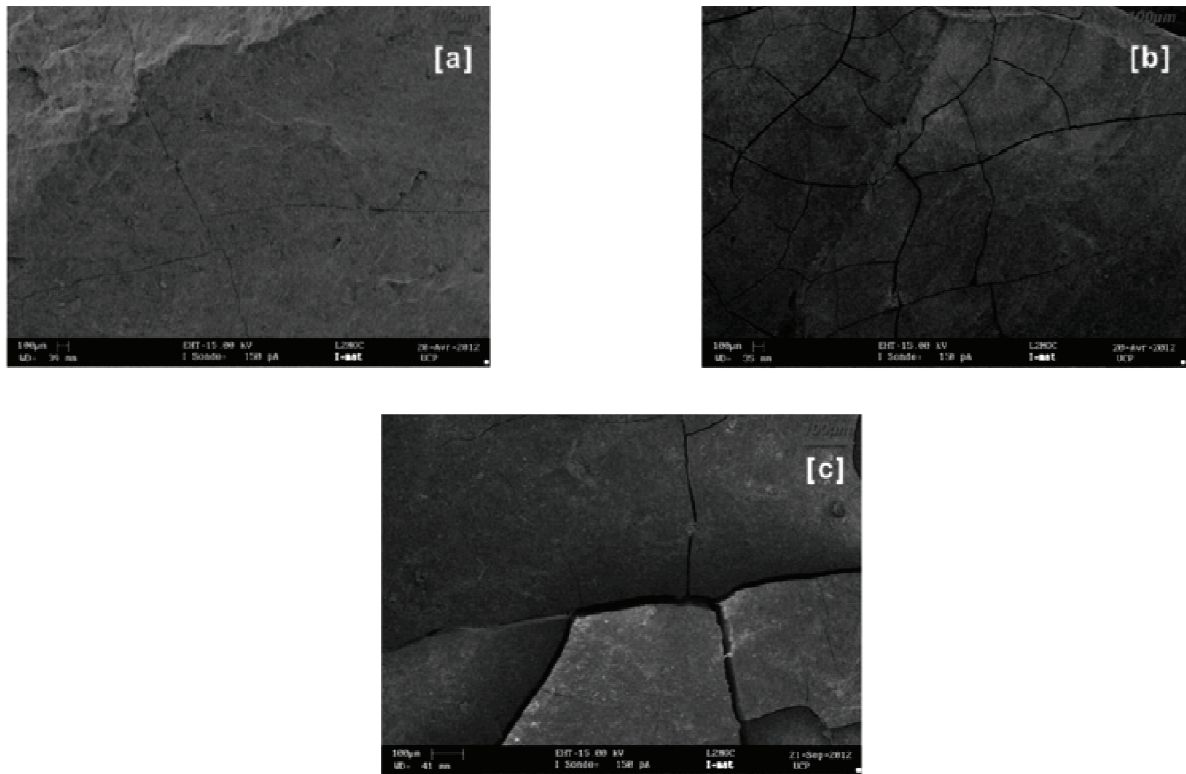


Figure 31: Flint's cracking by SEM as function of temperature [Niry et al., 2013].

2.1.1.2.4 Dimensional stability of aggregates

Different types of aggregates present different thermal behaviour depending on their nature and origin. In Figure 32 are collected the dilatometric curves for ten types of rocks (Harmathy, 1993).

In Figure 32, it can be observed that the lowest dilatation with increasing temperature (up to 900°C) is detected for Anorthosite and Basalt, followed by Syenite. Dolomite presents increasing dilatation up to 800°C, than a contraction up to 900°C. Intermediate behaviour is observed for Quartz and Rhyolite. The highest dilatation has been measured for Granodiorite, followed by Quartz Monzonite and then Granite and Limestone. Thus, from these experimental data, the aggregates that present the highest thermal stability are anorthosite and basalt, because they present the lowest length variation in function of increasing temperature.

2. LITERATURE REVIEW

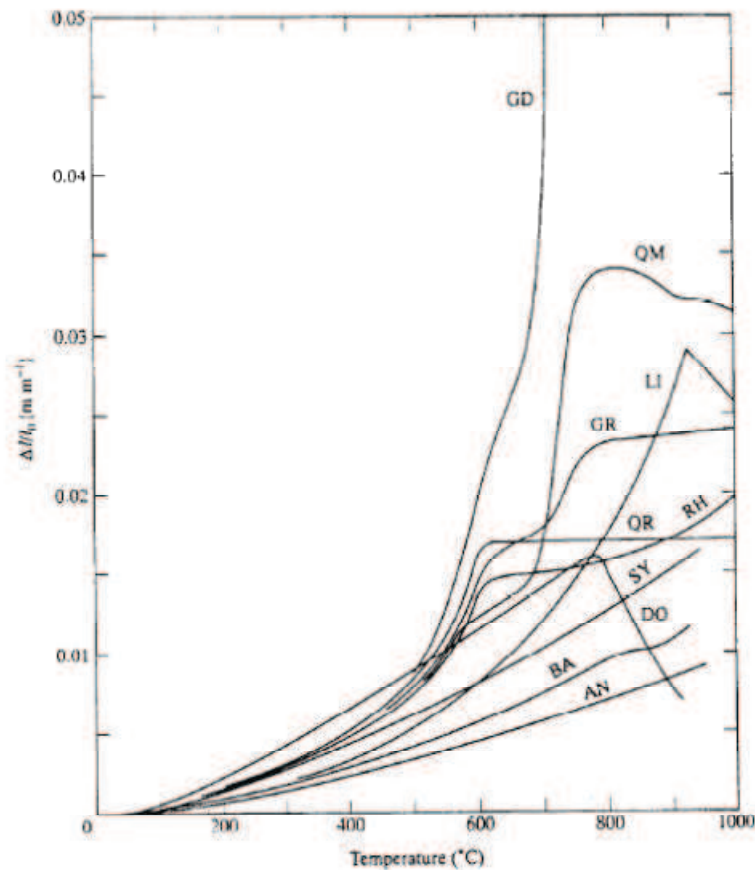


Figure 32: Dilatometric curves for ten rocks: AN=Anorthosite, BA=Basalt, DO=Dolomite, GD=Granodiorite, GR=Granite, LI=Limestone, QM=Quartz Monzonite, QR=Quartz, RH=Rhyolite, SY=Syenite [Harmathy, 1993].

From literature, the thermal expansion coefficients of different aggregates have been collected and they are summarized in Figure 33 as function of thermal expansion coefficient of concrete (Harmathy, 1993).

From Figure 33, it arises that the lowest thermal expansion coefficient is detected for limestone and the corresponding concrete, followed by basalt and granite aggregates (and related concrete). An intermediate values is detected for limestone marble, while the highest values are recorded for chert.

Taking into account that the volume fraction of aggregates in concrete mixes is not less than 70%, in Figure 33 it appears evident the effect of dilatometric behaviour of aggregate on resulting behaviour of concrete. In fact in the graph, the relation between the two dilatometric behaviours is linear.

2. LITERATURE REVIEW

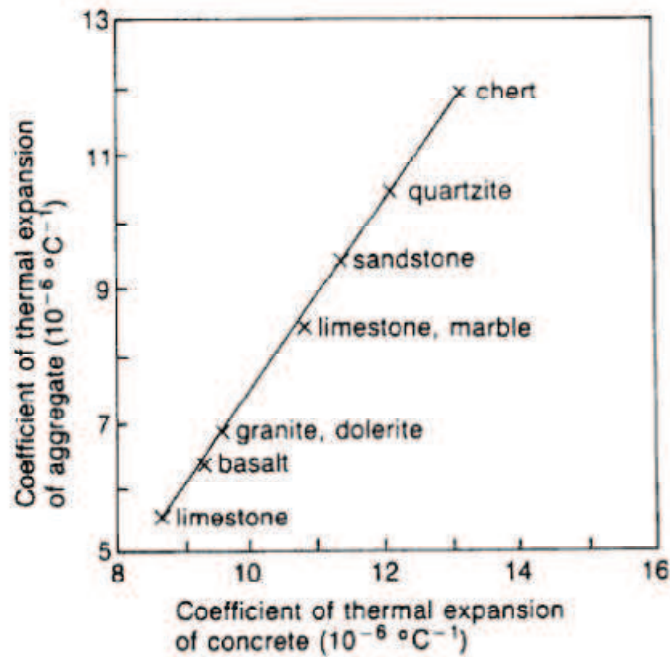


Figure 33: Thermal expansion coefficient of aggregates in function of thermal expansion coefficient of concrete [Harmathy, 1993].

2.1.2 Concrete system

2.1.2.1 Heating rate effect on intrinsic damage of concrete

The previous experimental works have been carried out applying a thermal exposure to the samples following a slow heating rate, normally some units of $^{\circ}\text{C}/\text{min}$. It can be interesting to evaluate how the intrinsic damage changes by increasing the heating rate.

After collecting the literature data regarding hardened cement pastes (Paragraph 2.1.1.1.4 and 2.1.1.1.5), the effect of heating rate can be considered also on concrete materials. In this context, some Authors have carried out an experimental campaign on High Strength Concrete (HSC) used as nuclear waste storage material, because in the field of nuclear applications, concrete might be exposed to specific thermo-hydro-mechanical stresses as well as high temperature, as already mentioned in paragraph 1.1. In the experimental program on the effect of heating rate on residual thermo-hydro-mechanical properties of a HSC, they have been submitted to temperatures between 110 and 250 $^{\circ}\text{C}$, with rates ranged from 0.1 to 10 $^{\circ}\text{C}/\text{min}$ (Gallè et al., 2003).

2. LITERATURE REVIEW

In the considered work, the studied parameter directly linked to intrinsic damage is the mass loss. In Figure 34 are collected the mass loss curves detected reaching the temperatures of 110, 150, 200 and 250°C with three different heating rate (0.1, 1 and 10°C/min). Moreover, Figure 35 is related to the evolution of mass loss in function of temperature and heating rate.

In Figure 34 the curves proved that the mass loss plateau was reached for each thermal loading and it has been checked that there was no significant amount of water unremoved for each temperature level. Slight differences, observed mainly at 150°C, are probably related to discrepancies in the initial water content of the specimens.

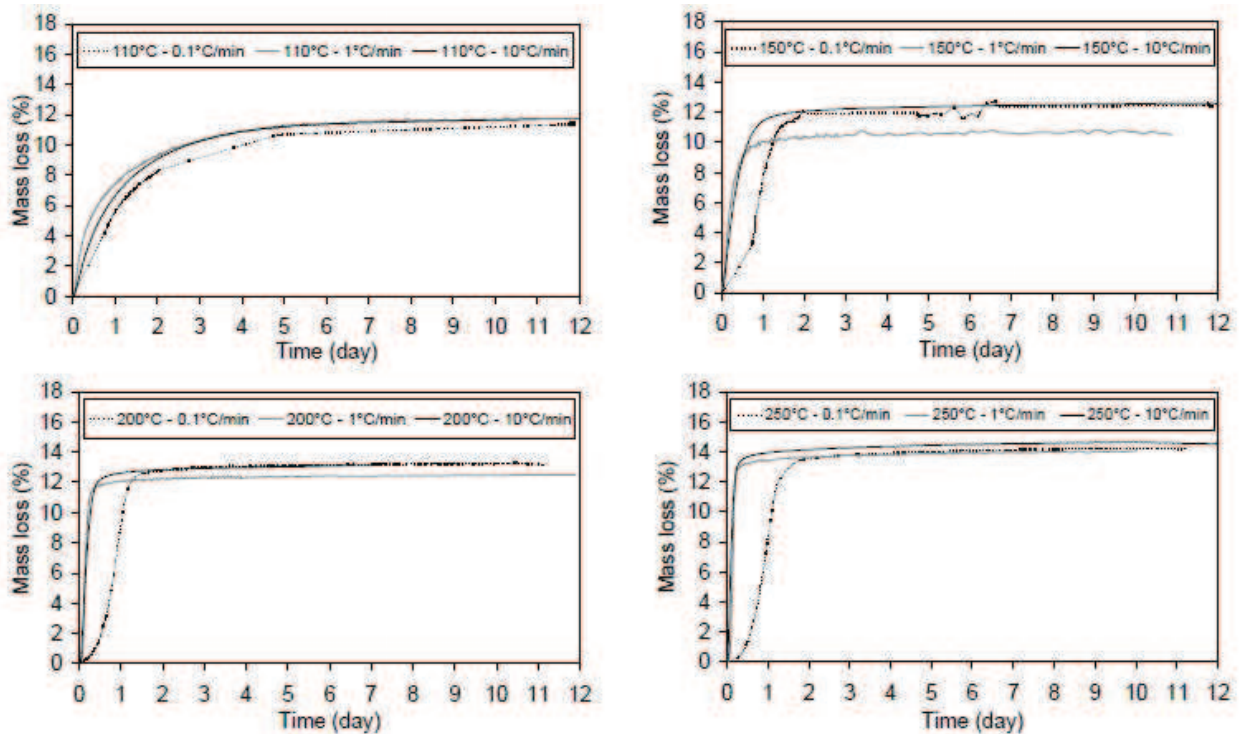


Figure 34: Evolution of the mass loss kinetics at 110, 150, 200 and 250°C with heating rate [Gallè et al., 2003].

2. LITERATURE REVIEW

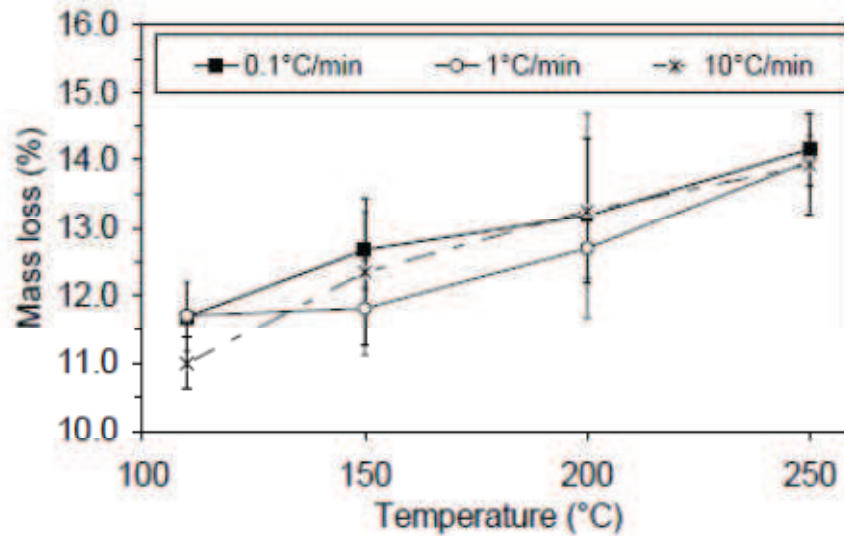


Figure 35: Evolution of the mass loss with temperature and heating rate [Gallè et al., 2003].

The mass loss values obtained after thermal treatments, plotted in Figure 35 evolves linearly with the temperature. Taking into account experimental uncertainties, it is assumed that the mass loss did not evolve with the heating rate. This result confirms that the intensity of dehydration is only controlled by temperature level and that there is no artefact effect due to the heating rate. Slightly different conclusions were drawn in a previous study by Noumowè dedicated to the behaviour of ordinary concrete and high-strength concrete heated up to 600°C. This study showed that, up to 350°C, the mass loss slightly increased with the decrease of the heating rate. But as concrete probes were heated during a relatively short time (one hour), it is possible that the mass loss was not totally completed (Noumowè, 1995).

In the experimental work of Gallè, other physical and mechanical properties have been considered in order to study the effect of heating rate. The results will be shown in the Paragraph 2.2.1.4 related to the effect of thermal exposure on mechanical properties and transport mass phenomena. However, it is important to anticipate that the effect of heating rate on concrete residual properties remains difficult to evaluate. In fact, the influence of this environmental factor depends on the material nature (hardened paste, concrete), on the constituents (aggregates) and also on temperature. In the case of concrete, the cement paste and aggregates thermal incompatibility and their differential behaviour at high temperature probably play a major role.

2. LITERATURE REVIEW

2.1.2.2 Microstructural changes in concrete after thermal exposure

2.1.2.2.1 Concrete microstructure after thermal exposure

After the analysis of thermal exposure on cement pastes and aggregates separately, it is important to consider the study of microstructural changes in concrete due to high temperature treatment and consequent intrinsic damage. In particular, the comparison among the behaviour of Normal Strength Concrete (NSC), HSC and High Performance Concrete (HPC) is fundamental to understand their peculiarities linked to intrinsic damage. It is obvious that the intrinsic degradation of the material affects the mechanical properties of concrete (addressed in the next paragraphs), so these two aspects are maintained separated only for an editorial reason.

Moreover, the microstructure evolution is correlated to the water expulsion from the concrete at normal as well as at high temperature. Therefore the pore structure at high temperature may have a considerable influence on the spalling behaviour on the considered materials (Noumowe, 2005).

Several experimental studies are present in literature about this topic and they are based on the concrete microstructural characterization in residual conditions, after a thermal cycle involving different maximum temperatures. The analytical techniques used to carry out these types of determinations and to understand the mechanism of concrete deterioration due to thermal exposure are commonly the already mentioned SEM and TGA. Moreover, a complete study of microstructure is performed by means of Mercury Intrusion Porosimetry (MIP), technique that allows to detect the pore size distribution inside the cementitious-based material. X-Ray Diffraction (XRD) and Differential Scanning calorimetry (DSC) can complete the overview of the material composition but it is not fundamental in order to study the microstructure.

Concretes considered in these studies differ each other not only on the basis of compressive strength (NSC, HPC or HSC), but also in terms of cement type, aggregate nature and presence of Polypropylene (PP) and steel fibers.

The first type (PP) of fibers are commonly added to concrete mixes in order to contrast the explosive spalling due to high temperature and/or fire exposure, as will be explain more in particular in the following paragraphs. The second type of fibers is used to increase concrete toughness in the post-peak range, and reduces spalling sensitivity too, even if less efficiently than PP fibers (Bhargava et al., 2006).

2. LITERATURE REVIEW

Noumowe has performed an experimental study in order to characterize the microstructure and mechanical properties of HSC with and without PP fibers exposed to a maximum temperature of 200°C (HSC are named B3 and B1 respectively).

PP fibers are commonly added to HSC exposed to high temperature because these materials present low permeability, low porosity, low thermal transmission and high moisture content, that are supposed to lead to increase spalling risk. Thus, the presence of PP fibers will have an impact on microstructure, that in case of this work, have been principally characterized by means DSC and SEM, before and after the thermal exposure. The DSC curves are collected in Figure 36.

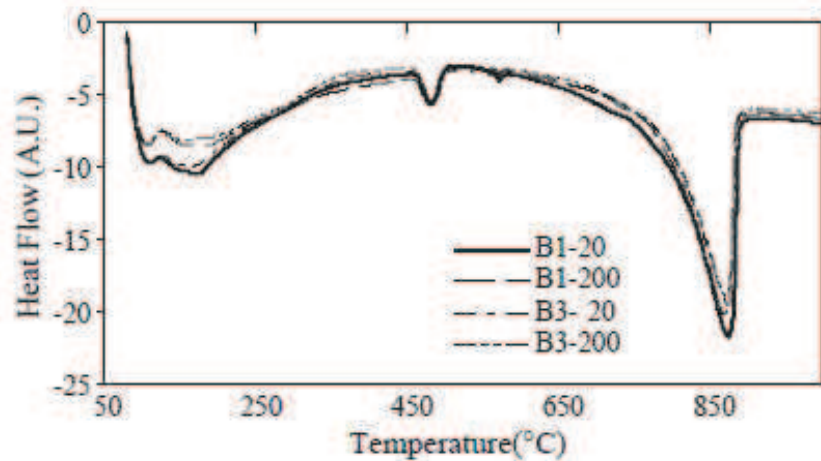


Figure 36: DSC curves of both strength concretes [Noumowe, 2005].

As already reported in case of TGA of cement paste (Paragraph 2.1.1.1), in the DSC curves of both B1 and B3 concretes the following transformations can be identified, as temperature of the maximum of the peak (considering that transformations take place in a specific range of temperatures):

- Free water evaporation up to 110°C;
- Fiber melting at about 170°C;
- First stage of C-S-H dehydration at 170°C;
- The peak at almost 480°C in all the curves is reasonably due to portlandite. Although both B1 and B3 HSC included silica fume that reacts with calcium hydroxide during cement hydration, a non negligible amount of portlandite is suspected;
- Quartz transformation from a rhomboedric (α -quartz) shape to hexagonal (β -quartz) shape at 573°C;

2. LITERATURE REVIEW

- At about 870°C a large peak can be observed, mainly due to decarbonation of calcium carbonate and dehydration of C-S-H phases.

It can be noticed that, after 250°C, the behaviour of B3 concrete is very close to that of B1 concrete. The effect of fiber is mainly significant in the temperature region from 100 to 250°C before the entire melting.

The SEM observations on HSC samples containing PP fibers before (Figure 37) and after thermal exposure (Figure 38) are significant in order to illustrate how the fibers appear after their melting.



Figure 37: PP fibers in HSC, before thermal exposure [Noumowe, 2005].

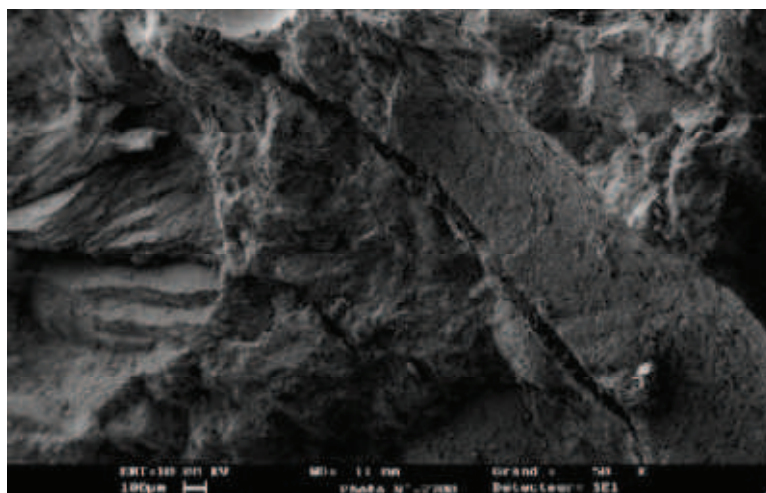


Figure 38: Traces of melted fibers in HSC [Noumowe, 2005].

2. LITERATURE REVIEW

As shown in Figure 38 at 200°C PP fibres lost their solid structure. There was a significant difference between the porosity of B1 and B3 concretes after exposure at 200°C. When the high strength polypropylene fiber concrete is heated up to 200°C, fibers readily melt, forming additional pores and small channels in the concrete that may act to reduce high internal moisture pressures. Clearly, the use of fibers affects the porosity at high temperature of HSC. This may decrease the pore pressure inside the material. The fibers affect the porosity then the release of moisture from the concrete matrix, so it means lower risk of concrete spalling in case of accident.

Other Authors have considered different types of HSC for characterize their microstructure after exposure to high temperature, in particular up to 750°C (Guerrini, Gambarova e Rosati, 2004). These HSC differ each other for the cement type, the nature of aggregates and types of fibers (synthetic and micro-steel fibers). These parameters have been considered because it is well known, as already mentioned in Paragraph 2.1.2, that the thermal properties of concrete at high temperature depend on aggregate composition and on the relative thermal expansion of the concrete components (Koury, 1992).

In case of HSC prepared with different aggregates, two types have been considered: limestone and dolomitic ones. It has been detected that, even though the right choice of the aggregate may avoid the explosive failure of the material without fibers (as in the case of the limestone aggregates), adding fibers is an effective solution to guarantee material integrity (especially in the case of dolomitic aggregates).

HSC containing hybrid fibers (both PP and micro-steel fibers) has been observed by SEM after different exposure temperatures (between 250 and 750°C), as well as the concrete without fibers and the related images are reported in Figure 39 and Figure 40.

As observed in Figure 39 and Figure 40 internal cracking within the cement paste, cracking around and across the aggregate grains and modifications of the fibers (melting and evaporation of the synthetic fibers, partial melting of the steel fibers) were observed.

The author has observed a particular behaviour in presence of steel fibers: brass-coated steel microfibers were found to lose most of their mechanical properties and to change their color from yellow to brown. Fiber oxidation was confirmed by the changes in the morphology of the fibers observed with SEM and by the chemical changes investigated with XRD.

2. LITERATURE REVIEW

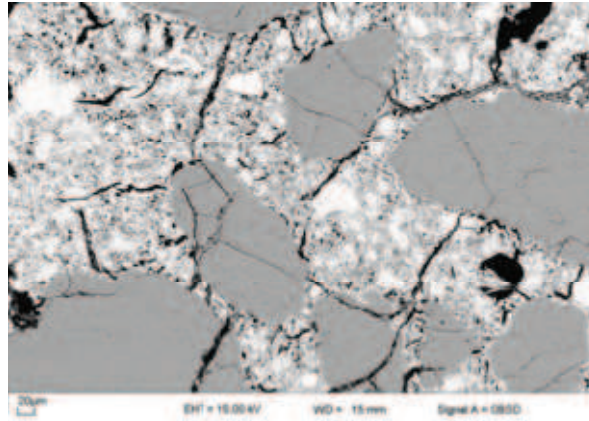


Figure 39: SEM analysis of HSC without fibers, after 750°C [Guerrini et al., 2004].

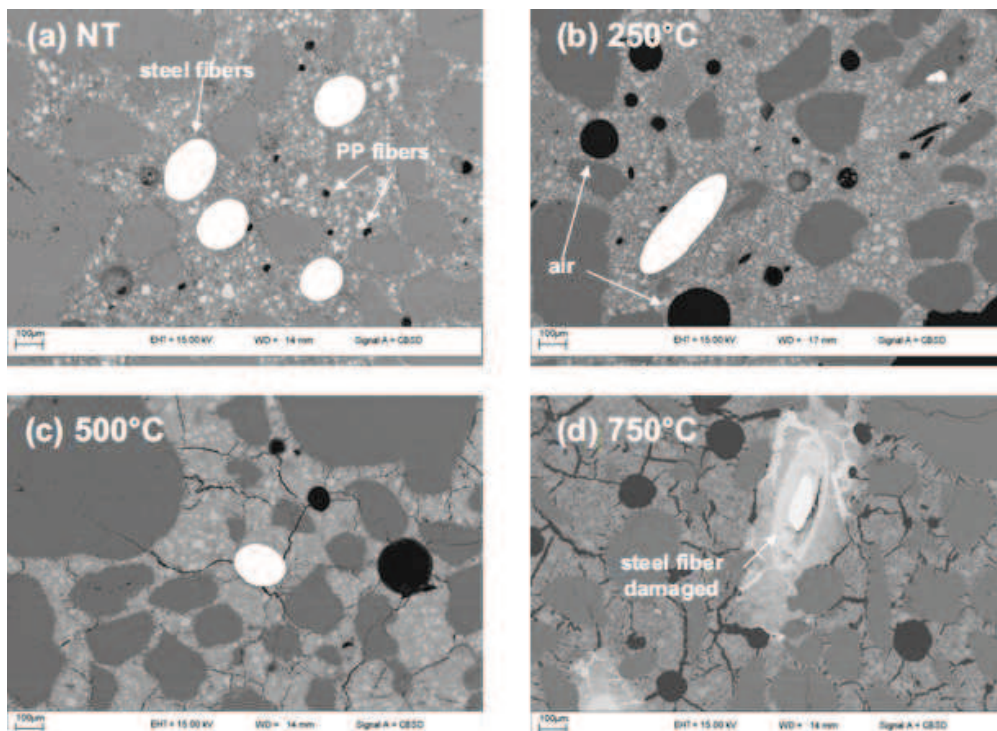


Figure 40: SEM analysis of a hybrid HSC concrete, at different temperatures [Guerrini et al., 2004].

Another group of Authors performed an experimental program to study both the compressive strength and the pores structure of different HPC using a mercury intrusion porosimeter, after exposure to temperature up to 800°C (Chan et al., 2000). The comparison has been performed between NSC and HPC without (HPC-1) and with steel (HPC-2) and PP (HPC-3) fibers. The comparison among the porosimetry data of all considered concretes before and after thermal exposure at 800°C are collected in Figure 41.

2. LITERATURE REVIEW

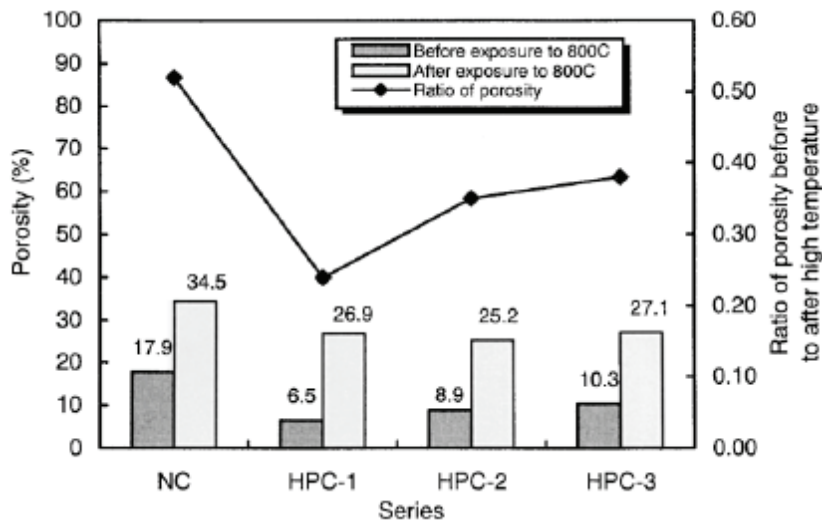


Figure 41: Porosity before and after high temperature exposure [Chan et al., 2000].

Before thermal exposure, NSC shows a higher porosity than those related to HPC, because of their more compact matrix. The comparison between the two different conditions (before and after thermal exposure) for all the tested concrete highlights a significant increase in porosity due to high temperature exposure. The largest increase is detected for HPC-1, which quadruples its total porosity due to high temperature induced damage. The concrete that seems to be less affected by thermal damage is NSC, presenting a doubled total porosity.

The differential curves related to concrete pore size distribution are plotted in Figure 42.

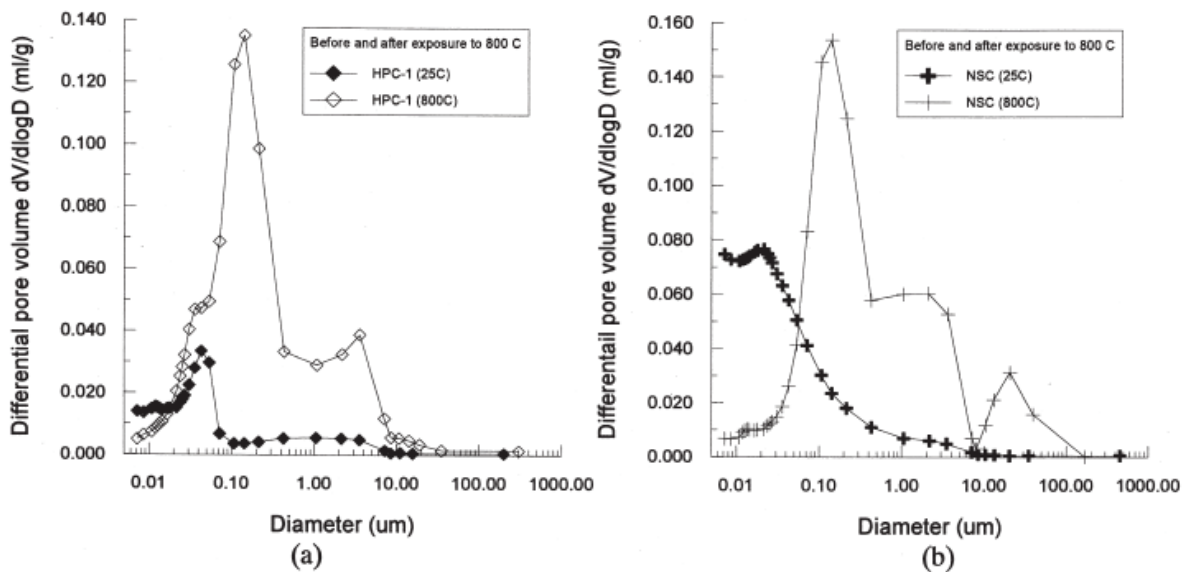


Figure 42: Pore size distribution before and after exposure to high temperature for NSC and HPC-1 [Chan et al., 2000].

2. LITERATURE REVIEW

Comparing the differential curves, it arises that both for NSC and HPC-1 porosity increases after thermal exposure, confirming the total porosity data above explained, and the highest peak occurs within a narrow range between 0.10 and 0.15 μm . This means that a great increment of pore size occurs in this pore size range, which results more affected by high temperature up to 800°C. Beyond pore size diameter of almost 1 μm , a significant increase in porosity is detected for NSC, resulting higher than that of HPC-1, as well as beyond pore size diameter of 10 μm . Thus, it seems that NSC is more affected by thermal exposure damage comparing with HPC-1, especially beyond a pore size diameter of 1 μm .

The Authors concluded that the variation of pore structure, including porosity and pore size distribution, could be used to explain the degradation of mechanical properties of HPC subjected to high temperature.

2.1.2.2.2 Concrete microstructure: the mode of action of PP fibers

The incorporation of microfibers to cementitious materials introduces alterations in their performance at high temperature. These changes depend on the type and fiber content, especially PP fibers, and on the concrete properties (Kalifa et al., 2001). Many Authors have investigated the mode of actions of PP fibers in decrease the spalling risk in HPC, by means of microstructural observation. Several works have highlighted the positive effect of the introduction of PP fibers to prevent the risk of explosion of dense concretes under fire. However, the mechanism that contributes to this beneficial effect needs to be clarified in order to use PP fibers in optimal conditions. In fact, several mechanisms have been proposed to explain the thermal response of PP fibers in concrete at high temperature, although none of them have been fully demonstrated at microstructural level.

A possible proposed mechanism for PP fibers to reduce explosive spalling is the possibility that, due to their melting at almost 160 °C, micro channels emerge and become available for the transport of the water vapour. This theory has been proposed by Kalifa et al., which assume that the melted fiber penetrates into the cement matrix (Kalifa et al., 2001). Moreover, the micro channels represent damage mechanical defects at whose edges crack formations are initiated (Pistol et al., 2011). Khoury, on the other hand, is of the opinion that the high viscosity and the molecule dymension suggest the opposite effect (Koury, 2008).

2. LITERATURE REVIEW

The experimental work carried out by Alonso et al., considered more in detail, makes a study at micro and macro level in the region of temperatures where PP fibers are melted but present in the bulk of the concrete in order to address the reason for their beneficial effect in reducing the risk of spalling of concrete at high temperature. The microstructural analysis of the interfacial transition zone (ITZ) and the interaction of PP fibers with mortar in the temperature region 170 to 300°C have been considered (Alonso et al., 2013).

The microstructural changes in mortar induced by the PP fibers were analysed before and after heating. Porosity and pore size distributions were determined by MIP; SEM using back scattering mode was also employed.

One of the first aspects to be clarified is related to the modifications due to PP fibers incorporation in the microstructure of the concrete bulk, in particular if additional percolation paths are nucleated starting from the initial condition inside the ITZ on the cement paste and in the ITZ between aggregates and voids, as indicated in literature (Bentz, 2000).

The analysis of the pore size distribution can contribute to highlight this aspect: capillary pore region is not altered with the presence of PP fibers, both with their considered content of 0.06 and 0.09% in volume, as observed in Figure 43.

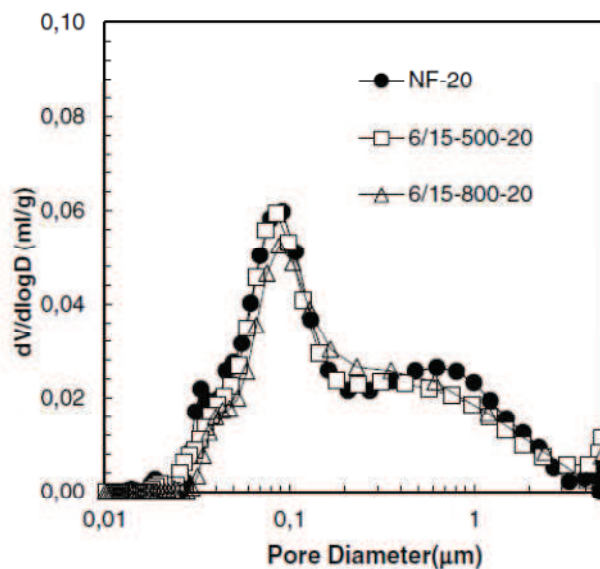


Figure 43: Micropores size distribution in initial mortar with and without PP fibers [Alonso et al., 2013].

On the other side, the Authors observed that pore sizes from 5 to 100 μm, region of macropores, are significantly altered due to the addition of PP fibers.

2. LITERATURE REVIEW

This increase in percolation of the pore structure (2 or 3 times higher) due to PP fibers addition is also confirmed with SEM (Figure 44) and develops in two forms: growing of perpendicular microcracks from the fiber settlement through the neighbouring cement paste (Figure 44, a) and formation of wide gaps at the interface of PP fibers/adjacent-cement paste, less relevant at the ITZ of the aggregate/cement paste, despite the higher aggregate size (Figure 44, b).

Considering the evolution of microstructure of the mortar containing PP fibers due to thermal action, above 160°C (melting temperature of PP fibers), the thermal response of PP also induces changes at microstructural level. In the pore structure two effects are detected: decrease in capillary pores at all temperatures tested after melting of PP fibers, from 170°C up to 300°C (Figure 45) and the increase in pore size content of the macro poresregion. After the total decomposition of PP fibers, this region of pores grows significantly due to the empty space at the fiber settlement. So, as the degradation of the PP fibers evolves with temperature, the percolation of the ITZ is increased at the macro poresregion, and the percolation of the ITZ from the cement paste near to the PP fiber settlement is decreased. The above results suggest that the beneficial effect of PP fibers for spalling control is a balance between percolation decrease in micropores and percolation increase of macropores.

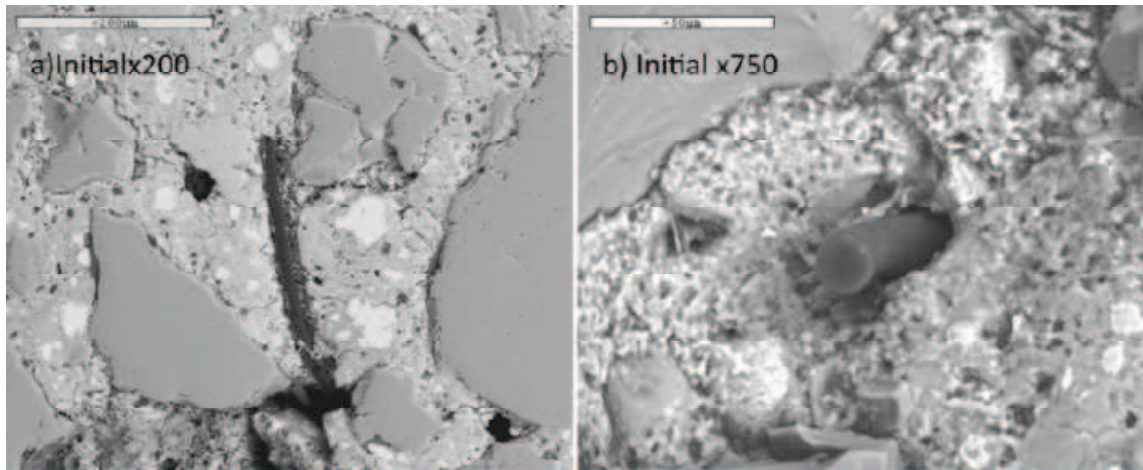


Figure 44: SEM microstructure of PP fibers distribution in the bulk of initial mortar (before heating) a) Microcracks, b) Gap at ITZ PP fiber/cement paste and aggregate/cement paste [Alonso et al., 2013].

2. LITERATURE REVIEW

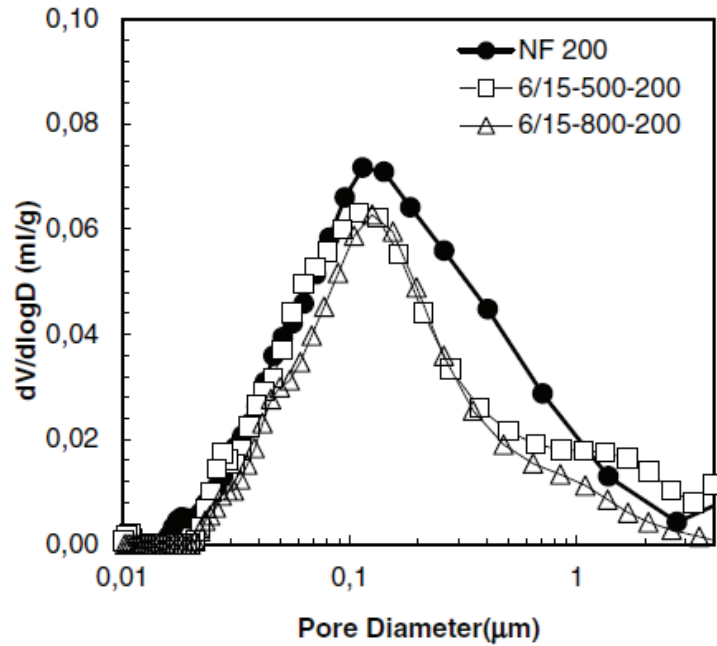


Figure 45: Pore size distribution of capillary pores after heating of mortars (200°C) [Alonso et al., 2013].

The consequences of the changes in the pore structure due to thermal exposure were analysed with SEM (Figure 46). After 170°C the PP fibers melted and the ITZ at the channel of the fibered mortar is increased and also new microcracks have grown. Besides, some pores of the adjacent cement paste are polluted with PP, which suggest that the melted fiber has flowed and has been absorbed by the mortar out of the fiber channel. According to the Authors, this diffusion effect, which can extend several mm outwards the fiber channel, is more evident at higher temperatures as consequence of a viscosity decrease of the polypropylene with the increase of temperature (Figure 46, b).

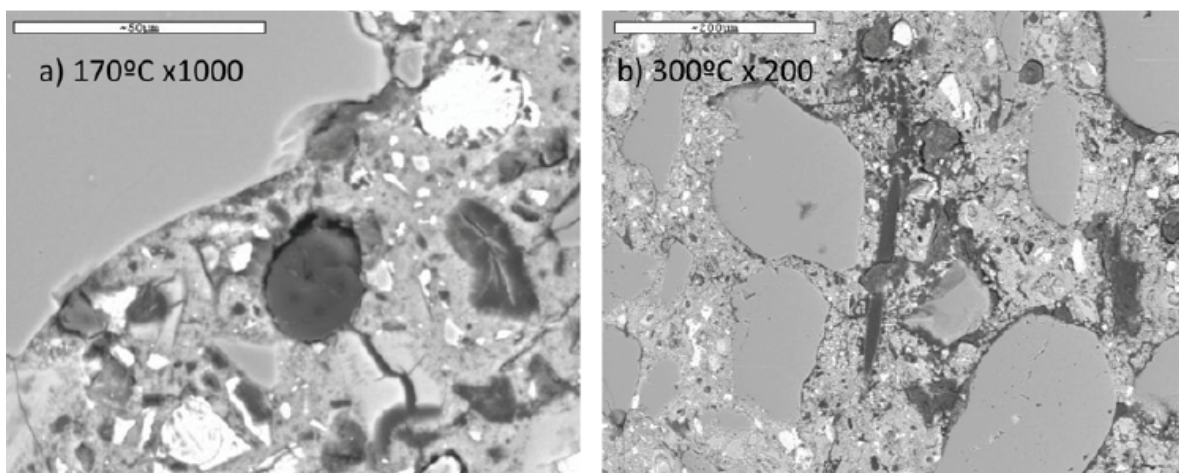


Figure 46: SEM microstructure of PP fibers in the bulk of mortar after heating a) after 170°C, b) after 300°C [Alonso et al., 2013].

2. LITERATURE REVIEW

The Authors conclude that the addition of PP fibers changes the porosity of concrete at the macro poreslevel. The increase of ITZ at the PP fiber/cement paste together with the formation of microcracking is the responsible for this increase. After melting of PP fibers due to thermal exposure, a decrease micropores of the mortar is detected, seems due to the diffusion of the melted polypropylene and the absorption at the neighbourhood cement paste, but this effect is accompanied by a simultaneous increase of macro poresdue to the increase of the interfacial region of PP fibers channel and to the growth of microcracks.

2.2 Mechanical damage and Spalling

2.2.1 Mechanical damage of concrete after thermal exposure

From literature, it is well-known that concrete undergoes to decay in mechanical properties due to thermal exposure. Several Authors have performed experimental test on different types of concrete, NSC and HSC, in order to determine how mechanical properties are affected by high temperature and/or fire exposure. In the current Paragraph, the mechanical properties trends in concrete specimens in residual conditions (taken from literature) will be explained, considering the main mechanical parameters, such as compressive strength, stress-strain curves, modulus of elasticity and indirect tensile strength determined by splitting test. The effect of different types of aggregate, pozzolanic additions, presence of PP and steel fibers on mechanical properties will also be considered as well as the effect of heating rate.

2.2.1.1 Compressive strength

Before illustrating the literature experimental data for NSC and HSC regarding the decay on compressive strength due to thermal exposure, the test methods used to determine this parameter are summarized. They are related to stress test, unstressed test and unstressed residual test. The first two are carried out in order to determine the material performance at high temperature, in presence and absence of applied load respectively; the third is suitable to test the material in residual conditions, without pre-load. Considering for example calcareous concrete, the compressive strength values at

2. LITERATURE REVIEW

different exposure temperatures measured applying the three mentioned test set-up are plotted in Figure 47 (Koury, 1992).

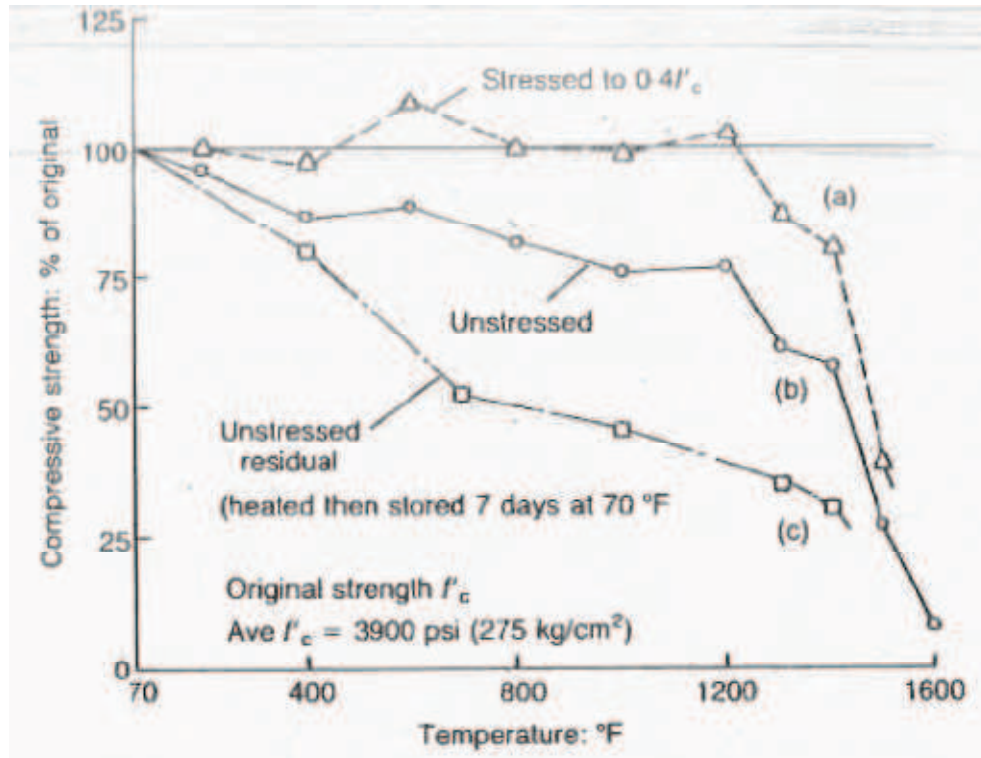


Figure 47: Compressive strength for calcareous concrete in function of temperature obtained by means of stressed and unstressed tests at high temperature and unstressed residual test, after heating [Koury, 1992].

Observing Figure 47, the compressive strength values obtained during the high temperature exposure are higher than that recorded in unstressed residual conditions. In particular, the stressed specimens provide strength values significantly higher than that obtained without the load application, during the heating (at almost 600°C an increase in strength more than 100% has been detected in high temperature loaded conditions). It arises that is very important to define the experimental conditions in which the compressive strength data are recorded because they can be markedly different depending on test set-up.

Phan e Carino collected several experimental data from different researchers (see Table 1), investigating compressive strength values in function of increasing temperature exposure. HSC were considered, containing different types of aggregate, in comparison with NSC (Phan e Carino, 1998).

2. LITERATURE REVIEW

Test programs (1)	Compressive strength (MPa) (2)	Test Methods Used			Concrete or aggregate type (6)	Specimen size (mm) (7)	Observed explosive spalling (8)
		I (3)	II (4)	III (5)			
Castillo and Durani (1990)	28, 62 ^a	X	X		Conventional portland cement	51 × 102 ^e	320–360°C
Hertz (1984)	31, 63, 89 ^b 170 ^a 150 ^a			X	Silica fume concrete with steel fiber	100 × 200 ^e 57 × 100 ^e 28 × 52 ^e	350–650°C
Diederichs et al. (1988)	33–114 ^a		X		Blast furnace slag, silica fume, fly ash, OPC	100 × 100 × 100 ^d 80 × 300 ^e	350°C
Hammer (1995)	69–118 ^b		X		Silica fume concrete with LWA and NWA	100 × 310 ^e	300°C
Sullivan and Shansar (1992)	38–65 ^a		X	X	Combinations of cement, silica fume, slag, and two types of aggregate	64 × 64 ^e	Not observed
Abrams (1971)	23–45 ^a	X	X	X	NWA (carbonate and siliceous) and LWA	75 × 150 ^e	Not observed
Morita et al. (1992)	20, 39, 59 ^a 20, 74 ^b			X	Conventional portland cement	100 × 200 ^e	Not observed
Furumura et al. (1995)	21, 42, 60 ^a 38, 55, 79 ^b		X	X	Conventional portland cement	50 × 100 ^e	300°C
Felicetti et al. (1996)	72, 95 ^a			X	Silica fume concrete	100 × 300 ^e 100 × 150 ^e	Not observed
Noumowe et al. (1996)	38, 61			X	Silica fume with calcareous aggregate	80 × 275 × 500 ^d 160 × 320 ^e 100 × 100 × 400 ^e	300°C

Table 1: Summary of materials and related compressive strength data reviewed by Phan and Carino (1998).

The Authors have considered all the three above-mentioned compressive strength set-up tests, but only the one in residual conditions is reported in the current Paragraph; HSC containing Normal Weight Aggregate (NWA) and LightWeight Aggregates (LWA) concrete are compared with NSC, respectively in Figure 48 and Figure 49.

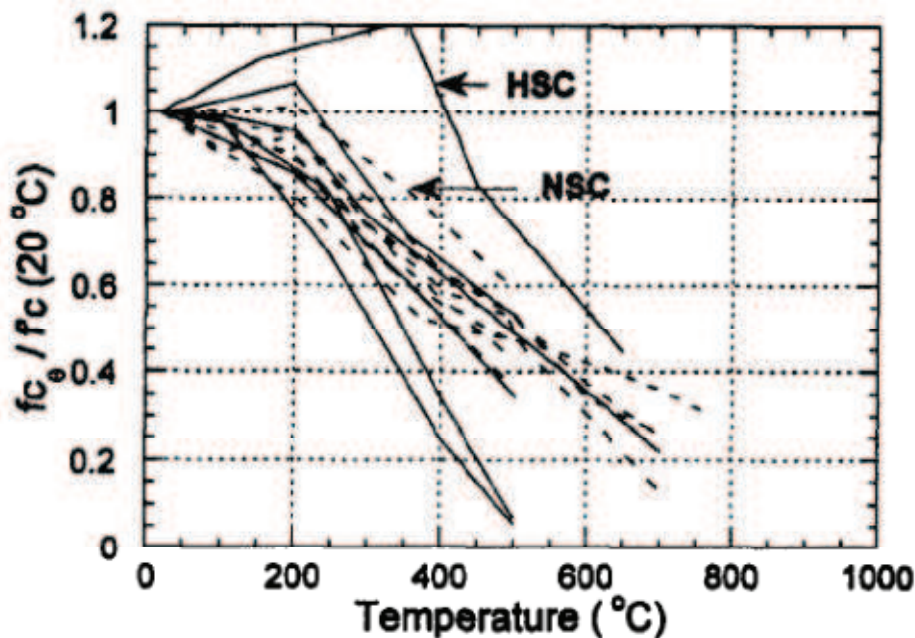


Figure 48 : Compressive strength-temperature trends for NSC and NWA Concretes by unstressed residual-strength test [Phan and Carino, 1998].

2. LITERATURE REVIEW

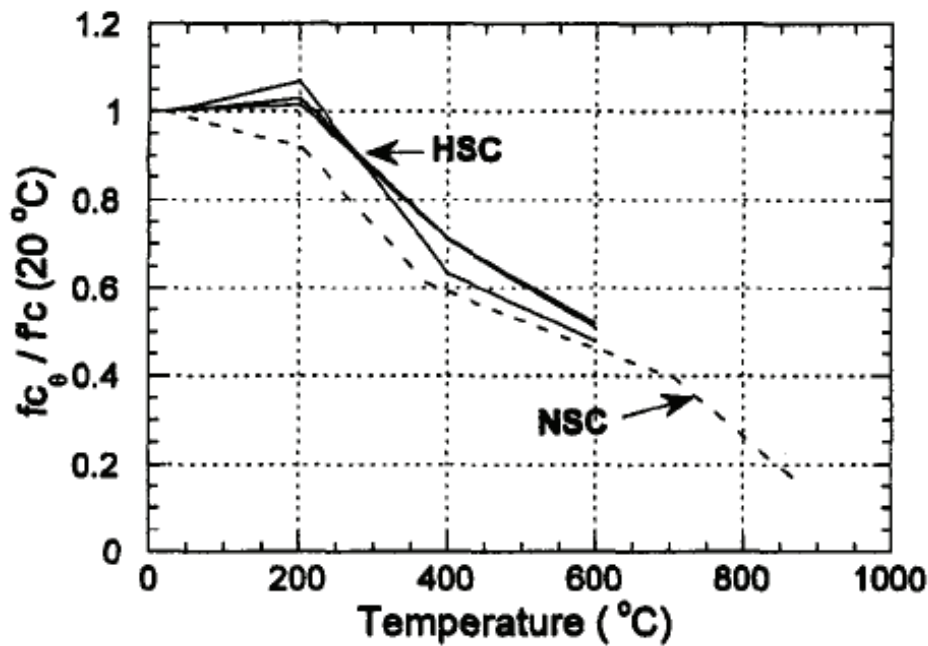


Figure 49: Compressive Strength-Temperature trends for NSC and LWA Concretes by unstressed residual-strength test [Phan and Carino, 1998].

The compressive strength-temperature relations for HSC are characterized by a first stage of increasing in strength or minor strength-loss stage, from room temperature up to 200°C, for both NWA and LWA concretes. In particular one of the considered LWA concrete shows a significant gain up to 350°C in compressive strength, more pronounced in comparison with one related to NWA concrete.

The second stage consists of a general permanent strength-loss stage, which begins from approximately 200°C for both HSC. The unstressed residual strength-temperature relationships for HSC and NSC are somewhat similar for the entire range of temperature.

The pozzolanic additions play an important role in influencing thermal behaviour of HSC in terms of compressive strength. Some experimental works have been carried out in order to study the performance of HSC containing different types of pozzolanic additions after thermal exposure, in substitution of Ordinary Portland cement (OPC).

Poon et al. investigated the residual compressive strength of HSC and NSC prepared with SF (Silica Fume), FA (Fly Ash) and GGBS (Ground Granulated Blast Furnace Slag) subjected to thermal exposure up to 800°C (Poon et al., 2001). The residual compressive strength values for all the considered mixes are plotted in Figure 50.

2. LITERATURE REVIEW

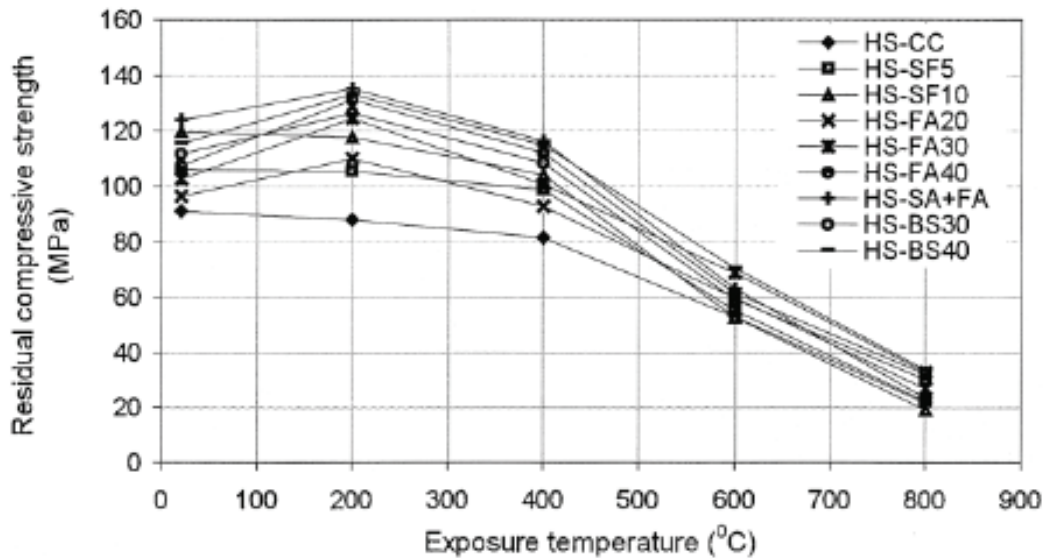


Figure 50: Residual compressive strength values for HSC containing pozzolanic additions [Poon et al, 2001].

In Figure 50 it arises that each temperature range shows a distinct pattern of strength loss or gain:

- From 20°C to 200°C, the FA and GGBS concretes shows increases in strength, especially for FA concretes. In fact, the maximum strength gain was shown by the HSC containing 40% FA. A slight strength loss was observed in OPC and SF concretes. The strength gain was probably due to the formation of tobermorite, which was formed by the reaction between unhydrated FA or GGBS particles and lime (calcium oxide, CaO) at high temperatures. However, this increase in strength was more pronounced in HSC as compared to NSC, probably because of the greater amount of unhydrated FA or GGBS particles in HSC due to its dense structure.
- From 200°C to 400°C, most HSC maintained almost their original strength, while a significant decrease was observed in NSC, thus the pozzolanic concretes performed better and showed higher residual strength.
- A severe loss in strength was observed between 400 and 600°C, more severe for NSC than for HSC. The maximum strength was retained by the HSC containing 30% FA replacement; the better performance of FA and GGBS concretes in this temperature range is due to the reduced amount of portlandite, which otherwise results in strength loss and disintegration.
- At 800°C, all the concretes showed severe deterioration due to the decomposition of C-S-H gel. The residual strength is higher for HSC than for NSC.

2. LITERATURE REVIEW

In each temperature range, HSC maintained a higher percentage of residual compressive strength than NSC. The reason is the coarsening of the pore structure and increase in pore diameter, which was found to be more pronounced in NSC at elevated temperatures than in HSC. Due to this effect, NSC shows a gradual decrease in strength, while sharp decrease was observed in HSC between 400°C and 800°C. The beneficial effect of pozzolanic additions is more pronounced at temperatures below 600°C, and in particular FA concretes give the best performance followed by GGBS, OPC and SF concretes.

As shown in the previous graphs, aggregate type affects residual behaviour of HSC. In fact, some Authors have considered also NSC and HSC containing calcareous and siliceous aggregates, heated up to 750°C (Savva et al., 2005). The residual compressive strength losses for calcareous and siliceous aggregate concretes are collected in Figure 51.

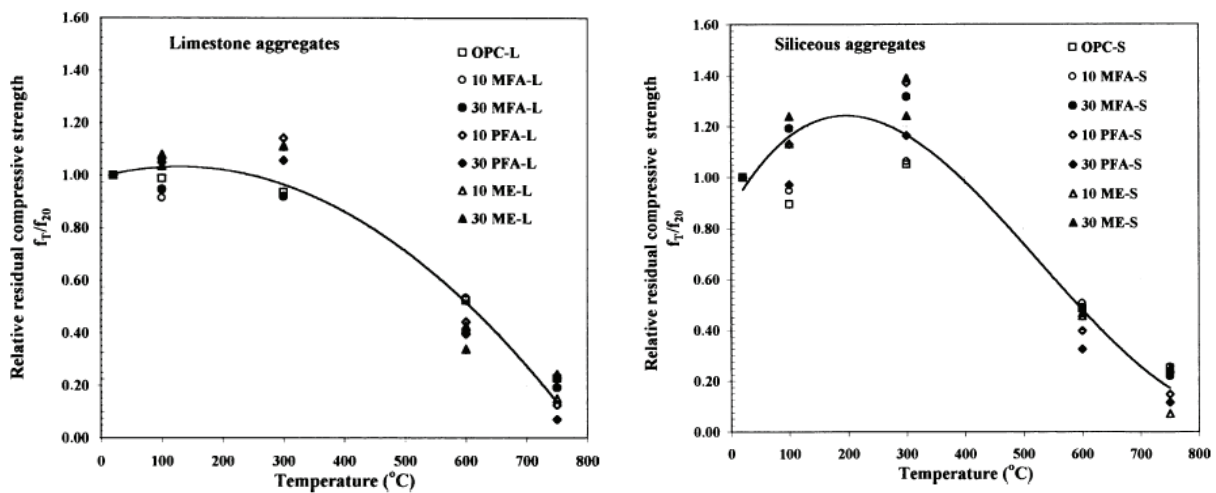


Figure 51: Relative residual compressive strength of limestone (on the left) and siliceous (on the right) aggregates [Savva et al., 2005].

Observing the experimental trends in Figure 51 siliceous concretes present an increase in residual compressive strength up to 200°C more significant than that recorded for limestone concretes. Beyond this temperature, the calcareous concrete show a less pronounced decrease in strength compared with the siliceous ones, indicating that the latter appears more affected by thermal exposure for temperature higher than 200°C.

The different compressive strength trends of previous concretes can be explained referring to the well-known behaviour of quartzite silica which gives rise to hydrothermal reactions at high

2. LITERATURE REVIEW

temperature (between 150 and 200°C) and pressure conditions leading to a welding between cementitious matrix and quartz aggregates. This produces stronger bond between them and consequent increase in mechanical properties of siliceous concrete in comparison with the calcareous ones (Massazza et al., 1980, Tognon et al. 1980).

Some Authors have studied the effect of PP and steel fibers on residual compressive strength of HSC, after high temperature exposure. In particular Poon et al. determined the mechanical residual properties of HSC mixes reinforced with either or both steel and PP fibers (Poon et al., 2004).

Steel fibers are seen to be useful in minimizing the damage effect of high temperature for all the considered concrete mixes. However, although the use a small percentage of PP fibers slightly increased the residual strength of concretes after exposure to 600°C, it had negative effects on the compressive strength of the concrete at 800°C. When the PP fibers were used together with steel fibers, the residual strength of the concrete was lower than that of the concrete with steel fibers alone, but was slightly higher that of the concrete without any fibers (prepared with Portland cement and with partial substitution of metakaolin).

2.2.1.2 Stress-strain curves and modulus of elasticity

Several Authors have performed experimental tests detecting stress-strain behaviour and modulus of elasticity of HSC in function of thermal exposure. Siddique and Noumowe collected experimental data from different Authors highlighting the importance of these data in order to assess the overall response of a structural element (Siddique and Noumowe, 2010). Not much has been reported regarding this topic but some experimental works are presented in the current Paragraph.

Gambarova and Felicetti studied the effect of high temperature on residual properties of two HSC, lower and higher-grade, heated at 500°C, by means of stress-strain curves; mechanical properties, such as modulus of elasticity, have been determined (Felicetti and Gambarova, 1998). The stress-strain curves are collected in Figure 52.

2. LITERATURE REVIEW

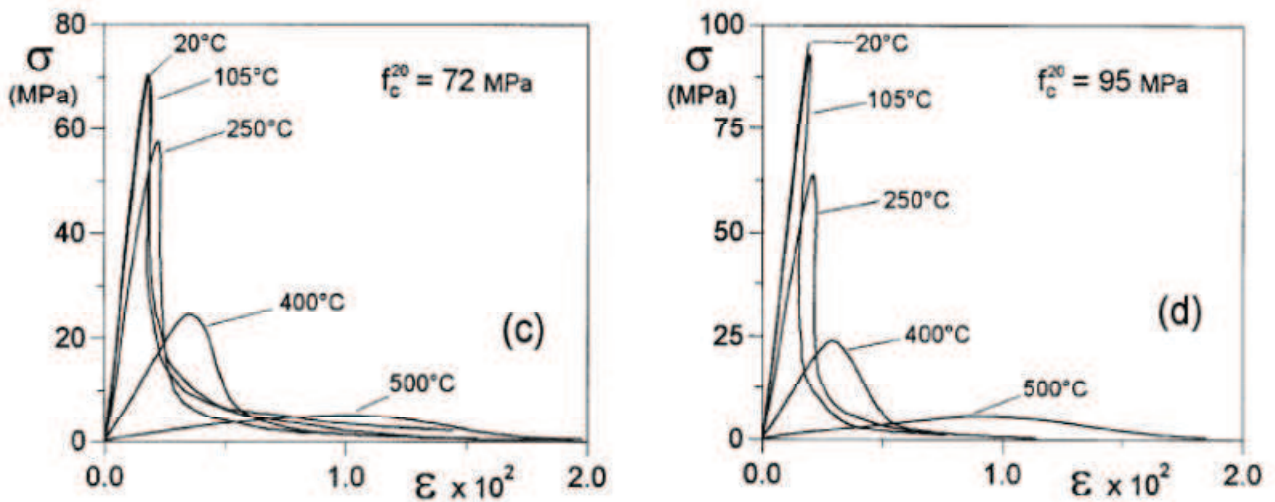


Figure 52: Stress-strain curves for lower (on the left) and higher (on the right) grade HSC at different exposure temperatures [Felicetti and Gambarova, 1998].

The material response is very brittle for both concretes up to 250°C, with a more or less pronounced snap-back, which is certainly fostered by the slenderness of the specimens ($h/\varnothing = 3$). Beyond 250°C, both concretes soften, to the detriment of the strength and to the advantage of the strain corresponding to the peak stress.

The decay in elasticity modulus after the first load and after 4 to 5 loading cycles are reported in Figure 53.

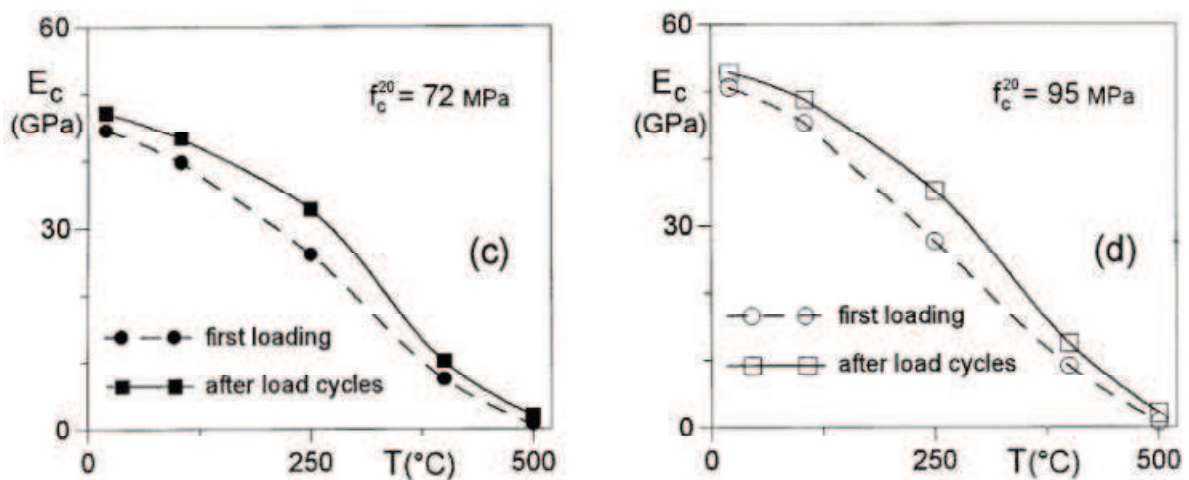


Figure 53: Modulus of elasticity curves for lower (on the left) and higher (on the right) grade HSC at different exposure temperatures [Felicetti and Gambarova, 1998].

2. LITERATURE REVIEW

For both HSC, the detrimental effect on elasticity modulus of high temperature exposure can be observed, but not significant differences are detected between the higher and lower-grade concretes, especially after 250°C. Moreover, it results that higher values of modulus of elasticity is maintained higher after some load cycles than after only one, in the overall range of temperatures.

The effect of different aggregate types and presence of steel fibers in HSC on stress-strain curves have been studied by some Authors, which collected these experimental trends as well as the modulus of elasticity decays, plotted in Figure 54 (Cheng et al., 2004).

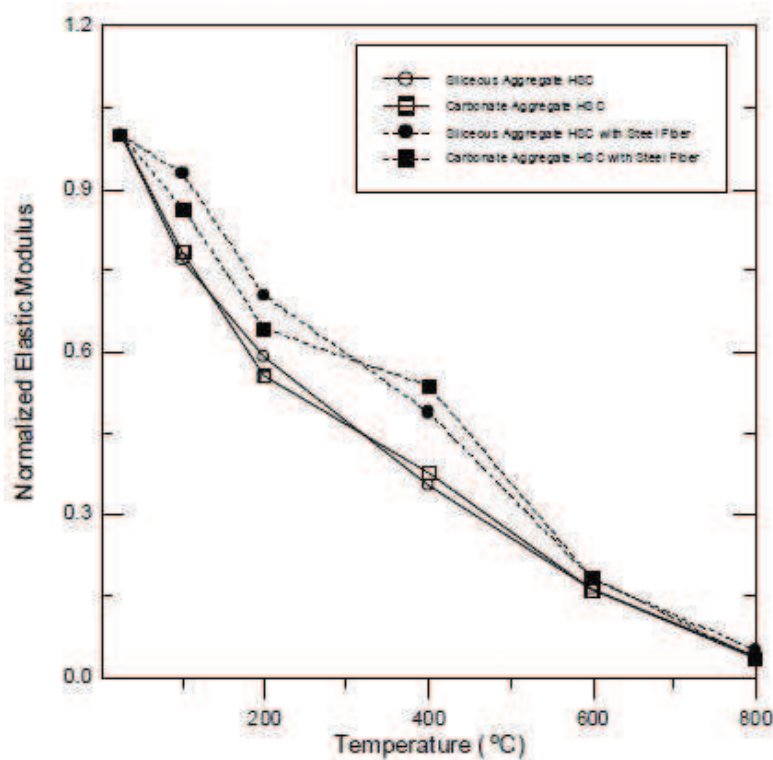


Figure 54: Modulus of elasticity curves for HSC, with different aggregates and presence/absence of steel fibers, at different exposure temperatures [Cheng et al., 2004].

From Figure 54, it arises that the decay in elastic modulus is less pronounced in presence of steel fibers and, in this case, the carbonate aggregate concrete results more penalized up to 200°C, but not between 200 and 400°C, than the one with siliceous aggregates.

Moreover, the Authors observed from the stress-strain curves (not reported in the current text) that HSC with no fibers exhibit brittle properties below 600°C, and ductility above 600°C; when steel fibers are present, HSC exhibit ductility for temperatures over 400°C. From the stress-strain curves, it arises also that the strain at peak loading increases with temperature and the increase in strains for HSC with carbonate aggregate is larger than that for HSC with siliceous ones.

2. LITERATURE REVIEW

Phan and Carino plotted the experimental results for modulus of elasticity both in case of unstressed and residual strength tests (Phan and Carino, 1998). As for compressive strength, they compared the data related to Normal-Weight and LightWeight HSC with the ones related to NSC (see Figure 55).

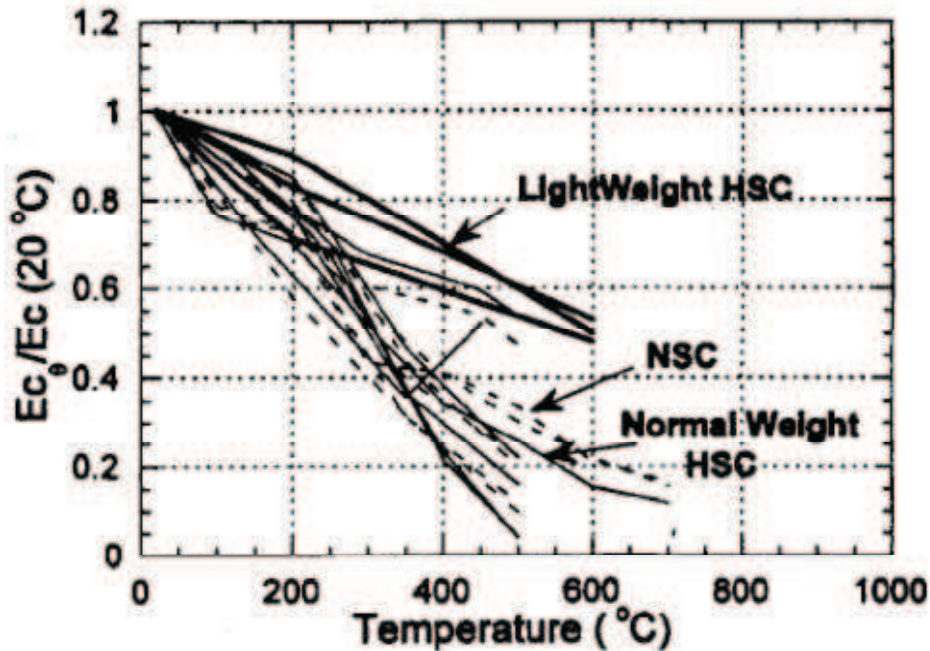


Figure 55: Modulus of elasticity-temperature trends for LWA, NWA and NSC concretes by unstressed residual-strength test [Phan and Carino, 1998].

The modulus of elasticity decay for NWA HSC and NSC is quite similar, while significant differences are observed for LWA HSC in comparison with them. LWA HSC seems to be less affected by high temperature exposure, presenting a less pronounced decay in elastic modulus in comparison with the other considered materials.

From the experimental data shown in the current Paragraph, it seems that the decay in modulus of elasticity is more prominent compared with the one related to compressive strength.

2.2.1.3 Splitting tensile strength

Considering the review carried out by Siddique and Noumowe, not much work has been published regarding the effect of high temperature exposure on indirect tensile strength determined by splitting test. Some experimental data were recorded by Noumowe, which studied the behaviour of HSC, with and without PP fibers, after exposure up to 200°C (Noumowe, 2005).

2. LITERATURE REVIEW

The experimental data confirm a significant reduction in splitting tensile strength as already observed for the others mechanical properties. In particular, the heat resistance of the splitting tensile strength appeared to decrease when PP fibers were incorporated into concrete, while the same non-heated concrete presented splitting tensile strength value higher than the one without fibers. In the opinion of the Author, the behaviour of PP fibers mix is probably due to the additional porosity and small channels created in the mortar by the fibers melting.

2.2.1.4 Effect of heating rate on mechanical properties

As already considered for microstructural parameters, the effect of heating rate has been studied in order to define which influence could have on HSC mechanical properties (Gallè et al., 2003). Three different heating rates have been considered: 0.1, 1 and 10°C/min; the residual compressive and tensile strength, as well as elastic modulus, have been detected. The compressive and tensile strength trends in function of temperature and heating rate are reported in Figure 56 and Figure 57 respectively.

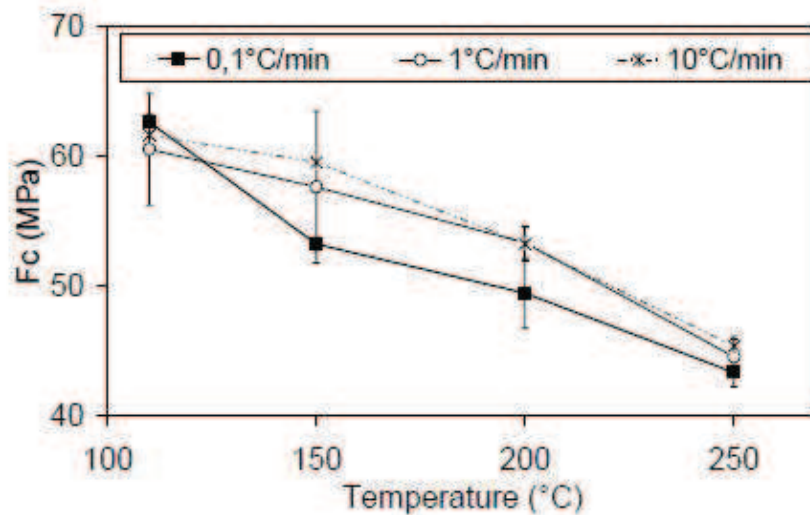


Figure 56: Evolution of the compressive strength with temperature and heating rate [Gallè et al., 2003].

2. LITERATURE REVIEW

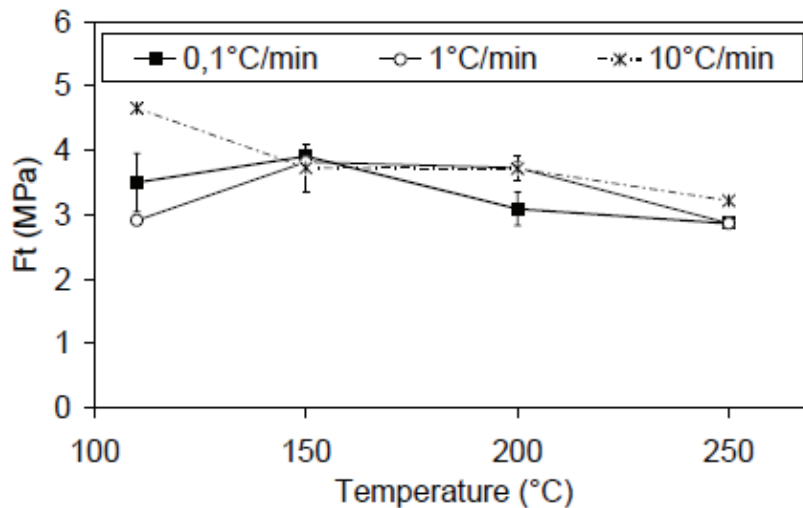


Figure 57: Evolution of the tensile strength with temperature and heating rate [Gallè et al., 2003].

From Figure 56, it appeared that the lowest compressive strength values were found with the lowest heating rate (except at 110°C). However, the relative discrepancy between the average values detected at 0.1 and 10°C/min were rather limited and approximately about 10%.

The effect of heating rate observed on this mechanical property is consistent with the one detected on the dehydration of hydrated phases in Paragraph 2.1.1.1.4. In fact, at a fixed temperature, the lower the heating rate, the higher the conversion degree of dehydration reactions, the lower the compressive strength.

Concerning tensile strength, the results in Figure 57 showed not a clear tendency or influence of heating rate on this parameter. After thermal exposure at 150°C, the experimental data are very close, but also after the other temperature treatments the values for the different heating rate are comprised between 3 and 4 MPa.

In Figure 58 the trends of elastic modulus in function of temperature and heating rate are plotted. A linear decay was detected for all the different heating rates; the 0.1 and 1°C/min rates presented very close trends, with no significant discrepancy. The 10°C/min heating rate was characterized by the lowest elastic modulus values and the relative variation between the values provided by the 0.1 and 10°C/min rates was almost 10%. Thus, it is possible to conclude that a slow heating rate is favorable in order to detect the residual elastic modulus, while for the compressive strength evaluation the higher heating rate seems to be more suitable.

2. LITERATURE REVIEW

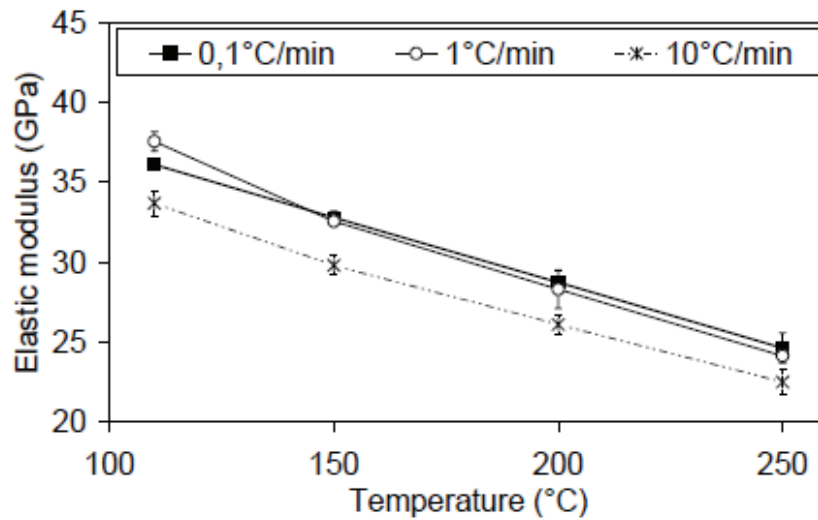


Figure 58: Evolution of the elastic modulus with temperature and heating rate [Gallè et al., 2003].

From these experimental observations, it arises that the effect of heating rate on concrete residual mechanical properties remains difficult to evaluate, even if the heating rate of 1°C/min seems to be the most indicated for a good evaluation of both compressive strength and elastic modulus.

2.2.2 Explosive spalling in concrete

Explosive spalling is the most evident form of damage for concrete and can occur in the material when exposed to high temperature and/or fire; it consists in the detaching of material fragments from the heated surface of concrete elements. It follows that this phenomenon presents structural implications, because when it occurs the structural element integrity is compromised.

Nowadays, explosive spalling is a critical and still highly-debated issue, not well explained; two principal causes have been introduced in order to explain this complex phenomenon (Anderberg 1997, Kalifa et al. 2000, Mindeguia et al. 2010 and 2011):

- Hygro-thermal process, related to the pore-pressure build-up due to water vaporization. If this pressure values overtake the tensile strength of concrete, the spalling can be initiated;
- Thermo-mechanical process, linked to the thermal gradients, induced especially by rapid heating, which generate high compressive stress close to the heated surface.

From the numerical analysis, it arises that under fast heating conditions, thermal stress induced by temperature gradients plays a dominant role in explosive spalling, while under the slow heating condition, the damage is mainly caused by vapor pressure induced stress (Zhao, 2012).

2. LITERATURE REVIEW

The two above-mentioned processes need a specific deepening in the next Paragraphs, in order to better explain their peculiarities and the way in which they act on the material causing spalling phenomenon.

2.2.2.1 Pore pressure build-up

Hygro-thermal processes can be explained considering that thermal exposure produces water vapor in concrete. Being that HPC are characterized by dense matrix and low permeability, this fact limits the ability of vapor to escape, thus a build-up of vapor pressure is generated inside the material. When heating continues, the vapor pressure increases until the internal stresses/energy becomes very high, resulting in explosive spalling.

In order to analyze the vapor pressure, two aspects have to be considered:

- The determination of vapor pressure **(A)**;
- The mechanical effect analysis of vapor pressure **(B)**.

(A) The determination of **vapor pressure** can be carried-out starting from the explanation of relationship between the state properties of the system, such as pressure, specific volume and temperature, which is illustrated in Figure 59 (Moran and Shapiro, 2008).

Observing Figure 59, when water is heated under certain pressure, a phase transition (vaporization) from water to water vapor will happen at a certain temperature. The area grey colored is related to a liquid-vapor region, where water and vapor coexist in equilibrium and are called saturated water and saturated vapor. Within the two-phase region, the pressure and the temperature are dependent on one another and the state can only be described by the specific volume and either the pressure or the temperature.

2. LITERATURE REVIEW

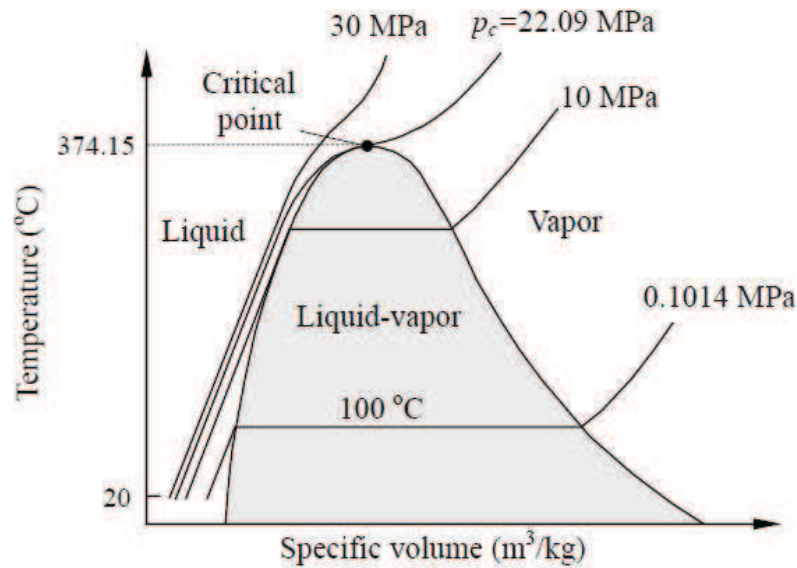


Figure 59: Pressure, specific volume and temperature diagram for water [Moran and Shapiro, 2008].

The point at the top of the two-phase region is called critical point and the corresponding state parameters are called critical parameters. The critical temperature is the maximum temperature at which the liquid and vapor can coexist. If temperature exceeds the critical temperature, water will be present as gas, which differs from vapor because it can't be converted to liquid, also compressing. For water, the critical temperature and pressure are 374.15°C and 22.09 MPa, respectively. When liquid water is fully vaporized, the vapor phase on further heating is called superheated vapor/steam. Steam tables (tables of saturated water and superheated steam), can be used for retrieving the state data.

The great advantage of this diagram is to obtain the pressure value corresponding to starting values of specific volume and temperature. Considering the concrete pores (see Paragraph 2.1.1.1.4), if the related volume and temperature are known, the pressure inside them can be obtained through the previous diagram.

(B) The **mechanical effect analysis** of vapor pressure on the stress and strain field in a heated concrete material can be studied by means of the theory of poro-mechanics formulated by Biot, because concrete can be considered as a porous medium due to the presence of gel and capillaries pores.

2. LITERATURE REVIEW

According to Biot's theory, concrete, considered as a porous medium, is characterized by two linear constitutive equations (Biot, 1941):

1)

$$\varepsilon = \frac{\sigma}{K} + \frac{p}{H} \quad [23]$$

where:

- ε is the volumetric strain;
- σ is the hydrostatic pressure;
- K is the drained bulk modulus and $1/K$ is named as compressibility under drained conditions;
- p is the fluid pressure;
- $1/H$ is the Biot modulus, which is the specific volumetric strain caused by the pore pressure while the applied stress is held constant. Its calculation has been addressed by Zhao (2012).

This first equation [23] states that the changes in applied stress and pore pressure produce a fractional volume change;

2)

$$\zeta = \frac{\sigma}{H_1} + \frac{p}{R_1} \quad [24]$$

where:

- ζ is the increment of fluid content;
- $1/H_1$ is the specific storage of fluid due to the applied stress (equals to $1/H$);
- $1/R_1$ is the specific storage of fluid due to the pore pressure.

The second constitutive equation [24] describes that the changes in applied stress and pore pressure require fluid to be added to or removed from the porous medium.

According to the poro-mechanical theory, two coupling phenomena reflect the poroelastic behavior of a porous medium: the solid-to-fluid coupling and the fluid-to-solid coupling (Biot, 1941; Coussy, 2004). The first coupling occurs when the applied stress change causes a fluid pressure or fluid storage change, while the second one refers to the change in fluid pressure or fluid

2. LITERATURE REVIEW

storage which produces a change in the volume of the porous medium. The extent of the solid-to-fluid coupling depends on the compressibilities of the solid skeleton and the pore fluid; since the solid skeleton of concrete is much more incompressible in comparison with water vapor, the solid-to-fluid coupling can be negligible. Thus, considering the one-way coupling mathematically simplifies the analysis and the fluid-flow problem can be solved independently of the stress field. In fact, the generalized linear elastic constitutive relation incorporating the one-way coupling of the fluid-to-solid and the thermal expansion is the following:

$$\varepsilon_{ij} = \frac{1}{2G} \left[\sigma_{ij} - \frac{\nu}{1+\nu} \sigma_{kk} \delta_{ij} \right] + \frac{1}{3H} p \delta_{ij} + \varepsilon_{th}^e \delta_{ij} \quad [25]$$

where:

- G is the drained shear modulus;
- ν is the drained Poisson's ratio
- p is the pore pressure;
- δ_{ij} is the Kronecker delta;
- ε_{th}^e is the effective thermal strain.

From the last equation, it arises that the bulk elastic volume change is governed by the combination of stress and pore pressure, which is called effective stress and expressed as follows (Coussy, 2004):

$$\sigma_{ij}^e = \sigma_{ij} + \alpha_b \cdot p \delta_{ij} \quad [26]$$

where:

- σ_{ij}^e is effective stress;
- α_b is the Biot-Willis coefficient and is defined as $\alpha_b = \mathbf{K}/\mathbf{H} = \mathbf{f}_{cap}$

Replacing the expression of α_b in the last expression, it results that:

$$\sigma_{ij}^e = \sigma_{ij} + p_e \delta_{ij} \quad [27]$$

where:

2. LITERATURE REVIEW

- p_e is the effective vapor pressure and is defined as: $p_e = f_{cap} \cdot p$

It arises that the effective stress, given by the stress induced by pore pressure in addition to the initial stress field, controls the elastic volume change and the failure behavior of the porous medium.

2.2.2.2 Thermal gradients in heated concrete

The second principal cause of concrete spalling is ascribed to thermal gradients generated by heat transport phenomenon, which induce consequent thermal stresses inside the exposed material. Moreover, heating causes the thermal expansion of concrete. Considering that different concrete components present different thermal behaviour, thermal stresses are induced by the incompatibility of volume changes. This effect causes a sudden failure (spalling) of the solid together with the release of the potential energy.

Some Authors have studied this phenomenon and the possible mechanism leading to explosive thermal spalling can be resumed in Figure 60 (Bažant 1997, Ulm 1999a and 1999b, Mazars 1989).

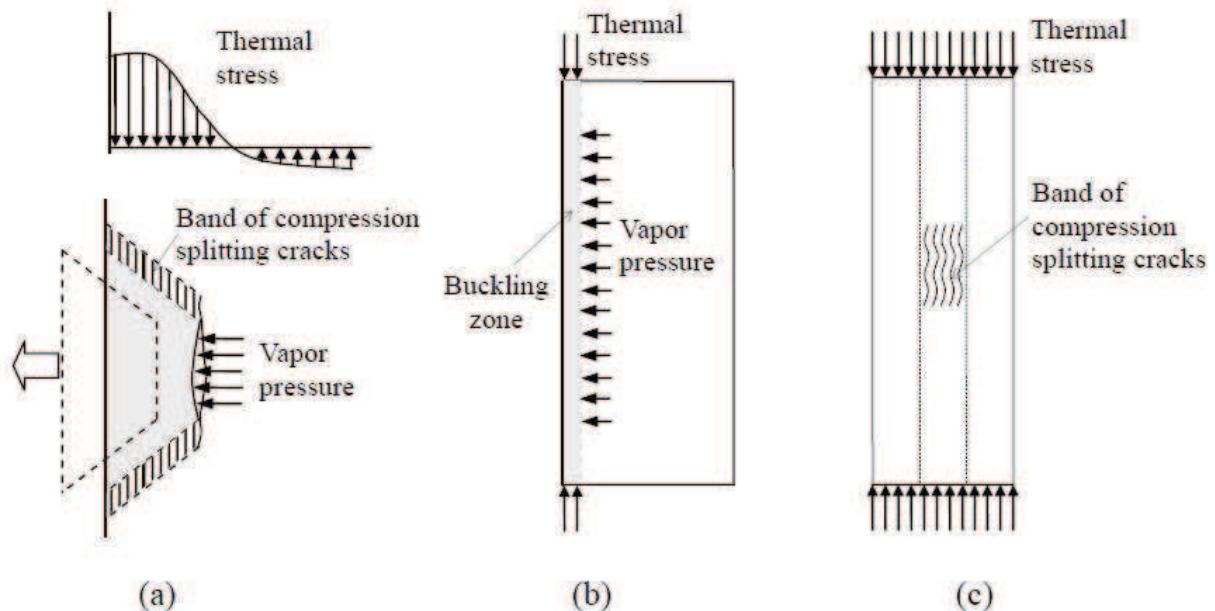


Figure 60: Possible mechanisms of explosive thermal spalling: (a) pressure shear model, (b) buckling model, and (c) compression splitting cracking model (Zhao, 2012).

2. LITERATURE REVIEW

Bažant stated that the vapor pressure could only trigger the happening of explosive spalling and the thermal stress induced potential energy might play a dominant role in explosive spalling as shown in Figure 60 (a). Moreover, Ulm developed a chemo-plastic model to analyze the fire spalling of concrete rings of the Channel Tunnel (Chunnel). The plastic strain was used as an indicator for approximately evaluating the spalling depth in the concrete rings. It was concluded that spalling was caused by the restrained thermal dilatation induced compressive stress. The vapor pressure was, however, not considered.

Moreover, Mazars proposed a model in which spalling wasn't predicted directly. Instead, four different failure modes linked to thermal spalling occurring have been considered by the Author: the shear failure (Figure 60, a), the buckling failure (Figure 60, b), the simplified fracture failure (Figure 60, c), and the integrative failure, were used for the spalling prediction.

Beyond the different causes of thermal spalling illustrated in Figure 60, the mechanism that induced the explosive spalling is related to the high compressive strength generated on the surface following the thermal loading. When these stresses overtake the concrete strength, the ejection of pieces occurs.

Besides the presentation of the major effects linked to thermal spalling, the determination of temperature field is equally important to explain, in order to understand how the thermal front penetrates from the hot concrete surface to the material bulk and which is the time needed for it to advance in the material.

Generally speaking, in a solid, the heat transport phenomenon, from the high to low temperature region, is described by Fourier's law:

$$q_i = -\lambda_i \frac{\partial T}{\partial x_i} \quad [28]$$

where:

- q is the heat flux;
- λ is the thermal conductivity;
- T is the temperature.

2. LITERATURE REVIEW

Under an established heating condition, the temperature field in a solid can be described by a differential equation, deduced from the principle of energy conservation (the first law of thermodynamics) and Fourier's law and indicated as follow:

$$\rho c \dot{T} = \frac{\partial}{\partial x_i} \left(\lambda_i \frac{\partial T}{\partial x_i} \right) + \dot{\phi} \quad [29]$$

where:

- ρ is the mass density;
- c is the specific heat;
- \dot{T} is time derivative of temperature;
- $\dot{\phi}$ is the internal heat source.

In the last expression, indicating the Fourier's law in non-stationary conditions, are involved the parameters that define thermal diffusivity D :

$$D = \lambda / \rho \cdot c \quad [30]$$

Due to the parameters defining it, D can be considered as a thermal property of the material because controls heat diffusion through it, which also conditions the pressure build-up phenomenon.

2.2.2.3 Mass transport in concrete after thermal exposure

As concrete is a porous medium, the study of build-up vapor pressure in the heated material, explained in the previous Paragraph, shall be coupled with the **moisture transport**. In fact, the build-up vapor pressure is the driving force for the moisture transport and, in return, the moisture transport influences the vapor pressure build-up. In particular, the moisture content of concrete determines the magnitude of the build-up vapor pressure and the moisture transport determines the moisture content.

2. LITERATURE REVIEW

For better describe that in concrete, when exposed to elevated temperatures, a moisture transport driven by the build-up vapor pressure gradient occurs, and that its low permeability results in low velocity of the vapor flow, the Darcy's law is used:

$$q' = -k\nabla p \quad [31]$$

where:

- q' is the moisture flux;
- k is the permeability;
- p is the pore pressure.

The diffusion of moisture driven by the gradient of moisture concentration is also assumed negligible in view of the fact that the diffusion takes time and fire spalling occurs in the first several minutes of heating (Bažant and Kaplan, 1996).

Considering the mass balance of vapour in a differential concrete volume $dx dy dz$, it is possible to obtain the governing equation of moisture transport:

$$\left[\frac{\partial}{\partial x} \left(k \frac{\partial p}{\partial x} \right) + \frac{\partial}{\partial y} \left(k \frac{\partial p}{\partial y} \right) + \frac{\partial}{\partial z} \left(k \frac{\partial p}{\partial z} \right) \right] - \frac{\partial \rho}{\partial t} + \dot{m}_{dh} = [32]$$

where:

- \dot{m}_{dh} is the moisture source from the thermal decomposition of hardened cement, coming from the contribution given by the kinetic release of hydration water, explained in Parafgraph 2.1.1.1.3.

In the previous equation, the permeability parameter k is given by:

$$k = \rho \frac{k_e'}{\eta} \quad [33]$$

2. LITERATURE REVIEW

where:

- ρ is the mass density of vapor;
- k_e' is the effective intrinsic permeability in m^2 ;
- η is the dynamic viscosity of vapor.

As already mentioned in previous Paragraph, hardened cement paste will undergo thermal degradation when exposed to high temperature, resulting in a pore structure change and thus a variation in the permeability. It is considered a temperature dependent parameter, because is the results of the intrinsic permeability of the material at a certain temperature and that one coming from the thermal exposure.

From general expression of Darcy's law, it arise that, at a constant value of moisture flux (q'), if pore pressure decrease, an increase in permeability is expected. It means that, for reducing explosive spalling risk, the pore pressure must be reduced and this effect can be obtained increasing permeability, i.e. by using PP fibers which generate additional permeability by their melting and degradation.

2.2.2.4 Permeability determination in HPC at high temperatures

Permeability can be used to quantify the structural changes; in literature, permeability determination data at room temperature are common to find, but not much work has been carried out on the measurement of permeability at high temperature.

An innovative experimental set-up to measure permeability of HPC (in presence and absence of PP fibers) at temperature up to 300°C has been developed by Ožbolt and Bošnjak (2013) and shown in Figure 61.

2. LITERATURE REVIEW

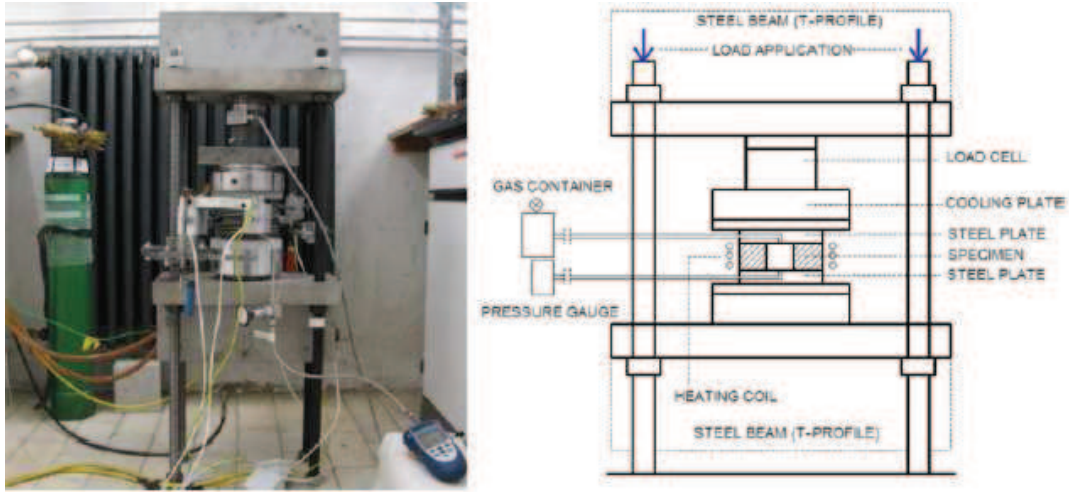


Figure 61: New test setup for the permeability measurements at elevated temperatures [Ožbolt and Bošnjak, 2013].

The concrete hollow cylindrical specimens, placed between two steel plates, are heated using a spiral heating collar fastened to the rods. A heating rate of 0.5°C/min was selected to avoid possible cracking due to thermal gradients. Nitrogen is used as permeating gas, owing to its inert behaviour with respect to concrete and because it does not enhance burning. Once a pressure of 20 MPa is applied, the initial permeability measurement is performed at room temperature. The hollow portion of the specimen is pressurized using nitrogen and the pressure is measured. The pressure history is obtained and apparent permeability (in m²) for every time step is calculated using the following expression derived from Darcy's and Clapeyron's law:

$$k = \frac{\eta \ln\left(\frac{r_2}{r_1}\right)}{\pi H} \frac{\frac{\Delta p}{\Delta t} V}{(p_2^2 - p_1^2)} \quad [34]$$

where:

- η is the viscosity of the permeating fluid;
- r_1 is the inner radius of the specimen;
- r_2 is the outer radius of the specimen;
- H is the height of the specimen;
- p_1 is the inlet pressure;
- p_2 is the outlet pressure (atmospheric pressure);
- V is the volume of the pressurized gas.

2. LITERATURE REVIEW

In each time interval t , the apparent permeability k is calculated according to last equation, while pressure decay history is obtained from the experiment.

In case of specimens tested at elevated temperature, once the specimen attained the desired temperature, three or more permeability tests are performed following the above-described procedure and the specimen is heated to the next target temperature. Upon finishing the test series at elevated temperatures, the specimen is gradually cooled to the room temperature. Residual permeability measurements are also performed.

The experimental permeability data in function of temperature, obtained by the Authors by means of the presented set-up, are plotted in Figure 62.

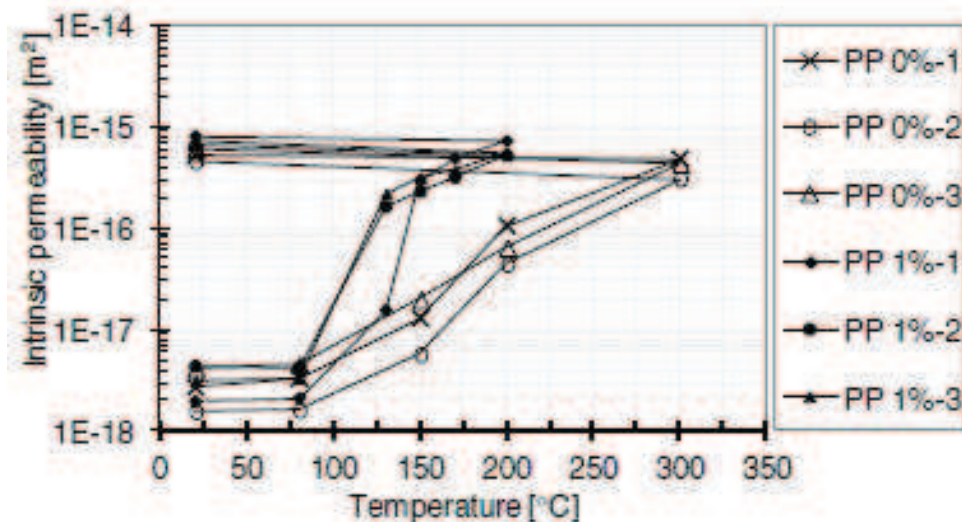


Figure 62: Intrinsic permeability of HPC with and without PP fibers in function of temperature [Ožbolt and Bošnjak, 2013].

From Figure 62, it arises that up to 80°C, the permeability data are quite similar between HPC with and without PP fibers. Between 80 and 200°C, the concretes containing PP fibers exhibit a two order of magnitude increase in permeability. Mixes without fibers presents similar values of permeability in comparison with those containing fibers, at 300°C. For all the HPC types, the permeability in residual condition is higher than those at elevated temperatures. These results clearly demonstrate, in case of PP fibers mixes, that there is a significant increase in the permeability of concrete with PP fibers and this result can explain the beneficial effect of the addition of PP fibers in mitigation of explosive spalling.

2. LITERATURE REVIEW

Another experimental work on high temperature determination of permeability has been performed (Schneider, 2010). As in the previous study, both HPC with and without fibers have been considered. The experimental set-up is reported in Figure 63.

Slightly conical concrete specimens, cured in rings, are installed in an electric furnace. The steel ring was loaded by an external steel frame with a hydraulic pressure system as to ensure the gas tightness according to the gas pressure difference on the concrete surfaces. The pressure difference between inflow and outlet of the gas (dry air or nitrogen) was measured. After the outlet, the gas was cooled to nearly ambient temperatures. Before cooling, the pressure difference between the inlet and outlet was recorded. The maximum gas pressure is 5 bar and temperatures up to 500°C were applied.

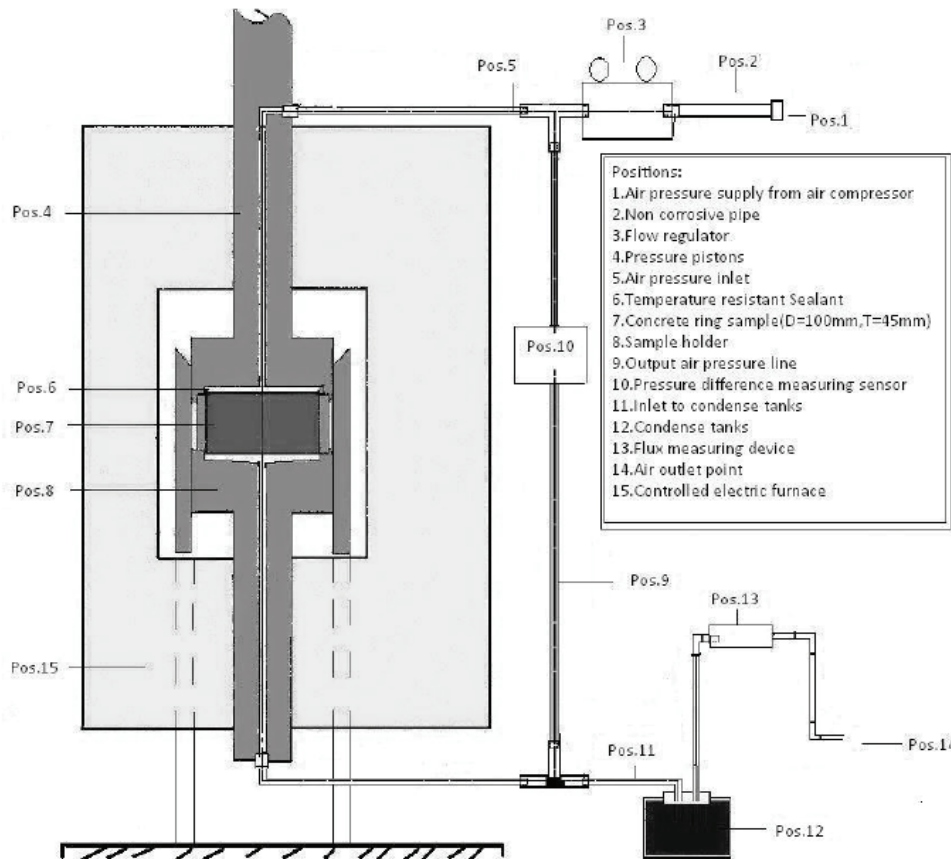


Figure 63: Test apparatus for permeability measurements at elevated temperatures [Schneider, 2010].

The experimental results obtained by means of the apparatus in Figure 63 are plotted in Figure 64, applying inlet pressure of 5 bar.

2. LITERATURE REVIEW

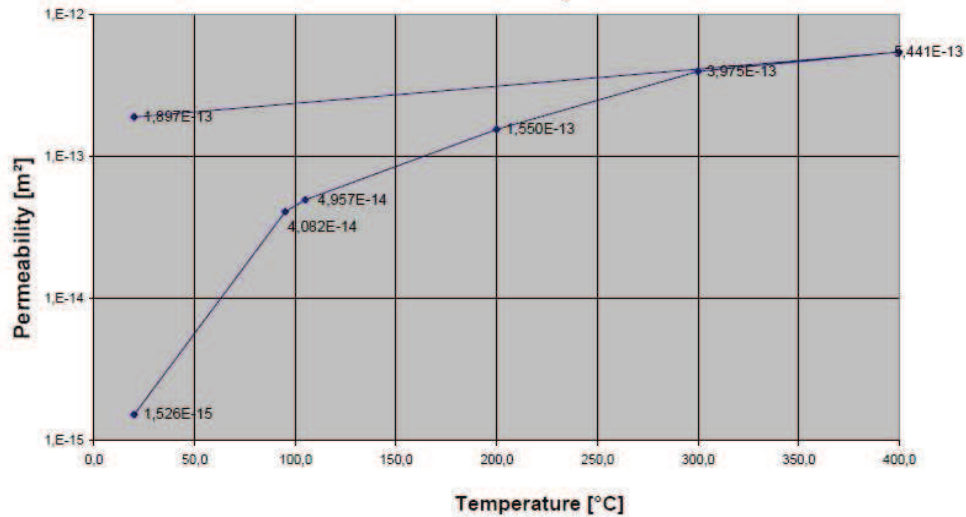


Figure 64: Permeability of HPC during heating and cooling ($p_1 = 5$ bar) [Schneider, 2010].

The trend of permeability data in function of temperature in Figure 64 is similar to those detected by the set-up by Ožbolt and Bošnjak. The permeability increases up to 400°C, more significantly between 20 and 100°C and also between 100°C and 300°C (in the latter interval, the slope is less rapid than in the interval between 20 and 100°C). As expected, the residual permeability measured after thermal exposure is higher than the one measured at the beginning of the test, indicating the permanent damage induced on the microstructure by high temperature exposure.

2. LITERATURE REVIEW

2.3 Literature review: concluding remarks

This extended literature review tried to link the chemical thermodynamic and kinetic aspects of degradation reactions, ascribed to the intrinsic material damage, to the decay in mechanical properties and spalling phenomenon, occurring in concrete exposed to high temperature/fire.

More in details, the main considerations can be summarized as follows:

A) **Intrinsic damage:**

- Cement pastes, when exposed to high temperature and/or fire, are subjected to chemical transformations, each of them occurring in a specific temperature range. They will have an impact on total porosity and its distribution, and this effect becomes more relevant as temperature increases;
- The replacement of cement with pozzolanic materials or mineral additions allows to enhance the residual compressive strength and thermal shock resistance, and to decrease damage phenomena of cement pastes;
- Considering the thermodynamic aspects of dehydration reactions of main hydrates compounds in cement matrix, the duration of the heating phase influences in a significant way their conversion degree;
- The heating rate exerts a remarkable influence on hardened cement paste degradation; when heating rate increases, the temperature corresponding to the complete decomposition of hydrated phases increases. Moreover, it has been observed that, at constant temperature value, the higher the heating rate the lower the degree of conversion and the slower the development of the capillary porosity;
- Regarding thermal stability of aggregates, the higher the material heterogeneity the more distributed are the microcracks induced by thermal exposure. In fact, calcareous and quartz aggregates are more homogeneous, thus they are significantly less affected by microcracks at high temperature (up to 600°C) in comparison with flints and granites, that are more heterogeneous materials, thus more affected by microcracks.
- Aggregate rocks are characterized by different thermal dilatation; from literature, it arises that basalts and anorthosite exhibit the highest thermal stability because of their lowest

2. LITERATURE REVIEW

length variation as temperature increases, while the worst seems to be quartz and granodiorite.

- Considering concrete, it has been observed that the addition of PP fibers affects the porosity at high temperature of HSC and decrease the pore pressure inside the material; in this way, the release of moisture from the concrete matrix is improved, leading to a lower risk of concrete spalling in case of accident. PP fibers action is explained in different ways from different Authors, with the common objective of justifying the effectiveness of PP fibers in limiting or preventing concrete spalling.

B) Mechanical damage and spalling:

- The decay in HSC mechanical properties has been considered, highlighting that the elastic modulus seems to be more affected by thermal exposure in comparison with compressive strength;
- The aggregate and binder types influence the mechanical behaviour of concrete at residual conditions. In particular, the beneficial effect of pozzolanic additions is more pronounced, especially at temperatures below 600°C.
- The heating rate effect on the compressive strength appears consistent with the dehydration of hydrated phases. At any given temperature, the lower the heating rate, the higher the conversion degree of dehydration reactions and the lower the compressive strength;
- The permeability is the key parameter in vapour transport phenomena and it may cause pressure build-ups. Thermal diffusivity controls heat transport through the concrete, which causes thermal gradients, and consequent thermal stresses. This means that the knowing permeability and diffusivity is the key factor in understanding explosive spalling phenomenon.

In the light of the previous considerations, for the scope of the present work, high temperature can be defined as any temperature exceeding 105°C, at which concrete starts being significantly affected by intrinsic damage.

3. OBJECTIVE OF THE THESIS WORK

The thermal exposure of concrete structures to fire or, more in general, to high temperature has relevant economical and social implications. Even if the number of deaths and injuries was strongly reduced in the last years, it remains considerable and preventive measures must be taken in order to reduce it.

Moreover, from the literature review, it arises that many efforts have been devoted to investigate the effect of thermal actions on mechanical properties of concrete, as well as the chemo-physical reactions occurring in cement pastes and aggregates. A relatively low number of studies (Noumowe, 2005, Chan et al., 2008), has been focused only on some particular aspects of the relationships between the intrinsic damage, due to chemo-physical reactions, and the damage at macro-level (mechanical damage). Nevertheless, there is no evidence in literature about a generalized approach based on the extensive investigation which takes into account the most influent parameters (related to the concrete composition and to the exposure conditions) on the above-mentioned relationships.

In this context, an extensive collaboration between CTG-Italcementi Group and Politecnico di Milano (Department of Civil and Environmental Engineering) has been activated to perform a joint research project, whose results are shown in this Ph.D. thesis, with the main objective of investigating:

- the relationships between the intrinsic damage, due to chemo-physical reactions and thermal incompatibility between cementitious matrix and aggregates, and the consequent mechanical properties;
- the thermo-mechanical damage deriving from vapour pressure build-up in concrete, attributable to the onset of temperature gradients with time and space.

The innovative aspects of the present work consist more in detail in investigating the intimate relationships between the processes occurring at nano-micro scale during high temperature exposure and the consequent effects on macro properties of concrete material (especially HPC), considering different parameters such as nature of aggregate, fiber type and content. The consequent advantages would result in a useful tool for design appropriate concrete mixes able to

3. OBJECTIVE OF THE THESIS WORK

resist to thermal actions, predicting and improving the material performances, also introducing a spalling sensitivity index. This can lead to significant economical advantages, allowing fire impact to be less severe as nowadays.

4. EXPERIMENTAL PROCEDURES

4. EXPERIMENTAL PROCEDURES

4.1 General planning of tests

The experimental activity has been focused on the microstructural and physico-mechanical characterization of eleven concrete mixes, including 1 NSC and 10 HPC, subjected to high temperature exposure and tested at residual condition. They differ for their compressive strength, type and content of fibers, as well as for the aggregate type.

The microstructural characterization has been performed by means of Thermogravimetric Analysis (TGA), Scanning Electron Microscopy (SEM), Mercury Intrusion Porosimetry (MIP) and X-Ray Diffraction Analysis (XRD). These determinations have been carried out in order to study the intrinsic damage of the material subjected to thermal cycle. In this context, the mechanical characterization has been also developed and focused on the stress-strain relationship determinations, from which to derive compressive strength and elastic modulus in residual conditions.

In order to study the spalling sensitivity, the eleven mix designs have been also subjected to pore pressure and thermal diffusivity measurements. In the following Paragraphs the selected materials and their characterization, as well as the mix design, the general planning of tests and the test method set-up will be explained. A schematic representation of the activity program is reported in Figure 65.

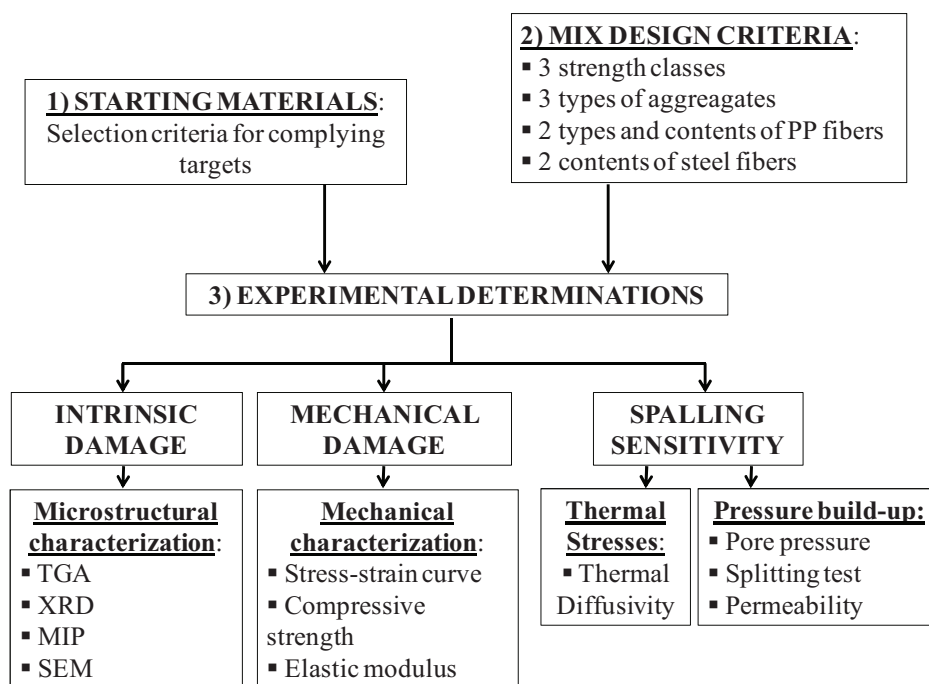


Figure 65: Schematic program of the experimental activity.

4. EXPERIMENTAL PROCEDURES

4.1.1 Characterization of starting materials

4.1.1.1 Cement, filler and pozzolanic addition

The cement identified as reference binder of HPC and NSC concrete mixes is the CEM I, 42.5 R. Its chemical and physico-mechanical analysis, determined according to UNI EN 196-1 (2005), UNI EN 196-3 (2009) and UNI EN 196-6 (2010) are collected in Table 2, while in Figure 66 is reported its laser granulometric distribution, obtained by means of a Laser Diffractometer Sympatec.

Determination	Values
Loss of ignition (%)	2.34
Insoluble residue in HCl-Na ₂ CO ₃ (%)	0.43
Total Sulphide (SO ₃) (%)	2.76
Chloride (%)	0.035
SiO ₂ (%)	20.17
Al ₂ O ₃ (%)	4.99
Fe ₂ O ₃ (%)	3.05
CaO (%)	63.50
MgO (%)	1.37
SO ₃ (%)	2.74
Na ₂ O (%)	0.43
K ₂ O (%)	0.83
SrO (%)	0.10
Mn ₂ O ₃ (%)	0.03
P ₂ O ₅ (%)	0.10
TiO ₂ (%)	0.18
Water for standard consistence (%)	25.0
Initial setting time (min)	135
Final setting time (min)	210
Stability (mm)	1
Compressive strength at 2 days (MPa)	30.5
Compressive strength at 28 days (MPa)	50.6
Fineness: Blaine method (cm ² /g)	3550
Specific gravity (g/cm ³)	3.118

Table 2: Chemical and physico-mechanical analysis for CEM I, 42.5 R.

4. EXPERIMENTAL PROCEDURES

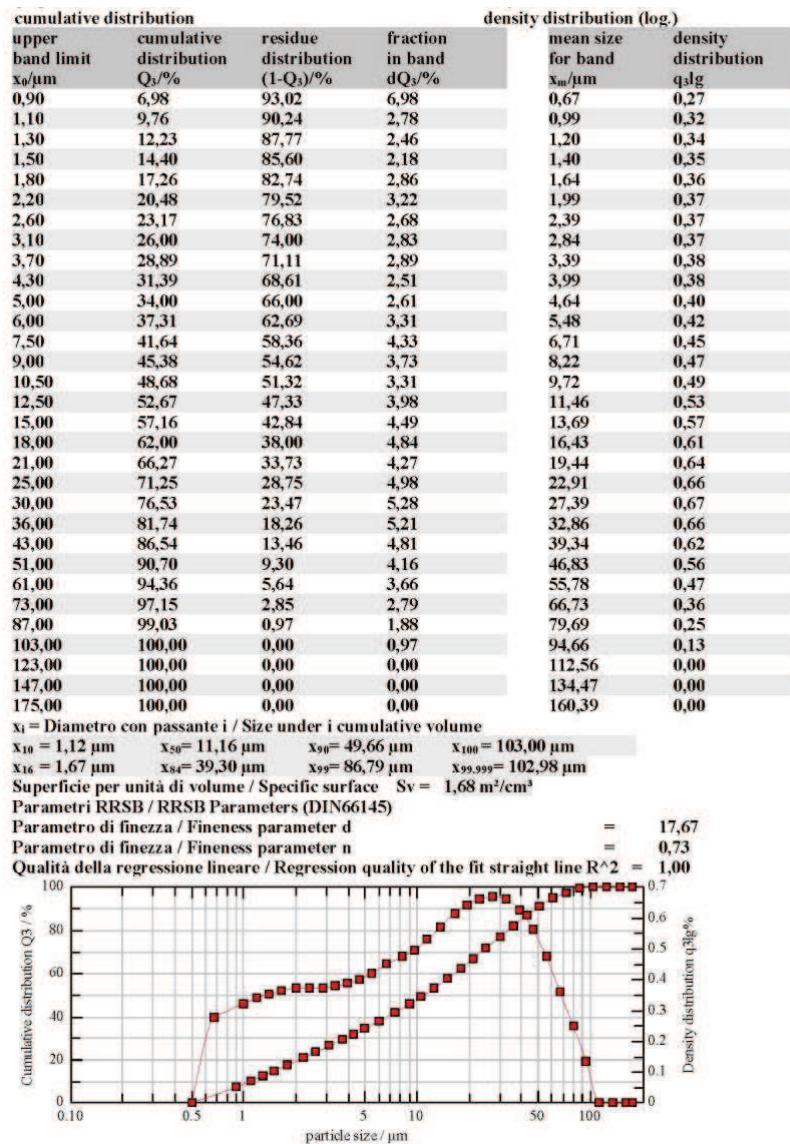


Figure 66: Laser granulometric distribution for CEM I, 42.5 R.

The adopted cement has been used in combination with Ground Granulated Blast Furnace Slag (GGBS) for HPC mixes, while for NSC GGBS was replaced by limestone filler (LF). The choice of using the mentioned type of cement and GGBS pozzolanic addition was required to maintain constant the volumetric fraction of cementitious matrix paste in concretes characterized by three different compressive strength grades.

The chemical and granulometric analysis for GGBS and LF are collected in Table 3 and Figure 67 and Figure 68 respectively.

4. EXPERIMENTAL PROCEDURES

Determination	LF	GGBS
Loss of ignition (%)	44	-0.51
Insoluble residue in HCl-Na ₂ CO ₃ (%)	-	0.11
Total Organic Carbon (TOC) (%)	-	-
Total Sulphide (SO ₃) (%)	-	-
Chloride (%)	-	0.004
SiO ₂ (%)	0.47	39.75
Al ₂ O ₃ (%)	0.26	11.13
Fe ₂ O ₃ (%)	0.07	0.42
CaO (%)	55.04	40.55
MgO (%)	1.08	5.41
SO ₃ (%)	0.03	1.56
Na ₂ O (%)	-	0.01
K ₂ O (%)	0.06	0.30
SrO (%)	0.02	0.09
Mn ₂ O ₃ (%)	-	0.06
P ₂ O ₅ (%)	0.03	0.02
TiO ₂ (%)	0.01	0.58
Fineness: Blaine method (cm ² /g)	6890	4810
Specific gravity (g/cm ³)	2.773	2.91
Amorphous phase (%)	-	> 95

Table 3: Chemical and granulometric analysis for LF and GGBS.

4. EXPERIMENTAL PROCEDURES

cumulative distribution				density distribution (log.)	
upper band limit	cumulative distribution	residue distribution	fraction in band	mean size for band	density distribution
$x_0/\mu\text{m}$	$Q_3/\%$	$(1-Q_3)/\%$	$dQ_3/\%$	$x_m/\mu\text{m}$	q_3/g
0,90	6,54	93,46	6,54	0,67	0,26
1,10	9,72	90,28	3,18	0,99	0,37
1,30	12,94	87,06	3,21	1,20	0,44
1,50	16,13	83,87	3,20	1,40	0,51
1,80	20,85	79,15	4,71	1,64	0,60
2,20	26,88	73,12	6,04	1,99	0,69
2,60	32,52	67,48	5,64	2,39	0,78
3,10	38,96	61,04	6,44	2,84	0,84
3,70	45,78	54,22	6,82	3,39	0,89
4,30	51,61	48,39	5,84	3,99	0,89
5,00	57,31	42,69	5,70	4,64	0,87
6,00	63,80	36,20	6,48	5,48	0,82
7,50	70,91	29,09	7,12	6,71	0,73
9,00	75,87	24,13	4,96	8,22	0,63
10,50	79,48	20,52	3,61	9,72	0,54
12,50	83,09	16,91	3,61	11,46	0,48
15,00	86,45	13,55	3,36	13,69	0,42
18,00	89,47	10,53	3,02	16,43	0,38
21,00	91,69	8,31	2,22	19,44	0,33
25,00	93,85	6,15	2,16	22,91	0,29
30,00	95,77	4,23	1,92	27,39	0,24
36,00	97,35	2,65	1,58	32,86	0,20
43,00	98,54	1,46	1,19	39,34	0,15
51,00	99,33	0,67	0,79	46,83	0,11
61,00	99,80	0,20	0,47	55,78	0,06
73,00	100,00	0,00	0,20	66,73	0,03
87,00	100,00	0,00	0,00	79,69	0,00
103,00	100,00	0,00	0,00	94,66	0,00
123,00	100,00	0,00	0,00	112,56	0,00
147,00	100,00	0,00	0,00	134,47	0,00
175,00	100,00	0,00	0,00	160,39	0,00

x_i = Diametro con passante i / Size under i cumulative volume

$x_{10} = 1,12 \mu\text{m}$ $x_{50} = 4,13 \mu\text{m}$ $x_{90} = 18,72 \mu\text{m}$ $x_{100} = 73,00 \mu\text{m}$
 $x_{16} = 1,49 \mu\text{m}$ $x_{84} = 13,18 \mu\text{m}$ $x_{99} = 47,64 \mu\text{m}$ $x_{99,999} = 72,94 \mu\text{m}$

Superficie per unità di volume / Specific surface $S_v = 2,22 \text{ m}^2/\text{cm}^3$

Parametri RRSB / RRSB Parameters (DIN66145)

Parametro di finezza / Fineness parameter d

Parametro di finezza / Fineness parameter n

Qualità della regressione lineare / Regression quality of the fit straight line $R^2 = 0,99$

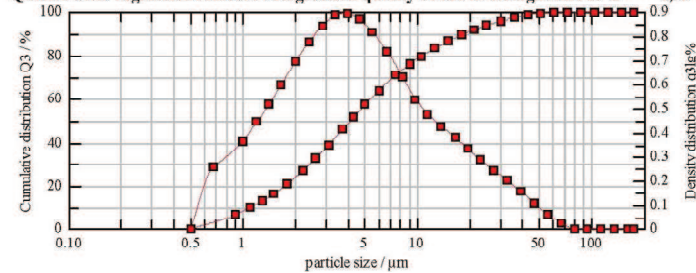


Figure 67: Granulometric analysis (laser distribution) for LF.

4. EXPERIMENTAL PROCEDURES

cumulative distribution				density distribution (log.)	
upper band limit	cumulative distribution	residue distribution	fraction in band	mean size for band	density distribution
$x_0/\mu\text{m}$	$Q_3/\%$	$(1-Q_3)/\%$	$dQ_3/\%$	$x_m/\mu\text{m}$	q_3/g
0,90	4,40	95,60	4,40	0,67	0,17
1,10	6,19	93,81	1,79	0,99	0,21
1,30	7,79	92,21	1,60	1,20	0,22
1,50	9,23	90,77	1,44	1,40	0,23
1,80	11,15	88,85	1,92	1,64	0,24
2,20	13,40	86,60	2,25	1,99	0,26
2,60	15,39	84,61	1,98	2,39	0,27
3,10	17,63	82,37	2,24	2,84	0,29
3,70	20,12	79,88	2,49	3,39	0,32
4,30	22,49	77,51	2,37	3,99	0,36
5,00	25,19	74,81	2,70	4,64	0,41
6,00	28,95	71,05	3,76	5,48	0,47
7,50	34,38	65,62	5,44	6,71	0,56
9,00	39,54	60,46	5,16	8,22	0,65
10,50	44,43	55,57	4,90	9,72	0,73
12,50	50,66	49,34	6,22	11,46	0,82
15,00	57,99	42,01	7,33	13,69	0,93
18,00	66,12	33,88	8,13	16,43	1,03
21,00	73,33	26,67	7,20	19,44	1,08
25,00	81,36	18,64	8,04	22,91	1,06
30,00	88,84	11,16	7,48	27,39	0,94
36,00	94,51	5,49	5,67	32,86	0,72
43,00	97,88	2,12	3,37	39,34	0,44
51,00	99,38	0,62	1,50	46,83	0,20
61,00	99,89	0,11	0,51	55,78	0,07
73,00	100,00	0,00	0,11	66,73	0,01
87,00	100,00	0,00	0,00	79,69	0,00
103,00	100,00	0,00	0,00	94,66	0,00
123,00	100,00	0,00	0,00	112,56	0,00
147,00	100,00	0,00	0,00	134,47	0,00
175,00	100,00	0,00	0,00	160,39	0,00

x_i = Diametro con passante i / Size under i cumulative volume
 $x_{10} = 1,62 \mu\text{m}$ $x_{50} = 12,29 \mu\text{m}$ $x_{90} = 31,22 \mu\text{m}$ $x_{100} = 73,00 \mu\text{m}$
 $x_{16} = 2,74 \mu\text{m}$ $x_{84} = 26,76 \mu\text{m}$ $x_{99} = 48,99 \mu\text{m}$ $x_{99,999} = 72,90 \mu\text{m}$
 Superficie per unità di volume / Specific surface $S_v = 1,30 \text{ m}^2/\text{cm}^3$
 Parametri RRSB / RRSB Parameters (DIN66145)
 Parametro di finezza / Fineness parameter $d = 16,24$
 Parametro di finezza / Fineness parameter $n = 1,05$
 Qualità della regressione lineare / Regression quality of the fit straight line $R^2 = 1,00$

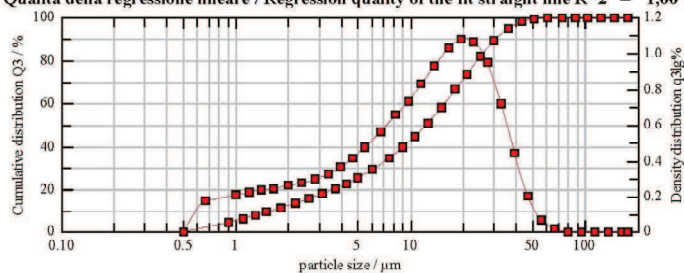


Figure 68: Granulometric analysis (laser distribution) for GGBS.

Comparing the LF and GGBS granulometric distributions, LF is characterized by higher finesses, indicated by higher specific surface value and confirmed by higher value of finesses parameter d , indicating the sieve opening under which 63% of the material is passing ($d_{LF}=6.67$ against $d_{GGBS}=16.24$). Moreover, the granulometric distribution is more enlarged for GGBS, in comparison with the one related to LF, confirmed by higher value of the finesses parameter n for GGBS ($n_{GGBS}=1.05$ against $n_{LF}=0.94$). The d and n parameters refer to Rosin, Rammler, Sperling, Bennet function (RRBS), DIN 66145 (1976), commonly used for results interpolation.

4. EXPERIMENTAL PROCEDURES

4.1.1.2 Aggregates

Three different types of aggregates (silico-calcareous, calcareous and basalt) have been selected for the present experimental study. They are differing each other for different origin (crushed and alluvional), different physico-mechanical (i.e. elastic modulus E) and thermal properties (thermal conductivity λ , thermal dilatation coefficient α and thermal diffusivity).

For all the HPC compressive strength grades, silico-calcareous aggregates (S), with alluvional origin, have been considered. Three granulometric fractions have been used for the mix and they are named as S1, S2 and S3.

The chemical analysis for silico-calcareous aggregate is reported in Table 4, while the specific gravity related to the three fractions (according to EN 1097-6, 2013) are reported in Table 5. The granulometric distributions for all fractions are shown in Figure 69 (according to EN 933-3, 2012).

Determination	Silico-calc. Aggreg (S)
Loss of ignition (%)	17.80
SiO ₂ (%)	45.56
Al ₂ O ₃ (%)	7.65
Fe ₂ O ₃ (%)	2.61
CaO (%)	18.03
MgO (%)	4.45
SO ₃ (%)	0.06
Na ₂ O (%)	1.37
K ₂ O (%)	1.34
SrO (%)	0.06
Mn ₂ O ₃ (%)	0.07
P ₂ O ₅ (%)	0.11
TiO ₂ (%)	0.31

Table 4: Chemical analysis for silico-calcareous aggregate.

Determination	Fr. S1	Fr. S2	Fr. S3
Specific gravity (Mg/m ³) (s.s.a.)	2.71	2.72	2.69

Table 5: Specific gravity for silico-calcareous aggregate fractions.

4. EXPERIMENTAL PROCEDURES

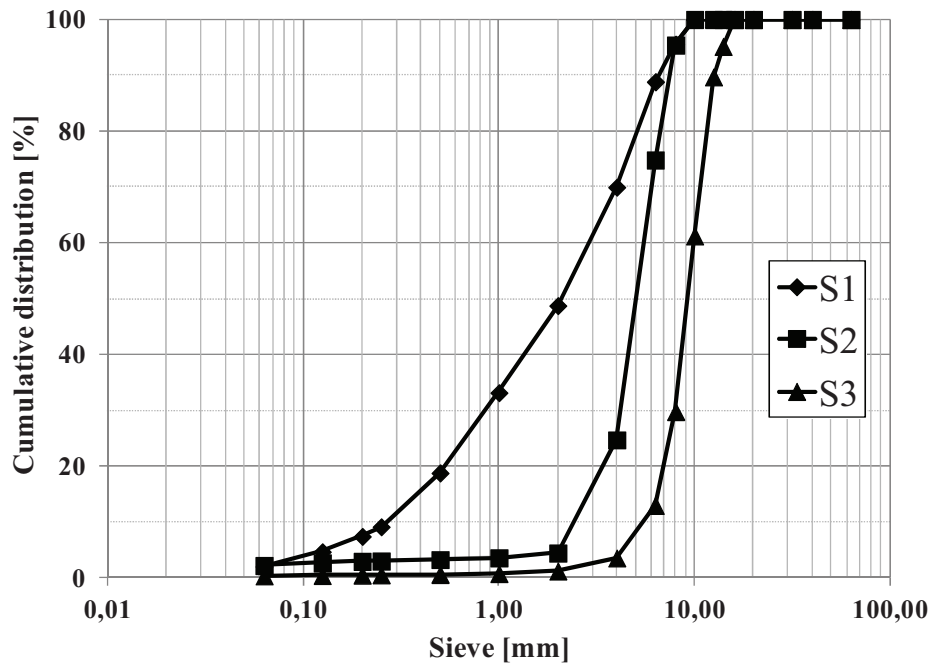


Figure 69: Granulometric distribution for silico-calcareous aggregates fractions.

Calcareous (C) and basalt (B) aggregates have also been considered. The calcareous aggregate has been added to the mix in seven fractions (from C1 to C7), while the basalt in two fractions (B1 and B2).

The chemical analyses for both materials are collected in Table 6 while the specific gravity related to the granulometric fractions are reported in Table 7 and Table 8. The granulometric distributions are shown respectively in Figure 70 and Figure 71. Because of the unavailability of higher diameter fraction, for basalt the limit for maximum diameter was 8 mm.

Determination	Calc. aggr. (C)	Basalt aggr. (B)
Loss of ignition (%)	44	0.10
SiO ₂ (%)	0.47	47.78
Al ₂ O ₃ (%)	0.26	17.80
Fe ₂ O ₃ (%)	0.07	10.13
CaO (%)	55.04	10.37
MgO (%)	1.08	5.25
SO ₃ (%)	0.03	
Na ₂ O (%)	-	3.89
K ₂ O (%)	0.06	1.48
SrO (%)	0.02	0.24
Mn ₂ O ₃ (%)	-	0.18
P ₂ O ₅ (%)	0.03	0.43
TiO ₂ (%)	0.01	1.49

Table 6: Chemical analysis for calcareous and basalt aggregates.

4. EXPERIMENTAL PROCEDURES

Determination	C1	C2	C3	C4	C5	C6	C7
Specific gravity (Mg/m^3) (s.s.a.)	2.67	2.66	2.66	2.69	2.69	2.70	2.72

Table 7: Specific gravity for calcareous aggregate fractions.

Determination	B1	B2
Specific gravity (Mg/m^3) (s.s.a.)	2.82	2.85

Table 8: Specific gravity for basalt aggregate fractions.

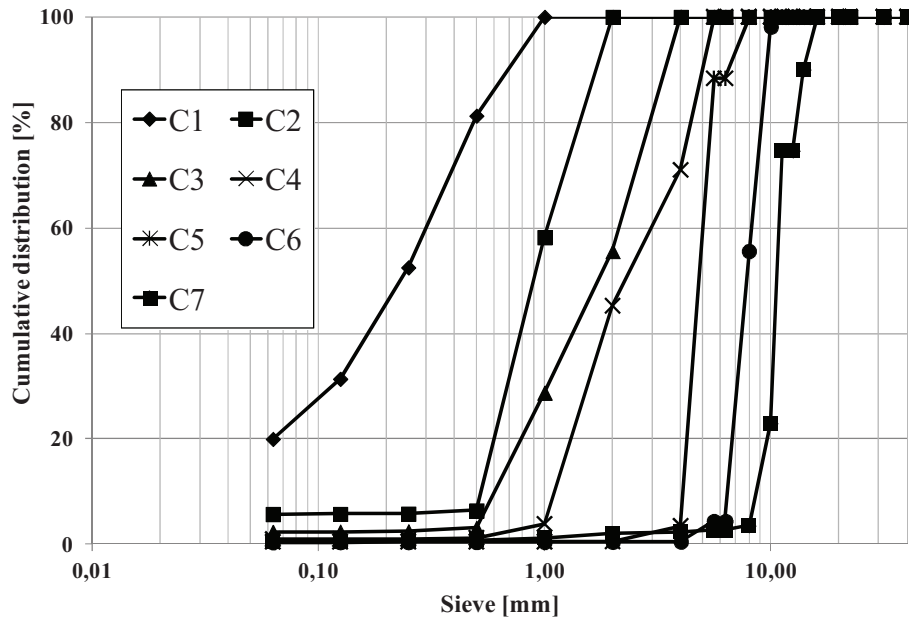


Figure 70: Granulometric distributions for calcareous aggregate fractions.

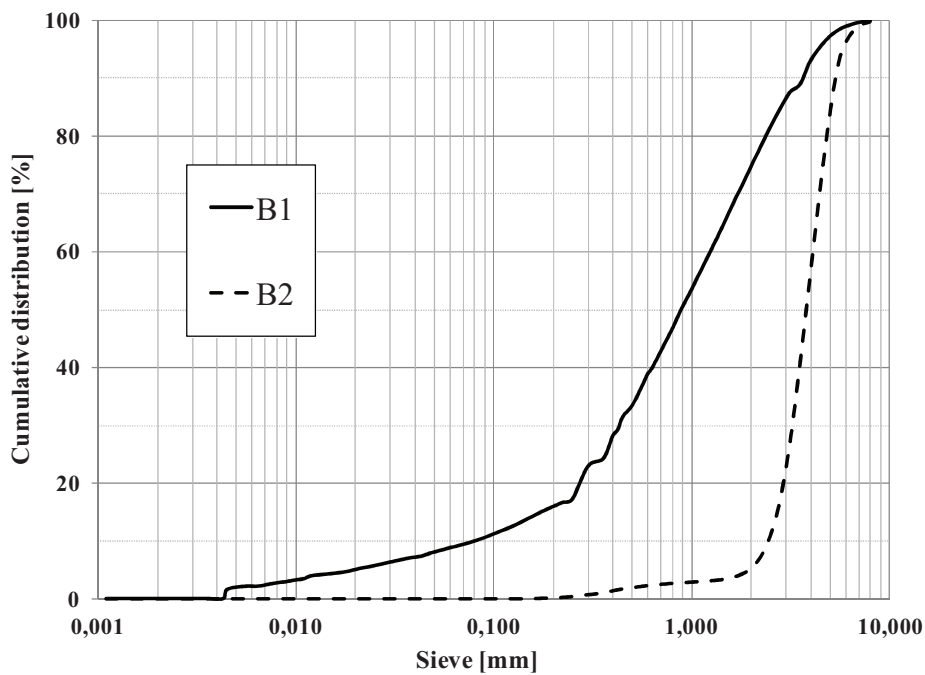


Figure 71: Granulometric distributions for basalt aggregates fractions.

4. EXPERIMENTAL PROCEDURES

4.1.1.3 Polypropylene and Steel fibers

Polypropylene (PP) fibers added to HPC intermediate grade have been selected in two types, monofilament and fibrillated. Monofilament fibers have been indicated in literature as specifically designed to prevent concrete spalling (Koury 2008). Fibrillated ones, generally used to limit early-age shrinkage (Bayasi and McIntyre, 2002), have been selected in order to perform a comparison between the two fiber types in terms of high temperature exposure and spalling resistance.

Their specific characteristics are indicated as follows:

- *Monofilament fibers* (mnf), from La Matassina SrL (MicroGraminflex 9/12), characterized by $L = 12$ mm and $\varnothing_{eq} = 20$ μm ($L/D = 600$). They appear as extruded straight fibers treated with a surfactant agent (Khoury, 2008);
- *Fibrillated fibers* (fbr), from La Matassina SrL (MicroGraminflex F9/12), characterized by $L = 12$ mm and $\varnothing_{eq} = 48$ μm ($L/D = 250$). They appear as straight fibers obtained by longitudinally cutting pp stripes, with a rectangular section.



PP Monofilament



PP Fibrillated

In order to have information regarding the thermal behaviour of these two types of PP fibers, DSC tests have been carried out. The tests have been carried out between -10°C and 500°C with a heating rate of $5^{\circ}\text{C}/\text{min}$ in oxygen and nitrogen atmospheres. From the first type of test, it is possible to obtain information about PP fiber transformations in presence of oxygen, such as combustion. In nitrogen atmosphere, the PP fiber phase transformations are detected, such as melting or degradation.

4. EXPERIMENTAL PROCEDURES

The thermograms in oxygen and nitrogen atmospheres for monofilament and fibrillated PP fibers are reported in Figure 72 and Figure 73 respectively (visualized from 0 to 500°C). Being the DSC a differential technique, the signal in mW is related to the power necessary to compensate, by Joule effect, the temperature differences between the sample and the reference.

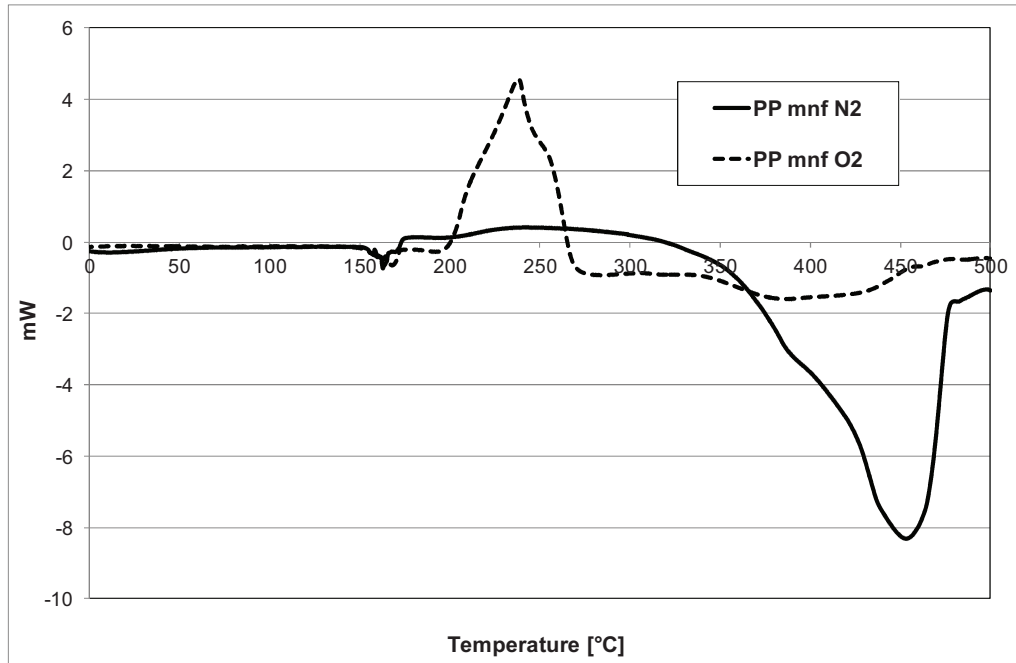


Figure 72: DSC thermograms for PP monofilament fibers.

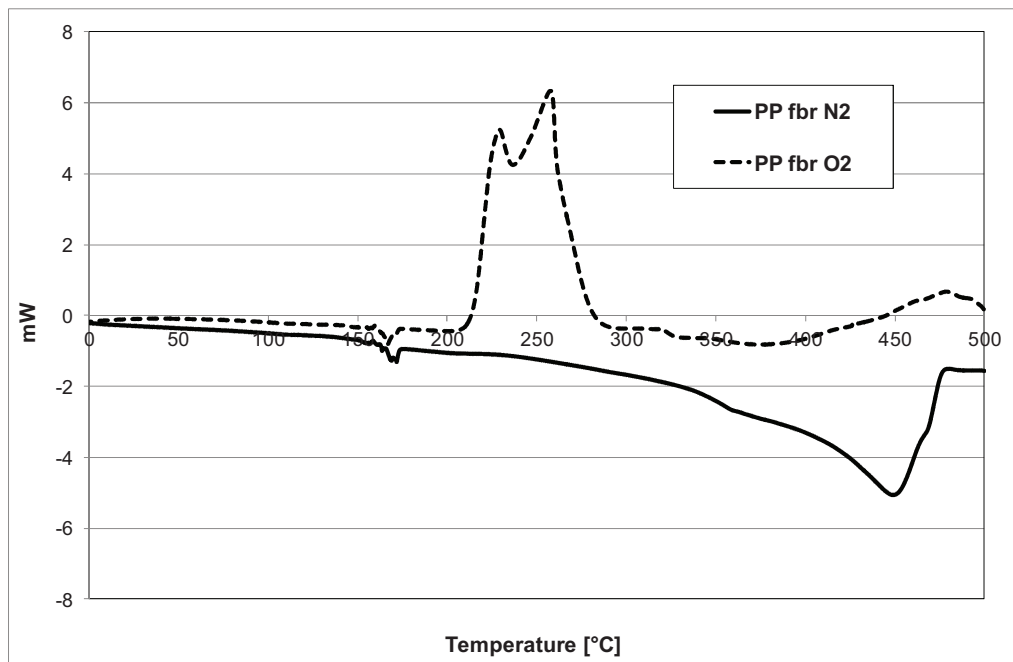


Figure 73: DSC thermograms for PP fibrillated fibers.

4. EXPERIMENTAL PROCEDURES

Even if the thermograms trends (in Figure 72 and Figure 73) are quite different in the shape of combustion and degradation peaks for the two types of fibers, it arises that both melt at almost 160°C and start their degradation at about 300°C, while the onset of their combustion is detected at 200°C.

Steel fibers (SF) added to HPC intermediate grade have been considered in this study in order to evaluate if they can have a beneficial effect in improving the thermal behaviour of concrete. It is well-known that they are commonly used to increase concrete toughness in the post-peak range, and reduces spalling sensitivity too, even if less efficiently than PP fibers (Bhargava, Sharma and Kaushik, 2006).

La Gramigna 0,55x35 hooked steel fibers from La Matassina SrL (see Figure 74) have been added to the concrete mixes; they are characterized by $L = 35$ mm and $\varnothing = 0.55$ mm ($L/D = 64$).



Figure 74: Hooked steel fibers added to HPC mixes [La Matassina].

4.1.1.4 Admixtures

Two different types of acrylic superplasticizers have been used for concrete casting. They differ each other regarding their chemical composition: they are both formed by a principal acid chain, but different degree of substitution of the secondary one. They are both used to maintain the workability over time, but they are suitable in one case for ready mix and for the other in case of precast concrete elements.

4.1.2 Mix design: criteria and main characteristics

The experimental activity has been focused on the microstructural and physico-mechanical characterization of eleven concrete mixes, including NSC (1 mix) and HPC (10 mixes). They differ for their compressive strength, type and content of fibers, as well as for the aggregate type.

Three concrete grades has been considered with $f_{cm,cube} \geq 45, 70, 95$ MPa (determined at 28 days on 100 mm-side cubes), whose mix design includes silico-calcareous aggregates.

4. EXPERIMENTAL PROCEDURES

For the HPC intermediate class ($f_{cm, cube} \geq 70$ MPa), polypropylene (PP) and steel fibers (Sf) have been added, considering different types and contents. The effect of the type of aggregate was evaluated on the same compressive strength grade class by comparing silico-calcareous aggregates with calcareous and basaltic ones.

Mix designs have been defined in order to keep the volumetric fraction of the cementitious paste as constant as possible. The volumetric fraction (VF) can be defined as follows:

$$VF = [(mass_{cement}/\rho_{cement}) + (mass_{replacement}/\rho_{replacement}) + (mass_{water}/\rho_{water})] / 100 \quad [35]$$

In this way, comparing mechanical and microstructural properties is feasible; in fact, it has been considered that only in this condition, the comparison can be carried out in a correct way, avoiding the possible masking among all the considered parameters. Moreover, as reported in Paragraph 2.1.1.1.5, the volumetric fractions are the most suitable parameters in order to describe the thermodynamic and kinetic transformations occurring in the matrix, thus they become fundamental in order to study explosive spalling phenomenon, described in the previous Paragraphs in terms of volumetric fraction.

Several preliminary tests have been carried out in laboratory to identify the optimal composition to obtain the cement paste volumetric fraction as constant as possible among all the eleven concrete mixes types. The optimized mix designs for the three compressive strength grades concretes and the ones having different aggregate types are collected in Table 9, while in Table 10 are represented the mix designs related to the intermediate grade with and without PP and steel fibers. In both Tables, ρ is the density at fresh state, determined according to EN 12350-6 (2009), while the slump tests were carried out according to EN 12350-2 (2009). $f_{cm,cyl}$ is the average compressive strength on cylindrical specimens ($\phi=150$ mm, $h=300$ mm) and $f_{cm, cube}$ is the average compressive strength on 100 mm-side cubes, both measured at the age of 28 days, according to EN 12390-3 (2009). For all the eleven concretes mixes, the Bolomey curve was selected as reference.

4. EXPERIMENTAL PROCEDURES

Mix N.	1	2	3	4	5
Mix designation	45-S	70-S	95-S	70-C	70-B
CEM I (kg/m³)	400	400	480	400	400
Limestone Filler (kg/m³)	200	-	-	-	-
GGBS (kg/m³)	-	200	300	200	200
S1 Fraction (kg/m³)	883	860	821	-	-
S2 Fraction (kg/m³)	105	63	60	-	-
S3 Fraction (kg/m³)	505	636	608	-	-
C1 Fraction (kg/m³)	-	-	-	146	-
C2 Fraction (kg/m³)	-	-	-	238	-
C3 Fraction (kg/m³)	-	-	-	276	-
C4 Fraction (kg/m³)	-	-	-	140	-
C5 Fraction (kg/m³)	-	-	-	217	-
C6 Fraction (kg/m³)	-	-	-	296	-
C7 Fraction (kg/m³)	-	-	-	235	-
B1 Fraction (kg/m³)	-	-	-	-	1086
B2 Fraction (kg/m³)	-	-	-	-	470
PP mnf (kg/m³)	-	-	-	-	-
PP fbr (kg/m³)	-	-	-	-	-
Steel fibers (kg/m³)	-	-	-	-	-
Superplasticizer (kg/m³)	1.8	2.76	12.79	2.04	0.84
Water/cement ratio	0.56	0.54	0.39	0.54	0.57
Volumetric Fraction	0.43	0.41	0.44	0.41	0.43
$\rho_{\text{fresh state}}$ (kg/m³)	2340	2390	2440	2380	2400
Slump (mm)	230	250	260	225	220
$f_{\text{cm,cyl}}$ (MPa)	40	62	90	64	66
$f_{\text{cm,cube}}$ (MPa)	47	72	99	73	73
$f_{\text{cm,cyl}}/f_{\text{cm,cube}}$	0.85	0.86	0.91	0.88	0.90

Table 9: Mix design and mechanical properties of concretes with different compressive strength grades and different aggregates.

4. EXPERIMENTAL PROCEDURES

Mix No	2	6	7	8	9	10	11
Mix designation	70-S	70-S- Pm 0.5	70-S- Pm 1	70-S- Pm 2	70-S- Pf 2	70-S- Sf 40	70-S- Sf 60
CEM I (kg/m ³)	400	400	400	400	400	400	400
GGBS (kg/m ³)	200	200	200	200	200	200	200
S1 Fraction (kg/m ³)	860	860	860	860	860	860	860
S2 Fraction (kg/m ³)	63	63	63	63	63	63	63
S3 Fraction (Kg/m ³)	636	636	636	636	636	636	636
PP mnf (kg/m ³)	-	0.5	1	2	-	-	-
PP fbr (kg/m ³)	-	-	-	-	2	-	-
Steel fibers (kg/m ³)	-	-	-	-	-	40	60
Superplasticizer (kg/m ³)	2.76	2.76	2.76	2.76	2.76	2.76	2.76
Water/cement ratio	0.54	0.54	0.54	0.54	0.54	0.54	0.54
Volumetric Fraction	0.41	0.41	0.41	0.41	0.41	0.41	0.41
$\rho_{\text{fresh state}}$ (kg/m ³)	2390	2380	2370	2350	2390	2410	2430
Slump (mm)	250	240	230	210	230	230	220
$f_{\text{cm,cyl}}$ (MPa)	62	63	60	60	61	63	60
$f_{\text{cm, cube}}$ (MPa)	72	70	70	69	72	72	73
$f_{\text{cm,cyl}}/f_{\text{cm, cube}}$	0.86	0.9	0.86	0.87	0.85	0.88	0.82

Table 10: Mix design and mechanical properties of concrete at intermediate grade with and without PP and steel fibers.

From Table 9 and Table 10, it arises that:

- For all the mix designs, the cement paste volumetric fraction values are very close, according to the restraint to carry out a correct comparison among the mixes in terms of physico-mechanical and microstructural properties;
- In case of intermediate grade, the compressive strength values among the different types of mixes are significantly repeatable;
- The surfactant agent covering the PP monofilament fibers is responsible for the decrease of the fresh state density at increasing values of the fiber content for the mixes 70-S-Pm 2, 70-S-Pm 1 and 70-S-Pm 0.5.

After casting, all the specimens were cured in water for 28 days according to 12390-3 (2009). They were subsequently kept at 10°C for further 28 days, in order to slow down the hydration process. At the end of this period, the specimens were tested in order to evaluate:

- Intrinsic damage induced by thermal exposure, by means of microstructural and mechanical characterizations in residual conditions;
- Spalling sensitivity, by means of diffusivity and pore pressure determinations.

4. EXPERIMENTAL PROCEDURES

4.1.3 Intrinsic and mechanical damage evaluation

In order to evaluate in the most correct way the intrinsic (microstructural) and mechanical damage of the 11 concrete mixes after thermal exposure, a thermal cycle is required to be selected.

4.1.3.1 Thermal cycle design

The thermal cycle, at which the test specimens were exposed, has been designed considering the time of exposure at the maximum temperature and the heating rate from 20°C up to the maximum temperature. For helping in the thermal cycle selection, a graphical elaboration has been carried out by the writer in order to estimate the time needed to reach an establish conversion degree X, in function of temperature.

In theoretical “static” exposure conditions, the CH dehydration has been considered and its related equation indicating the degree of conversion in function of temperature was integrated (see Paragraph 2.1.1.1.3, case A). In this way, an expression in which the parameter X is linked to temperature and time was obtained. Hence, by integrating the expression [7] vs. time it is possible to explicitate the same expression as:

$$X^{1/2} = (1.516 \times 10^7 / 2) \exp(-1.528 \times 10^4 / T) \cdot t \quad [36]$$

For assigned X values, between 0.004 and 0.554, it is possible to plot the time necessary to reach equilibrium conditions at fixed temperature (see Figure 75). In this plotting, temperatures lower than 300°C have been considered in order to predict, in a theoretical steady-state equilibrium condition of thermal exposure, the time needed for the CH conversion. This derive also from the information in Figure 19 showing the variation of dX/dT in function of T; it can be observed that before 320°C the value of the derivative is almost 0, but this means that the degree of conversion, however low it can be, it is constant but not equal to 0, thus, in a theoretical condition, it can be consider also a temperature lower than 250°C to investigate the reaction in a stationary condition. In fact, considering an extreme low temperature (20°C) it arises that at 20°C are necessary almost 10¹¹ hours to reach the CH conversion of 0.1, as shown in the next figure:

It is appropriate to underline that, in a real exposure condition, the conversion is unpropably due to the equilibrium constant mainly shifted towards CH up to almost 350°C

4. EXPERIMENTAL PROCEDURES

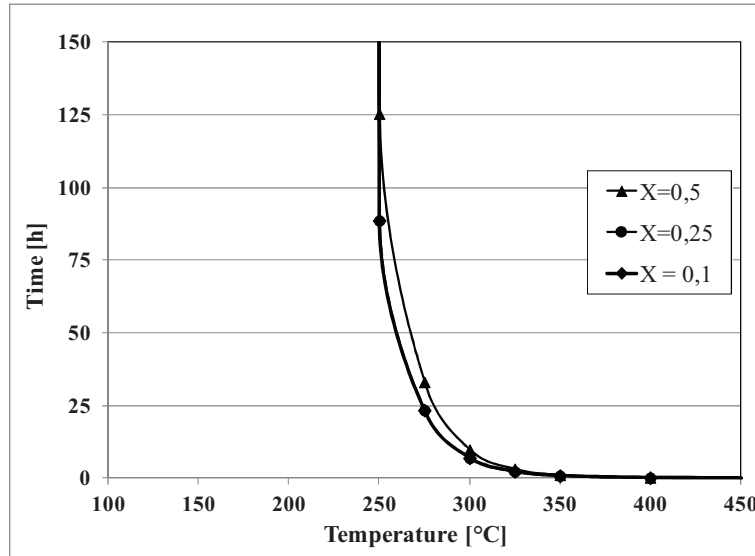


Figure 75: Time exposure as a function of temperature at different conversion degrees.

From Figure 75, it can be observed that the higher the conversion degree, the higher the time needed to reach a given conversion value. As an example, almost 125 hours are required to have a conversion of 50% of CH when exposed at 250°C, in a theoretical condition in which the system is considered in equilibrium condition. Moreover, at a given temperature in the graph, the higher the conversion degree the higher the time needed to reach this value. Depending on these considerations, it follows that the duration of a thermal cycle influences in a significant way the conversion degree of CH. More in general, the duration of treatment follows an exponential law; this means that at increasing target temperature a fixed degree of conversion is reached in a significant exponential decreasing time.

For the previous reasons, considering also that hydrated phases total conversion is favoured by slow heating (Paragraph 2.1.1.1.3 and 2.1.1.1.4), it was established to heat the concrete specimens inside an electric furnace with a heating rate value of 1°C/min; once the target temperature was reached, it was decided to keep it constant for 2 hours. This phase will be then followed by the cooling phase (cooling rate = -0.25°C/min down to 200°C and then natural cooling inside the closed furnace). The characterizations tests were performed in residual conditions considering five target temperatures: 20 (reference temperature), 105, 250, 500 and 750°C. The mentioned thermal cycle is reported in Figure 76.

4. EXPERIMENTAL PROCEDURES

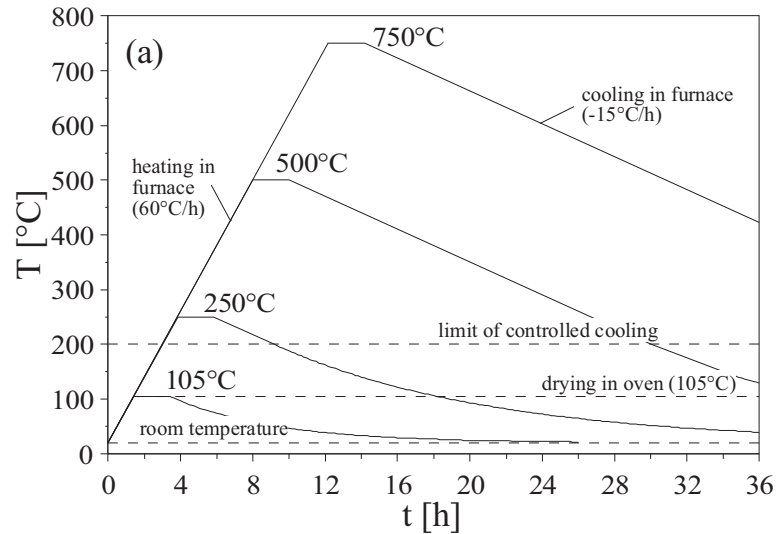


Figure 76 : Thermal cycle in electric furnace.

Both the microstructural and mechanical characterizations were carried out after the thermal cycle indicated in Figure 76. The concrete specimens were heated in the oven at the age of at least 56 days, at which the hydration reaction can be almost considered concluded (even if it is reasonable that the pozzolanic addition can slightly still contribute to the reaction). Starting from the indicated age, all the specimens were maintained in a conditioned room ($T = 25^{\circ}\text{C}$, RH $50\% \pm 5\%$) up to the equilibrium with the environment (constant mass), before being subjected to the thermal cycle.

4.1.3.2 Microstructural characterization: testing procedures

In order to characterize the concrete mixes from the microstructural point of view and to investigate heat-induced effects, several experimental techniques were used.

The specimens exposed to thermal cycle were small cylinders ($\phi = 20$ mm, $h = 100$ mm), cored from two concrete 100 mm-side cubes for each mix, having dimension suitable for sampling preparation in order to perform microstructural analysis. At the end of thermal exposure, after the cooling stage, all the specimens for microstructural analysis were maintained in a dryer in order to avoid as far as possible the rehydration reactions, before being prepared for the analysis and tested.

The experimental techniques, as well as the related testing procedures, are summarized as follows:

4. EXPERIMENTAL PROCEDURES

- Thermogravimetric Analysis (TGA): this technique allows in general to identify inorganic compounds depending on their chemical reactions, due to the test temperature rise, corresponding to a weight loss; in the present study, TGA has been used to have indications on:
 - free water present in the sample;
 - dehydration reactions on hydrated compounds;
 - decarbonation reactions.

The concrete sample was prepared by grinding some portions of the above-mentioned small cylinders in order to reach the maximum diameter of 90 μm , taking care to maintain the powder insulated from the external environment, in order to avoid as much as possible the rehydration reactions; 50 mg of this pulverized sample were subjected to the test. The samples, for each concrete mix at all the considered temperatures, were tested once, thus a single value will be taken into account as result.

The considered TGA thermal ramp was between 25°C and 975°C with heating rate 10°C/min, in nitrogen atmosphere, carried out in a Mettler Toledo TGA/SDTA851^e (see Figure 77).



Figure 77: TGA apparatus.

4. EXPERIMENTAL PROCEDURES

- X-Ray Diffraction (XRD): it is used to identify the crystalline phases present in the samples, before and after thermal exposure. A representative portion of each concrete samples were finely ground to pass the 45 μm sieve in order to improve powder homogeneity, taking care to maintain the powder insulated from the external environment, in order to avoid as much as possible the rehydration reactions.

X-Ray Diffraction patterns were collected on 1 g of pulverized sample using a Bruker D8 Advance Diffractometer (see Figure 78) with an angular 2θ range comprised between 5° a 70° with increments of 0.02° and a time steps of 0.4 seconds. The samples, for each concrete mix at all the considered temperatures, were tested once, thus a single value will be taken into account as result.

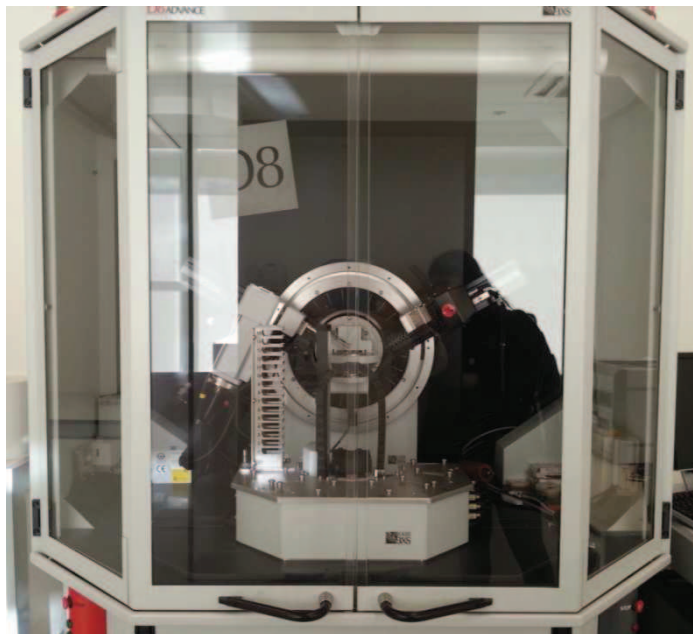


Figure 78: XRD apparatus.

- Mercury Intrusion Porosimetry (MIP): it is used to measure volume and dimension of pores (from unit to thousand nm), because of the non-wetting property of mercury, which allow to it to penetrate inside the open porosity of a solid sample by means of an external pressure (ΔP) imposed to the liquid. Measuring the quantity of mercury penetrated inside the pores for each pressure value, it is possible to calculate the porosimetric distribution in function of pore radius. In particular, this information derives from the Washburn equation:

$$\Delta P = (2\gamma / r_p) \cdot \cos\theta$$

where:

[37]

4. EXPERIMENTAL PROCEDURES

- γ is the mercury surface tension;
- r_p is the pore radius;
- θ is the contact angle between mercury and the sample ($>90^\circ$ for a non-wetting liquid as mercury).

Once the ΔP is measured and the contact angle θ is known, as well as the mercury surface tension γ , the pore radius r_p can be derived, thus the porosimetric distribution.

In order to perform MIP measurements, small portions of concrete samples (almost 15 g) were obtained from the above-mentioned small cylinders, thermally treated and untreated, by dry-cutting and then they were dried for three days at 40°C in a vacuum oven, in order to remove as much as possible the free water from the sample. Subsequently, they were tested, at least with two repetitions, in order to consider their mean value as result. The measurements were performed by means of Pascal 140 and 240 porosimeters (see Figure 79). The mercury intrusion and extrusion rate were rate was 5 for all concrete mixes, except the ones containing steel fibers, for which intrusion and extrusion rate have been considered as 8 (in order to reduce the risk of potential pollution of mercury by means of steel fibers).



Figure 79: MIP apparatus.

4. EXPERIMENTAL PROCEDURES

- Scanning Electron Microscopy (SEM): technique used to observe samples in a micrometric scale, in order to acquire information about the composition and possible presence of damage, as microcracks.

The tested sections were obtained in the central part of the above-mentioned small cylinders. Both polished sections and fractured surfaces were examined. The polished sections were prepared by impregnation with epoxy resin and subsequent polish. Then, the samples have been coated with carbon in order to prevent the charge-up on the surfaces. In case of polished sections the technique based on Back Scattered Electrons (BSE) was used, in order to obtain information on morphology and composition of the concretes. Fractured surfaces were also examined, after coating the surface with gold, by means of Secondary Electrons (SE) signals. All the section were observed by means of a Zeiss EVO MA15 (see Figure 80), using a thermoionic source in Lanthanum Hexaboride LaB₆. The samples, for each concrete mix at all the considered temperatures, were tested once, thus a single value will be taken into account as result.

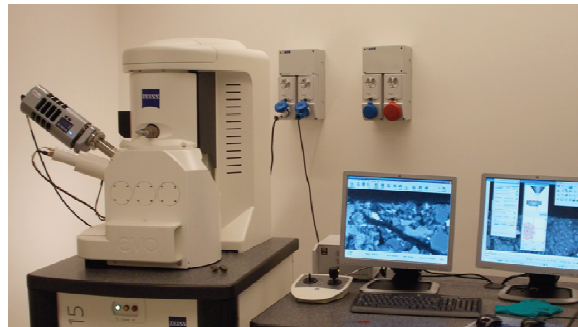


Figure 80: SEM apparatus.

4.1.3.3 Mechanical characterization: testing procedure

The mechanical characterization after exposure to thermal cycle was carried out acquiring the stress-strain (σ - ϵ) curve in compression. The compression tests were performed under displacement control; as feedback quantity, the relative displacement between the upper loading plate and the lower crosshead of the testing machine was used. These measures were carried out by three LVDT (Linear Variable Differential Transformer) having the following characteristics:

- measuring range: +/- 5 mm;
- sensitivity: 0.25 μ m

and placed at 120° each other.

4. EXPERIMENTAL PROCEDURES

Cylindrical concrete specimens ($\phi = 100$ mm, $h = 200$ mm) were instrumented by three displacement gauges DD1 having the following characteristics:

- resistive type strain transducer (full-bridge);
- measuring range: ± 2.5 mm;
- sensitivity: $0.25 \mu\text{m}$.

The three DD1 transducers were placed at 120° each other and used to acquire axial strains only during the ascending branch of σ - ϵ curve.

At the two heads of each specimen, a thin film of stearic acid was smeared in order to reduce the friction between the material and the loading plate. This was realized in order to avoid spurious components in stress data near the extremity of the specimens. The instrumented specimen can be observed in Figure 81. The concrete specimens, for each mix and exposure temperatures, were tested at least twice, and their mean value will be considered as result.



Figure 81: Instrumented specimen tested in compression (controlled displacement).

The tests were performed by means of an electro-mechanical testing machine (Schenck) having a load cell with a maximum capacity of 1000 KN; the upper loading plate is provided by a self-blocking spherical seat (EN 12390-4, 2002). The displacement rate was set-up to allow that the loading rate belonged to the range prescribed by EN 12390-3 (2009), thus between 0.4 and 0.8

4. EXPERIMENTAL PROCEDURES

MPa/s. No pre-loading cycles were carried out in order to settle the specimens, because after thermal exposure the elastic behaviour is lost.

During the compression test, in the first phase ($\sigma \leq 0.1 f_c$) the difference between the 3 DD1 was checked to be within the $\pm 10\%$ with respect to the mean value; otherwise the test was stopped and the specimen placed in order to minimize that scattering.

The elastic modulus was evaluated from the stress-strain curves in compression, as secant modulus considering as upper stress $\sigma_c = 0.5f_c$.

4.1.4 Spalling sensitivity

Spalling phenomenon, as explained in Paragraph 2.2.2, can be generated by two principal causes: thermal stresses and pressure build-up inside the material. These two aspects can be experimentally investigated by means of diffusivity and pore pressure measurements respectively.

4.1.4.1 Diffusivity determination

When concrete is exposed to high temperature, internal thermal stresses can arise. The propagation of the heat wave from the external to the inner part of the concrete elements is governed by thermal diffusivity (see Paragraph 2.2.2.2, equation [30]).

The thermal diffusivity determinations for all the concrete mixes were carried out on cylindrical specimens ($\phi = 100$ mm, $h = 300$ mm), instrumented with two thermocouples, one in the center of the specimen (1) and one at a depth of 5 mm from the external surface (2). The specimens were introduced inside an electric oven, within which they were surrounded by a steel tube for guaranty the heating uniformity (see Figure 82). The heating ramp consisted of a heating rate of $1^\circ\text{C}/\text{min}$ from 20 to 1000°C and four temperatures were monitored during the test: both the sample temperatures (by means of the thermocouples indicated before as 1 and 2) as well as the oven and the tube ones (Koury et al., 1984, Felicetti et al., 2003). Each concrete mix was tested once, thus a single value will be taken into account as result.

4. EXPERIMENTAL PROCEDURES

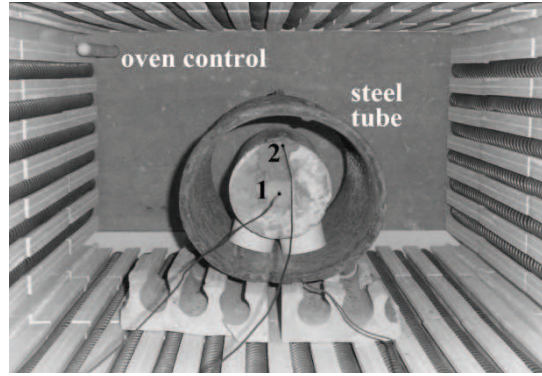


Figure 82: Test specimen for thermal diffusivity inside the oven (1: thermocouple in the center of the specimen, 2: thermocouple near the external specimen surface).

Diffusivity values [mm^2/s] were calculated by using the following formula:

$$D = V_{h,eq} \cdot R^2/4 \Delta T \quad [38]$$

where:

- $V_{h,eq}$ is the heating rate ($^{\circ}\text{C}/\text{s}$) obtained as weighted average between the heating rate measured in the two thermocouples, 1 and 2, placed in the specimen (in order to minimize the transient effects), according to the formula:

$$V_{h,eq} = 0.25 V_{h,circ} + 0.75 V_{h,center} \quad [39]$$

- R is the distance (mm) between the thermocouples 1 and 2 placed in the specimen;
- ΔT is the temperature difference ($^{\circ}\text{C}$) between thermocouples 1 and 2.

4.1.4.2 Pore pressure measurement and splitting test procedure

The pressure build-up induced in the concrete during thermal exposure can be monitored by measuring the pore pressure inside the concrete.

An experimental set-up has been developed at Politecnico di Milano in order to measure the temperature and pore pressure build-up in the center of a 100 mm-side cubes during thermal exposure. For each concrete mix, a maximum number of ten specimens were tested. A typical response of test indicates that the vapour pressure values increase as temperature increases. After

4. EXPERIMENTAL PROCEDURES

that, a maximum value of vapour pressure (P_{lim}) is reached and this is recorded with the corresponding temperature (T_{lim}). The specimen is then quickly removed from the heating system and subjected to indirect tensile test, according to EN 12390-6 (2010). In order to define the reference tensile strength in virgin conditions, splitting tests were performed on unheated specimens (Felicetti et al., 2012 and 2013).

The heating system consisted of two radiant panels facing two opposite sides of the concrete sample in order to guarantee the symmetrical heating with respect to the mid-plane of the specimen. Radiant panels allowed to obtain a range of heating rates thanks to the built-in thermocouples connected to separate controller. Preliminary tests performed adopting a relatively high heating rate ($2^{\circ}\text{C}/\text{min}$) highlighted very low, and not realistic, values of pore pressure in concrete different from the 45-S mix, probably because this heating rate induced saturation in the specimens, reducing drastically the permeability. This is the reason why a moderate heating rate was chosen, $0.5^{\circ}\text{C}/\text{min}$, allowing a more stable and accurate testing procedure. The insulated specimens were placed between the two radiant panels as shown in Figure 83.

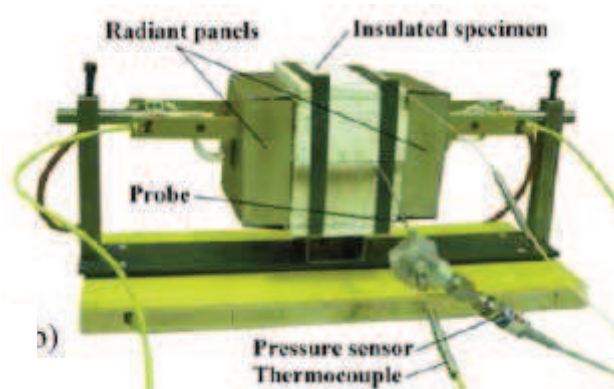


Figure 83: Insulated specimen during heating.

The pore pressure measurement was performed by using capillary stainless steel pipes ($\phi = 2$ mm) fitted with sintered metal heads (see Figure 84). Curved pipes were used, in order to prevent the probes from lying in the mid-plane of the cube (that is the fracture plane in the splitting test). The pipes were filled with silicon oil, as a diathermal fluid, and had a thermocouple inside. Hence, both pressure and temperature inside the head of the probe were measured during the heating performed by the radiant panels.

4. EXPERIMENTAL PROCEDURES



Figure 84: Cubic molds for pore pressure specimens, instrumented with curved pipes.

4.1.4.3 Permeability determination

Even if mentioned in the literature review as fundamental to understand the material behaviour, it wasn't possible to perform permeability determinations at high temperature; only permeability determinations at 20°C were carried out.

Cylindrical concrete specimens ($\phi = 150$ mm, $h = 50$ mm) were subjected to vapour permeability test according to EN 1015-19 (2008). Three specimens for each mix were maintained in contact to a saturated solution for 28 days and the mass variation at different time interval was measured. Elaborating these experimental data, the average permeability was obtained.

The test report of EN 1015-19 (2008) provides permeability $W_{p,t}$ values which are related to vapour permeance according to the following relationship:

$$W_{p,t} = \Lambda_p \cdot L \quad [40]$$

where:

- $W_{p,t}$ is the vapour permeability [$\text{Kg}/\text{m}\cdot\text{s}\cdot\text{Pa}$];
- Λ_p is the vapour permeance [$\text{Kg}/\text{m}^2\cdot\text{s}\cdot\text{Pa}$];
- L is the thickness of specimens [m].

General relationship between $W_{p,t}$ as expressed in EN 1015-19 (2008) and permeability K (expressed in darcy) deriving from Darcy law, is given by:

$$[41]$$

4. EXPERIMENTAL PROCEDURES

$$K = (\mu/\rho_w) \cdot \Lambda_p \cdot L = (\mu/\rho_w) \cdot W_{p,t}$$

where:

- μ is the viscosity of the fluid (vapour) [P];
- ρ_w is the density of the fluid (vapour) [Kg/m³].

5. EXPERIMENTAL RESULTS

5. EXPERIMENTAL RESULTS

In the current Paragraph the experimental results will be presented; they are grouped considering before the intrinsic damage characterizations, followed by the mechanical and the spalling sensitivity evaluation. The last one will be divided in determinations regarding thermal stresses (thermal diffusivity) and pressure build-up (pore pressure, splitting and permeability measurements).

5.1 Intrinsic damage evaluation: microstructural characterization

In the next Paragraphs, the microstructural experimental results concerning concrete intrinsic damage will be shown, starting from TGA then moving on XRD, MIP and SEM determinations.

5.1.1 Thermogravimetric Analysis (TGA) results

As mentioned in Paragraph 4.1.3.1, TGA allows to identify chemical compounds on the basis of the mass loss occurring at a precise test temperature.

In this context, as already explained in Paragraphs 2.1.1.1 and 2.1.1.2.2, the main degradation reactions involving cement paste and aggregate are due to dehydration of hydrated products and degradation of crystalline compounds present in the aggregate, i.e. calcite decarbonation.

It is obvious that these reactions lead to a mass loss due to water or CO₂ expulsion, thus new voids and spaces are generated inside the cement matrix and aggregate, as well as in the interface zone between them (ITZ).

In the present Paragraph, the most important TGA results will be plotted and compared, while all the TGA curves obtained for the 11 concrete mixes are collected in Annex B.

In Figure 85, the TGA results, in terms of mass losses, are reported for 70-S mix reference sample (20°C), as well as the ones subjected to thermal cycles.

5. EXPERIMENTAL RESULTS

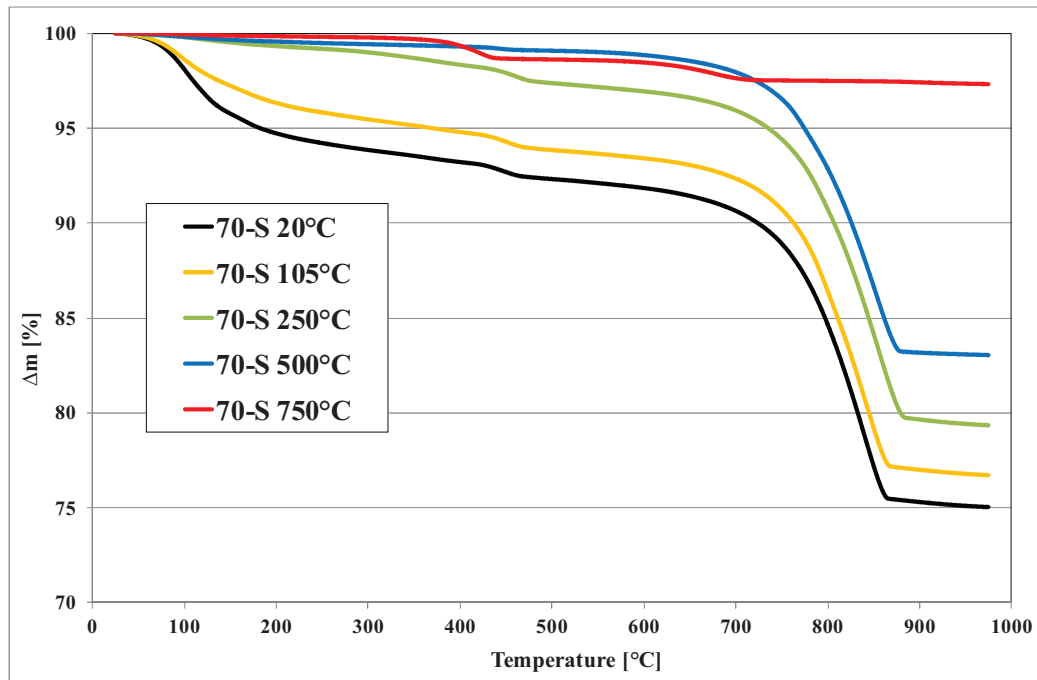


Figure 85: TGA experimental trends for 70-S after all exposure temperatures.

In Figure 85, three main steps related to significant mass losses can be identified as follows, confirming the mentioned literature results (Alonso and Fernandez, 2004):

- Between 20 and 300°C, due to the expulsion of free and bound water, the latter mainly from C-S-H gel. This step becomes less significant passing from the sample at 20°C to the ones exposed to increasing temperatures; in particular, the difference between the curves at 20°C and after exposure to 105°C can be attributed to free water expulsion, generally considered just expelled up to 105°C. In case of higher temperatures exposure, no significant mass losses in this range are observed, due to the water (free and bound) removal caused by thermal treatment;
- Between 400 and 500°C, mainly due to portlandite dehydration. This mass loss is significant considering the samples at 20°C and after exposure to 105 and 250°C, but is not detected after 500°C exposure, owing to the fact that this reaction already occur during the thermal treatment. Instead, the mass loss is observed in the curve related to exposure at 750°C probably due to the rehydration of cement paste sample;
- Between 550 and 850°C, due to decarbonation of calcite contained in the silico-calcareous aggregate. This is the most predominant region in the thermograms because of the higher calcite content in comparison with the cement paste hydrated phases. This mass loss

5. EXPERIMENTAL RESULTS

becomes less significant in case of the sample exposed to 750°C because this temperature overlaps with the temperature range in which the calcite decarbonation generally takes place.

After considering the behaviour of the same concrete mix at different temperatures exposure, the comparisons among the concrete mixes are needed. The first is carried out between two concrete grades with silico-calcareous aggregate, 70-S and 95-S, at 20°C, as shown in Figure 86. These two mixes have been considered because they are characterized by the same type of cement and addition (thus the same type of hydrated phases and same volume fraction of cement paste) but different related amounts, as well as different w/c ratio (needed to reach distinct compressive strength grade).

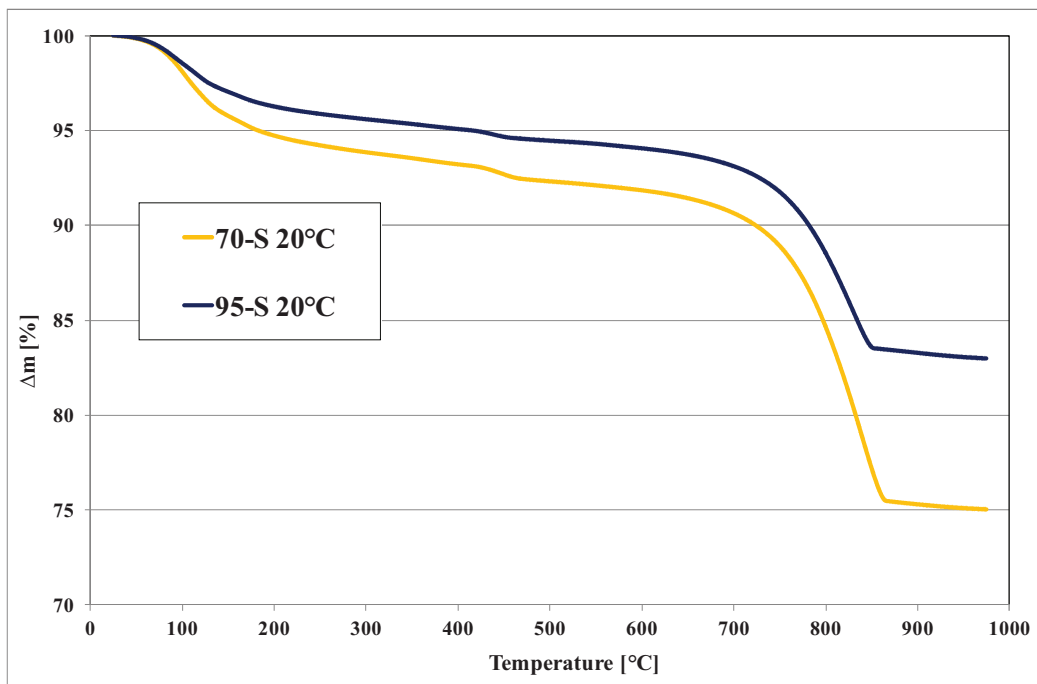


Figure 86: TGA experimental trends for two different concrete grades.

As expected, the 95-S mix, characterized by lower w/c, shows less significant mass loss between 20 and 200°C, due to the fact that it contains lower amount of free and bound water, as well as portlandite content. In fact, the mass loss step related to its dehydration, is slightly greater for 70-S than for 95-S. Moreover, it can be observed that the calcite decarbonation is less significant for 95-S than for 70-S, probably due to the lower aggregate content in the mix.

5. EXPERIMENTAL RESULTS

Another important comparison has to be performed among the mixes containing different types of aggregates, at the same compressive strength grade, thus 70-S, 70-C and 70-B, at 20°C. Their related curves are collected in Figure 87.

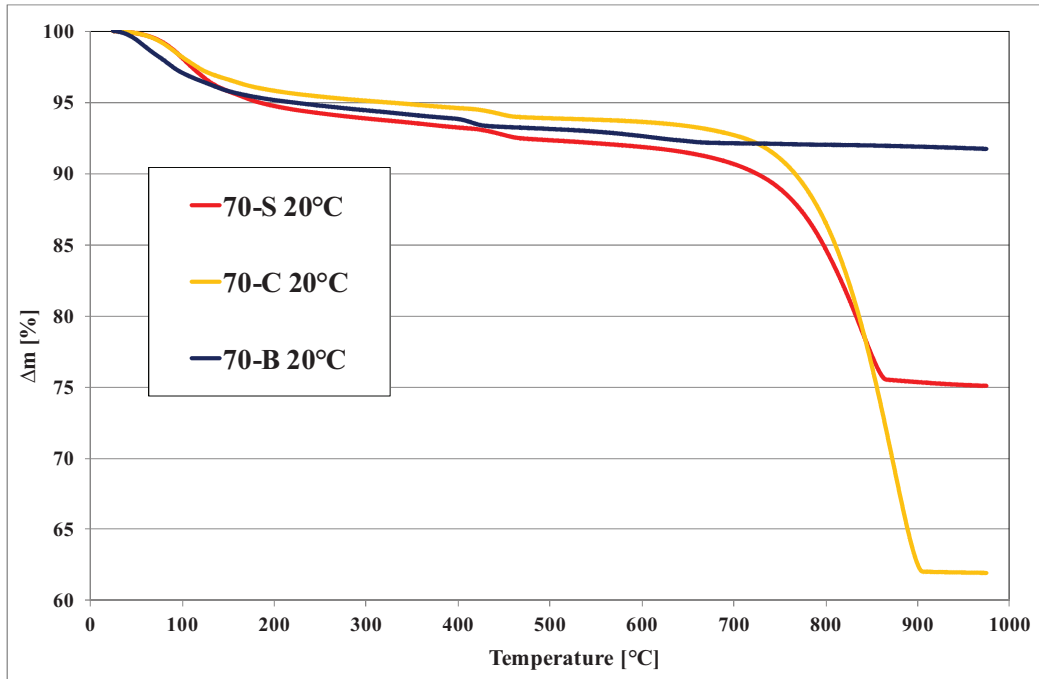


Figure 87: TGA experimental trends for concretes with different aggregate types.

In Figure 87, the 70-S and 70-C mixes show the calcite decarbonation mass loss step because both aggregate types contain this chemical compound, obviously the second one in higher content indicated by almost double mass loss in the range between 550 and 850°C. 70-B doesn't show the calcite decarbonation step because basalt is characterized by different crystallographic composition. 70-B also presents higher mass loss in the range 20-105°C, thus it seems to contain higher amount of free water in comparison with the other two mixes.

The PP and steel fibers impact on TGA behaviour has been also evaluated. In Figure 88 are collected the curves related to the mixes containing three different amounts of monofilament PP fibers and the mix containing the fibrillated ones, at 20°C. Instead, in Figure 89 are plotted the curves related to mixes prepared with different steel fibers contents, at 20°C. In both case, the curves are compared with the one without fiber (70-S).

5. EXPERIMENTAL RESULTS

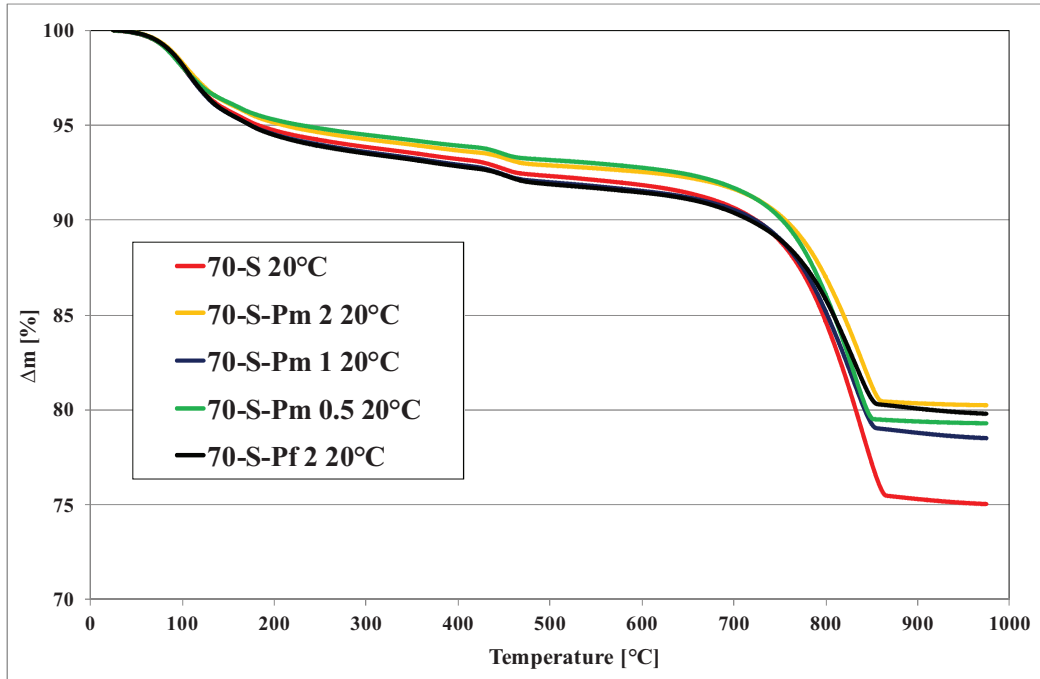


Figure 88: TGA experimental trends for concretes with different PP fibers types and contents.

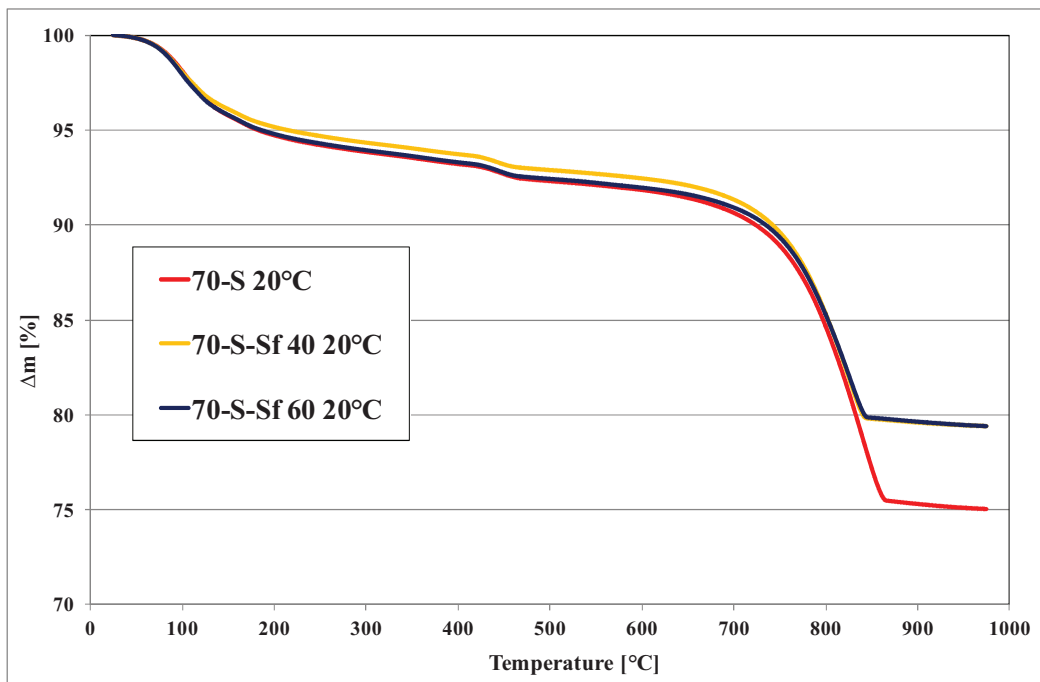


Figure 89: TGA experimental trends for concretes with different steel fibers contents.

5. EXPERIMENTAL RESULTS

Both in Figure 88 and Figure 89, it arises that the presence of PP and steel fibers doesn't impact on the evolution of hydrated phases in cement pastes, thus no significantly different behaviours have been detected as dehydration reactions. This trend is confirmed in Figure 90 in which the TGA curves related to 70-S-Pm2, 70-S-Pf 2 and 70-S-Sf 60 are compared with 70-S, in order to show that PP and steel fibers don't affect in a significant way the cement paste hydration.

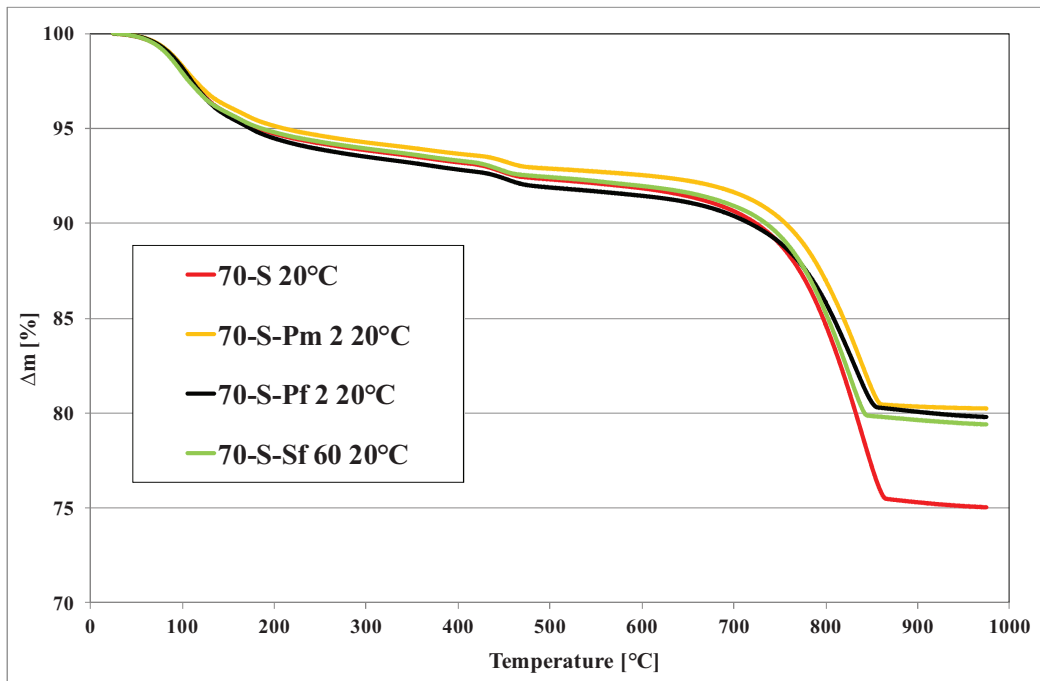


Figure 90: TGA experimental trends for concretes with different fibers types (PP and steel fibers).

5.1.2 X-Ray Diffraction (XRD) results

X-Ray Diffraction allows to identify crystalline phases presented in the concrete samples and, in this context, to follow how they change with the effect of thermal treatment. In particular, depending on the exposure temperature, some hydrated phases will disappear and their dehydration products will be detected in function of their degradation temperature.

In the current Paragraph, the most significant XRD patterns will be highlighted, while the curves obtained for all the concrete mixes at all exposure temperatures are collected in Annex C.

As for the case of TGA, the evolution of concrete phases due to the increasing temperature exposure is considered. For this reason, the XRD patterns detected for 70-S in residual conditions

5. EXPERIMENTAL RESULTS

are plotted in Figure 91, in which are indicated the chemical compounds interested by the main degradation reactions.

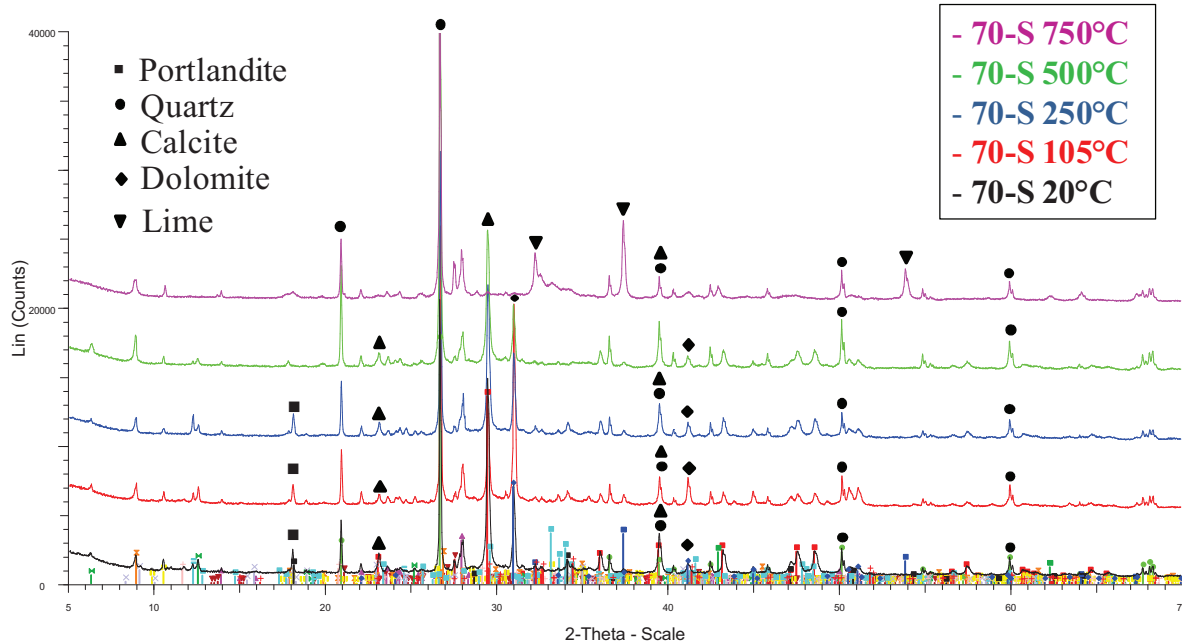


Figure 91: XRD patterns for 70-S after all exposure temperatures.

From Figure 91 it can be observed that:

- As expected, the disappear of ettringite characteristic peaks in the XRD pattern indicates that its dehydration occurs at a considerably lower temperature ($< 105^{\circ}\text{C}$);
- Increasing temperature leads to the transformation of portlandite into lime (calcium oxide, CaO), due to its dehydration process; in particular the signal related to portlandite disappears starting from the curve related to 500°C exposure;
- The most important reactions observed between 500°C and 750°C are: the decarbonation of calcite and dolomite to give lime and periclase (magnesium oxide, MgO), the dehydration of some clay minerals (clinochlore and lizardite) and the reaction of lime with silica present to give belite;
- No β -quartz is detected (above 750°C) because of the slow cooling of the concrete to room temperature, that turns β -quartz into α -quartz (due to process reversibility).

Considered the most important changes in XRD patterns due to exposure temperature, a comparison among the crystalline composition of different concrete grades and the presence of different PP fibers contents is reported in Figure 92 at 20°C .

5. EXPERIMENTAL RESULTS

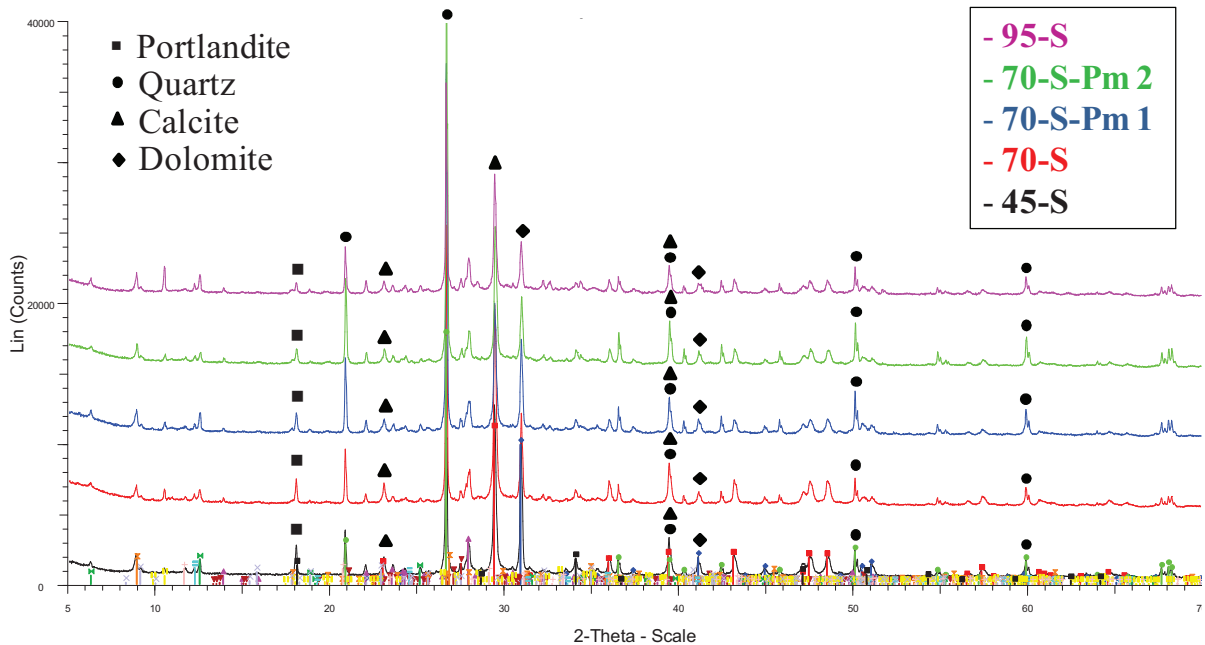


Figure 92: XRD patterns for different concrete grades and different PP fibers contents at 20°C.

In Figure 92, the crystalline phases of silico-calcareous aggregate can be recognized, and specifically quartz, dolomite, calcite and clay minerals. The portlandite content decreases for increasing values of GGBS content. It is also confirmed that, as expected and observed in TGA curves, no fiber influence has been detected on cement hydrated phases, also in case of presence of steel fibers (see Annex C).

The different aggregate type can be also considered in order to compare the XRD pattern related to each aggregate before and after thermal exposure. For this reason, in Figure 93 and Figure 94 are plotted the pattern for 70-S, 70-C and 70-B at 20°C and after 750°C exposure, respectively.

5. EXPERIMENTAL RESULTS

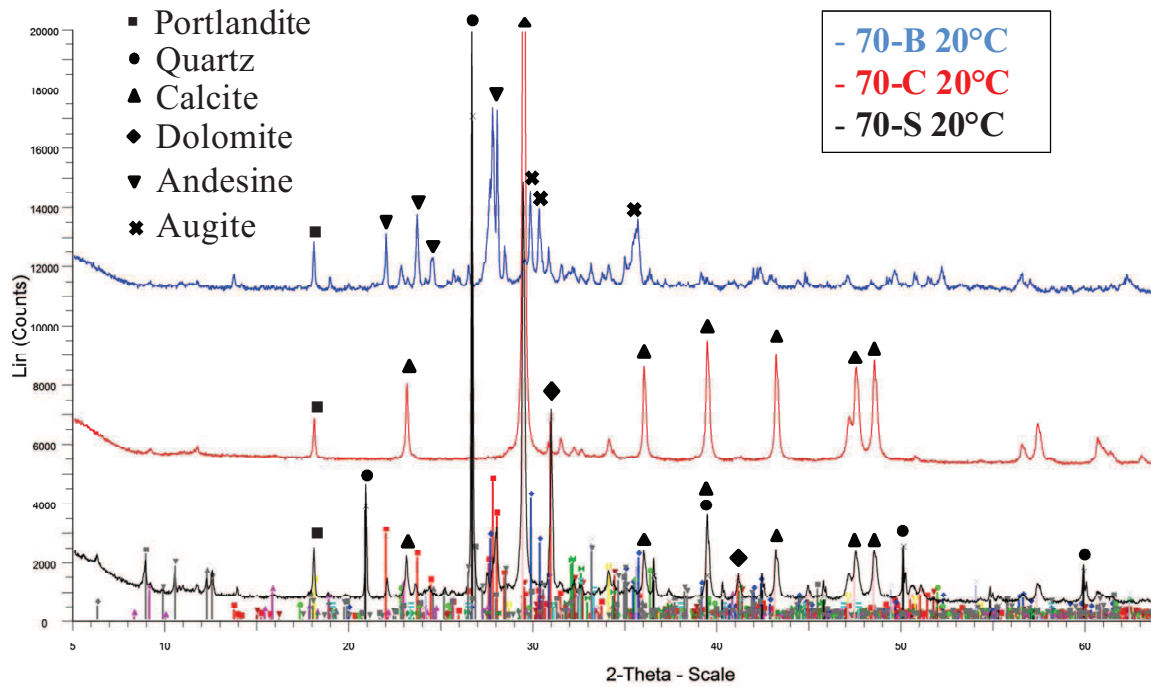


Figure 93: XRD patterns for 70-S, 70-C and 70-B at 20°C.

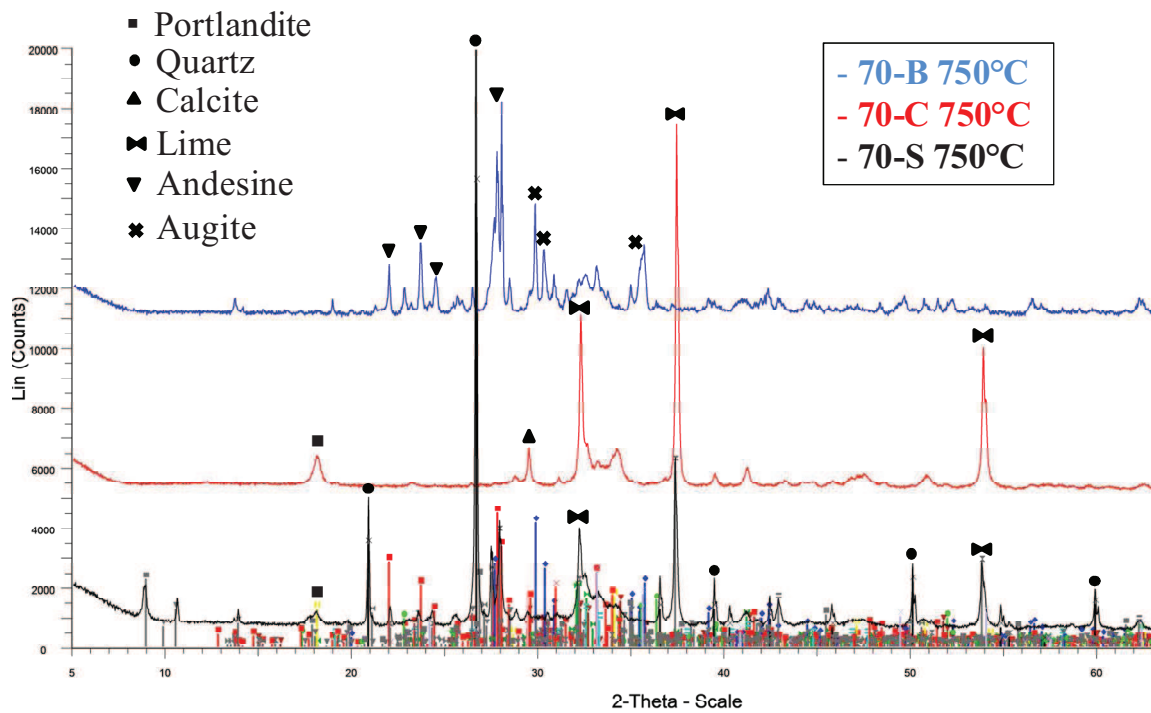


Figure 94: XRD patterns for 70-S, 70-C and 70-B at 750°C.

5. EXPERIMENTAL RESULTS

From Figure 93 and Figure 94, it arises that:

- Basalt aggregate (mix 70-B) shows no significant differences in its mineralogical composition after heating; the only changes are related to the cementitious matrix due to the appearance of a different polymorph of belite (α or α') at 750°C;
- After heating to 750°C, mix 70-C exhibits lime as its principal phase (due to decarbonation). Belite is also observed;
- In spite of its silico-calcareous aggregate, mix 70-S shows no α - β quartz transition after heating.

5.1.3 Mercury Intrusion Porosimetry (MIP) results

Thermal degradation reactions, as already observed, lead to a mass loss due to water or CO₂ expulsion, generating new voids and spaces inside the cement matrix and aggregate, as well as in the interface zone between them (ITZ), with consequent increasing in porosity.

Being that this effect is extremely important in case of concrete subjected to thermal treatment, a particular emphasis is devoted to the porosimetric experimental results in describing the changes in concrete microstructure due to high temperature exposure.

The porosimetric distributions related to all the considered concretes mixes are collected in Annex D, while in this Paragraph will be reported the most significant and explanatory ones.

Two types of distributions are reported, the cumulative and the differential, in function of pore radius. The first shows the cumulative pattern of porosity with increasing values of pore radius, while the second is the differential representation of the first one, considering also that its integral must be equal to 100% of the total cumulative porosity.

The effect of increasing temperature on cumulative and differential porosimetric distributions can be graphically observed in Figure 95 and Figure 96, respectively, referred to 95-S mix. The experimental curves after the exposure to 750°C is not reported in general for all the concrete mixes, except for 70-B mix, because the samples were not intact after heating at 750°C, thus wasn't possible to carry out the MIP analysis on them.

5. EXPERIMENTAL RESULTS

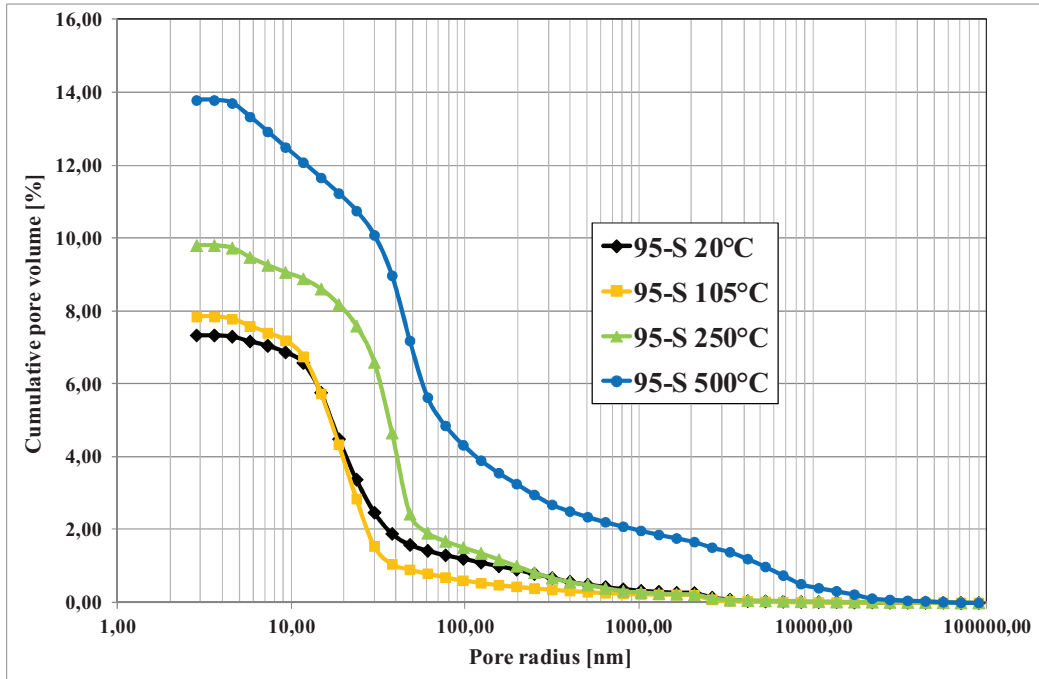


Figure 95: Cumulative distributions for 95-S after heating (different exposure temperatures).

From Figure 95 cumulative distributions, it arises that the higher the temperature exposure, the higher the total porosity because of thermal degradation reactions occurring in the samples (mainly water losses due to dehydration), leading to the formation of new voids and spaces inside the microstructure.

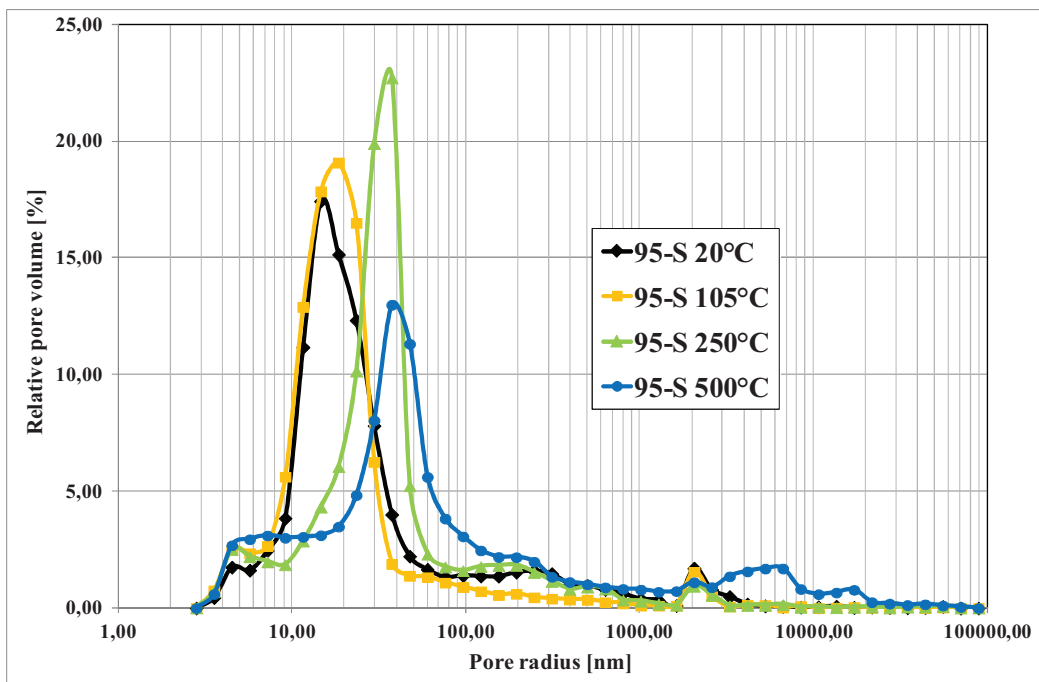


Figure 96: Differential distributions for 95-S after heating (different exposure temperatures).

5. EXPERIMENTAL RESULTS

In Figure 96, it can be observed that increasing the exposure temperature, a shift of the maximum peak of the distribution towards higher values of pore radius occurs. This means that thermal exposure causes not only an increase in total porosity but also the generation of a pore system characterized by higher dimensions, especially passing from capillary pores to macropores. These experimental data confirm the bibliographic results, from different Authors, collected both in Paragraph 2.1.1.1.5 and 2.1.2.2.1 (Zhao, 2012, Chan et al., 2000).

As already done in the previous Paragraphs, the comparison among the three compressive strength grades and the different type of aggregate concretes has to be carried out. First of all, the total porosity values at 20°C and after the exposure temperatures for the mentioned concrete mixes are collected from Table 11 to Table 15.

f_{cm}	Calcareous (%)_20°C	Silico-Calcareous (%)_20°C	Basalt (%)_20°C
45	-	14.02	-
70	8.26	8.60	13.19
95	-	7.34	-

Table 11: Total porosity values for different compressive strength grades and different type of aggregate concretes at 20°C.

f_{cm}	Calcareous (%)_105°C	Silico-Calcareous (%)_105°C	Basalt (%)_105°C
45	-	15.34	-
70	10.03	11.17	13.28
95	-	7.84	-

Table 12: Total porosity values for different compressive strength grades and different type of aggregate concretes at 105°C.

f_{cm}	Calcareous (%)_250°C	Silico-Calcareous (%)_250°C	Basalt (%)_250°C
45	-	15.56	-
70	10.27	10.66	16.09
95	-	9.80	-

Table 13: Total porosity values for different compressive strength grades and different type of aggregate concretes at 250°C.

f_{cm}	Calcareous (%)_500°C	Silico-Calcareous (%)_500°C	Basalt (%)_500°C
45	-	22.77	-
70	19.33	14.77	23.30
95	-	13.79	-

Table 14: Total porosity values for different compressive strength grades and different type of aggregate concretes at 500°C.

5. EXPERIMENTAL RESULTS

f_{cm}	Calcareous (%)_750°C	Silico-Calcareous (%)_750°C	Basalt (%)_750°C
45	-	-	-
70	-	-	34.55
95	-	-	-

Table 15: Total porosity values for different compressive strength grades and different type of aggregate concretes at 750°C.

As expected, the higher the temperature exposure, the higher the total porosity value for all the concrete mixes because of the expulsion of water during dehydration reactions, as already mentioned. Moreover, the higher the compressive strength grade, the lower the total porosity, because the cementitious matrix is more compact to reach higher values of compressive strength (and lower w/c ratio).

Considering the different aggregate types, the 70-C mix presents lower total porosity in comparison with 70-S at temperature exposure up to 500°C, at which the related value is higher than the 70-S one. For basalt aggregate, the total porosity is significantly higher than the other two concrete mixes at all temperature; one explanation to this fact can be referred to its slightly higher w/c ratio in comparison with the others, in order to reach the assigned intermediate compressive strength. For 70-B, the MIP measurement after heating at 750°C has been also carried out, because the sample remained intact after thermal treatment. In order to better analyze the total porosity in function of increasing temperatures, the corresponding tabulated data are collected in Figure 97.

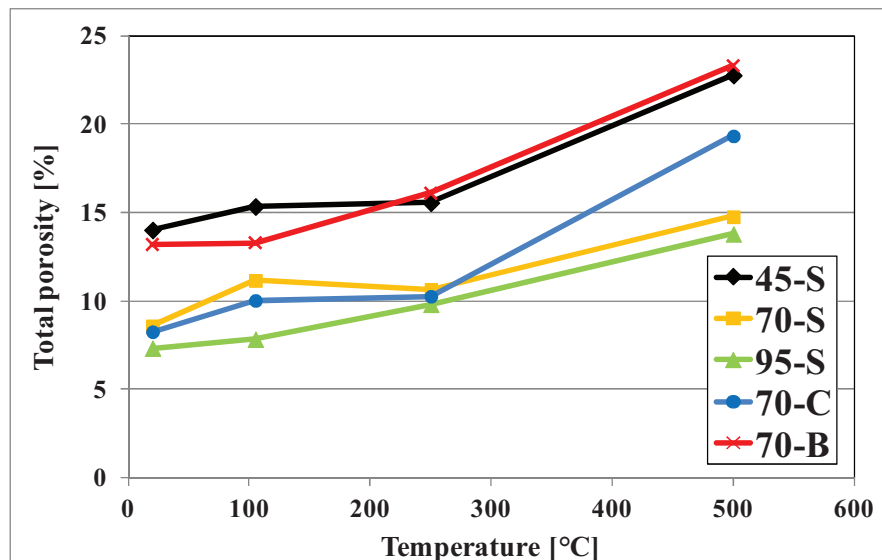


Figure 97: Concrete total porosity as a function of the temperature for different concrete grades and aggregate types.

5. EXPERIMENTAL RESULTS

In Figure 97 is confirmed the increase of total porosity with increasing exposure temperature, as well as the higher values of the same parameter for lower concrete grade.

Moreover, in case of calcareous aggregate, the 70-C trend is close to the one related to 70-S, except for the value after 500°C exposure, significantly higher for 70-C. 70-B mix presents the highest total porosity values in comparison with 70-S and 70-C, as already mentioned, and its trends is very close to the one related to 45-S.

Graphically, the cumulative and differential porosimetric distributions for the three concrete grades at 20°C are collected in Figure 98 and Figure 100, while the ones related to different aggregate types mixes are plotted in Figure 99 and Figure 101.

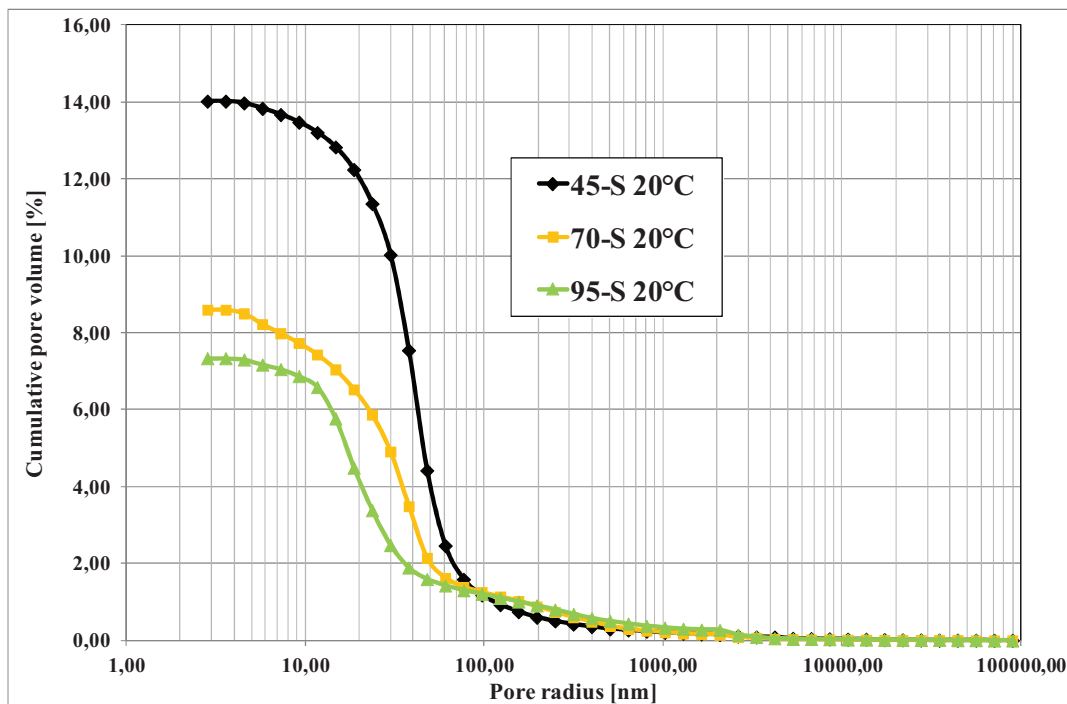


Figure 98: Cumulative distributions for different concrete grades at 20°C.

From Figure 98, it arises that the main differences in porosity distributions fall in the range of pore radius $< 80 \mu\text{m}$. In particular, 45-S mix shows a remarkable difference in pore size distribution in this range of pore dimensions, while for 70-S and 95-S mixes this difference is reduced. This confirms the fact that below a certain limit value of porosity even a little reduction in porosity causes a significant increase in compressive strength.

5. EXPERIMENTAL RESULTS

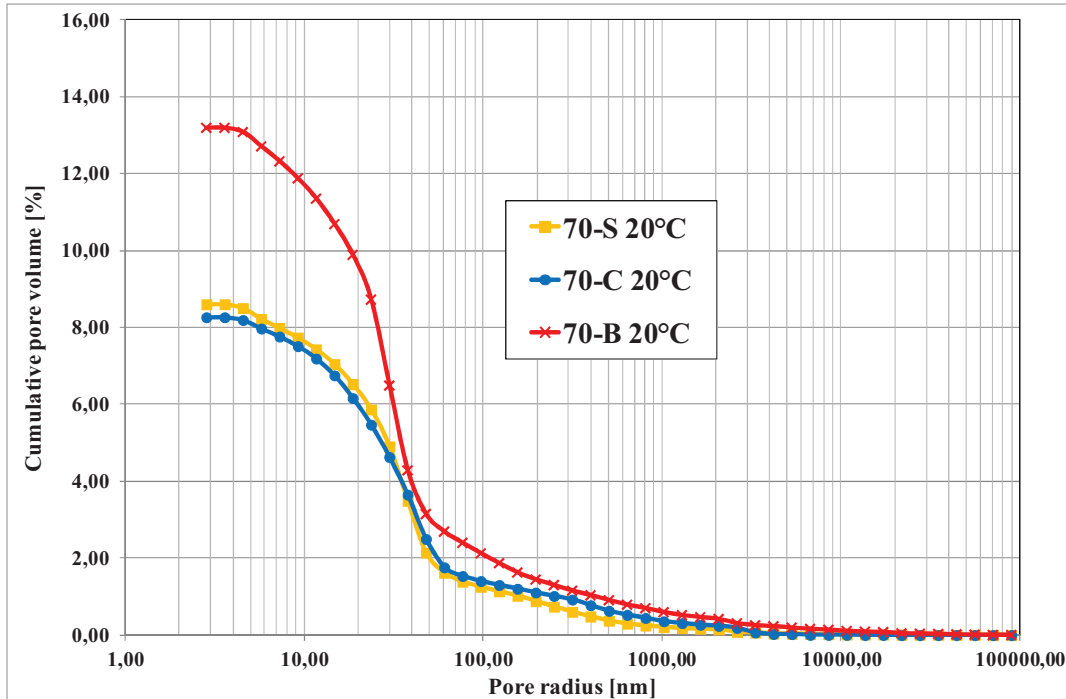


Figure 99: Cumulative distributions for different aggregate types at 20°C.

The cumulative distributions in Figure 98 and Figure 99 reflect the data collected in Table 11. In the latter Figure, the higher porosity value is detected for 70-B, followed by 70-S and 70-C, whose values are quite similar.

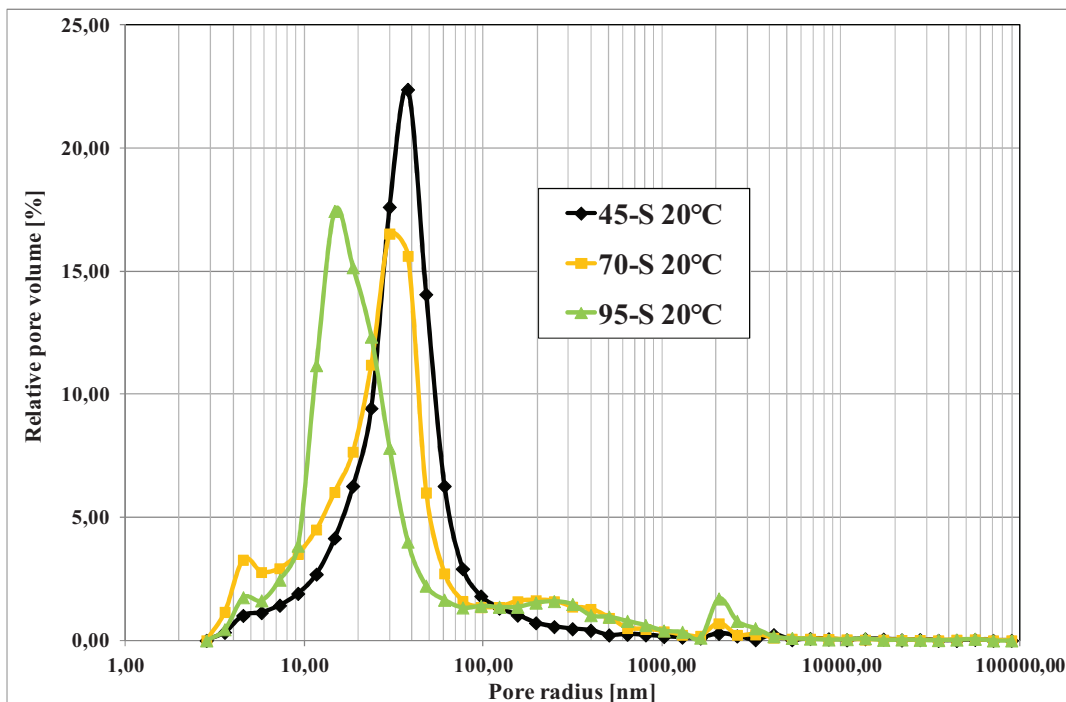


Figure 100: Differential distributions for different concrete grades at 20°C.

5. EXPERIMENTAL RESULTS

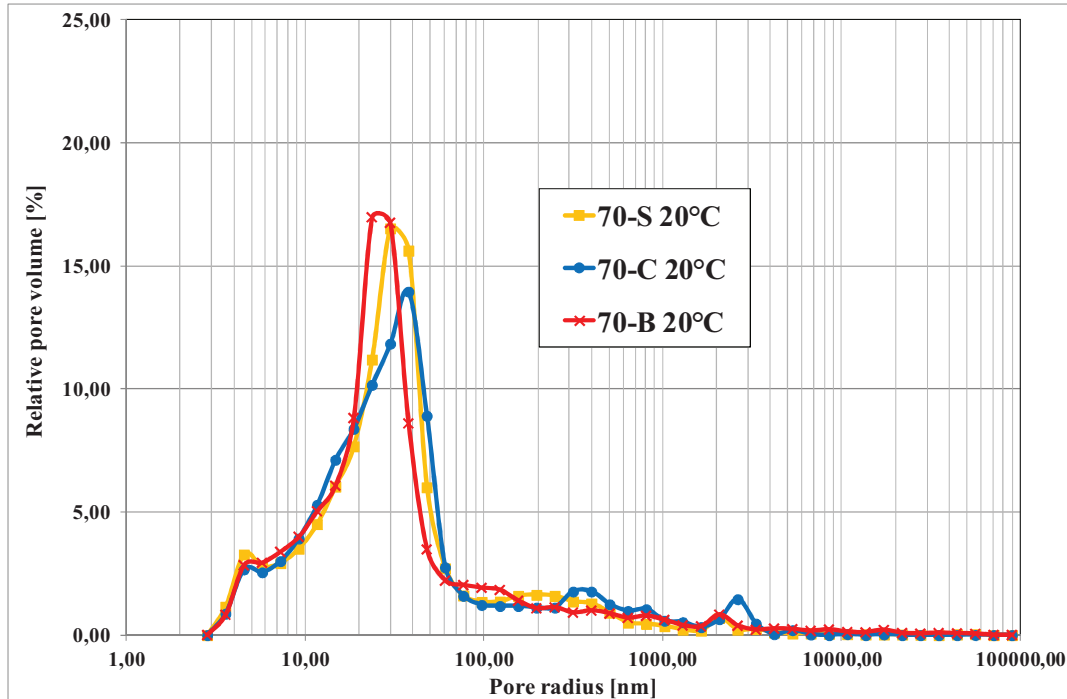


Figure 101: Differential distributions for different aggregate types at 20°C.

From Figure 100, it arises that increasing the compressive strength values, the pore size distributions move towards lower values of pore radius.

In Figure 101, it can be observed that different aggregate type doesn't affected in a significant way the pore size distribution in the field of capillary pores, even if for the calcareous aggregate the curve presents a quite different trend in comparison with the others. Some differences can be detected in the field of macro pores, in case of 70-C and 70-B, indicating that this type of aggregate may have an influence in this pore region.

The effect of temperature exposure in the previous mixes at different grades is shown in Figure 102 and Figure 103, considering the cumulative and differential distributions respectively.

5. EXPERIMENTAL RESULTS

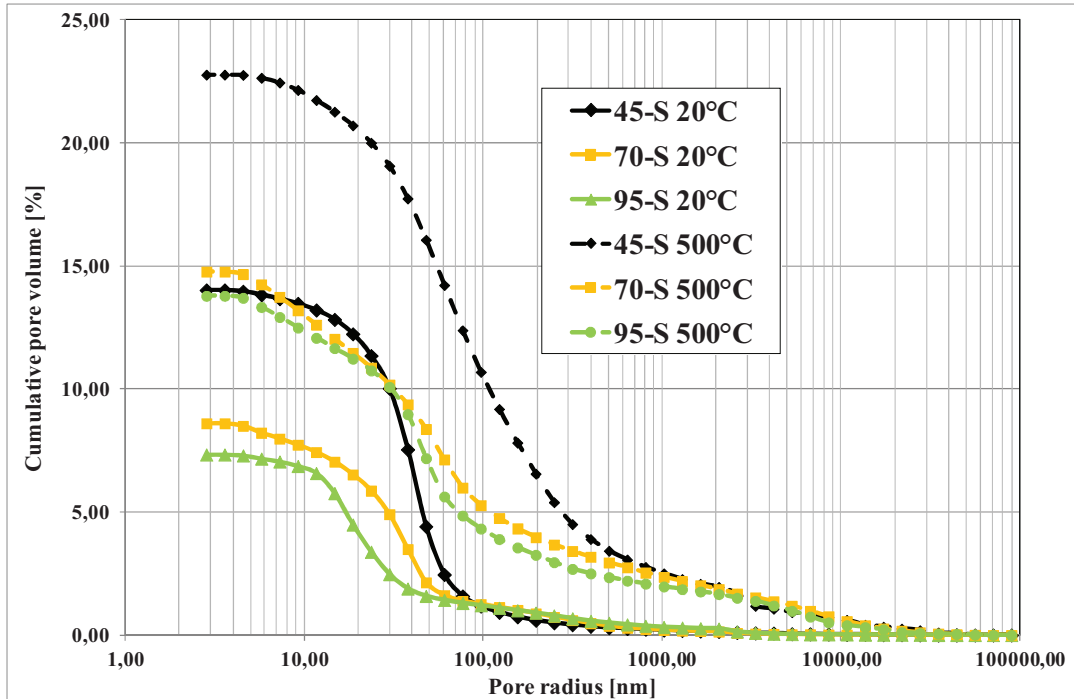


Figure 102: Cumulative distributions for different concrete grades at 20 and 500°C.

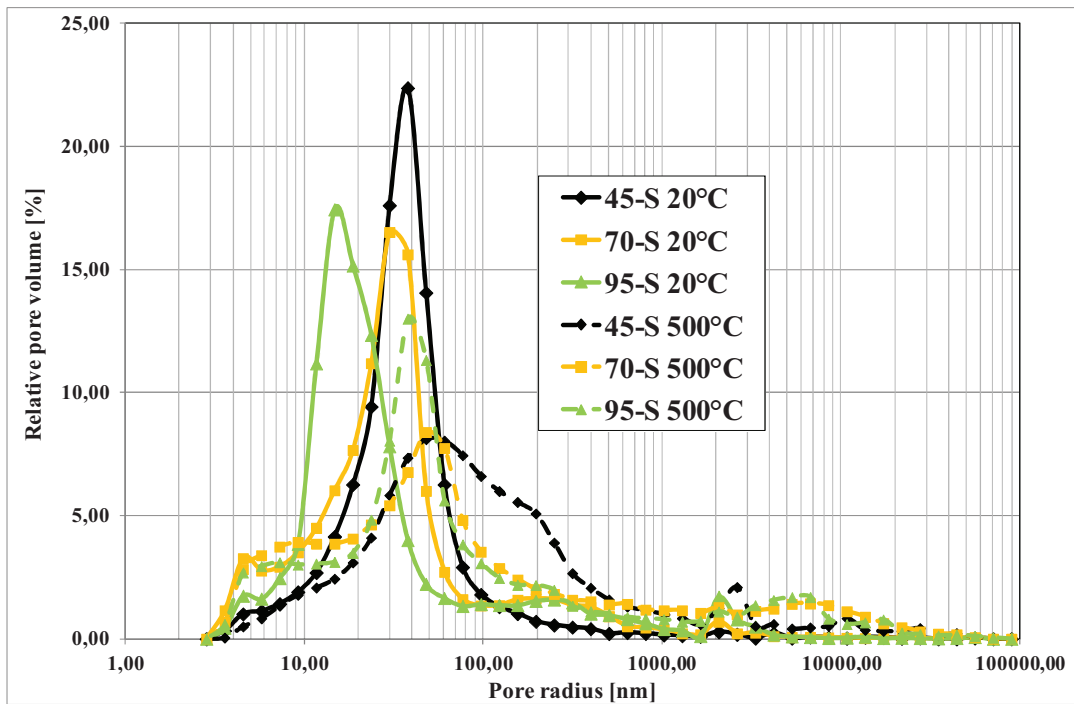


Figure 103: Differential distributions for different concrete grades at 20 and 500°C.

5. EXPERIMENTAL RESULTS

From Figure 102 it can be observed that the thermal exposure at 500°C affects the total porosity, which significantly increases for the three mixes of almost 40%, as already reported in Table 11 and Table 14.

As expected, in Figure 103 the maximum of the peak for all the distributions at 500°C shifts towards higher values of pore radius in comparison with the ones related to 20°C. Moreover, the distributions are more enlarged and new peaks appear in the field of macro pores (pore radius between 1 and 10 μm), indicating the formation of new voids due to thermal exposure, more pronounced for 45-S.

In case of different aggregate types, the effect of temperature exposure is indicated in Figure 104 and Figure 105, considering the cumulative and differential distributions respectively.

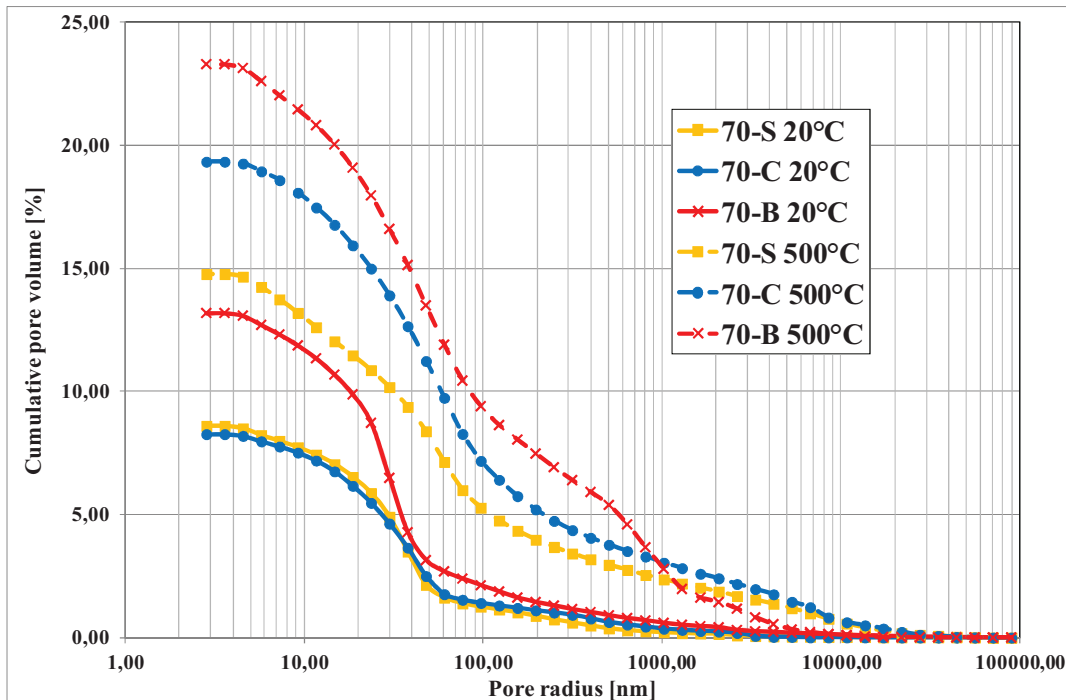


Figure 104: Cumulative distributions for different aggregate types at 20 and 500°C.

From Figure 104 it can be observed as expected that the thermal exposure at 500°C affects the total porosity, which increases more significantly for 70-C (almost 60%) than for the others mixes (almost 40%), as already reported in Table 11 and Table 14.

5. EXPERIMENTAL RESULTS

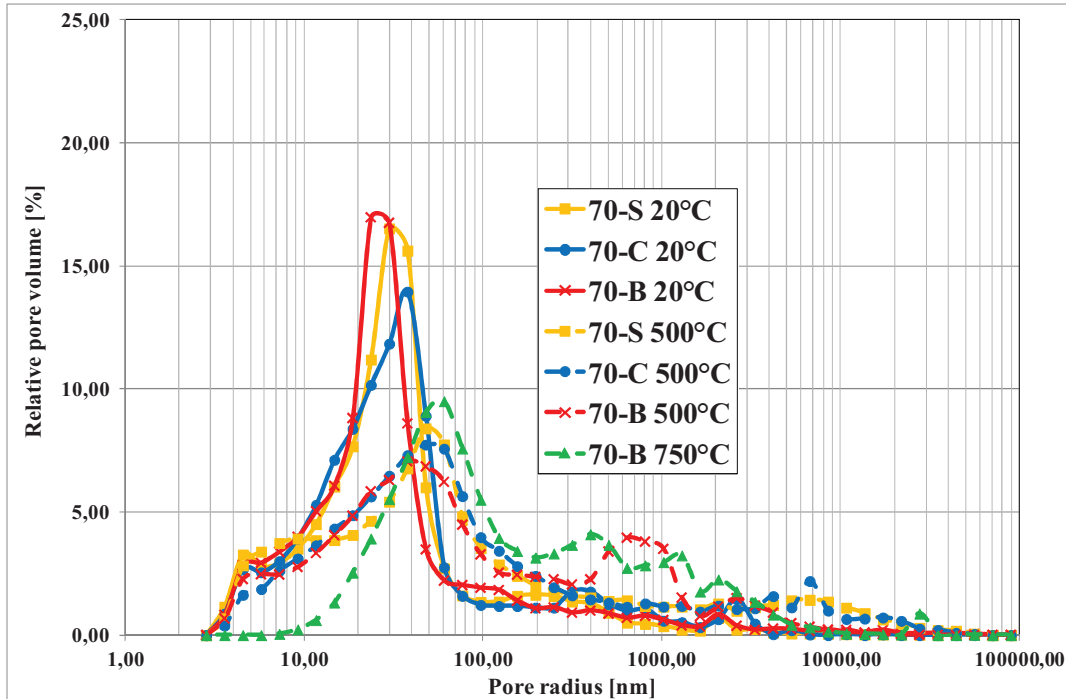


Figure 105: Differential distributions for different aggregate types at 20 and 500°C.

As for the previous mixes considered, in Figure 105 the shift of the maximum of the peak of sample at 500°C is observed. In particular, the 70-B presents a large peak which appears after thermal exposure in the range between 200 nm and 1200 nm and a secondary peak between 1 and 10 μm , while for 70-C two peaks appear at almost 10 μm . This means that these two mixes are different affected by thermal exposure. Moreover, for 70-B, in Figure 105 is plotted the curve after thermal exposure at 750°C, indicating the increasing in porosity in a range between capillary to macro pores, due to the widespread thermal damage induced in the microstructure.

The presence of PP fibers in the mixes has to be also considered, thus the total porosity values at 20°C and after the exposure temperatures for the mixes containing different PP monofilament fibers contents, as well as the one with PP fibrillated fibers, are collected from Table 16 to Table 19.

PP fibers	0.5 Kg/m ³ _20°C	1 Kg/m ³ _20°C	2 Kg/m ³ _20°C
mnf	9.57	9.13	8.37
fbr	-	-	8.67

Table 16: Total porosity values for different type and content of PP fibers concretes at 20°C.

5. EXPERIMENTAL RESULTS

PP fibers	0.5 Kg/m ³ _105°C	1 Kg/m ³ _105°C	2 Kg/m ³ _105°C
mnf	9.07	10.36	10.77
fbr	-	--	10.19

Table 17: Total porosity values for different type and content of PP fibers concretes at 105°C.

PP fibers	0.5 Kg/m ³ _250°C	1 Kg/m ³ _250°C	2 Kg/m ³ _250°C
mnf	9.06	12.23	12.87
fbr	-	-	10.95

Table 18: Total porosity values for different type and content of PP fibers concretes at 250°C.

PP fibers	0.5 Kg/m ³ _500°C	1 Kg/m ³ _500°C	2 Kg/m ³ _500°C
mnf	18.91	18.05	19.21
fbr	-	-	17.31

Table 19: Total porosity values for different type and content of PP fibers concretes at 500°C.

In order to better analyze the total porosity in concrete mixes containing PP fibers in function of increasing temperatures, the corresponding tabulated data are collected in Figure 106.

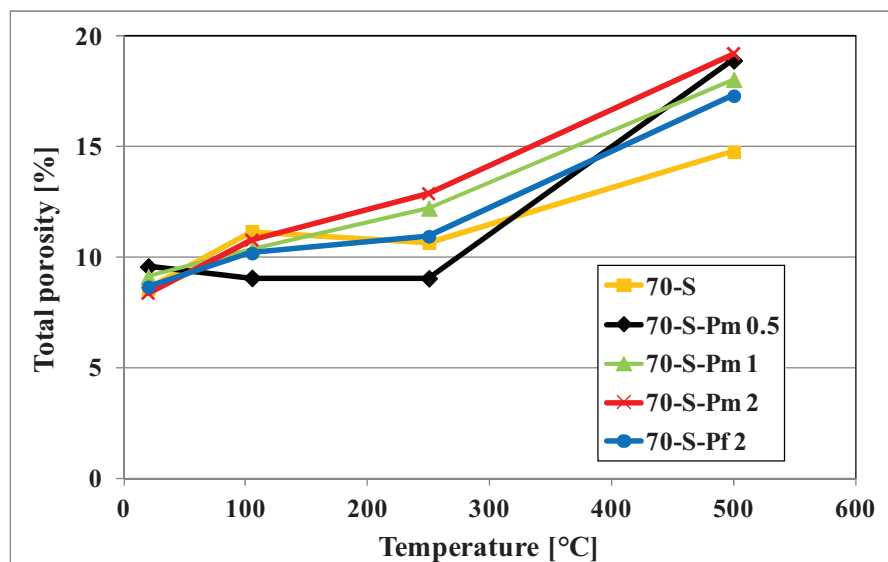


Figure 106: Concrete total porosity as a function of the temperature for different types and contents of PP fibers.

5. EXPERIMENTAL RESULTS

As already observed in case of previous mixes, when PP fibers are present in the concretes it arises that the higher the temperatures exposure, the higher the total porosity values. In this case, from Table 16 to Table 19 and Figure 106, the total porosity in mixes containing PP fibers is slightly higher at 20°C, and significantly higher after 500°C exposure; this additional porosity comes from the voids left free from the fibers after their melting and, especially, their degradation.

In order to show this type of additional porosity, the differential distribution for 70-S-Pm 1 after the exposure temperatures are plotted, as a representative example, in Figure 107, while the cumulative ones are collected in Figure 108.

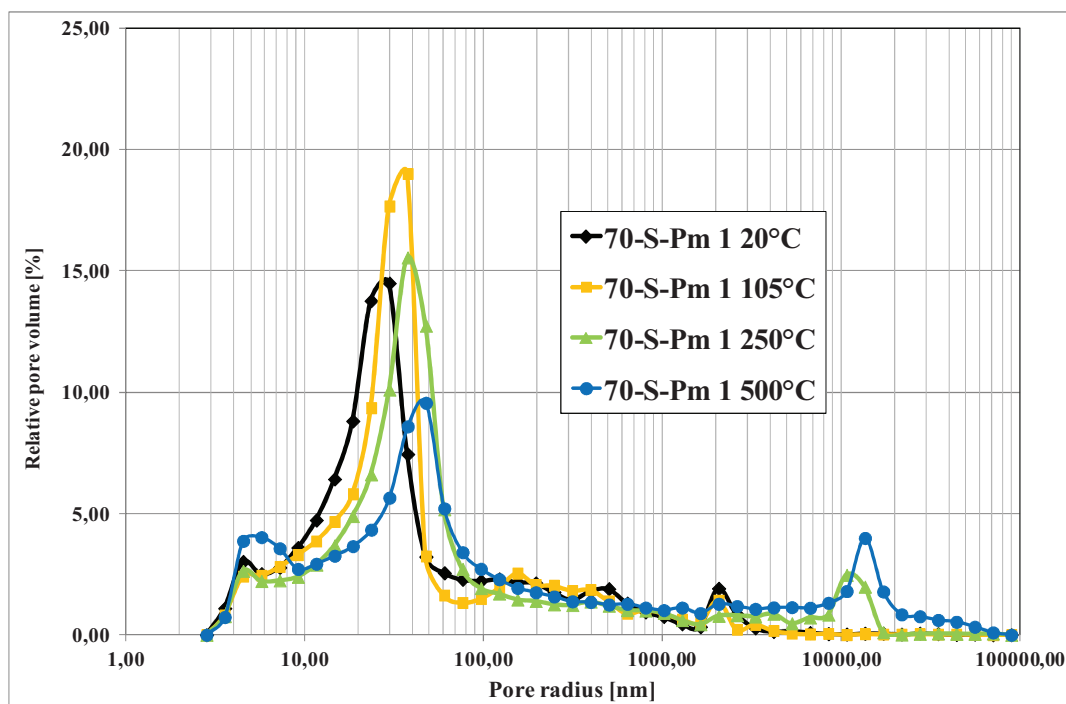


Figure 107: Differential distributions for 70-S-Pm 1 after heating (different exposure temperatures).

In Figure 107 the new porosity generated after thermal exposure due to melting and degradation of PP fibers can be observed at values of pore radius higher than 10 μm (as already observed by Alonso et al., 2013), attributable to new voids left free by PP monofilament fibers, having diameter equals to 20 μm . In particular, this peak becomes more pronounced, and slightly shifted, after 500°C exposure, because after this temperature the fibers turn out to be degraded, as well as melted.

5. EXPERIMENTAL RESULTS

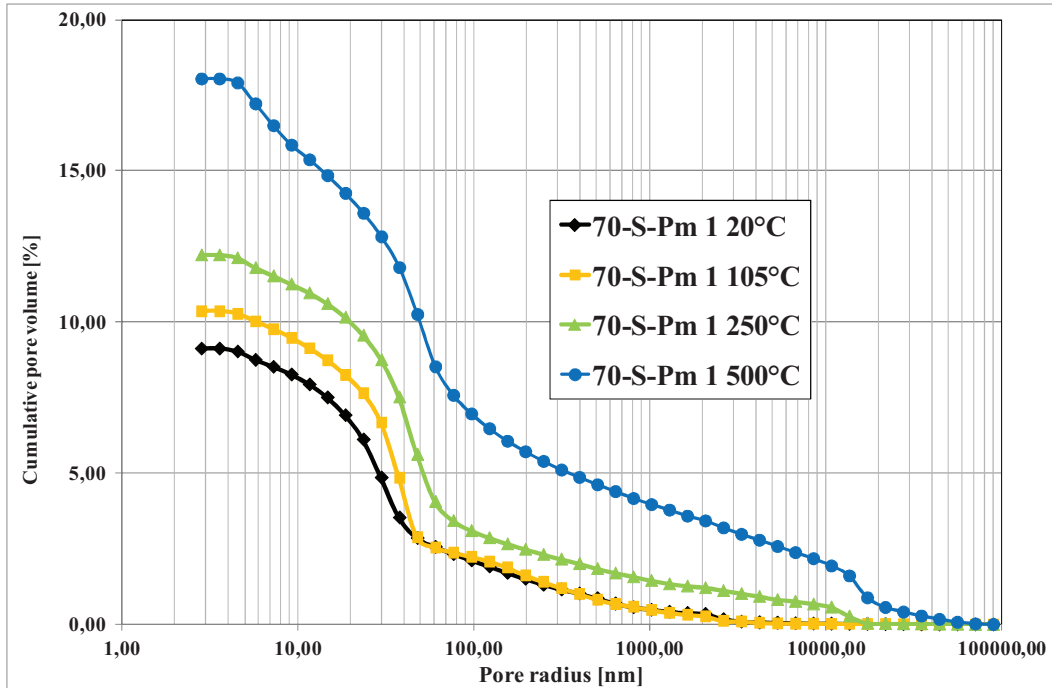


Figure 108: Cumulative distributions for 70-S-Pm 1 after heating (different exposure temperatures).

From Figure 108, the effect of temperature exposure on total porosity is confirmed, showing that with increasing temperatures the total porosity increases significantly.

Different contents of PP monofilament fibers have been considered and compared in Figure 109, as differential distributions, in order to evaluate the effect of this parameter on the evolution of pore size distribution.

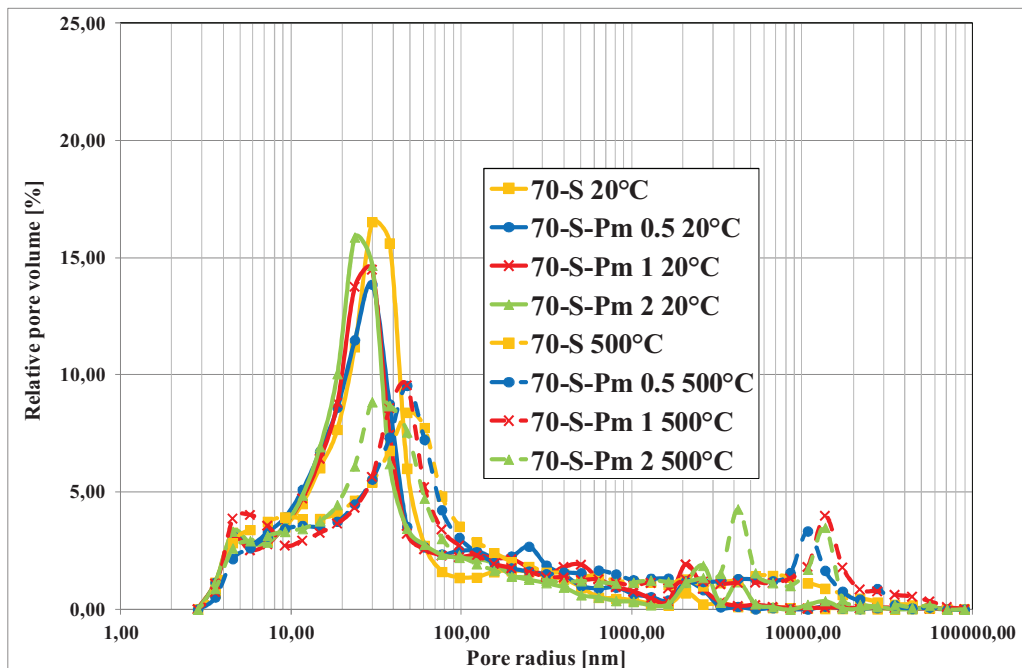


Figure 109: Differential distributions for different PP mnf fibers contents concretes at 20 and 500°C.

5. EXPERIMENTAL RESULTS

From Figure 109, it can be observed that the peak attributable to the porosity generated from melting and degradation of PP fibers (at almost 10 μm) increases in height, reflecting the increase in content of PP fibers. It arises that the higher the PP fibers content, the higher the peak abundance linked to PP fibers degradation.

In order to evaluate if the different type of PP fibers, monofilament and fibrillated, can have an impact on the evolution of porosity distributions with increasing temperatures, the cumulative and differential distributions of 70-S, 70-S-Pm 2 and 70-S-Pf 2 are plotted in Figure 110 and Figure 111 respectively.

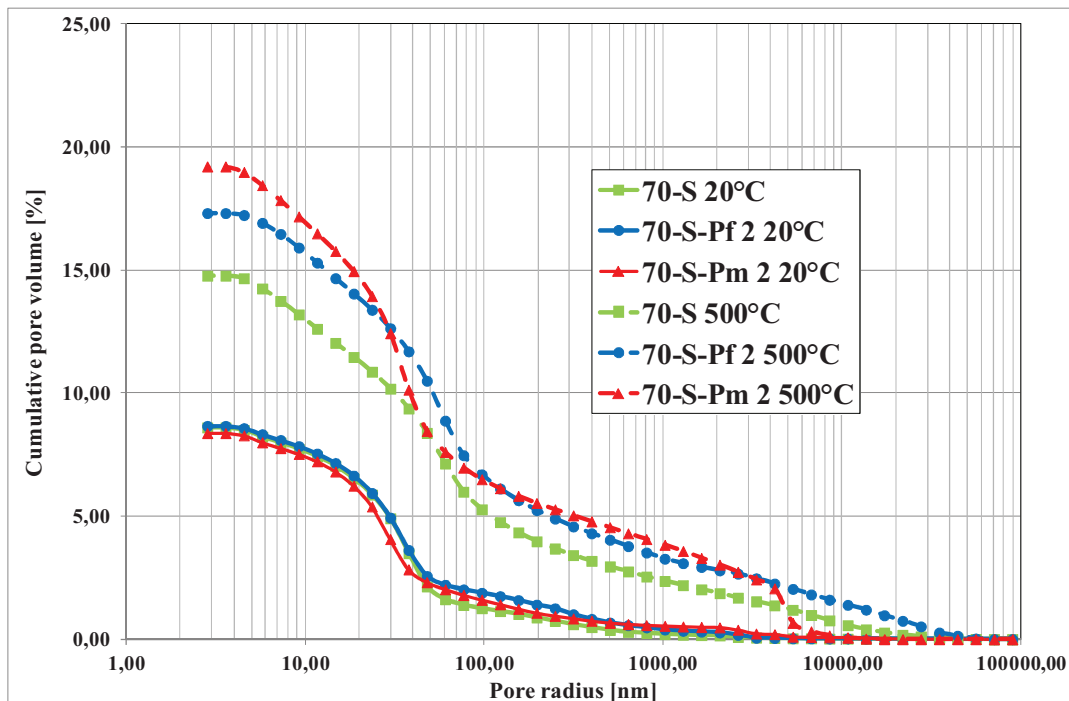


Figure 110: Cumulative distributions for 70-S, 70-S-Pm 2 and 70-S-Pf 2 at 20 and 500°C.

5. EXPERIMENTAL RESULTS

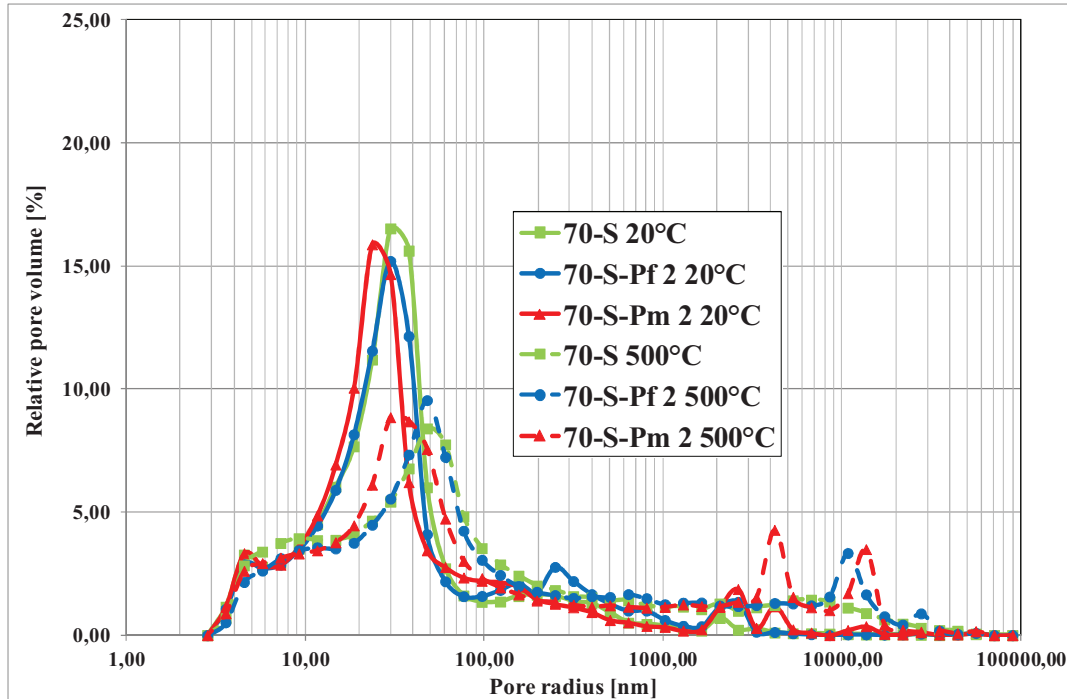


Figure 111: Relative distributions for 70-S, 70-S-Pm 2 and 70-S-Pf 2 at 20 and 500°C.

From Figure 110, it can be observed that PP fibers induce a significant increase in porosity above 250°C, which results higher in case of monofilament fiber in comparison with fibrillated. Moreover, from Figure 111, it arises that after heating at 500°C, some peaks appear in the zone of macropores, as a consequence of melting/degradation of PP fibers, both in case of monofilament and fibrillated. The peak height in case of both type of fibers are comparable, considering that they are added to the mix in the same content.

Concrete mixes containing steel fibers in different contents were also characterized by MIP before and after thermal exposure and the total porosity trends in function of increasing temperature are shown in Figure 112.

5. EXPERIMENTAL RESULTS

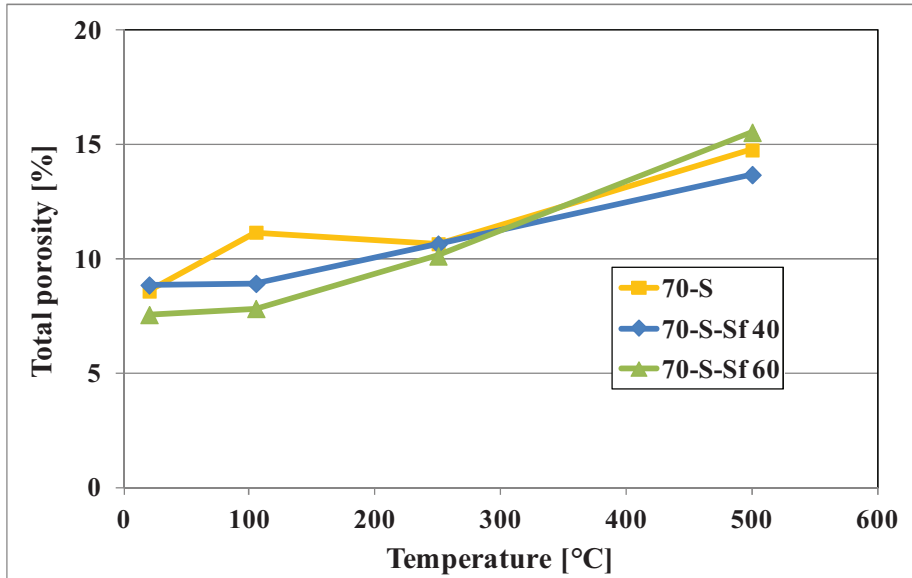


Figure 112: Concrete total porosity as a function of temperature for different steel fibers contents.

In Figure 112, it arises that the total porosity doesn't change significantly in concrete containing steel fibers compared with the one with no fiber (70-S) after thermal exposure at 250 and 500°C. No significant differences in porosimetric distributions are also observed for the same concrete types before and after thermal exposure, as can be seen in Figure 113.

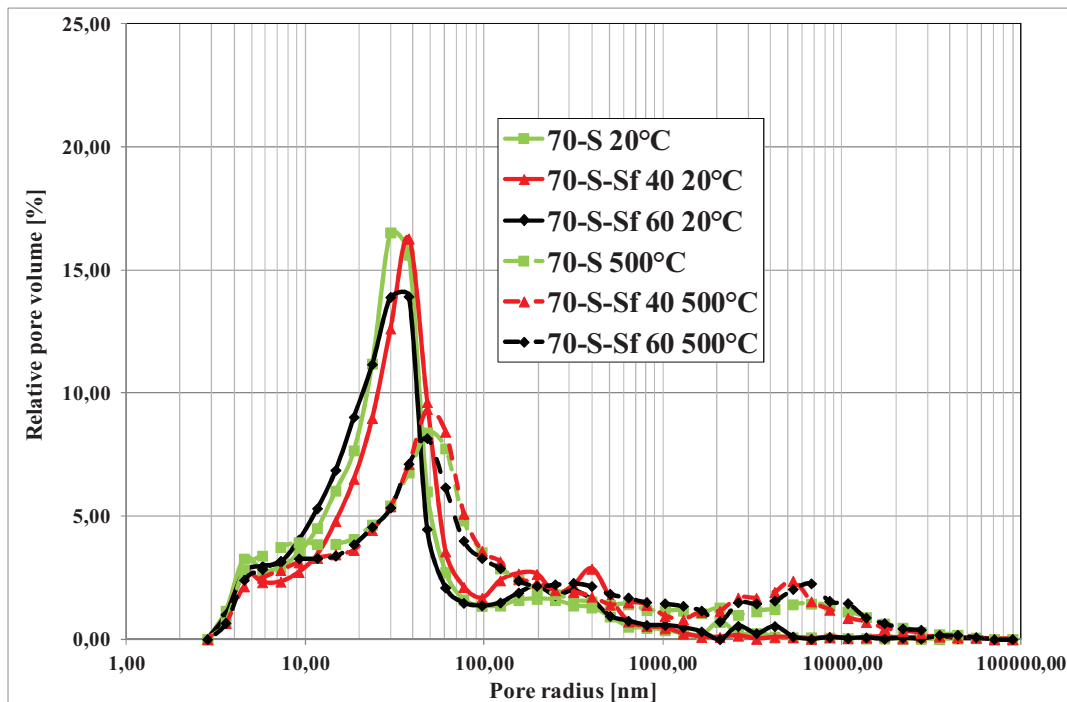


Figure 113: Relative distributions for 70-S, 70-S-Sf 40 and 70-S-Sf 60 at 20 and 500°C.

5. EXPERIMENTAL RESULTS

5.1.4 Scanning Electron Microscopy (SEM) results

The intrinsic damage caused by high temperature exposure inside the material, which is revealed by mass loss and generation of additional porosity, can be observed also by means of Scanning Electron Microscopy. This technique allows to investigate the microstructural variations and the microcracks distributions due to thermal exposure, both in cement paste and aggregate, as well as in the ITZ.

In the current Paragraph, the most significant SEM images, regarding the considered concrete mixes, will be shown, while all the experimental evidences collected for the entire group of samples will be collected in Annex E.

First of all, the effect of exposure temperature on microstructure has been considered. As a representative example, the 70-S images, obtained on polished sections in BSE (Back Scattered Electrons) mode, are collected in Table 20, at two different magnitudes.

From Table 20 it arises that for 70-S no significant microcracks are generated up to 250°C. At this temperature, few microcracks mostly appear departing from interface zone between cement matrix and aggregate (see 70-S at 250°C, 1000X). More pronounced cracks appear at 500°C, in particular crack bridging between aggregate interface and inside the cement paste are present. After 750°C exposure, the crack distribution appears widely diffused, with higher crack opening in comparison with 500°C exposure, indicating the most severe damage condition.

5. EXPERIMENTAL RESULTS

Mix	70-S images 100X	70-S images 1000X
20°C		
105°C		
250°C		
500°C		
750°C		

Table 20: SEM images for 70-S at 100X and 1000X magnitude after all exposure temperatures.

5. EXPERIMENTAL RESULTS

A comparison among the different concrete grades can be carried out. The considered SEM images are related to residual conditions after thermal exposure at 250, 500 and 750°C. From Table 21 to Table 23 are collected these images, obtained on polished sections in BSE mode, at two different magnitudes, at the three indicated temperatures, respectively.

Concrete Mix	250°C images 100X	250°C images 1000X
45-S		
70-S		
95-S		

Table 21: SEM images for different concrete grades at 100X and 1000X magnitude at 250°C.

5. EXPERIMENTAL RESULTS

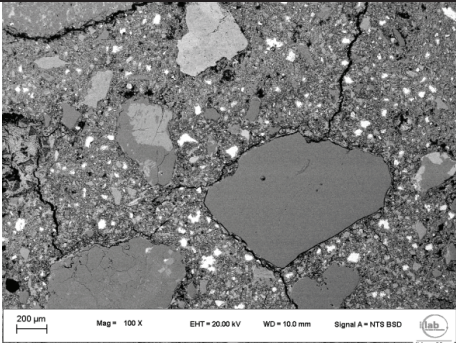
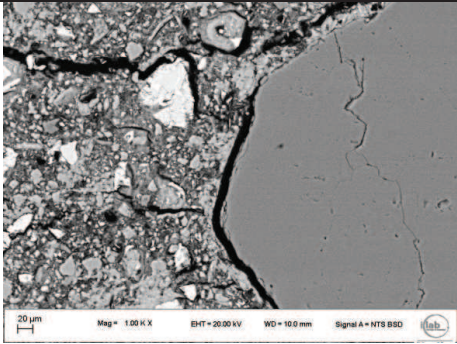
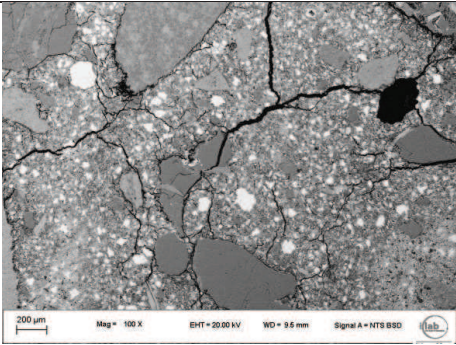
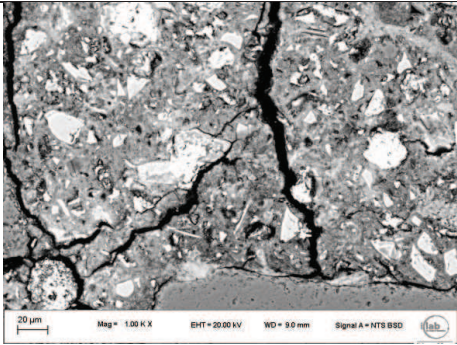
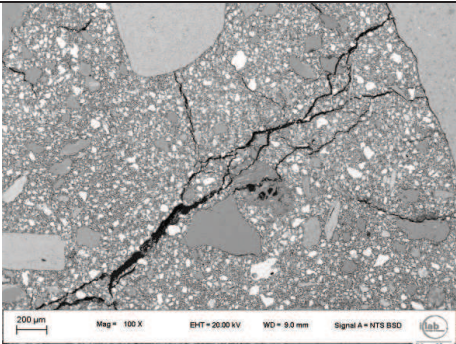
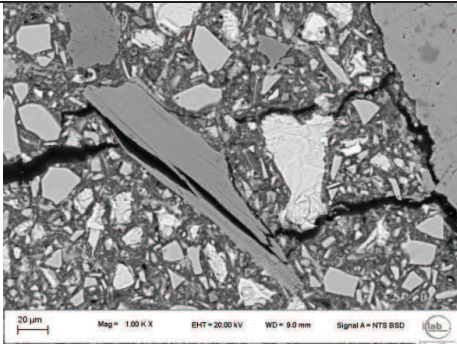
Concrete Mix	500°C images 100X	500°C images 1000X
45-S		
70-S		
95-S		

Table 22: SEM images for different concrete grades at 100X and 1000X magnitude at 500°C.

Comparing the three concrete grades after thermal exposure at 250°C in Table 21 few microcracks mostly appear departing from interface zone between cement matrix and aggregate for 45-S and 70-S (see 1000 X); no evidence has been found for 95-S.

After 500°C (see Table 22), for all the concretes mixes microcracking occurs more frequently and can be observed just at 100 X of magnitude; cracking in Mix 45-S is hardly distributed, being mainly located at the aggregates-matrix interface, while in 70-S and 95-S cracking appears more distributed and extended to the cementitious matrix, also constituting a bridge between aggregate interface. This crack distributions are confirmed by 1000 X of magnitude observations, in which the thermal damage inside the aggregate particle is also shown in case of 95-S.

5. EXPERIMENTAL RESULTS

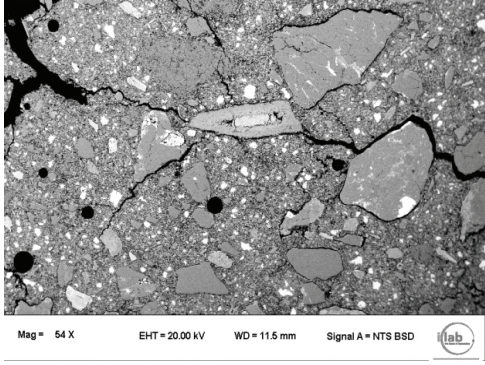
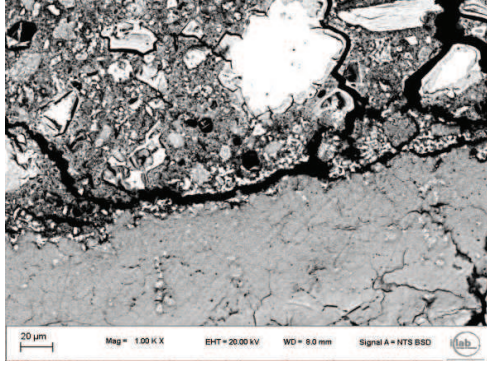
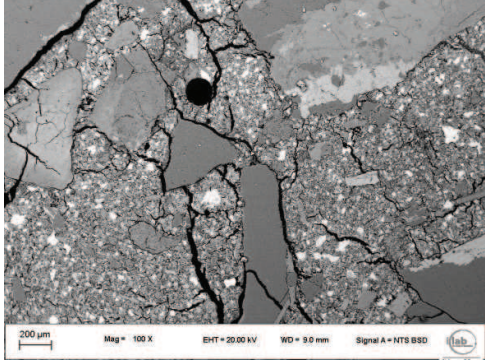
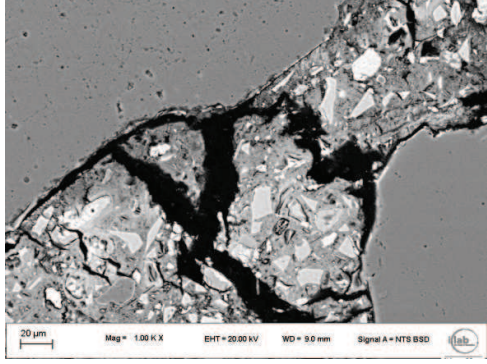
Concrete Mix	750°C images 100X	750°C images 1000X
45-S		
70-S		
95-S	-	-

Table 23: SEM images for different concrete grades at 100X and 1000X magnitude at 750°C.

In Table 23, the most diffused cracking due to thermal exposure at 750°C can be seen for the 45-S and 70-S (fro 95-S wasn't possible to perform the SEM observation), also in this case more distributed for 70-S than for 45-S. More in details, cracks in the interface between aggregate and cement paste have been highlighted for 45-S and bridging between aggregate in cement matrix for 70-S.

The same type of comparison has been carried out for different aggregate types. The considered SEM images, related to residual conditions after thermal exposure at 250, 500 and 750°C, are collected from Table 24 to Table 26, obtained on polished sections in BSE mode, at two different magnitudes, at the three indicated temperatures, respectively (for 70-C the images after 750°C exposure wasn't possible to acquire because the sample was damaged).

5. EXPERIMENTAL RESULTS

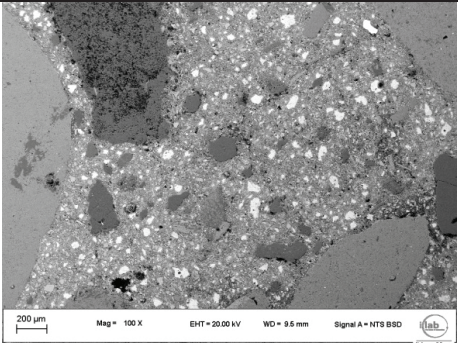
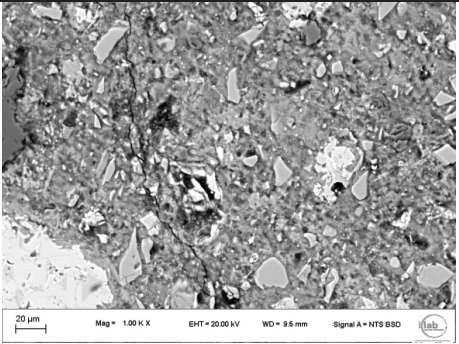
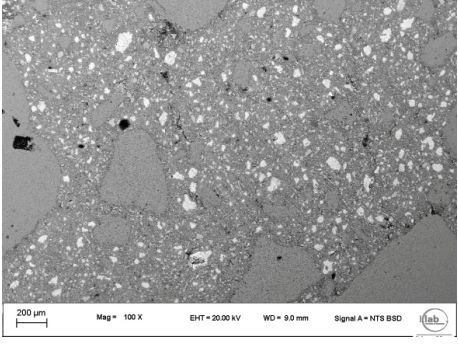
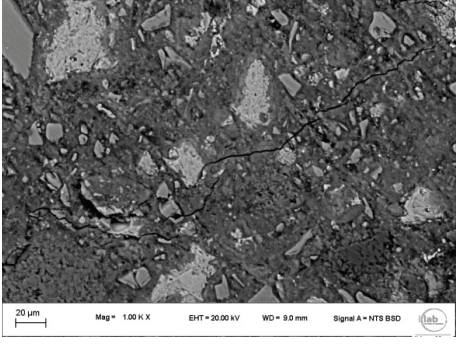
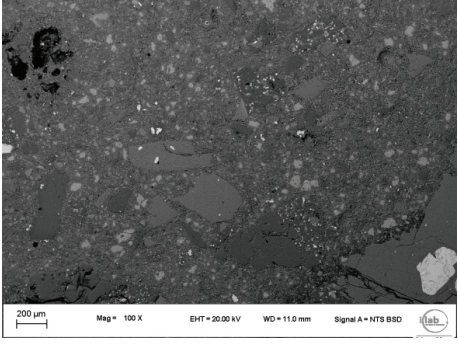
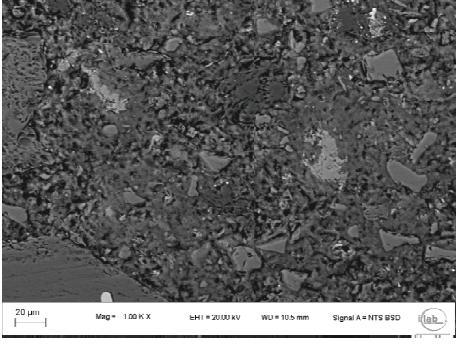
Concrete Mix	250°C images 100X	250°C images 1000X
70-S		
70-C		
70-B		

Table 24: SEM images for different aggregate types at 100X and 1000X magnitude at 250°C.

5. EXPERIMENTAL RESULTS

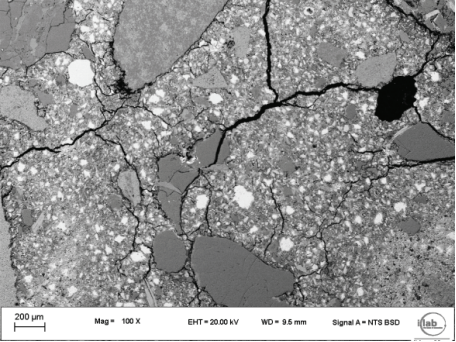
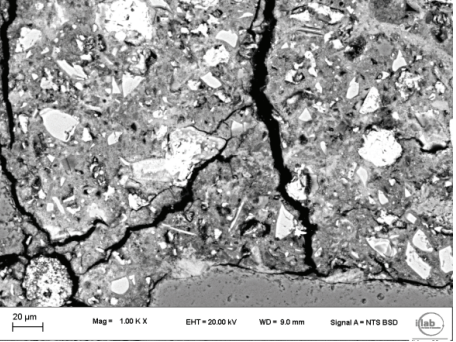
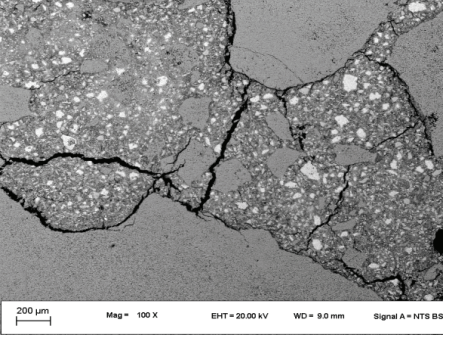
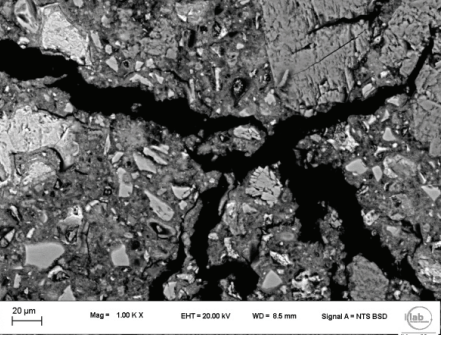
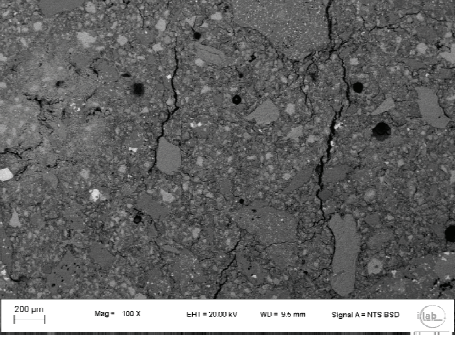
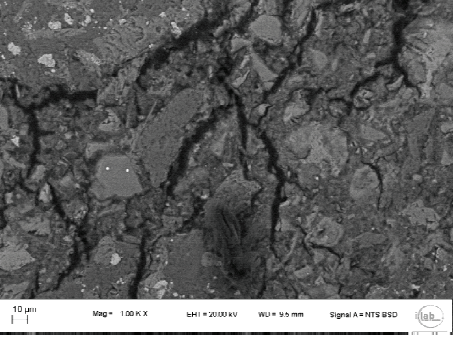
Concrete Mix	500°C images 100X	500°C images 1000X
70-S		
70-C		
70-B		

Table 25: SEM images for different aggregate types at 100X and 1000X magnitude at 500°C.

5. EXPERIMENTAL RESULTS

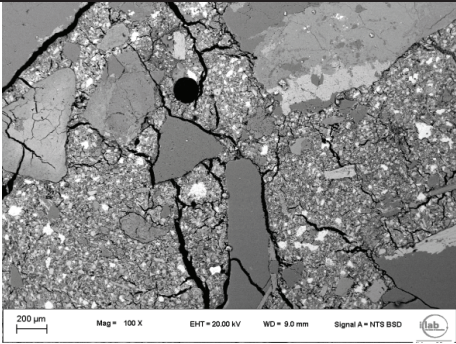
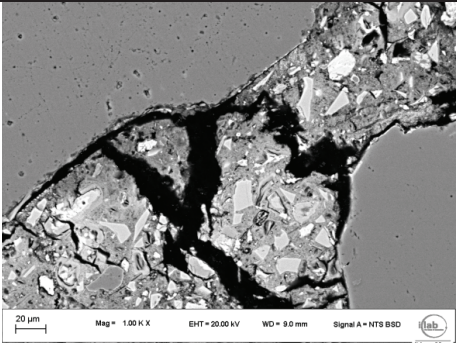
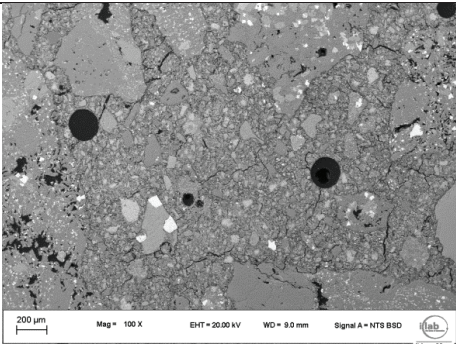
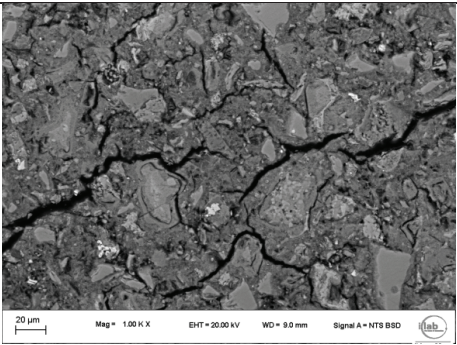
Concrete Mix	750°C images 100X	750°C images 1000X
70-S		
70-C	-	-
70-B		

Table 26: SEM images for different aggregate types at 100X and 1000X magnitude at 750°C.

Considering the thermal exposure at 250°C (see Table 24), only for 70-S and 70-C few microcracks can be observed passing through the cement paste, but not for 70-B (see 1000 X).

After exposure at 500°C, in case of silico-calcareous and calcareous aggregate concretes, a more diffused cracks distribution is shown, in comparison with 70-B, which present less distributed cracks characterized by smaller crack openings.

The basalt aggregate gives to concrete mix the best behaviour after thermal exposure also at 750°C; in fact, for 70-B the crack distribution is significantly less diffused and the crack opening is smaller in comparison with 70-S.

The presence of PP fibers, in different contents and types, has to be considered, in order to acquire also information regarding the way of action of PP fibers in contrast explosive spalling. The comparison between the intermediate concrete grades with (70-S-Pm 2 and 70-S-Pf 2) and without (70-S) PP fibers is reported in Table 27, showing the polished sections (BSE mode) observed after thermal exposure at 500°C at two different magnitudes.

5. EXPERIMENTAL RESULTS

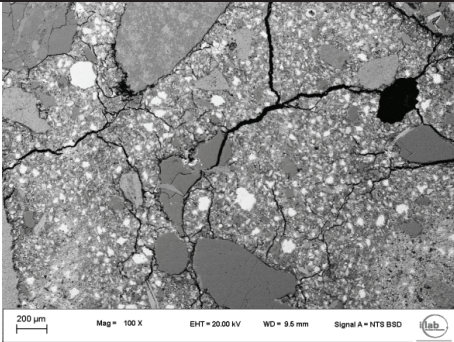
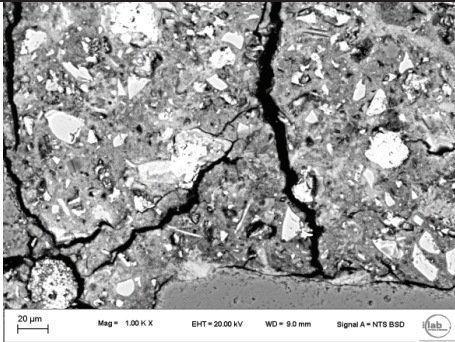
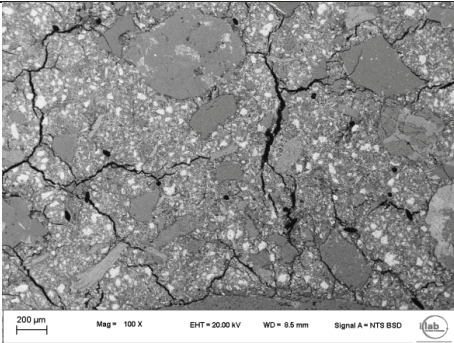
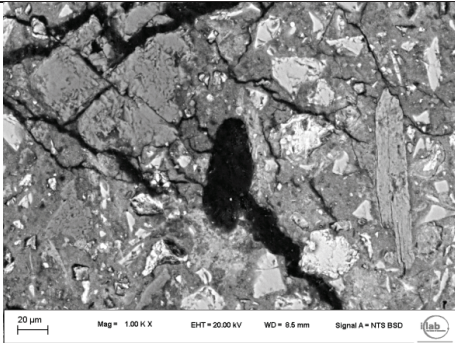
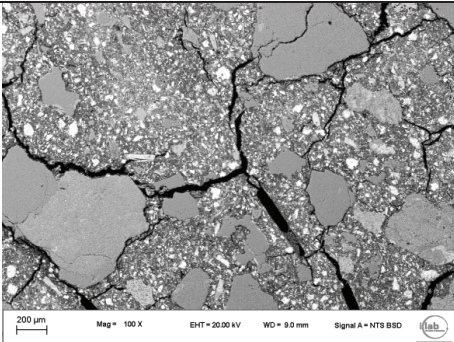
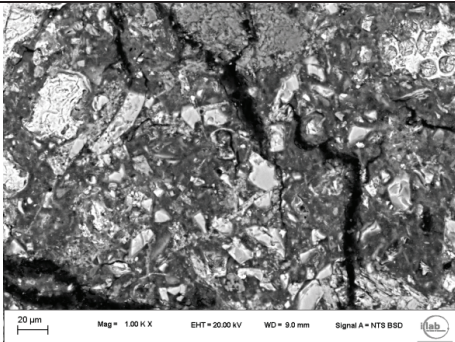
Concrete Mix	500°C images 100X	500°C images 1000X
70-S		
70-S-Pm2		
70-S-Pf 2		

Table 27: SEM images for concrete with different types and contents of PP fibers at 100X and 1000X magnitude at 500°C.

The PP fibers seem to not affect in a significant way the crack distribution after thermal exposure, in a general overview of the sections (see 100 X in Table 27). In case of 1000 X of magnitude, the mix originally prepared with PP monofilament fiber shows a crack starting from the space left free after thermal degradation of fiber. This experimental evidence is confirmed observing fractured sections of 70-S-Pm1 mix, before and after thermal exposure, collected in Figure 114.

5. EXPERIMENTAL RESULTS

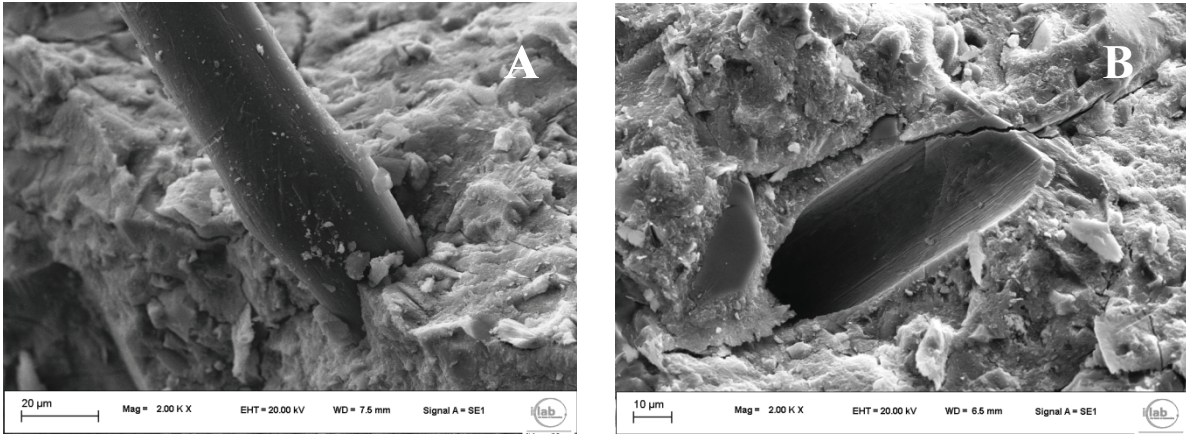


Figure 114 : A) PP monofilament fiber in 70-S-Pm 1 not exposed concrete; B) typical void left free by a fiber after heating at 250°C (70-S-Pm 1).

In Figure 114 (B), it can be observed that spaces originally occupied by PP fibers appear empty because of melting and degradation of the fibers, as already observed by other Authors (Noumowe, 2005, Alonso et al., 2013, Kalifa et al., 2001). Moreover few new cracks propagate through the channels left free by the fibers.

The presence of steel fibers in concrete has been studied by comparing the intermediate grade mixes with and without steel fibers. The related images obtained on polished sections after thermal exposure at 500°C, at two different magnitudes, are reported in Table 28.

From Table 28, it arises that steel fibers don't influence the cracks distribution after thermal exposure; moreover, it is possible to observe the fiber section (the white portion of image) and its interface zone in the 1000 X image. A darker grey zone can be seen between the fibers and the cement matrix, indicating a partial degradation of the fiber, as already seen by Guerrini et al. (2004). In order to better investigate this phenomenon, the concrete sample exposed to 750°C is considered (see Figure 115).

5. EXPERIMENTAL RESULTS

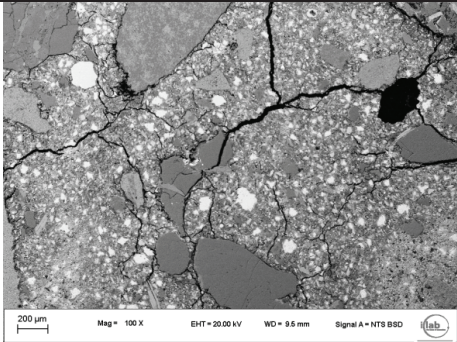
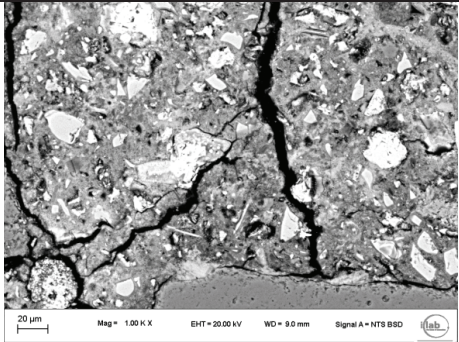
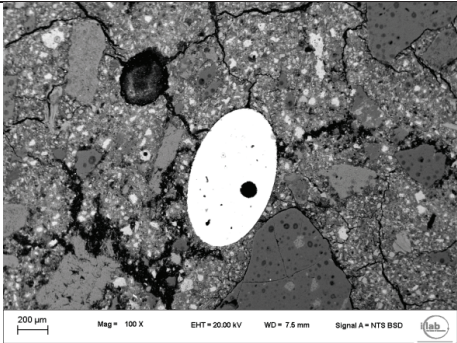
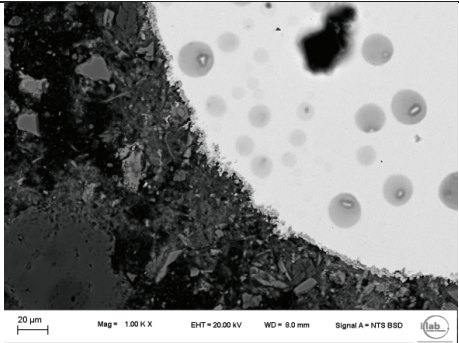
Concrete Mix	500°C images 100X	500°C images 1000X
70-S		
70-S-Sf40		

Table 28: SEM images for concretes with and without steel fibers at 100X and 1000X magnitude at 500°C.

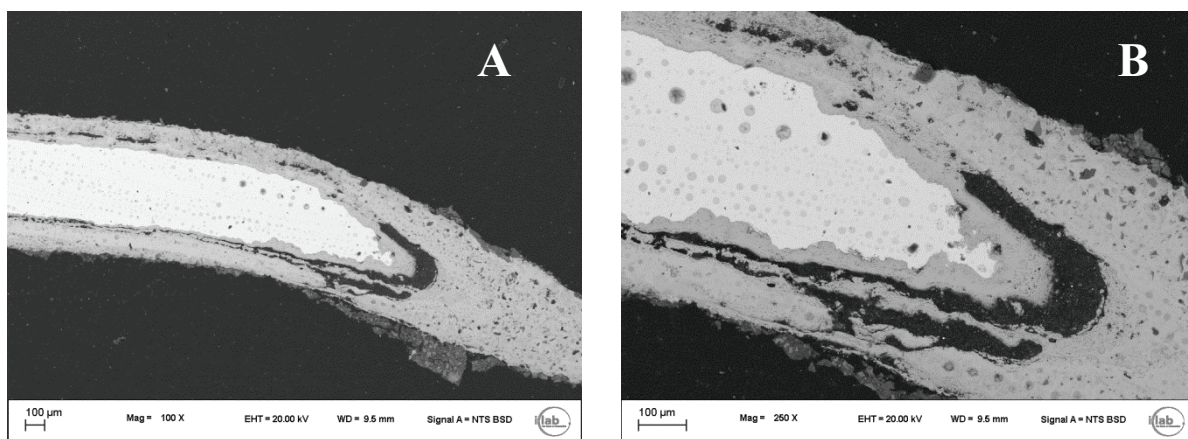


Figure 115: Steel fiber in 70-S-Sf 40 mix after 500°C exposure 100 X (A) and 250 X (B).

From Figure 115 it can be observed that the steel fiber, after 750°C exposure, change its composition in the external part, in contact with cement paste. The composition of these different layers has been investigated by means of SEM microanalysis and the results are indicated in Figure 116.

5. EXPERIMENTAL RESULTS

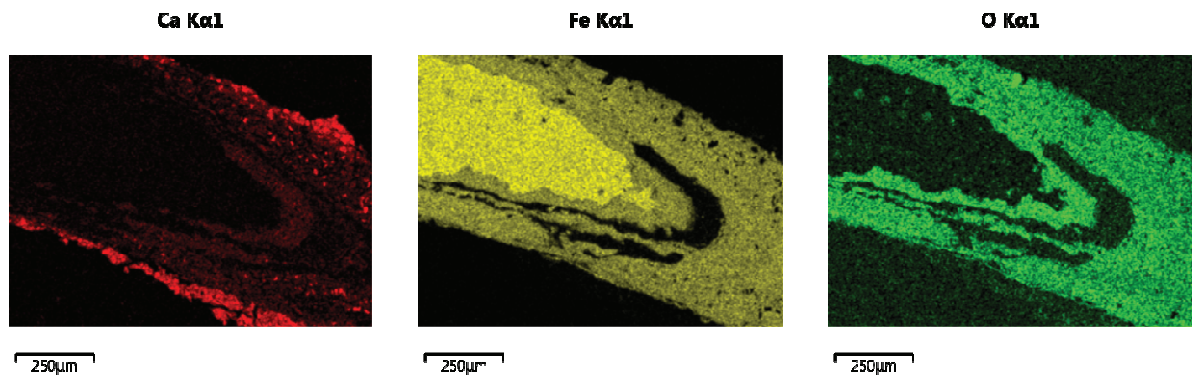


Figure 116: SEM microanalysis of the interface between steel fiber and cementitious matrix.

From the microanalysis, it arises that the fiber is partially oxidized and this effect is probably accentuated by high temperature exposure. In fact, this transformation is more evident after exposure to 750°C in comparison with the one at 500°C.

5. EXPERIMENTAL RESULTS

5.2 Mechanical characterization

In the current Paragraph, the experimental results concerning the mechanical characterization of concrete mixes in residual conditions will be shown, regarding the stress-strain curves, the compressive strength and elastic modulus trends in function of increasing temperatures.

5.2.1 Stress-strain curves

The stress-strain curves detected in residual conditions for all the concrete mixes will be presented in this Paragraph, starting from the ones related to the three concrete grades, whose average curves are collected in Figure 117.

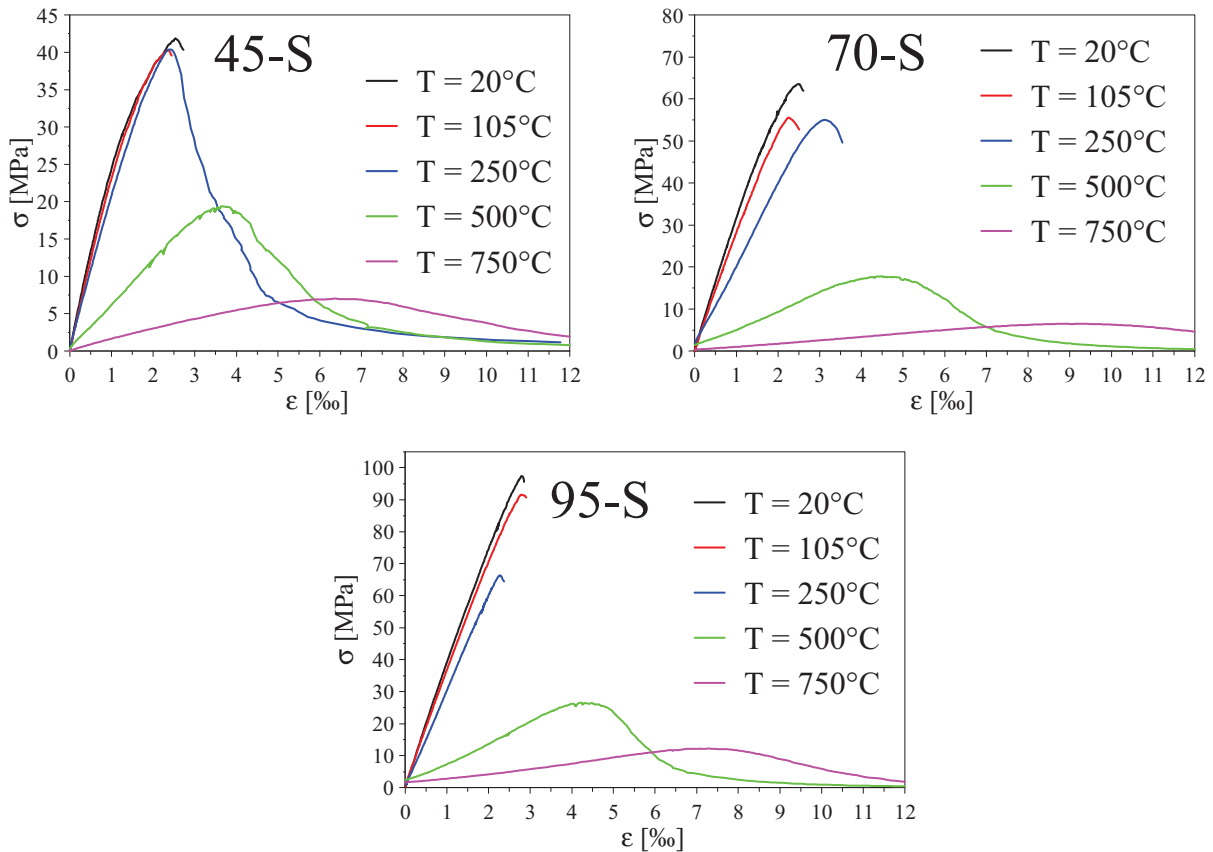


Figure 117: Residual stress-strain curves for different concrete grades after all exposure temperatures.

In Figure 117, it can be observed that it has been possible to acquire the complete σ - ϵ curve (including post-peak branches) only after thermal exposure at 500 and 750°C (except for 45-S, which present also the one after 250°C). This fact is due to the inability of testing machine set-up to

5. EXPERIMENTAL RESULTS

control fracture process in the post-peak region, characterized by a very steep slope of the “virtual” σ - ε curve, for high strength specimens (70 and 95 grade).

Moreover, specimens after exposure up to 250°C present significantly higher values of elastic modulus in comparison with the ones related to 500 and 750°C exposure. In particular, 45-S seems to be less affected by thermal exposure up to 250°C because the rising branches are very close each other, while for 70-S and 95-S, the higher the temperature exposure, the lower the branch slope.

In general terms, it arises that the higher the temperature exposure, the lower the concrete stiffness and the arising branch slope in stress-strain curve, confirming the experimental data also from other Authors (Felicetti and Gambarova, 1998, Chang et al., 2006). Moreover, for each temperature, the higher the concrete grade, the higher the stiffness up to 250°C.

As in the previous Paragraph, the comparison among the different aggregate types is performed; the related curves are reported in Figure 118.

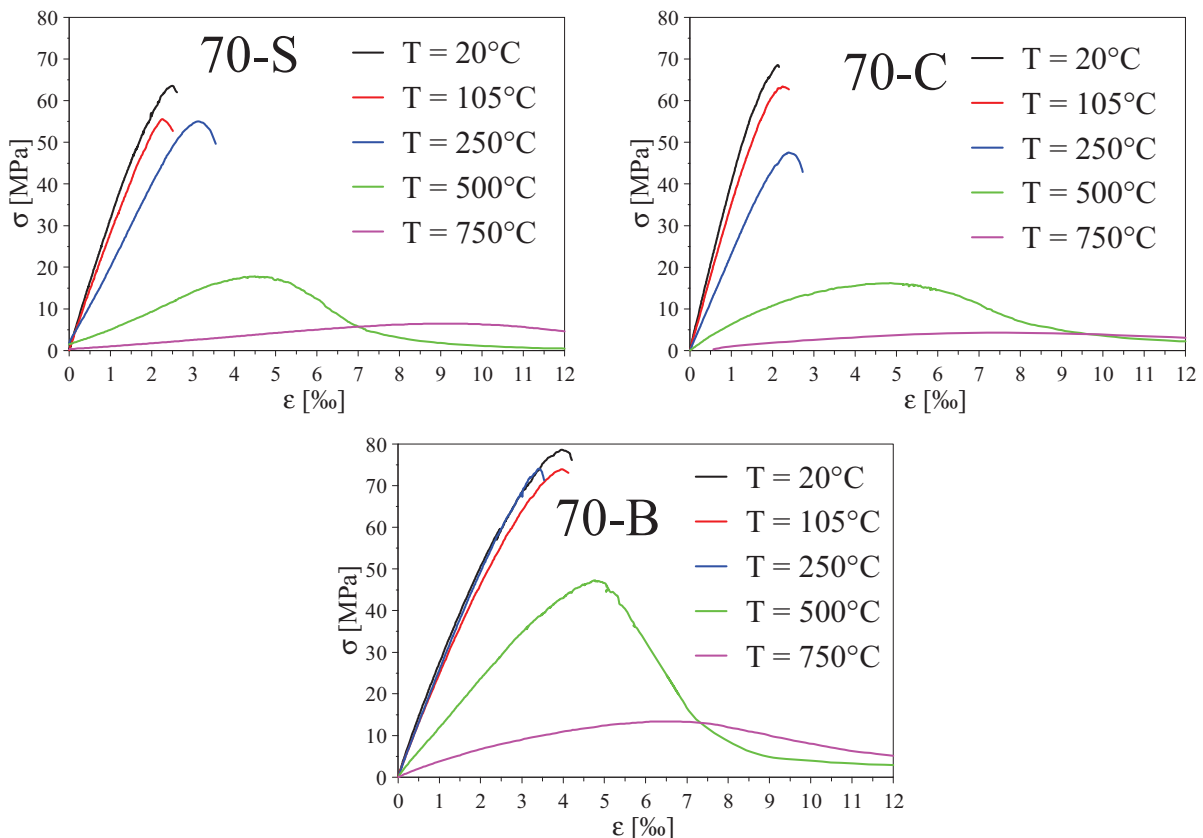


Figure 118: Residual stress-strain curves for concretes with different aggregate types after all exposure temperatures.

5. EXPERIMENTAL RESULTS

From Figure 118, 70-B mix appears less stiff in comparison with 70-S and 70-C up to 105°C exposure, but this trend is reversed from 250°C. Moreover, 70-B mix presents the highest compressive strength values after all the exposure temperatures among these concrete mixes, as well as the lowest deformation after 750°C exposure.

In order to investigate the effect of different content and type of PP fibers, as well as the different content of steel fibers, the related curves are all collected in Figure 119, compared with 70-S one (without any fibers).

As already seen in the previous Figures, also in this case the post-peak branches were not detected up to 250°C, except for mixes containing steel fibers, which are characterized by a more ductile and deformable behaviour.

Comparing all these curves, it arises that they are closed each other up to 250°C exposure. After 500°C, the mixes containing steel fibers exhibit the highest values of compressive strength as well as highest deformation than all the considered mixes, followed by the ones with PP fibers. All these curves significantly deviate from the 70-S curve.

After 750°C, the steel fibers mixes already show the highest compressive strength and deformation values, in particular the one with the higher steel fiber content. PP monofilament fiber mixes present similar behaviour in comparison with 70-S, while 70-S-Pf 2 shows higher compressive strength than 70-S, but similar deformation values.

5. EXPERIMENTAL RESULTS

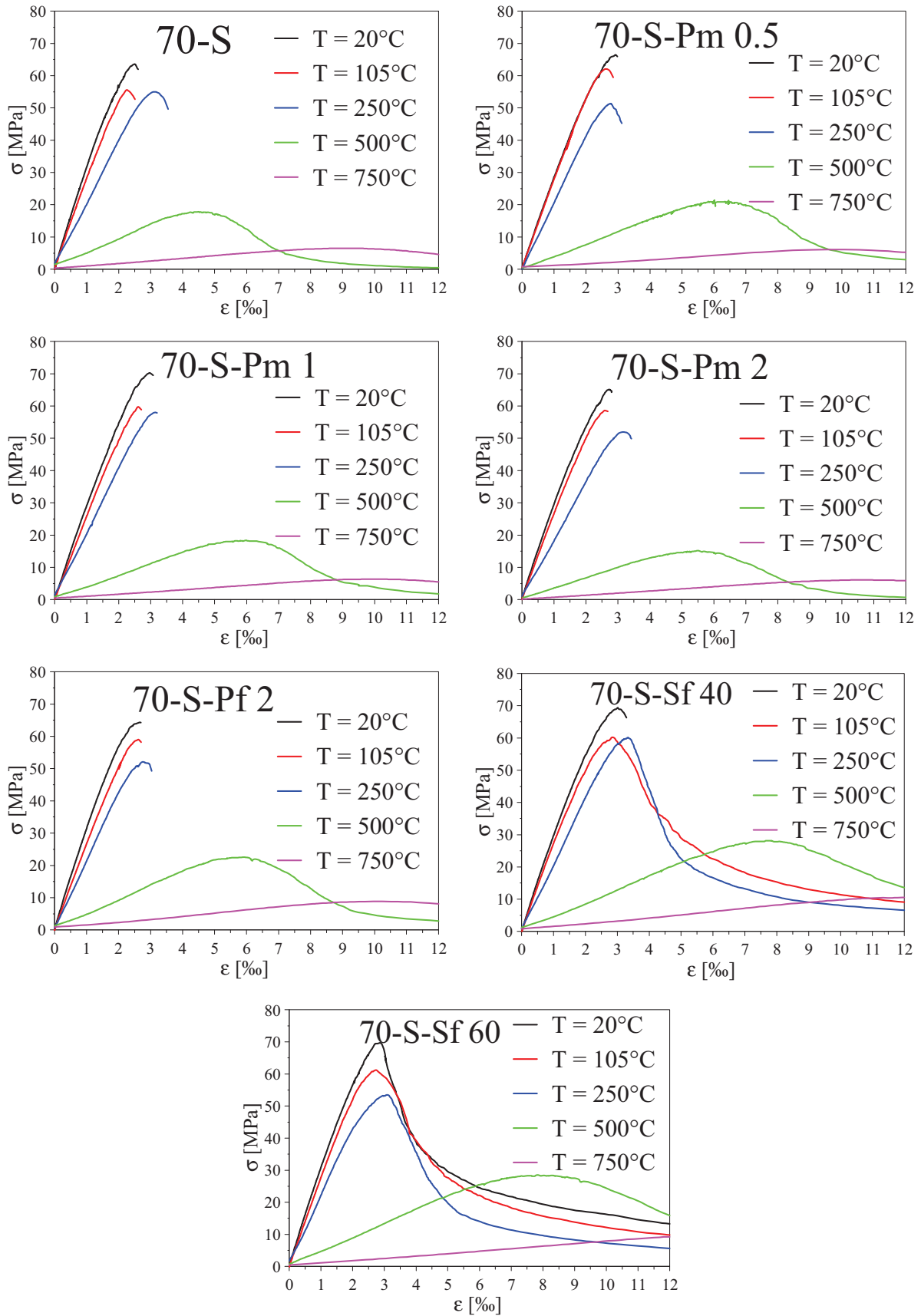


Figure 119: Residual stress-strain curves for concretes with different contents and types of PP fibers and different contents of steel fibers after all exposure temperatures.

5. EXPERIMENTAL RESULTS

5.2.2 Compressive strength

In this Paragraph, the concrete compressive strength values, obtained in residual conditions from stress-strain curves, in function of temperature will be shown, in order to evaluate the mechanical performance decay after thermal exposure.

A first comparison is carried out between the concretes cylindrical compressive strength values at 20°C tabulated in Table 9 and Table 10 with the ones obtained from stress-strain curves (see Table 29). These values could not be directly compared because obtained from different cylindrical specimens, but they can give an indication of the robustness of the measurement methods.

Concrete mixes	$f_{cm,cyl}$ (MPa) at 28 days ($\phi=150$ mm, $h=300$ mm)	$f_{cm,cyl}$ (MPa) <60 days ($\phi=100$ mm, $h=200$ mm)
45-S	40	42
70-S	62	64
95-S	90	97
70-C	64	69
70-B	66	79
70-S-Pm 0.5	63	67
70-S-Pm 1	60	69
70-S-Pm 2	60	65
70-S-Pf 2	61	65
70-S-Sf 40	63	70
70-S-Sf 60	60	70

Table 29: Compressive strength values at 20°C for different cylindrical specimens at different ages.

From Table 29, a good correlation between the compressive strength values from different test methods is observed. In particular, the data obtained as reference in stress-strain curves are slightly higher than those at 28 days because of longer curing and presence of pozzolanic addition, besides different geometrical characteristics of cylindrical specimens.

After the previous preliminary comparison of reference experimental data, all the residual compressive strength data detected for the 11 mixes after all the exposure temperatures are collected in Table 30.

5. EXPERIMENTAL RESULTS

Concrete mixes	$f_{cm,cyl}$ 20°C (MPa)	$f_{cm,cyl}$ 105°C (MPa)	$f_{cm,cyl}$ 250°C (MPa)	$f_{cm,cyl}$ 500°C (MPa)	$f_{cm,cyl}$ 750°C (MPa)
45-S	41.9	40.5	40.8	19.5	7.0
70-S	63.6	55.7	55.2	17.9	6.5
95-S	96.8	91.6	66.5	26.7	12.3
70-C	68.7	63.4	47.7	16.4	4.3
70-B	78.8	74.2	74.2	47.4	13.5
70-S-Pm 0.5	66.6	62.2	51.5	21.1	6.1
70-S-Pm 1	68.9	59.9	58.2	18.4	6.4
70-S-Pm 2	65.2	58.7	52.0	15.2	6.1
70-S-Pf 2	64.6	59.1	52.3	22.7	8.9
70-S-Sf 40	69.5	60.3	60.3	28.3	10.6
70-S-Sf 60	69.9	61.4	53.6	28.6	10.8

Table 30: Compressive strength values for all concrete mixes after all temperatures.

The first graphical comparisons are carried out among the different concrete grades, in Figure 120, and among the different aggregate types, in Figure 121. The residual values (f_c^T) are normalized in function of compressive strength at 20°C (f_c^{20}) in order to perform a correct comparison.

From Figure 120, it arises that, in general terms, the higher the temperature exposure, the lower the residual compressive strength, confirming the literature review data (Phan and Carino, 1998). In this case, 45-S appears to be the less affected by thermal exposure, while 95-S the most affected. 70-S presents an intermediate behaviour except at 105°C, where it seems to be the more damaged.

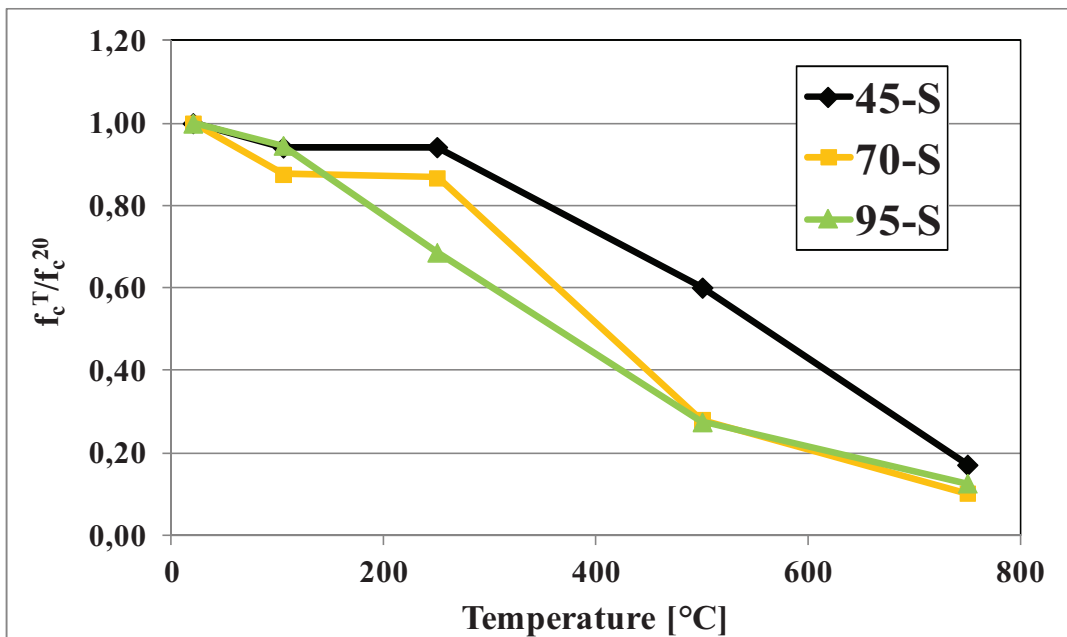


Figure 120: Residual compressive strength as a function of the temperature for different concrete grades.

5. EXPERIMENTAL RESULTS

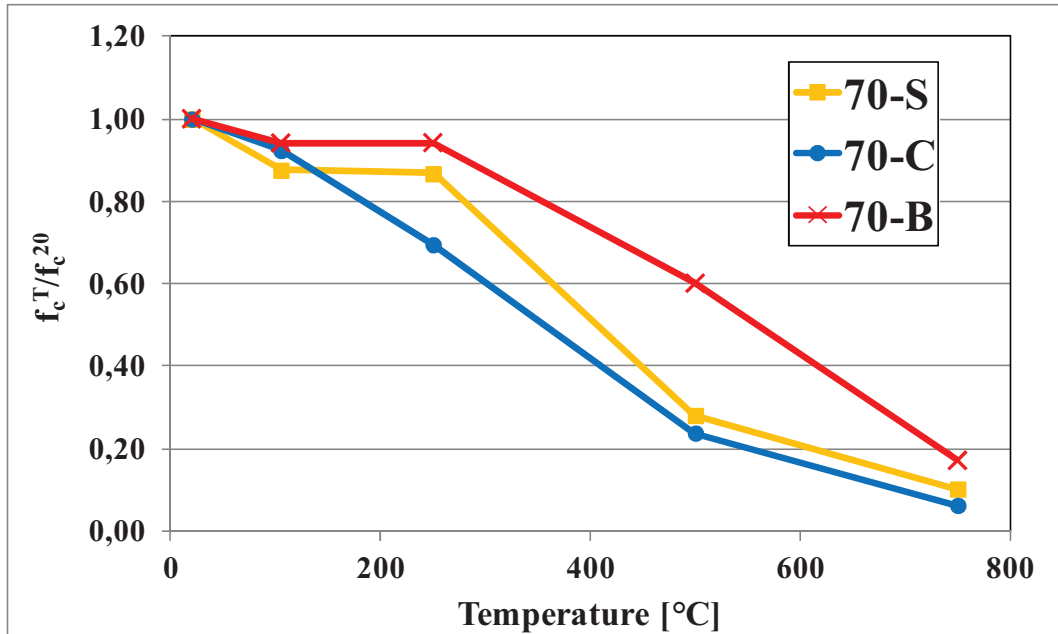


Figure 121: Residual compressive strength as a function of temperature for different aggregate types.

In Figure 121, it can be observed that the concrete containing basalt aggregate is the least affected by high temperature exposure, especially at 500°C (compared to the others), while the calcareous one seems to be the most damaged. As in the previous case, 70-S presents an intermediate trend, even if it shows the lowest residual compressive strength values after 105°C exposure. These experimental trends seem to confirm the ones foreseen for siliceous and calcareous concretes according to ACI provisions (2007).

The effect of the addition of PP fibers on residual compressive strength can be also evaluated, considering different fiber type and contents and this comparison is reported in Figure 122. Instead, in Figure 123 are plotted the curves related to concrete mixes containing different content of steel fibers, compared with 70-S mix, as in the case of Figure 122.

All the curves in Figure 122 are very close, but some considerations can be made. The presence of PP fibers induces a slight decrease in the residual compressive strength after 250°C exposure compared with 70-S mix, but this effect is not observed after 105, 500 and 750°C, at which the intermediate concrete without fibers has an intermediate behaviour with respect to the other concretes.

5. EXPERIMENTAL RESULTS

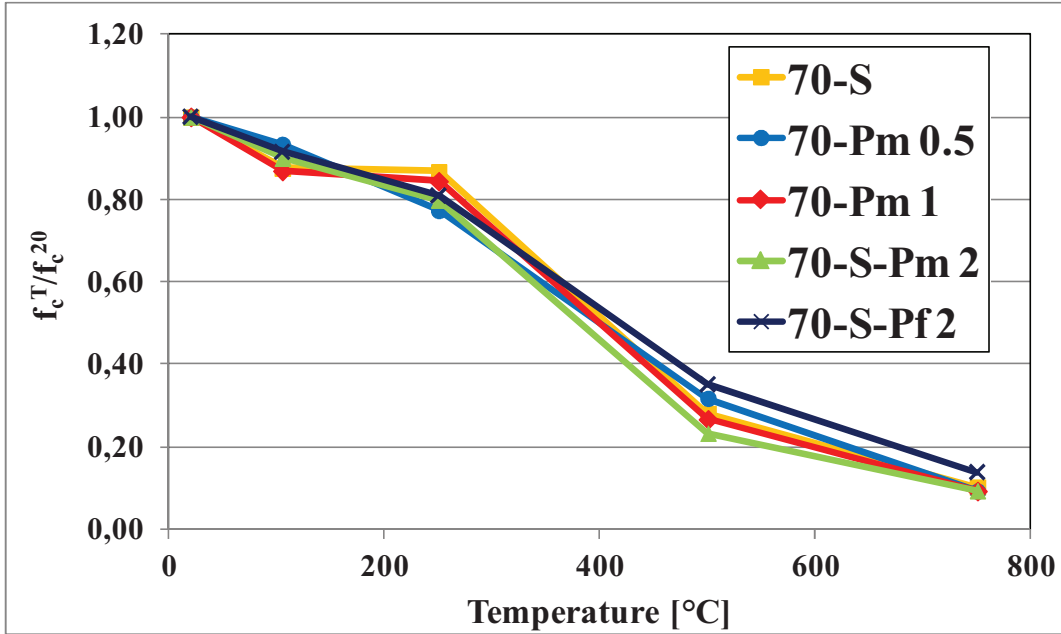


Figure 122: Residual compressive strength as a function of temperature for concrete with different types and contents of PP fibers.

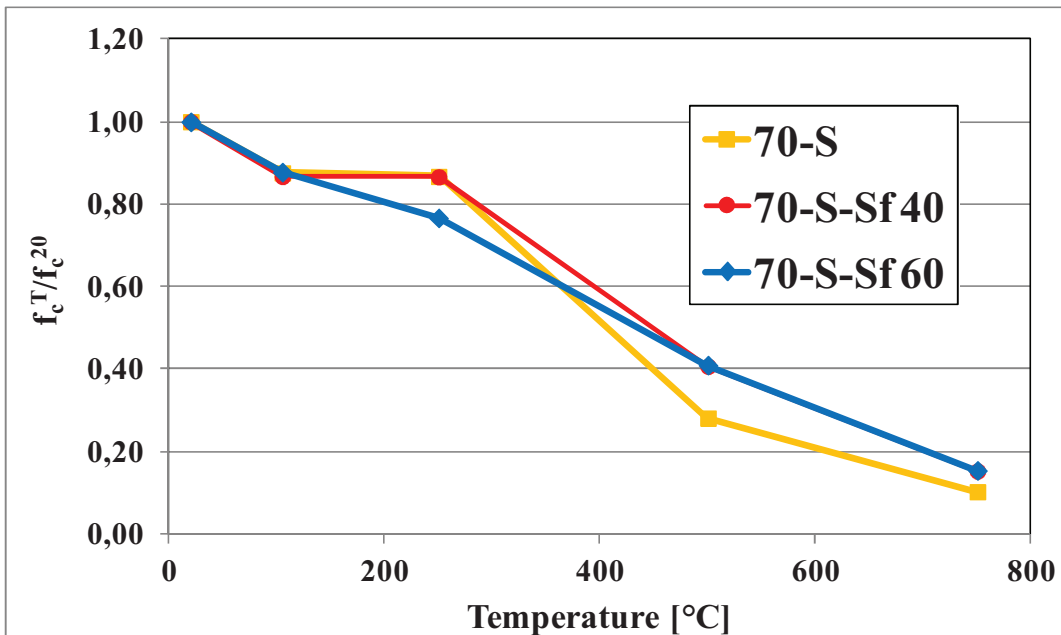


Figure 123: Residual compressive strength as a function of temperature for concretes with different contents of steel fibers.

As already observed from the stress-strain curves, the presence of steel fibers enhances the concrete residual compressive strength after 500°C and 750°C exposures. In case of 250°C

5. EXPERIMENTAL RESULTS

exposure, for 70-S-Sf 60 was detected a lower value in comparison with the others, while in case of 105°C, the data for all the concrete mixes are almost coincident.

In Figure 124 are plotted the previous curves related to the highest PP and steel fibers content mixes compared with 70-S mix. It arises that after 105°C no fiber effect is detected, while after 250°C the presence of both types of PP fibers and steel fibers decreases the residual compressive strength values. At 500°C, only steel fibers enhance the concrete thermal behaviour in comparison with 70-S, while no significant differences are observed after 750°C exposure.

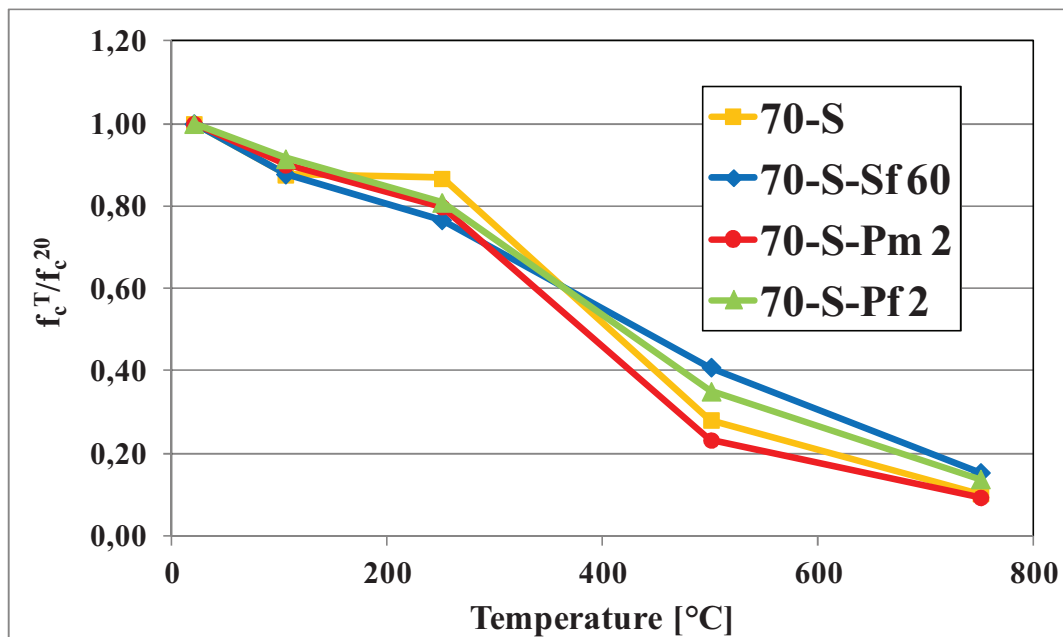


Figure 124: Residual compressive strength as a function of temperature for concretes with highest contents of PP and steel fibers.

5.2.3 Elastic modulus

In the current Paragraph, the trend of residual elastic modulus (as secant modulus considering $\sigma_c = 0.5f_c$, see Paragraph 4.1.3.2) obtained from stress-strain curves, will be shown in function of increasing temperature.

In Figure 125 are plotted the residual elastic modulus values (E_c^T), normalized in function of elastic modulus at 20°C (E_c^{20}) in order to perform a comparison among different concrete grades and different aggregate types.

5. EXPERIMENTAL RESULTS

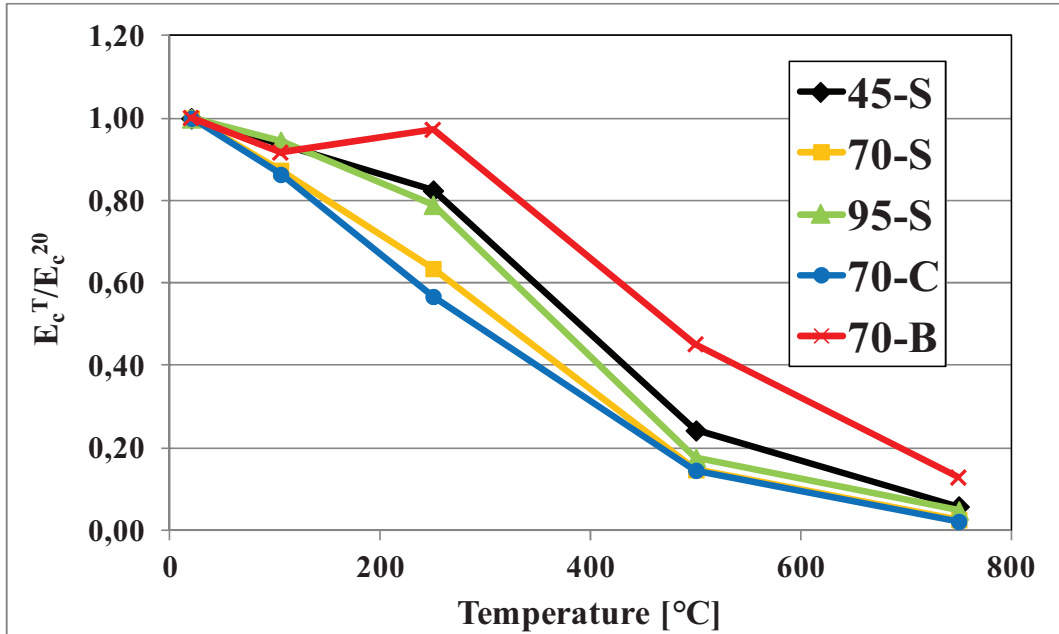


Figure 125: Residual elastic modulus as a function of temperature for different concrete grades and aggregate types.

From Figure 125, it arises that the decay in elastic modulus with increasing temperature is very close considering the 45-S and 90-S mixes, while 70-S seems to be more affected by thermal exposure, because it presents lower values in residual modulus especially after 105 and 250°C exposure.

The concrete containing basalt aggregate shows the less damaged behaviour because it presents an increasing modulus value after 250°C exposure with respect to the one after 105°C and higher values after 500 and 750°C in comparison with the other intermediate grade mixes. The concrete prepared with calcareous aggregate presents a similar behaviour in terms of elastic modulus decay as 70-S.

In order to study the effect of different types and contents of PP and steel fibers on concrete residual elastic modulus, all values have been collected in Figure 126 and compared with 70-S ones, at increasing temperatures.

5. EXPERIMENTAL RESULTS

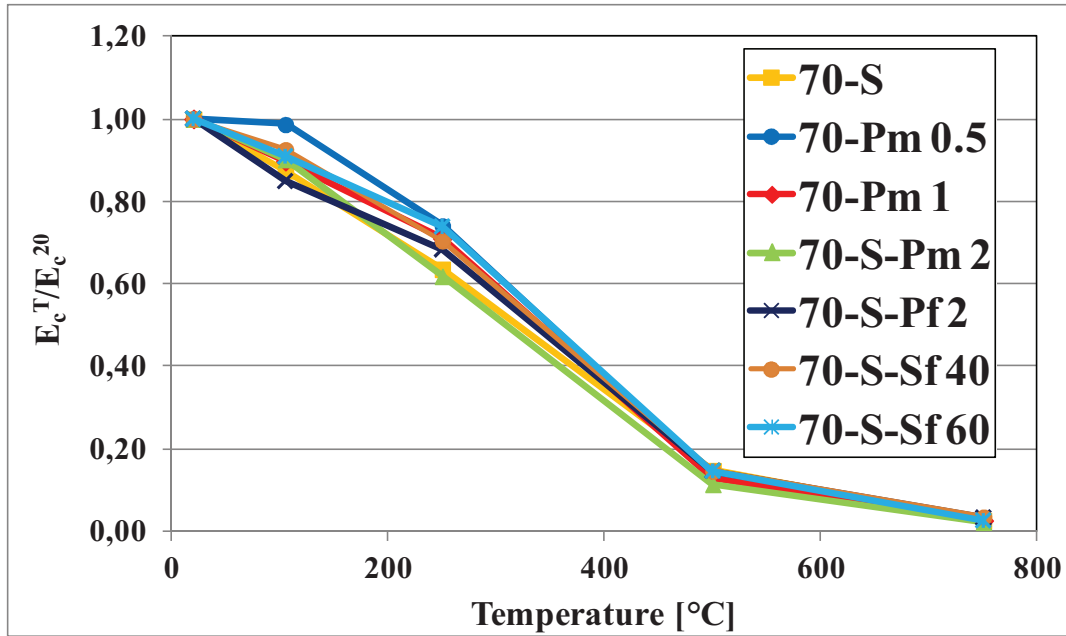


Figure 126: Residual elastic modulus as a function of temperature for concretes with different types and contents of PP and steel fibers.

Considering all the curves in Figure 126 not specific trends are observed. In general terms, the residual values for mixes containing fibers show a slightly better behaviour in comparison with 70-S, presenting higher elastic modulus values, especially after 250°C exposure. No significant differences have been highlighted in presence of different type of PP fibers, as well as in terms of different contents (also in case of steel fibers).

In general terms, the higher the temperature exposure, the lower the residual elastic modulus values, as already seen by other Authors (Phan and Carino, 1998, Felicetti and Gambarova, 1998, Cheng et al., 2004).

5.3 Spalling sensitivity

In the present Paragraph, the experimental results collected for the parameters characterizing the evaluation of explosive spalling will be shown. They are divided between thermal diffusivity determinations (indirectly linked to thermal stresses generating spalling) and pore pressure, splitting and permeability tests (linked to pressure build-up phenomenon).

5. EXPERIMENTAL RESULTS

5.3.1 Spalling due to thermal stresses: diffusivity determination results

The thermal diffusivity tests have been performed according to the procedure explained in Paragraph 4.1.4.1. The results obtained for the different compressive strength grades concrete, as well as the ones with different aggregate type, are collected in Figure 127.

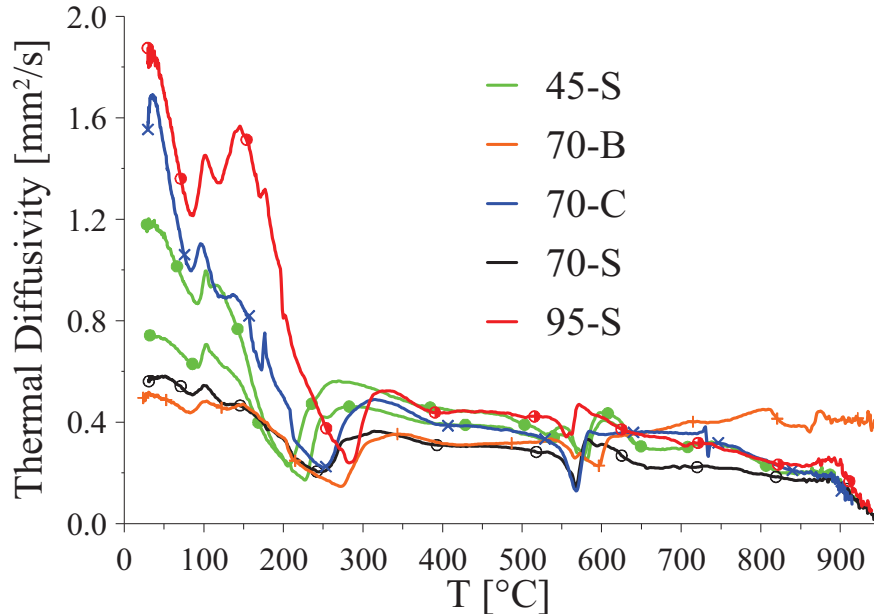


Figure 127: Thermal diffusivity tests for different concrete grades and different aggregate types.

In Figure 127, it can be observed that the peak related to free and bound water, between 105 and 250°C, move towards higher values of temperatures passing from the lowest to the highest compressive strength grade, because of denser cementitious matrix. In case of different aggregates, the peak shift is detected for basalt concrete (70-B) in comparison with the ones with silico-calcareous and calcareous aggregates (70-S and 70-C), very close each other. 70-B mix yields the lowest values than the other intermediate grade, with different aggregate type.

No significant shifts are shown in case of α - β quartz transition (573°C) for all the considered concretes, while is partially visible the onset of calcination after 700°C, except for 70-B.

The effect of PP and steel fibers on thermal diffusivity can be evaluated in Figure 128, in which the related experimental trends are collected.

5. EXPERIMENTAL RESULTS

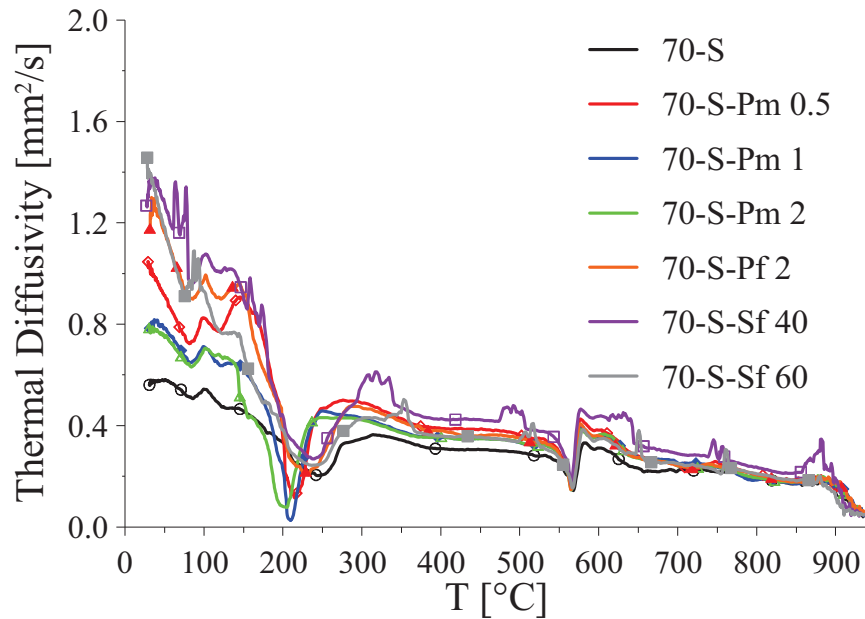


Figure 128: Thermal diffusivity tests for concretes with different types and contents of PP and steel fibers.

From Figure 128, it arises that in presence of PP fibers, the peak related to free and bound water anticipates with respect to those of steel fibers mixes, which are closer to 70-S mix. No marked difference are shown in case of the other transitions.

5.3.2 Spalling due to pressure build-up

In order to characterize the pressure build-up inside the material exposed to thermal action, the pore pressure measurements have been carried out, as well as the ones related to splitting and permeability determinations before and after thermal exposure.

5.3.2.1 Pore pressure measurement results

The temperature and pressure measurements performed on concrete mixes as indicated in Paragraph 4.1.4.2 are collected in Figure 129. The concrete containing steel fibers were not tested because this type of fiber is not expected to have an interesting effect on pore pressure inside the exposed material.

5. EXPERIMENTAL RESULTS

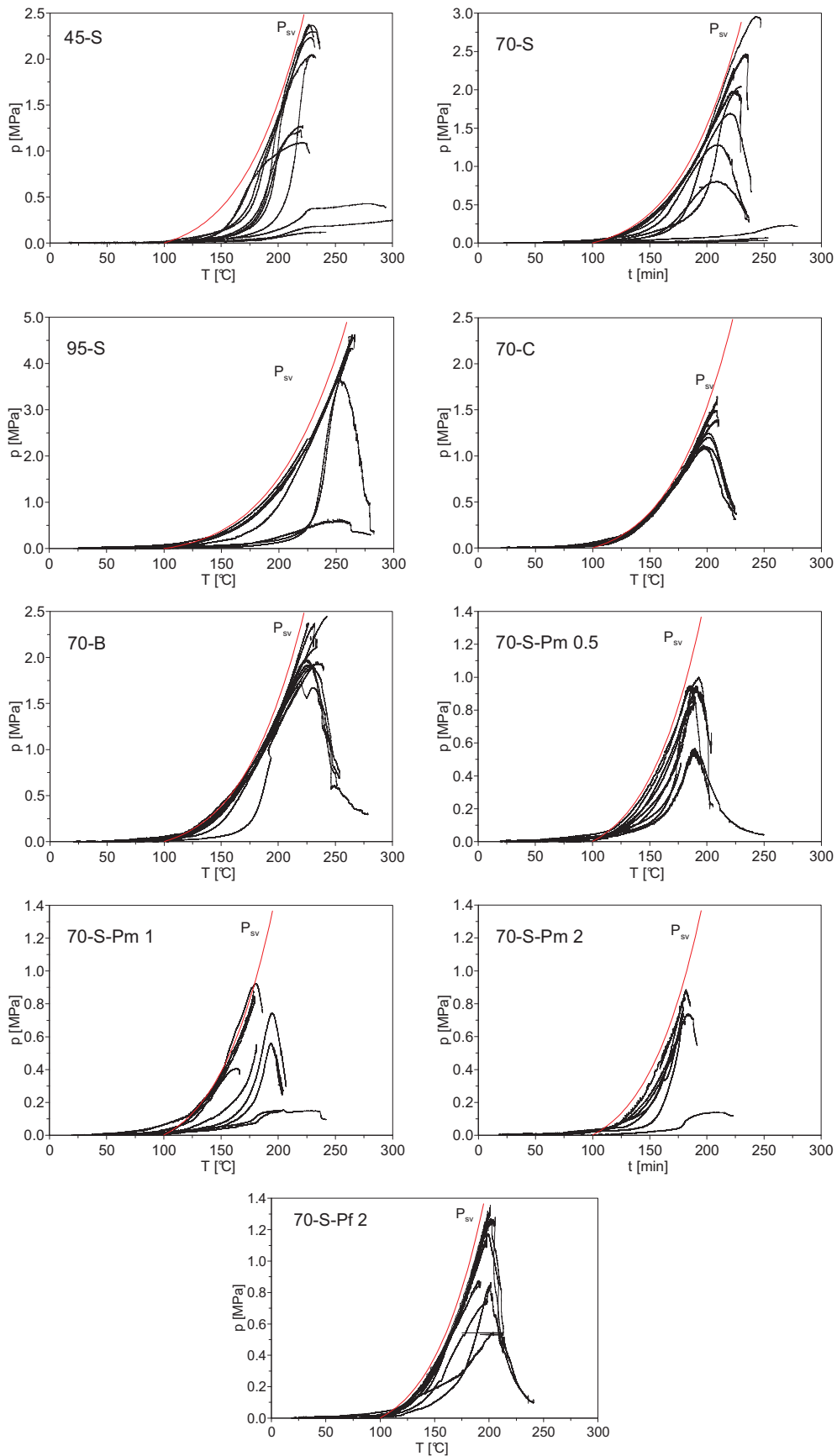


Figure 129: Pore pressure versus temperature trends for each concrete mixes (except the steel fiber mixes).

5. EXPERIMENTAL RESULTS

In order to compare the maximum pressure values, with related temperatures, for the previous concretes, the elaboration in Figure 130 has been carried out.

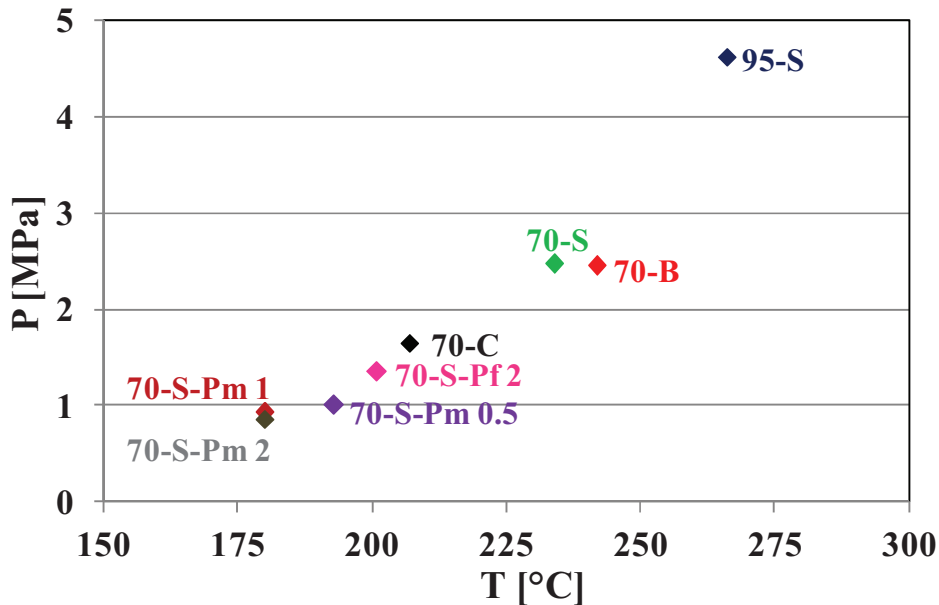


Figure 130: Pore pressure as a function of temperature for concrete mixes.

From Figure 130, it can be observed that the higher the compressive strength grade, the higher the pore pressure inside the material, because of denser matrix. In fact, in case of cementitious matrix characterized by fine microstructure, with low connectivity, the permeability is reduced; as consequence, the vapour escape is restrained and pressure build-up is favored. The 45-S data is not reported in the graph because it has been determined using 2°C/min as heating rate, while for the others 0.5°C/min, thus they can't be compared.

Among different aggregate type, limestone presents the lowest pore pressure.

The presence of monofilament PP fibers significantly decreases the pore pressure, more than the fibrillated ones, confirming the positive effect on reducing the explosive spalling risk. Moreover, the higher the PP monofilament fibers content, the lower the pore pressure, in particular passing from 0.5 to 1 Kg/m³.

From these experimental evidences, it seems that PP monofilament fibers are more indicated in order to reduce explosive spalling risk, and the higher the PP fiber content, the lower the pore pressure inside the material.

5. EXPERIMENTAL RESULTS

5.3.2.2 Splitting test results

The splitting tests have been carried out before and after thermal exposure. In particular, in case of residual measurements, the tests have been performed when maximum pore pressure (P_{lim}) was reached during the pore pressure determinations, as indicated in Paragraph 4.1.4.2.

The splitting tensile strength results at 20°C are collected in Table 31.

Concrete mixes	Splitting tensile strength 20°C (MPa)
45-S	3.98
70-S	4.70
95-S	5.39
70-C	4.57
70-B	4.97
70-S-Pm 0.5	4.71
70-S-Pm 1	4.63
70-S-Pm 2	5.31
70-S-Pf 2	4.89
70-S-Sf 40	6.74
70-S-Sf 60	7.25

Table 31: Splitting tensile strength values at 20°C for all concretes.

From Table 31, it arises that the higher the concrete grade, the higher the tensile strength value, as expected. Considering different aggregate type, the lowest tensile value was detected for 70-C, while the highest for 70-B.

Other important information is obtained considering different PP fibers type: the tensile strength value obtained in case of fibrillated fiber is lower than the one obtained in case of monofilament fibers, maintaining constant their content. Moreover, for 70-S-Pm 2 was detected the highest value among concrete with different PP monofilament fibers contents.

The highest splitting tensile strength among all the considered concretes were measured for the ones containing steel fibers, and the higher the steel fibers content, the higher the value. These results confirm that steel fibers enhance the concrete tensile strength, and this effect is more pronounced increasing the steel fibers content.

The splitting tensile strength has been also detected when the P_{lim} value was reached in the concrete specimens (the mixes containing steel fibres have not be considered, as already indicated in the previous Paragraph). In order to collect the experimental data (indirect tensile strength f_{ct} and

5. EXPERIMENTAL RESULTS

the temperature when it has been measured ($T_{sp} < T_{lim}$), referred to the nine mixes subjected to the test, the Table 32, Table 33 and Table 34 have been prepared. The first contains the splitting test results for the 45-S, which have been detected after heating at 2°C/min, as already reported. The second one collected the data related to 70-S, 70-B and 70-C mixes, as well as 95-S mix. In the third Table are shown the results related to intermediate concrete strength grade concrete containing different types and amount of PP fibers. All the data reported in Table 33 and Table 34 have been detected with heating rate of 0.5°C/min.

45-S specimens	f_{ct} values [MPa]	T_{sp}[°C]
1	3.24	244.2
2	1.62	238.8
3	2.30	234.6
4	2.54	226.1
5	2.87	235.1
6	2.32	244.0
7	2.48	222.6
8	1.72	228.8
9	2.89	241.4
10	1.85	238.6
Average value	2.39	234.5

Table 32: Splitting test values for 45-S mix and related T_{sp}.

70-S		95-S		70-B		70-C	
f_{ct} [MPa]	T_{sp} [°C]	f_{ct} [MPa]	T_{sp} [°C]	f_{ct} [MPa]	T_{sp} [°C]	f_{ct} [MPa]	T_{sp} [°C]
3.89	273.4	3.62	262.8	2.58	230.6	3.26	210.9
3.22	231.3	4.27	266.5	3.92	240.3	2.76	208.1
3.15	223.9	3.57	262.9	2.95	221.9	2.70	209.1
3.03	223.0	3.17	260.5	2.99	242.7	2.70	207.4
3.24	230.8	3.97	262.6	3.87	234.6	3.04	201.0
4.34	237.7	3.57	263.5	3.22	222.0	3.22	201.9
4.73	237.1	4.70	283.6	4.67	278.9	3.61	225.1
3.55	239.5	-	-	3.76	252.5	3.99	223.7
-	-	-	-	3.91	254.9	3.87	226.6
-	-	-	-	3.81	254.4	4.40	226.0
3.64	232.6	3.84	266.1	3.57	243.3	3.36	214.0

Table 33: Splitting test values for 70-S, 95-S, 70-B and 70-C mixes and related T_{sp}.

5. EXPERIMENTAL RESULTS

70-S-Pm 0.5		70-S-Pm 1		70-S-Pm 2		70-S-Pf 2	
f_{ct} [MPa]	T_{sp} [°C]	f_{ct} [MPa]	T_{sp} [°C]	f_{ct} [MPa]	T_{sp} [°C]	f_{ct} [MPa]	T_{sp} [°C]
3.72	188.1	3.98	186.3	3.21	181.1	3.48	202.0
3.22	189.3	3.36	178.9	3.77	180.9	2.83	191.8
3.15	188.5	3.11	179.4	2.99	179.0	2.83	195.6
3.35	184.4	3.24	178.7	2.98	179.3	2.88	201.4
3.17	177.5	3.61	181.2	4.21	192.4	3.30	198.4
4.35	237.4	3.59	207.2	-	-	3.24	204.2
4.18	206.2	3.92	203.2	-	-	4.03	241.4
3.39	203.3	-	-	-	-	3.58	236.7
4.48	205.2	-	-	-	-	3.98	213.7
-	-	-	-	-	-	4.18	214.3
3.67	197.8	3.55	187.8	3.43	182.5	3.43	210.0

Table 34: Splitting test values for 70-S mix containing different types and contents of PP fibers and related T_{sp} values.

In the previous Tables, the average data of f_{ct} and T_{sp} have been calculated in order to have an approximate indication about the trend of results, even if the data are quite dispersed. It can be observed that also at the failure condition, the higher the compressive strength the higher the f_{ct} (comparing 70-S and 95-S). In presence of PP fibers, a small reduction in average f_{ct} data can be seen, which is more pronounced in case of the highest content of fibers. In case of different aggregate types, the highest average f_{ct} value has been detected for 70-S, followed by 70-B and 70-C mixes.

5.3.2.3 Permeability results

Permeability data at 20°C have been detected on the eleven concrete mixes as indicated in Paragraph 4.1.4.3. The average values of permeability ($W_{p,t}$) calculated according to EN 1015-19 (2008) are collected in Table 35.

Concrete mixes	$W_{p,t}$ 20°C (Kg/m·s·Pa)
45-S	$6.47 \cdot 10^{-11}$
70-S	$1.86 \cdot 10^{-11}$
95-S	$4.77 \cdot 10^{-12}$
70-C	$1.49 \cdot 10^{-11}$
70-B	$2.14 \cdot 10^{-11}$
70-S-Pm 0.5	$1.86 \cdot 10^{-11}$
70-S-Pm 1	$1.84 \cdot 10^{-11}$
70-S-Pm 2	$1.48 \cdot 10^{-11}$
70-S-Pf 2	$1.94 \cdot 10^{-11}$
70-S-Sf 40	$1.87 \cdot 10^{-11}$
70-S-Sf 60	$1.53 \cdot 10^{-11}$

Table 35: Permeability data for all concrete mixes at 20°C.

5. EXPERIMENTAL RESULTS

From Table 35, it arises that the higher the compressive strength, the lower the permeability because of more dense cementitious matrix. For intermediate grade, not appreciable differences are observed among the concretes containing different types and contents of fibers, as well as the ones containing different aggregate types.

5. EXPERIMENTAL RESULTS

5.4 Experimental results: concluding remarks

In the light of the previous microstructural and mechanical results, some important considerations concerning the thermal behaviour of HPC can be summarized as follows:

A) Microstructural characterization:

- XRD indicates that two main thermal degradation processes take place in the considered concretes: dehydration and decarbonation, both quantitatively assessed using TGA;
- XRD allows identify the main heat-induced transformations in basic concrete constituents. Increasing temperature leads to CH dehydration and calcite decarbonation, with the formation of CaO (α - β quartz transition has not been detected). Different mineralogic compositions are detected for different aggregate types, before and after heating: basalt aggregate (mix 70-B) shows no significant differences in its mineralogical composition after heating; the only changes are related to the cementitious matrix. After heating to 750°C, mix 70-C exhibits lime as its principal phase (due to decarbonation);
- TGA analysis shows that up to 300°C the mass loss is due to the expulsion of free and bound water and, at almost 450°C, dehydration of CH starts. The largest mass loss is detected for calcareous aggregate due to calcite decarbonation, while no significant one is observed for basalt aggregate;
- Both TGA and XRD allows confirm that PP fibers have no influence on hydrated phases;
- MIP measurements indicate that the higher the concrete grade, the lower the total porosity; pore-radius peaks move towards smaller values, as concrete grade increases. Moreover, the higher the maximum temperature, the higher the total porosity and pore-radius peaks move towards coarser pores, thus the distributions become larger new peaks appear for larger pore diameters (macropores). In the concrete mixes containing polymeric fibers, after heating at 250 and 500°C, some peaks appear in the zone of macropores, as a consequence of melting/degradation of PP fibers;
- SEM observations allow monitor crack pattern evolution with the increasing of exposure temperature. Considering different concrete grades, at 250°C, few microcracks appear, originating mainly at the interface between cement matrix and aggregate; no evidence is found for mix 95-S. More pronounced cracks appear at 500°C, with some bridging between aggregate particles and, at 750°C, cracks are more distributed and wider, which is consistent with very severe thermal field. In the case of different aggregate type, in basalt concrete (70-

5. EXPERIMENTAL RESULTS

B mix), the cracks evolution is strongly limited, even after exposure at 750°C, and only few thin cracks are observed. In calcareous (70-C) and silico-calcareous (70-S) concretes, cracks are wider and more diffused. Moreover, calcareous concrete behaves worse than silico-calcareous one;

- In case of concrete containing PP fibers, after heating, the volume originally occupied by the fibers appears to be empty because of the “channels” left by the fibers, as shown by SEM images, because of their melting and chemical degradation. New microcracks propagating from and through the channels may increase the connectivity of the pores;
- On the basis of XRD and TGA results, it is reasonable to ascribe the increase in porosity and the pore coarsening mainly to the dehydration process in the range of temperature up to 250°C. It is worth nothing that the build-up pressure phenomena take place, as pointed up in the next Paragraph, just in the range of temperature between 200 and 250°C.

B) Mechanical characterization:

- The stress-strain curves have been used to provide the following information:
 - compressive strength;
 - elastic modulus;
 - slope of their descending branches following the maximum load reached during the test.

Owing to high post-peak stiffness of High Strength specimens, the test set-up was not able to detect their complete σ - ε curve, not only for reference temperature (20°C), but also for specimens subjected to thermal exposure (up to 250°C).

The benefit effect of steel fibers has been highlighted by reducing the post-peak stiffness which is reflected in an increase of their toughness.

The mix 95-S exhibits the highest stiffness up to 250°C, while mix 70-B mix becomes the stiffest at higher T; the latter, at and above 250°C, exhibits the highest residual compressive strength, followed by mix 95-S. Moreover, in the same thermal conditions, 70-C mix appears to be the most heat-damaged, especially in terms of both compressive strength and elastic modulus;

- The results concerning the compressive strength and elastic modulus show decay trends at increasing temperature, confirming values found by other Researchers [Phan and Carino, Felicetti and Gambarova, Cheng et al.]. In particular, the lowest grade mix 45-S is less affected than the other silico-calcareous mixes, in terms of both compressive strength and

5. EXPERIMENTAL RESULTS

MES. Basalt aggregate guarantees the best residual (normalized) properties compared to calcareous and silico-calcareous aggregates;

- The measurements of pore pressure (P_{lim}) according to the specific test procedure developed by Politecnico di Milano highlight that the higher the concrete grade, the higher the pore pressure inside the material. Moreover, for the intermediate grade (70 MPa), calcareous aggregate yields a much lower pore pressure, than either basalt or silico-calcareous aggregates. It is also observed that both PP fibers types are very effective in reducing pore pressure, but monofilament ones are slightly better, regardless of their content;
- Regarding thermal diffusivity, the higher the concrete grade, the higher the diffusivity in plain mixes (see mixes 95-S and 45-S, with little differences between 300 and 550°C). Basalt aggregate (mix 70-B) yields lower values than the other intermediate compressive strength, with no fiber. Moreover, steel fibers tend to increase the thermal diffusivity at high temperature, while PP fibers hardly affect the diffusivity, for any fiber content;
- Indirect tensile strength determination by means of splitting test indicate that the higher the concrete grade, the higher the f_{ct} value, both at 20°C and after heating (determined at failure condition). The influence of PP fibers are observed in case of f_{ct} after heating, by a small reduction in average f_{ct} data, which is more pronounced in case of the highest content of fibers;
- Regarding permeability data at 20°C, the higher the compressive strength, the lower the permeability because of more dense cementitious matrix. For intermediate grade, not appreciable differences are observed among the concretes containing different types and contents of fibers, as well as the ones containing different aggregate types.

6. DISCUSSION ON THE EXPERIMENTAL RESULTS

6. DISCUSSION ON THE EXPERIMENTAL RESULTS

In the present Paragraph, the link between microstructural results and mechanical response after thermal exposure has been investigated deepening some peculiar aspects of experimental part.

6.1 Intrinsic and mechanical damage evaluation

As indicated in the previous Paragraphs, the microstructural characterization was carried out by means of several techniques, differing each other according to the provided information. The intrinsic damage due to dehydration processes was monitored by means of XRD and TGA, as well as MIP in the pore radius range up to 10^3 nm. In this pore size interval, it was observed an increase in porosity, caused by dehydration reactions, leading to a shift of pore radius towards higher values. The contribution to intrinsic damage due to thermal incompatibility was monitored by means of both MIP (in a pore radius range above 10^3 nm) and SEM images. Intrinsic damage influences then mechanical properties, monitored by means of σ - ε curves, from which the values of compressive strength and elastic modulus can be derived. The flow-chart coming from the characterization performed on concrete mixes is shown in the following Figure (Figure 131):

6. DISCUSSION ON THE EXPERIMENTAL RESULTS

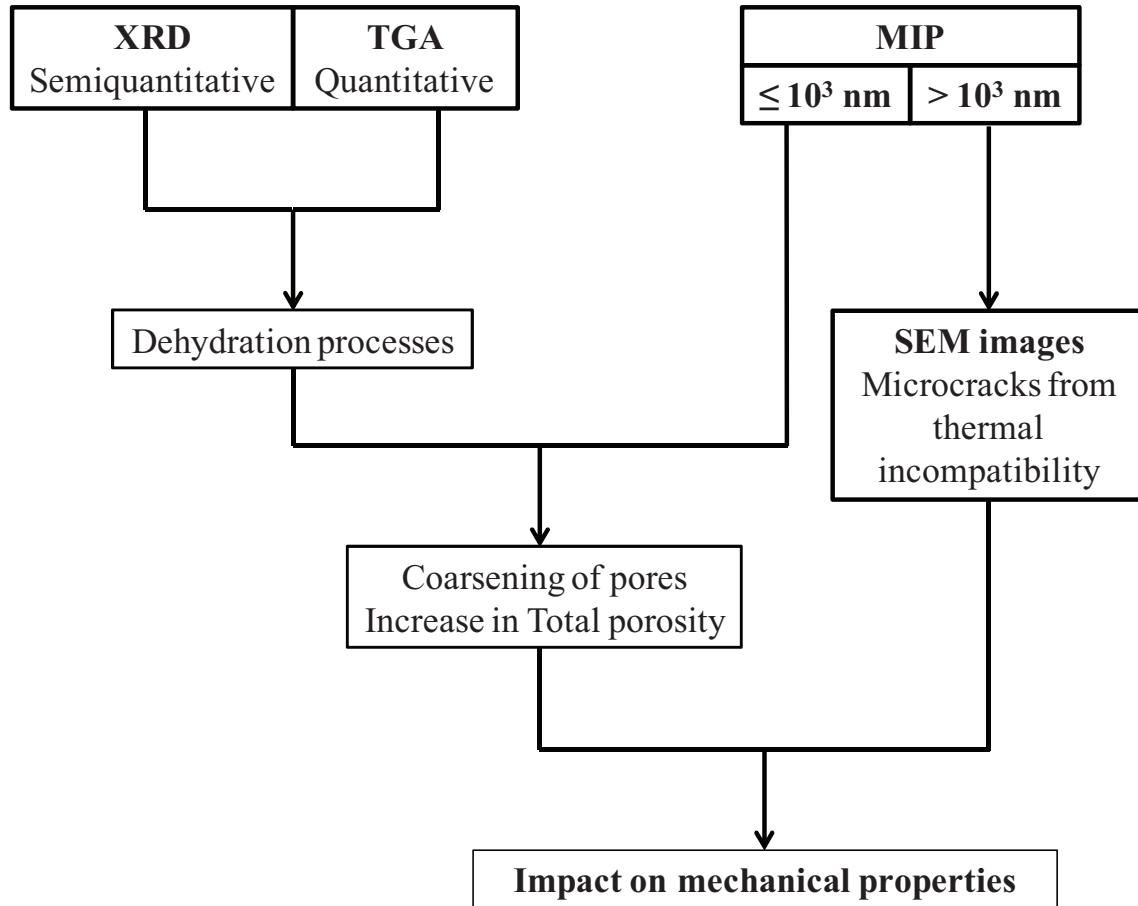


Figure 131: Characterization performed on the concrete mixes.

In order to evaluate porosity variations due to dehydration, the pore radius corresponding to the maximum of the peak in MIP differential distributions at different exposure temperatures are reported in Table 36. Moreover, in Table 37 are collected the total porosity data detected between the pore radius corresponding to the maximum of the peak and the higher one detected by MIP, for increasing exposure temperatures.

T (°C)	Peak Max (nm) 45-S	Peak Max (nm) 70-S	Peak Max (nm) 95-S
20	38	30	15
105	48	38	19
250	77	48	38
500	48	48	38

Table 36: Pore radius corresponding to the maximum of the peak of the three different concrete grades from MIP differential distributions.

6. DISCUSSION ON THE EXPERIMENTAL RESULTS

T (°C)	Por. Peak Max-Higher Radius (%) 45-S	Por. Peak Max-Higher Radius (%) 70-S	Por. Peak Max-Higher Radius (%) 95-S
20	7.54	4.91	5.77
105	7.99	4.83	4.34
250	6.08	5.45	4.67
500	16.06	8.38	8.98

Table 37: Total porosity data detected between the pore radius corresponding to peak maximum and the higher one detected by MIP for the three different concrete grades.

In Table 36, for all strength grades, the higher the temperature exposure, the higher the value of pore radius corresponding to the maximum of the peak, with a shift of the peak towards higher values of pore size. Moreover, the higher the grade, the lower the pore radius values, because of the denser and finer matrix. In Table 37, the most significant contribute in increasing the porosity comes from thermal exposures in excess of 500°C for all concrete grades. This increase is highest for 45-S, while for 70-S and 95-S they are close each other.

In order to evaluate the effect of intrinsic damage on compressive strength and elastic modulus before and after thermal exposure, the related data (detected on cylindrical specimens) have been plotted versus the total porosity at 20°C and after heating, concerning the three concrete grades. The resultant graphic elaborations are reported in Figure 132 and Figure 133, including the regression curves plotted among the experimental data. In case of elastic modulus (Figure 133), the data related to concretes exposed at 500°C have not be included in the regression because, in this residual condition, concrete will no longer have an elastic behaviour; moreover, the circled point in Figure 133 (related to 70-S mix after exposure at 250°C) has been treated as outlier in performing the regression.

6. DISCUSSION ON THE EXPERIMENTAL RESULTS

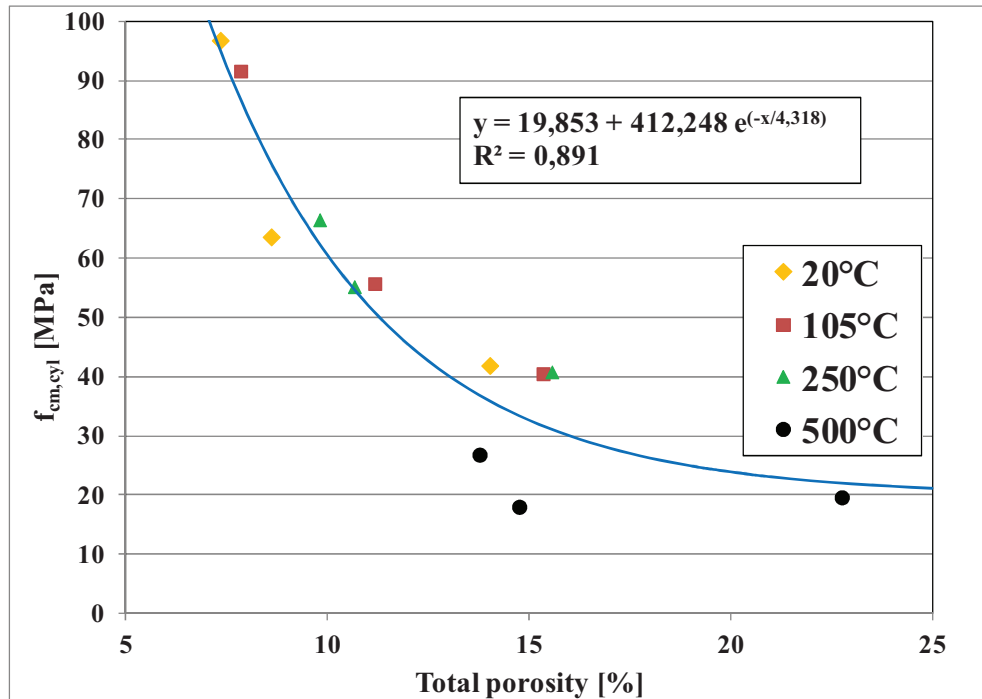


Figure 132: Compressive strength ($f_{cm,cyl}$) as a function of total porosity at 20°C and after heating for different concrete grades.

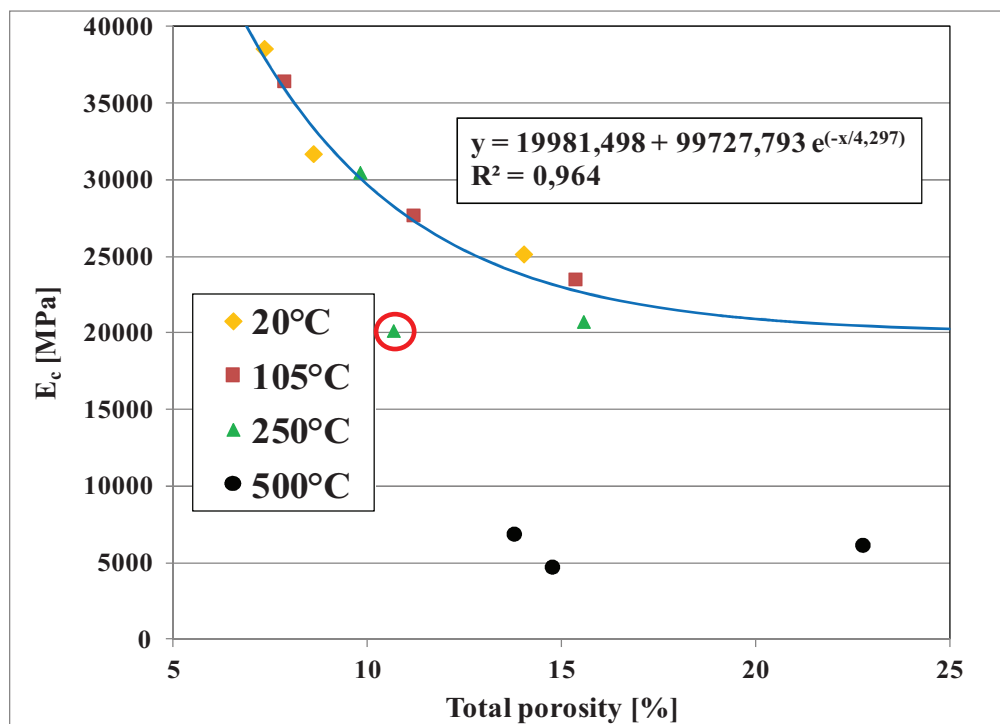


Figure 133: Elastic modulus (E_c) as a function of total porosity at 20°C and after heating for different concrete grades.

In Figure 132 and Figure 133, a good correlation between the mechanical properties and the porosity can be observed, taking into account the results before and after heating. The mechanical

6. DISCUSSION ON THE EXPERIMENTAL RESULTS

decay as a function of the total porosity at increasing exposure temperatures appears to follow an exponential law. This consideration is useful to understand the link between the microstructural and mechanical aspects.

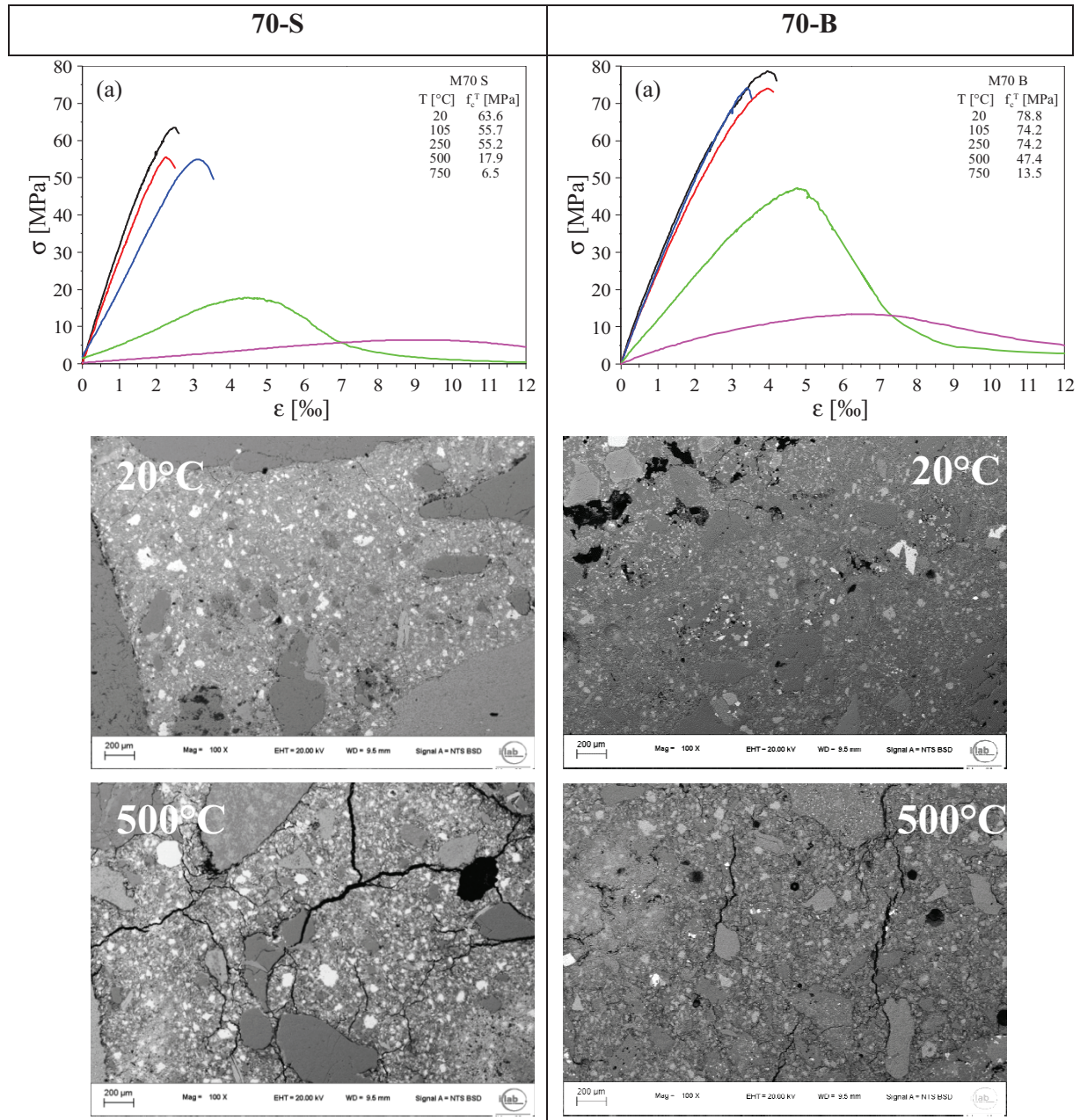


Figure 134: σ - ϵ curves and SEM images for 70-S and 70-B at 20°C and after thermal exposure at 500°C.

An additional evaluation of mechanical properties decay due intrinsic damage concerns the effect of thermal incompatibility between cement matrix and aggregate. This can be monitored by means of post-peak branch in σ - ϵ curves, coupled with SEM images. Significant differences in behaviour were observed for intermediate mixes, prepared with silico-calcareous and basalt

6. DISCUSSION ON THE EXPERIMENTAL RESULTS

aggregates. In this context, the σ - ε curves for 70-S and 70-B at different temperatures are collected in Figure 134, together with the SEM images recorded at 20°C and after exposure at 500°C, in order to show how crack distribution changes as a function of the thermal exposure and aggregate type.

SEM results allowed to identify the appearance of microcracks, whose size is similar to that of macro pores ($>10\mu\text{m}$). From these observations, in Figure 134, 70-B concrete exhibited less microcracking compared with the 70-S one after thermal exposure. This microstructural behavior was in some way reflected by the different post-peak behaviour of the σ - ε curves. Indeed, 70-B mix, presenting very thin microcracks, showed steeper post-peak branch than 70-S one.

The increase in total porosity (f_p) due to thermal exposure has also an impact on vapour pressure build-up inside the concrete pores. Consequently, it is suitable comparing the two groups of data in order to better understand the link between them. In order to perform this, the maximum pore pressure (P_{lim}) detected by means of the set-up described in Paragraph 4.1.4.2, and the residual total porosity data at 250°C detected by MIP, are plotted in Figure 135. The temperature of 250°C has been considered because it is the closest to the ones obtained in correspondence of the maximum pore pressure (T_{lim}); moreover, 45-S is not included in the comparison because it has been tested with a different heating rate (2°C/min instead of 0.5°C/min); also the calcareous and basalt aggregate have not been included because the comparison has been carried out for the aggregate type characterized by the most numerous experimental data, thus silico-calcareous one.

From Figure 135, it arises that a robust exponential relationship exists between P_{lim} and the total porosity (f_p). The exponential trend of the curve indicates that in the range of low porosity values, a little reduction of porosity causes a dramatic increase of P_{lim} . On the other hand, in the same Figure, it is evident the beneficial effect of polymer fibers in reduction of P_{lim} for 70-S concrete specimens.

6. DISCUSSION ON THE EXPERIMENTAL RESULTS

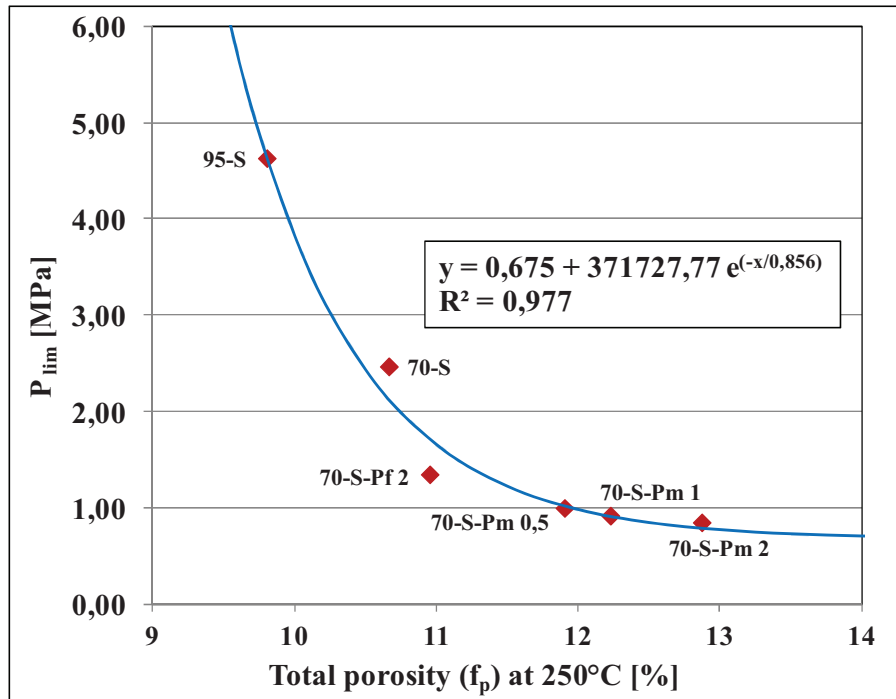


Figure 135: Maximum pore pressure (P_{lim}) versus total porosity (f_p) at 250°C for silico-calcareous mixes.

The high sensitivity of P_{lim} to small variation of f_p (%) in the range of low values of total porosity can be explained as follows.

In Table 38 are collected the P_{lim} and T_{lim} values related to 70-S and 95-S, which differences can be deduced from their different matrix finesses (95-S is characterized by a denser cementitious matrix). On the other hand, it can be observed that total porosity values (f_p) at 250°C are quite close each other, confirming what already mentioned regarding the exponential relationship between P_{lim} and f_p .

Concrete mixes	P_{lim} (bar)	T_{lim} (°C)	f_p (%) 250°C
70-S	24.7	234	10.66
95-S	46.3	266	9.80

Table 38: Maximum pressure (P_{lim}) and temperature (T_{lim}) and total porosity (f_p) at 250°C for 70-S and 95-S mixes.

This apparent discrepancy can be explained by analyzing the related porosity trend at 250°C versus pore radius in terms of cumulative and differential curves.

The first considered curves are the differential ones, related to the three concrete grades (see Figure 136).

6. DISCUSSION ON THE EXPERIMENTAL RESULTS

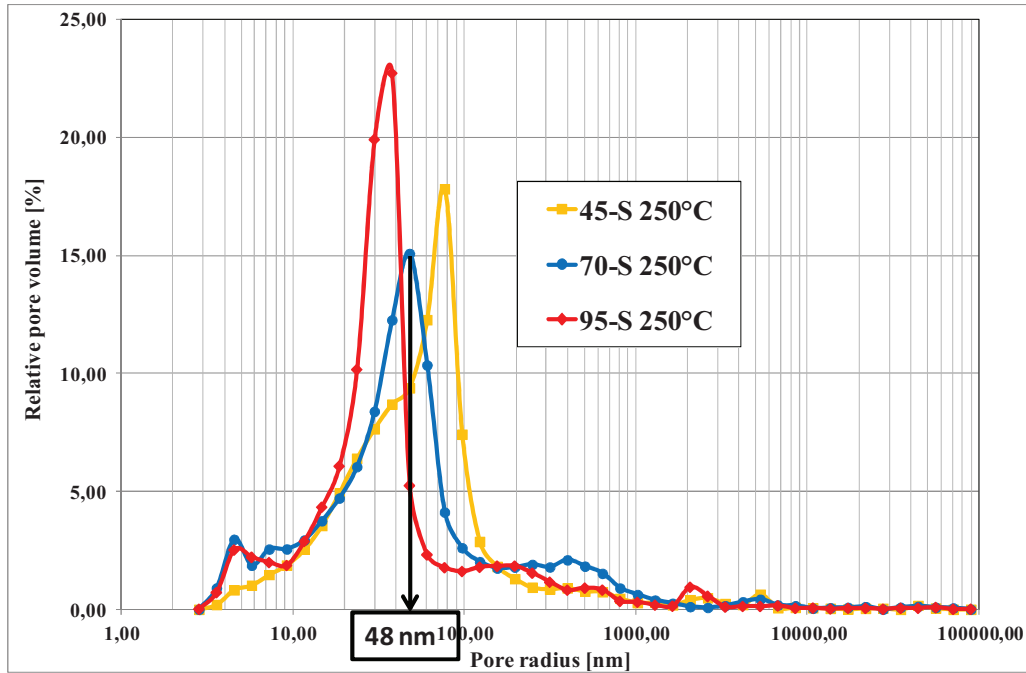


Figure 136 : Differential distributions at 250°C for different concrete grades.

In Figure 136, it can be observed that the curves differentiate each other for the area under the peaks, thus the pore radius distribution. In particular, if the maximum of the peak related to 70-S is considered as reference pore radius (48 nm), the porosity generated by thermal exposure can be evaluated in the pore range up to 48 nm for the 95-S and 70-S by means of cumulative curves, as shown in Figure 137.

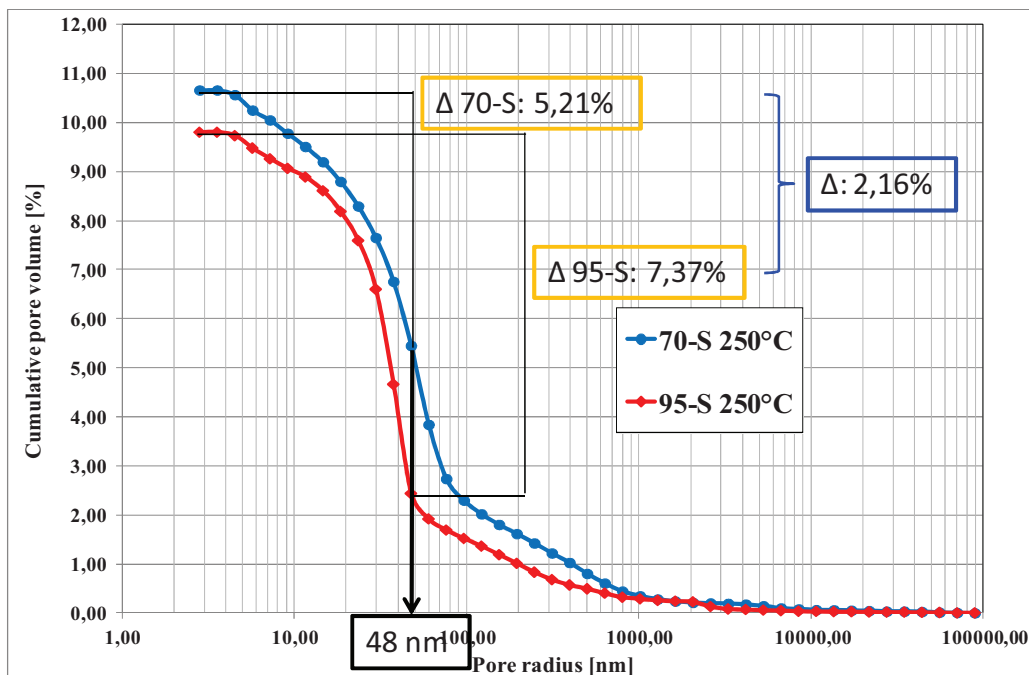


Figure 137: Cumulative distribution at 250°C for 70-S and 95-S mixes.

6. DISCUSSION ON THE EXPERIMENTAL RESULTS

As shown in Figure 137, the pore radius fraction below 48 nm is higher for 95-S (7.37%) in comparison with 70-S (5.21%), thus it arises that the porosity generated by thermal exposure at 250°C is higher for the first mix in this pore range. This means that the higher the concrete grade, the higher the pore radius distribution at lower pore radius, causing higher pore pressure inside the material.

The information acquired is that observing the total porosity and P_{lim} values at increasing concrete grades, in some cases the first parameter may be not sufficient to explain different measured level of pore pressure. It is necessary also to consider the distribution of porosity vs. pore radius, which appears to explain differences in pore pressure build-up. As a consequence, these considerations indicate that an appropriate selection of concrete constituents (type of cement and additions) can contribute to control the increase of pore pressure phenomena.

A comparison in terms of cumulative curves can be also carried out for better understanding the PP fibers mode of action (see Figure 138). In fact, if the cumulative distributions related to silico-calcareous mixes without and with different contents of PP monofilament fibers are compared, some consideration can be reported.

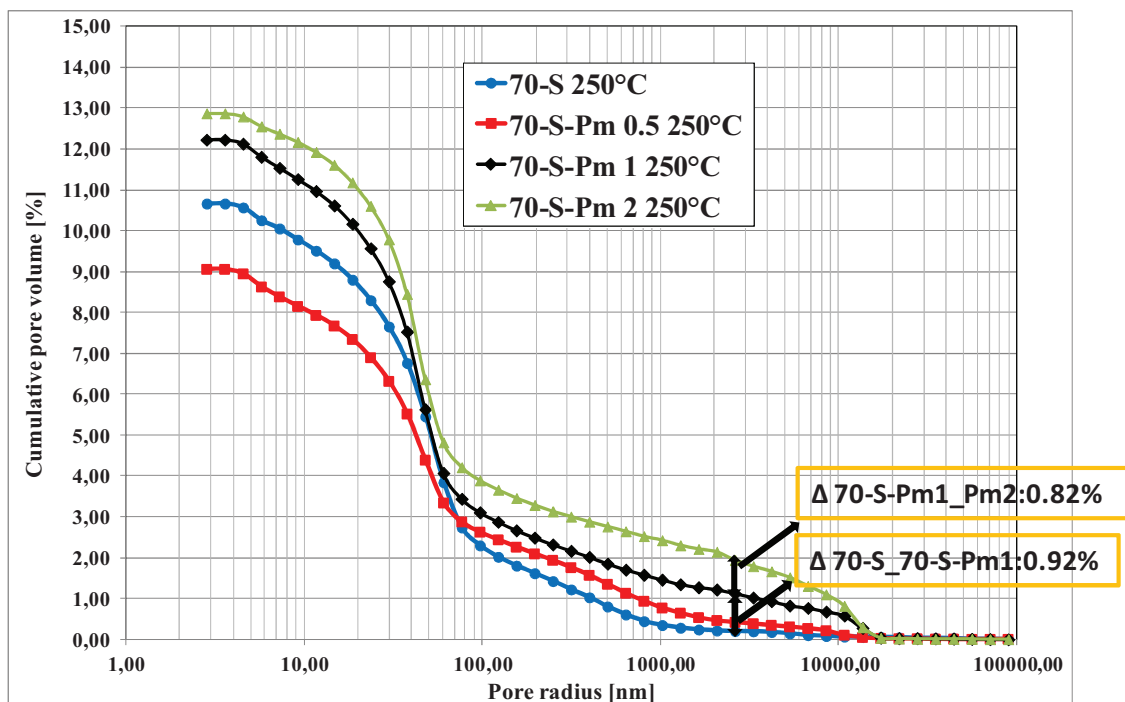


Figure 138: Cumulative distribution at 250°C for silico-calcareous mixes with and without PP monofilament fibers.

6. DISCUSSION ON THE EXPERIMENTAL RESULTS

From Figure 138, it can be observed that the thermal degradation of PP monofilament fibers impacts on the macroporosities. In order to show this effect, in the Figure are reported in porosity differences for pore radius higher than 1000 nm. It arises that the higher the amount of fibers in the mixes, the higher the macroporosities generated in the material, the lower the pressure measured. Comparing the P_{lim} values (Table 39), it arises that adding PP fibers decreases significantly the pore pressure just adding the lowest amount of fibers; the consequence is that increasing the PP content, the pore pressure doesn't decrease in a more significant way, even an increase in porosity in the field of macro porosis detected.

Concrete mixes	P_{lim} (bar)	T_{lim} (°C)
70-S	24.7	234
70-S-Pm 0.5	10.0	193
70-S-Pm 1	9.20	180
70-S-Pm 2	8.50	180

Table 39: P_{lim} and T_{lim} values for silico-calcareous mixes with and without PP monofilament fibers.

6. DISCUSSION ON THE EXPERIMENTAL RESULTS

6.2 Spalling sensitivity assessment

Other considerations can be carried out in the field of concrete spalling, in order to evaluate the sensibility of concrete regarding this phenomenon. It can be evaluate considering its main causes, that are pressure build-up and thermal gradients, that will be the object of the next Paragraphs.

6.2.1 Spalling due to pressure build-up

A theoretical prediction of pore pressure inside the concrete pores can be performed by means of water phase diagrams starting from the specific volume of water generated by thermal exposure, which can be calculated by means of concrete porosimetric data determined in residual conditions.

A “control” unit volume (1 m^3) of concrete ($V_{o,c}$) is considered under the following hypothesis (see Figure 139):

- The pore system is completely interconnected;
- Interface with the external environment totally impermeable to vapour and liquid water (closed volume);
- Constant volume, not influenced by temperature increase;
- Water can be contained in the entire pore radius range detected with MIP technique;
- The porosity increase owing to thermal exposure at 250°C corresponds to the equivalent volume release of bound water (this hypothesis is supported by XRD, TGA and MIP results as previously discussed).

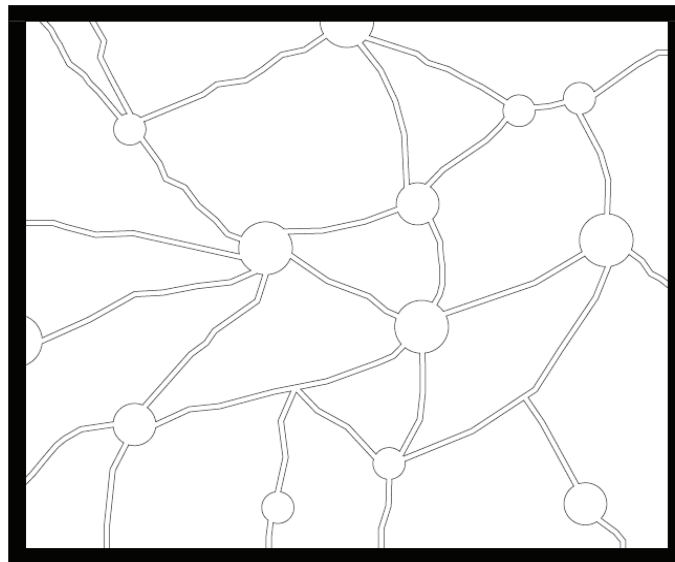


Figure 139: Concrete control unit volume totally insulated from the external environment.

The following quantities can be introduced:

6. DISCUSSION ON THE EXPERIMENTAL RESULTS

- $f_p(T)$ is the volume fraction of pore system referred to $V_{o,c}$;
- the total pore volume (in m^3), referred to the bulk unit volume of concrete $V_{o,c}$ at the temperature T , as $f_p(T) \cdot V_{o,c}$;
- total quantity of water m_w (in Kg) contained at the temperature T in the volume $f_p(T) \cdot V_{o,c}$, as the sum of two contributions, the liquid water ($m_{w,l}$) and the vapour ($m_{w,v}$):

$$m_w(T) = m_{w,l} + m_{w,v} \quad [42]$$

The total quantity of water $m_w(T)$ is also given by the contribution of two terms:

$$m_w(T) = m_{w,free} + m_{w,bound} \quad [43]$$

where $m_{w,free}$ is the free water, while $m_{w,bound}$ is the bound water at temperature T .

The amount of total water $m_w(T)$ is contained in the pore volume of the system $f_p(T) \cdot V_{o,c}$, thus the **specific volume** (m^3/Kg) of the liquid-vapour mixture ($m_w(T)$) is given by:

$$V_{sp}(T) = f_p(T) \cdot V_{o,c} / m_w(T) \quad [44]$$

Once the specific volume $V_{sp}(T)$ is known, as well as the temperature T of the mixture, the corresponding pressure value ($P_w(T)$) can be determined in the P - V_{sp} state diagram for water, known as Clapeyron's diagram, represented in a schematic way in Figure 140 (see Nuovo Colomo, 1997 for tabulated data related to Clapeyron's diagram).

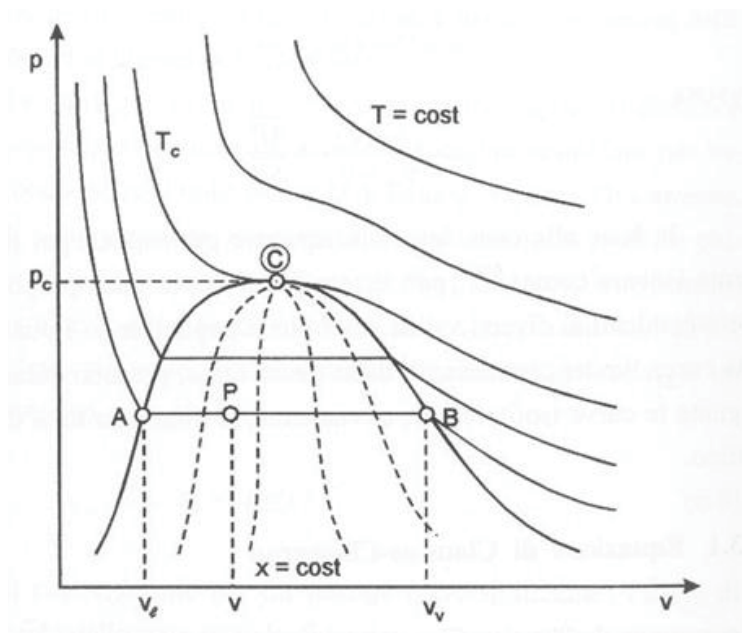


Figure 140: Clapeyron's diagram for water (P - V_{sp} water phase diagram).

6. DISCUSSION ON THE EXPERIMENTAL RESULTS

In Figure 140 is sketched a typical P-V diagram, where the bottom and the upper limit curves are reported (respectively curve A-C and C-B). For an assigned value of V_{sp} (given by Equation [44]) and temperature T it is possible to determine the corresponding pressure value. It is interesting to observe that for temperature values less than the critical value T_c , a range of V_{sp} between the two extreme values V_1 and V_v exists, where pressure and temperature are constant (isothermobaric condition). It is also interesting to note that for V_{sp} values satisfying the condition:

$$V_1(T) \leq V_{sp}(T) \leq V_v(T) \quad [45]$$

a change of V_{sp} doesn't imply any variation in pressure build-up.

It can be also observed that if $V_{sp}(T) \geq V_v(T)$, for increasing values of porosity or decreasing values of $m_w(T)$ the pressure drastically decreases. On the other hand, if $V_{sp,w}(T) \leq V_1(T)$, for decreasing values of porosity or increasing values of $m_w(T)$, the pressure considerably increases.

Under the previous hypothesis and with reference to the closed system $V_{o,c}$, it is possible to define a failure risk, that can be interpreted also as "spalling sensitivity" ($S_{s,o}$), due to pressure build-up at an assigned heating rate adopted for the actual experimental campaign (0.5°C/min).

In fact, in the Clapeyron's plane P-V it is possible to identify a limit curve for the pressure:

$$P_{lim} = P_{lim}(f_p \cdot V_{o,c}) \quad [46]$$

fitting the P_{lim} values measured for concrete mixes having different total porosity and specific volume V_{sp} of water mixture.

For thermodynamic conditions of water mixture (liquid+vapour) in the pore system of $V_{o,c}$, that satisfy the basic condition:

$$P_w(T) < P_{lim} \quad [47]$$

where $P_w(T)$ is the equilibrium pressure at a given temperature T and specific volume $V_{sp}(T)$, no failure should take place at less than statistical considerations.

On this basis, it is possible to define a local (referred to $V_{o,c}$) risk of failure $S_{s,o}$, which can be interpreted as spalling sensitivity index:

$$S_{s,o} = P_w(T) / P_{lim} \quad [48]$$

6. DISCUSSION ON THE EXPERIMENTAL RESULTS

If:

- $S_{s,0} \geq 1$: the system is not able to sustain the $P_w(T)$ at a specific temperature exposure, thus failure occurs;
- $S_{s,0} < 1$: the system is in a “safe” condition.

In order to explore the context regarding spalling risk, the silico-calcareous mixes have been considered. In particular, it has been taken into account that:

- 45-S mix has not been included because its maximum pore pressure was detected with a higher heating rate ($2^\circ\text{C}/\text{min}$) in comparison with the one used for the other mixes ($0.5^\circ\text{C}/\text{min}$);
- The mixes containing steel fibers were not considered because for them the P_{lim} was not detected (see Paragraph 5.3.2.1);
- The total porosity values for 70-S-Pm 0.5 mix has been corrected because its trend at increasing temperature appeared as anomalous in comparison with the other (Figure 106) The corrected total porosity values have been obtained by interpolation from the initial porosity value and the one at 500°C and are indicated in Table 40;
- The free water, intended as concrete moisture content, is conventionally determined by measuring the mass loss of the specimens heated at 105°C until the constant mass is reached. In this experimental campaign these data are not available (•); the only available and the most closest to free water definition are referred to MIP results, where this information can be derived from the porosity generated after thermal exposure at 105°C . It is reasonable consider that the real moisture is probably higher than the one obtain by MIP, because with this technique is not possible to monitor the porosity under a lower limit of pore radius (which is instead included in the one detected at 105°C).

The calculation of specific volume has been carried out considering the temperature T as 250°C because it is the closest to the ones obtained in correspondence of the maximum pore pressure (T_{lim}).

Even if the free water ($m_{w,\text{free}}$) content in concrete specimens is not available, in any case this quantity has been considered negligible despite being aware that it is an approximation. The consequence is that the only kind of water included in the calculation [43] is the bound water ($m_{w,\text{bound}}$), which is released after thermal exposure at 250°C from cementitious matrix in the pore

6. DISCUSSION ON THE EXPERIMENTAL RESULTS

volume available at 250°C. It can be calculated starting from the difference between the porosity at 20°C and 250°C, and then considering the water (liquid) density at 250°C (798.7 Kg/m³), as follows:

$$m_{w, \text{bound}} (\text{Kg}) = [\Delta f_p (20\text{-}250^\circ\text{C}) \cdot \rho_{w,l} (250^\circ\text{C})] \cdot V_{o,c} \quad [49]$$

The $m_{w, \text{bound}}$ obtained for considered concrete mixes, as well as the volume available for water ($f_p(T) \cdot V_{o,c}$), are collected in Table 40.

Concrete mixes	$f_p(250^\circ\text{C}) \cdot V_{o,c} (\text{m}^3)$	$\Delta f_p(\%) (20\text{-}250^\circ\text{C})$	$m_{w,\text{bound}} (250^\circ\text{C}) (\text{Kg})$
70-S	0.1066	2.0649	16.49
95-S	0.0980	2.4665	19.70
70-S-Pm 0.5 (corr.)	0.1190	2.3178	18.51
70-S-Pm 1	0.1223	3.0971	24.74
70-S-Pm 2	0.1287	4.4968	35.92
70-S-Pf 2	0.1095	2.2882	18.28

Table 40 : Available pore volume ($f_p(250^\circ\text{C}) \cdot V_{o,c}$), porosity increase ($\Delta f_p(\%)$) between 20 and 250°C and bound water amount ($m_{w,\text{bound}}$) for silico-calcareous concrete mixes (considered totally dried).

Considering the $m_{w, \text{bound}}$ and $f_p(250^\circ\text{C}) \cdot V_{o,c}$ values in Table 40, the specific volume values at 250°C can be calculated and collected in Table 41.

Concrete mixes	$V_{sp,w} (250^\circ\text{C}) (\text{m}^3/\text{Kg})$
70-S	0.006466
95-S	0.004976
70-S-Pm 0.5 (corr)	0.006430
70-S-Pm 1	0.004943
70-S-Pm 2	0.003584
70-S-Pf 2	0.005993

Table 41: Specific volume at 250°C values for silico-calcareous concrete mixes (considered totally dried).

Once the specific volume calculated at 250°C is known, as well as the temperature (T_{lim}) corresponding to maximum pore pressure P_{lim} (experimentally detected), it can be possible to evaluate if the calculated specific volume is comprised or not in the range $V_1(T) - V_v(T)$, obtained

6. DISCUSSION ON THE EXPERIMENTAL RESULTS

from the water P-V diagram at T_{lim} . The T_{lim} , as well as the $V_l (T_{lim})$ and $V_v (T_{lim})$ values are reported in Table 42.

Concrete mixes	$T_{lim} (°C)$	$V_l (T_{lim}) (m^3/Kg)$	$V_v (T_{lim}) (m^3/Kg)$
70-S	234	0.0012163	0.06663
95-S	266	0.0012941	0.03753
70-S-Pm 0.5 (corr.)	193	0.0011464	0.1459
70-S-Pm 1	180	0.0011274	0.1943
70-S-Pm 2	180	0.0011274	0.1943
70-S-Pf 2	201	0.0011586	0.1237

Table 42: T_{lim} , $V_l (T_{lim})$ and $V_v (T_{lim})$ values for silico-calcareous concrete mixes.

Comparing the calculated specific volume with the $V_l (T_{lim})$ and $V_v (T_{lim})$ values in Table 42, it arises that $V_l (T_{lim}) \leq V_{sp} (250°C) \leq V_v (T_{lim})$, thus vapour and liquid coexist in the pore volume available after thermal exposure at 250°C. At this point, for each mix, the pressure value in correspondence to T_{lim} can be derived from the Clapeyron's diagram ($P_w(T_{lim})$). These values are collected in Table 43 together with the P_{lim} experimentally detected. In the same Table, the spalling sensitivity $S_{s,o}$ values are reported. It can be observed that $S_{s,o}$ is higher than 1 for all the concrete mixes, confirming the evidence that for the considered specimens the thermodynamic condition $P_w(T_{lim})$ overcomes the P_{lim} at failure, as expected.

Concrete mixes	$P_w(T_{lim}) (MPa)$	$P_{lim} (MPa)$	$S_{s,o}$
70-S	3.0	2.47	1.21
95-S	5.5	4.63	1.19
70-S-Pm 0.5	1.4	1.0	1.40
70-S-Pm 1	1.0	0.92	1.09
70-S-Pm 2	1.0	0.85	1.18
70-S-Pf 2	1.6	1.35	1.19

Table 43: $P_w(T_{lim})$, P_{lim} and $S_{s,o}$ values for silico-calcareous concrete mixes.

In order to represent graphically the specific volume in function of $P_w(T)$ and P_{lim} values, the Figure 141 has been drawn, showing the reference P- V_{sp} curves for saturated liquid (curve on the left) and vapour (curve on the right), as well as the calculated V_{sp} values in function of the two different indicated pressure.

6. DISCUSSION ON THE EXPERIMENTAL RESULTS

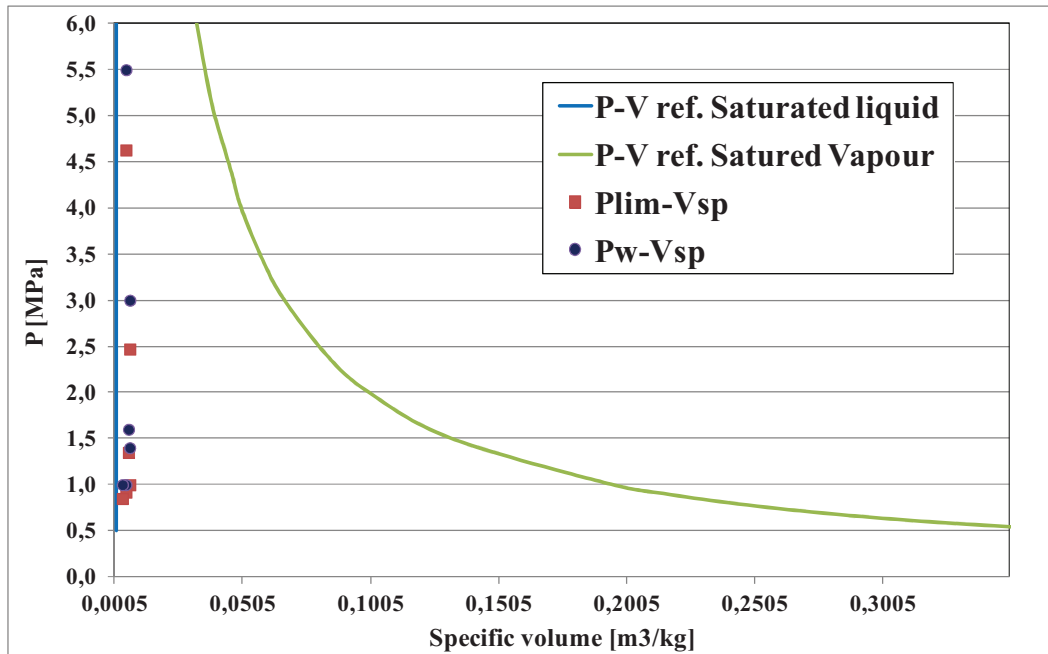


Figure 141: Specific volume V_{sp} versus P_{lim} and $P_w(T_{lim})$ of silico-calcareous concrete mixes, comprising the saturated liquid and vapour curves.

The Clapeyron's diagram zone where the P_{lim} and $P_w(T_{lim})$ values are present is better visualized by making a zoom of previous image (Figure 142).

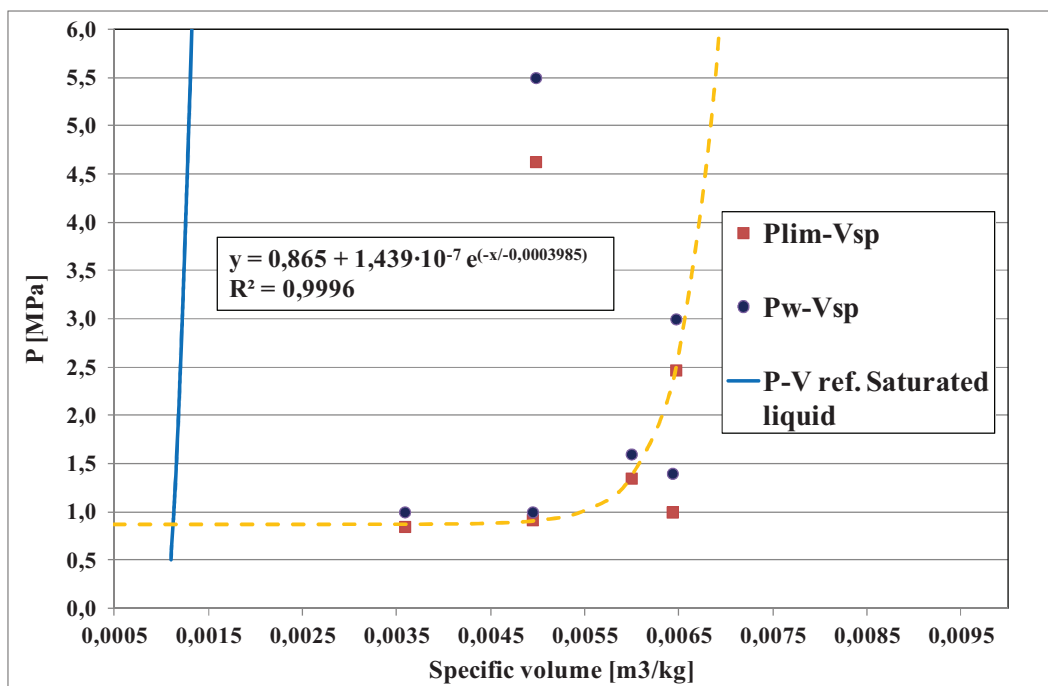


Figure 142: Close-up of specific volume V_{sp} versus P_{lim} and $P_w(T_{lim})$ of silico-calcareous concrete mixes, comprising the saturated liquid curve.

6. DISCUSSION ON THE EXPERIMENTAL RESULTS

In Figure 142, a regression curve has been plotted among the $P_{lim}-V_{sp}$ values, excluding the ones related to 95-S and 70-S-Pm 0.5 concretes, considered as outliers. This fitting suffers from low number of experimental data and this trend should be confirmed by an appropriate number of repetitions. However, this trend is supported by a good fitting between P_{lim} and Total porosity, as already shown in Figure 135; in order to pass from P_{lim} -Total porosity to $P_{lim}-V_{sp}$ trend, it is therefore necessary to acquire the porosimetric data, that should be further checked.

For the concrete mixes which corresponding values have been included in the regression curve $P_{lim}-V_{sp}$, this can represent the failure condition, below which the systems can be considered in a “safe” condition where the spalling sensitivity index $S_{s,o} < 1$.

An additional consideration can be done regarding the specific volume, and in particular the calculation of the difference between the calculated one and the specific volume of liquid intercepted in the reference saturated liquid curve at the same temperature. These values, including their difference, are collected in Table 44.

Concrete mixes	V_{sp} (250°C) (m ³ /Kg)	V_1 (T _{lim}) (m ³ /Kg)	V_{sp} (250°C) - V_1 (T _{lim}) (m ³ /Kg)	Water to reach saturated liquid curve (%)
70-S	0.006466	0.0012163	0.00525	0.178
95-S	0.004976	0.0012941	0.00368	0.115
70-S-Pm 0.5	0.006430	0.0011464	0.00528	0.192
70-S-Pm 1	0.004943	0.0011274	0.00382	0.142
70-S-Pm 2	0.003584	0.0011274	0.00246	0.092
70-S-Pf 2	0.005993	0.0011586	0.00483	0.174

Table 44: V_{sp} calculated and from reference saturated liquid curve and their difference for silico-calcareous concrete mixes.

The difference in specific volume determined in Table 44 constitutes the quantity of water that can be added to concrete in order to reach the saturated liquid curve. This limit should be taken into account because if the volume of water present in concrete is equals to that this specific volume limit, its value will be place in the over-saturated liquid zone of P-V diagram. In this part of the diagram, high increases in pressure correspond to small reductions in specific volume, thus this condition must be prevented in order to avoid failure.

6. DISCUSSION ON THE EXPERIMENTAL RESULTS

It is also important to underline that in real conditions, the accessible porosity is probably higher than the one considered in this calculation for the above mentioned reasons, thus the real V_{sp} will also be higher. This means that the range of water needed to reach the saturated liquid curve will be enlarged, permitting the addition of higher quantity of water to concrete (also coming from the storage condition), without occurring in failure spalling.

Starting from the previous elaboration, it is convenient to define more suitable parameters from the technological point of view, which are the follows:

- **Saturation degree (γ_s)**, at the temperature T, as the ratio between the volume (V) of water, which is present in the pores, and the accessible volume of pore. Its values are included between 0 and 1 and can be expressed as:

$$\gamma_s(T) = V \text{ water at temp. } T / \text{Total } V \text{ pores at temp. } T \quad [50]$$

- **Moisture content (U%)**, as the ratio between the the mass of water present in the concrete at 20°C and the one related to concrete (at 20°C) and it can be expressed as:

$$U\% = \text{Mass of water} / \text{Mass of concrete} \quad [51]$$

In order to correlate the previous parameters, the following relations are introduced and illustrated.

First of all, the definition of the specific volume V_{sp} is re-proposed (for $V_{o,c} = 1 \text{ m}^3$):

$$V_{sp}(T) = f_p(T) \cdot V_{o,c} / m_w(T) = (f_{p,0} + \Delta f_p(T)) / (m_{w,free} + m_{w,bound}) \quad [52]$$

where:

- $f_{p,0}$ is the total porosity at 20°C;
- $\Delta f_p(T)$ is the porosity increase between 20°C and the temperature T;
- $m_{w,bound} = \Delta f_p(T) \cdot \rho_w(T)$

Thus, the expression [52] can be explicitade as follows:

$$V_{sp}(T) = (f_{p,0} + \Delta f_p(T)) / (m_{w,free} + \Delta f_p(T) \cdot \rho_w(T)) \quad [53]$$

The saturation degree γ_s can be than expressed as:

$$\gamma_s(T) = ((m_{wf,0} \cdot \rho_w(T)^{-1}) + \Delta f_p(T)) / [f_{p,0} + \Delta f_p(T)] \quad [54]$$

6. DISCUSSION ON THE EXPERIMENTAL RESULTS

From equation [54] the total volume of pores ($f_{p,0} + \Delta f_p(T)$) at the temperature T can be derived:

$$f_{p,0} + \Delta f_p(T) = ((m_{wf,0} \cdot \rho_w(T)^{-1}) + \Delta f_p(T)) / \gamma_s(T) \quad [55]$$

Substituting the equation [55] in the expression [53] of V_{sp} , it can be obtained that:

$$V_{sp}(T) = [(m_{wf,0} \cdot \rho_w(T)^{-1}) + \Delta f_p(T) / \gamma_s(T)] \cdot 1 / (m_{wf,0} + \Delta f_p(T) \cdot \rho_w(T)) \quad [56]$$

Multiplying by $\rho_w(T)$ both the numerator and the denominator, V_{sp} can be expressed as:

$$V_{sp}(T) = [(m_{wf,0} + \Delta f_p(T) \rho_w(T)) / \gamma_s(T) \cdot \rho_w(T)] \cdot 1 / (m_{wf,0} + \Delta f_p(T) \cdot \rho_w(T)) \quad [57]$$

After the simplifications, it arises that:

$$V_{sp}(T) = 1 / [\gamma_s(T) \cdot \rho_w(T)] \quad [58]$$

At this point, the definition of moisture content (U%) at 20°C can be introduced:

$$U\% (20^\circ\text{C}) = \text{Mass of water} / \text{Mass of concrete} = m_{wf,0} / \rho_c(20^\circ\text{C}) \quad [59]$$

Substituting the expression [59] in the $\gamma_s(T)$ definition [54], the relationship between the saturation degree γ_s and moisture content U% can be obtained:

$$\gamma_s(T) = [(U\% (20^\circ\text{C}) \cdot \rho_c(20^\circ\text{C}) \cdot \rho_w(T)^{-1}) + \Delta f_p(T)] / [f_{p,0} + \Delta f_p(T)] \quad [60]$$

From expression [58] and once the following parameters are known:

- U% at 20°C;
- ρ_c at 20°C;
- $\rho_w = \rho_w(T)$, tabulated (not reported for the purposes of the present work);
- $f_{p,0}$ at 20°C;
- $\Delta f_p(T)$ from MIP measurements

$\gamma_s(T)$ can be calculated, and consequently $V_{sp}(T)$ as well as $P_w(T)$ from Clapyeron's plane (P- V_{sp}).

6. DISCUSSION ON THE EXPERIMENTAL RESULTS

From the discussion carried out in this Paragraph, the following indications can be drawn regarding the spalling sensitivity of concrete mixes:

- For a given value of temperature, the specific volume should be as high as possible (the optimal condition is $V_{sp,w}(T) \geq V_v(T)$), to have the lowest value of $P_w(T)$. This can be obtained by increasing concrete porosity and/or decreasing moisture content. On the other hand, increasing the porosity may generally lead to a decrease in the tensile strength which is reflected by the value of P_{lim} too much lower than $P_w(T)$. For this reason, knowing the relationship $P_{lim} = P_{lim}(f_{ct})$ plays a fundamental role;
- In case of mixes containing PP fibers, because of the opening of new macropores at about 250°C due to the PP fibers melting, the f_p increases without an equivalent release of water from the surrounding matrix. This mechanism leads to an increase in V_{sp} , (which does not correspond to an equivalent release of water from surrounding pores) with a subsequent reduction of the pressure build-ups and a decrease of the spalling risk.

The main phases of the above-mentioned discussion, regarding concrete spalling assessment, are summarized in the flow diagram in Figure 143.

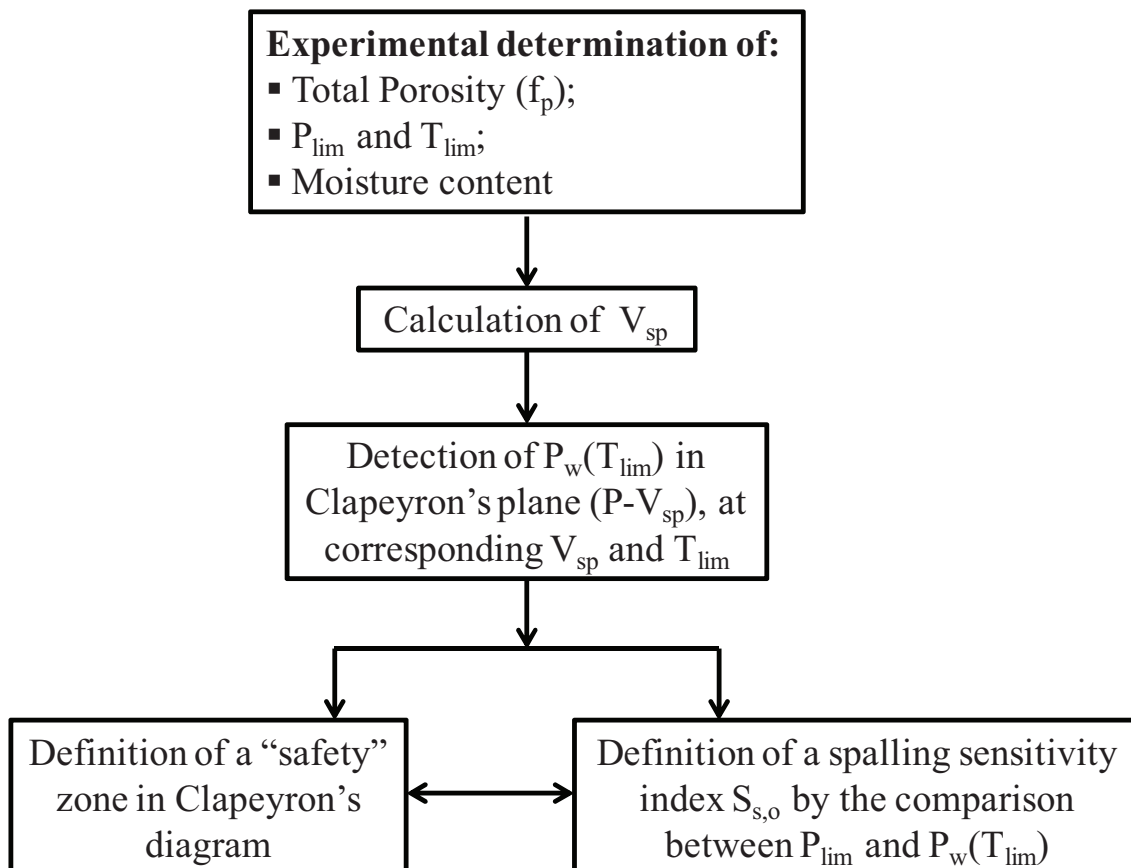


Figure 143: Main phases of concrete spalling assessment (from experimental results discussion).

6. DISCUSSION ON THE EXPERIMENTAL RESULTS

6.2.2 Generalization of the problem of pressure build-up taking into account the mass transport processes

The experimental results obtained from the measurement of the maximum pore pressure (P_{lim}) and of the related temperature (T_{lim}) can be plotted in a P-T diagram, in order to make a comparison with a reference P-T water curve taken from the thermodynamic tables (see Figure 144).

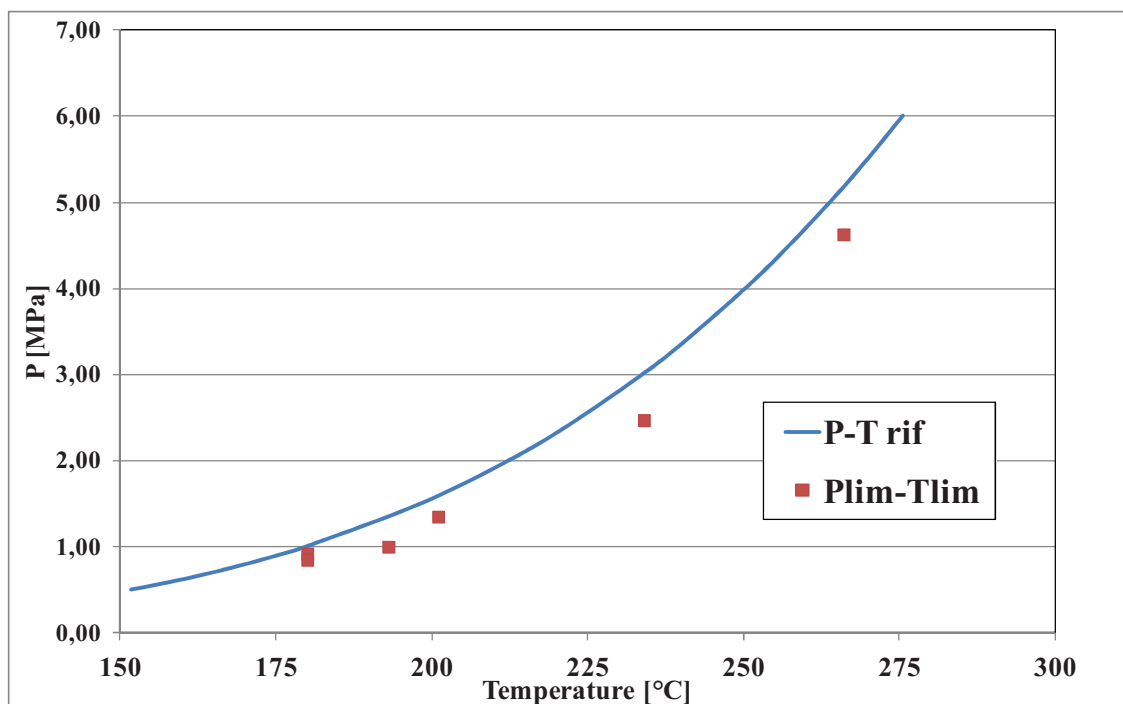


Figure 144: Reference Pressure-Temperature curve and Pressure-Temperature values obtained by experimental set-up for pore pressure measurement.

In Figure 144, it can be observed that P_{lim} values are distributed under the reference P-T curve, and the mutual differences increase for increasing values of T_{lim} . These differences are to be ascribed to the simplified assumption concerning the “closed” reference unit volume. In the test conditions for pore pressure measurement (see Paragraph 4.1.4.2), the concrete specimens are open to the outside environment, as shown in Figure 145. Hence vapour escapes from the concrete mass with a consequent pressure release.

6. DISCUSSION ON THE EXPERIMENTAL RESULTS

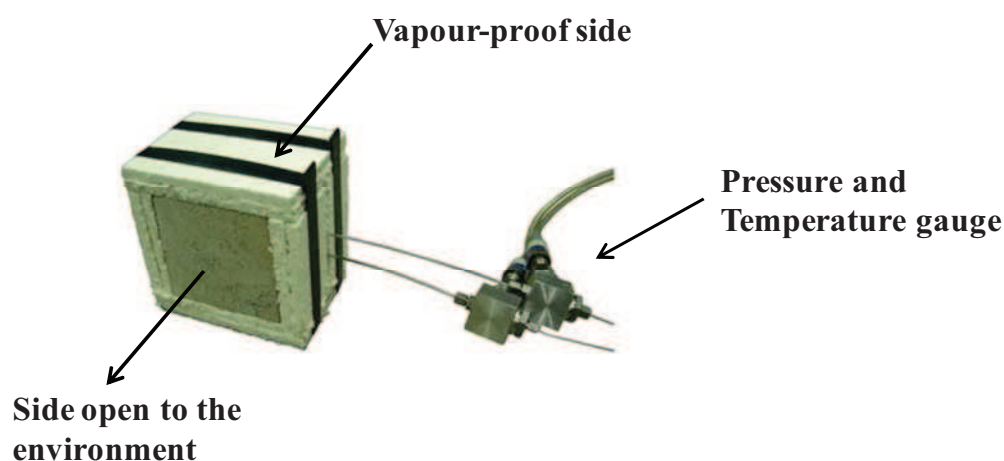


Figure 145: Sealed and insulated specimen ready for pore pressure determination.

These experimental evidences, related to a specific set-up of test specimens, allow us to propose a more generalized approach to the problem of pressure build-up which implies also the role of permeability of the concrete in a real condition.

The discussion presented in Paragraph 6.2.1 is related to a quasi-stationary condition in a concrete unit volume perfectly closed, with external surfaces perfectly impermeable. This system, whose mass and energy exchanges with the external environment are prevented, can be defined as “frozen”. In real conditions, the concrete is characterized by a specific value of permeability, which allows to liquid and vapour phase to migrate outside the material, increasing the specific volume available for water during the thermal exposure. Consequently, V_{sp} value will move away from the saturated liquid curve in the Clapeyron plane; in these conditions the material will result farther from the critical condition of spalling. The mass transport phenomenon, regulated by Darcy’s law, causes a decrease in pressure, which results lower in comparison to the theoretical one.

In order to analyze the “frozen” condition at initial time and then in real conditions of concrete with non zero permeability in case of thermal exposure, the following discussion will be reported.

The initial “frozen” state, at time $t = t_0$ in the reference unit volume $V_{o,c}$ can be described by the following initial boundary conditions:

- $T_0 = 20^\circ\text{C}$ (uniformly distributed);
- $P_0 = 1 \text{ bar} = 0.1 \text{ MPa}$;
- $m_w = m_{w,\text{free}}$
- $V_{sp,0} = (f_{p,0} \cdot V_{o,c}) / m_{w,\text{free}}$

6. DISCUSSION ON THE EXPERIMENTAL RESULTS

When temperature increases with time, porosity will increase according to the relationship:

$$f_p = f_p [T(t)] \quad [61]$$

If a time interval Δt_1 anyway small is defined and imposed, the system can be described with the next expressions:

- $t_1 = t_0 + \Delta t_1$
- $T(t_1) = T_0 + \Delta T (t_1)$
- $P(t_1) = P_0 + \Delta P (t_1)$
- $m_w (t_1) = m_{w,free} + m_{w,bound} (t_1)$
- $m_{w,bound} (t_1) = \rho_w [T(t_1)] \cdot \Delta f_{p1}[T(t_1)]$
- $V_{sp,1} = (f_{p,1} [T(t_1)] \cdot V_{o,c}) / m_w (t_1)$, always according to the hypothesis that the increase in porosity is equals to the water released during heating.

Once $V_{sp,1}$ is known, $P(t_1)$ can be determined.

At this point, the concrete unit volume is still insulated from the external environment. If thereafter it is exposed to external environment only at two sides, removing the imaginary insulating barrier (see Figure 146), the permability of concrete will become different from zero and water can migrate outside the material according to the Darcy's law. The quantity of water that can escape from the material is called m_c .

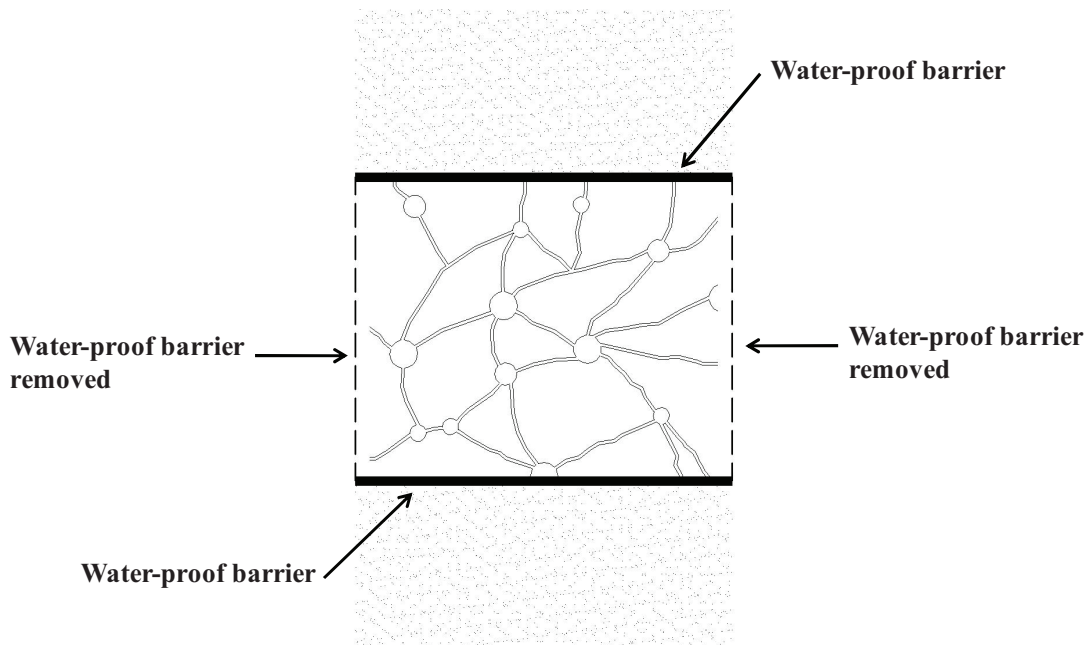


Figure 146: Concrete unit volume in which the water-proof barriers are removed.

6. DISCUSSION ON THE EXPERIMENTAL RESULTS

According to Darcy's law, which has been already expressed by Zhao (2012), in the current discussion, it can be defined that:

$$\Phi = [K (f_{p1}) \cdot \Delta P (t_1)] / (\mu(T_1) \cdot L) = m_e / (\Delta t_1 \cdot \rho_w (T_1)) \quad [62]$$

where:

- Φ is the flux of water m_e directed outside the concrete unit volume [m^3/s]
- $K (f_{p1})$ is the permeability value at temperature T_1 , at which porosity f_{p1} was detected [m^2];
- $\mu(T_1)$ is the viscosity of water at temperature T_1 [P];
- L is the length of concrete portion considered (in this case for unit volume $L = 1$ m).

From the previous expression, m_e is given by:

$$m_e(t_1) = [K (f_{p1}) \cdot \Delta P (t_1) \cdot \Delta t_1 \cdot \rho_w (T_1)] / \mu(T_1) \quad [63]$$

In steady-state conditions, the mass balance condition is simply represented by the equation:

$$m_{w,b} (t_1) = m_e(t_1) \quad [64]$$

that is at time t_1 , the mass of water released by pore system owing to temperature increase ΔT_1 , equal to the water that can escape from the pore system.

Taking into account that also the free water $m_{w,f} (t_1)$ can contribute to pressure build-up, in the real case the following condition shall be satisfied:

$$[m_w (t_1) = m_{w,f} (t_1) + m_{w,b} (t_1)] \leq m_e(t_1) \quad [65]$$

By substituting the expression [65] in [62], the following one can be obtained:

$$m_{w,f} (t_1) + m_{w,b} (t_1) \leq [K (f_{p1}) \cdot \Delta P (t_1) \cdot \Delta t_1 \cdot \rho_w (T_1)] / \mu(T_1) \quad [66]$$

that is:

$$[(m_{w,f} (t_1) + m_{w,b} (t_1)) \cdot \mu(T_1)] / [\Delta P (t_1) \cdot \Delta t_1 \cdot \rho_w (T_1)] \leq K (f_{p1}) \quad [67]$$

The condition expressed in [67] simply means that the permeability coefficient of concrete shall be the one indicated, thus no water build-up (accumulation) should take place in the pore system.

However, the expression [67] represents only a necessary condition to avoid spalling but it is not still enough. The further condition should express the situation in which $m_e(t_1)$ is such that $V_{sp}(t_1)$ expressed as:

6. DISCUSSION ON THE EXPERIMENTAL RESULTS

$$V_{sp}(t_1) = ((f_{p,0} + \Delta f_p(t_1) - m_e(t_1)) / (m_{w,free} + \Delta f_p(t_1) \cdot \rho_w(t_1))) \quad [68]$$

should increase sufficiently so that the corresponding pressure $P_w(T)$ (detectable in Clapeyron's plane) satisfy the condition:

$$P_w(T) < P_{lim} \quad [69]$$

The heating rate plays an important role in this context because it will influence the velocity with which the saturated liquid curve (upper part of the "safety" zone) is reached in the Clapeyron's plan in limit conditions, when spalling can occur. The higher the heating rate, the shorter the time needed to reach the saturation condition, the higher the risk of spalling.

In a first approximation, the concrete permeability data after heating can be estimate assuming that the relationship between permeability and total porosity at 20°C is valid also for specimens after thermal exposure (up to 250°C is the temperature range generally involved in failure spalling occurrence). For this reason, in Figure 147 the permeability data $W_{p,t}(\bullet)$ for the three concrete grades at 20°C are plotted in function of total porosity at 20°C. The data are related to the determination of vapour permeability already reported in Paragraph 5.3.2.3.

From the regression curve in Figure 147, known the total porosity after thermal exposure it should be possible to obtain the permeability data in residual condition (see the example illustrated in Figure 147). As already said, this approach is an approximation and it need to be checked and validated with permeability data obtained after thermal exposure.

The next step, that needs further research efforts, is to define a vector describing V_{sp} variation, whose module and direction depending on the heating rate, that never intercept the saturation curve, in order to define a limit safety condition. For making this, the previous calculation should be iterated until the temperature in which the material failed is reached.

The optimal vector can be defined as the one that never intercepts the saturation curve; to obtain it, it is recommended to act on experimental parameters, such as porosity, moisture content and permeability of the concrete in order to ideally direct the vector in the Clapeyron plane only in the "safety" zone.

6. DISCUSSION ON THE EXPERIMENTAL RESULTS

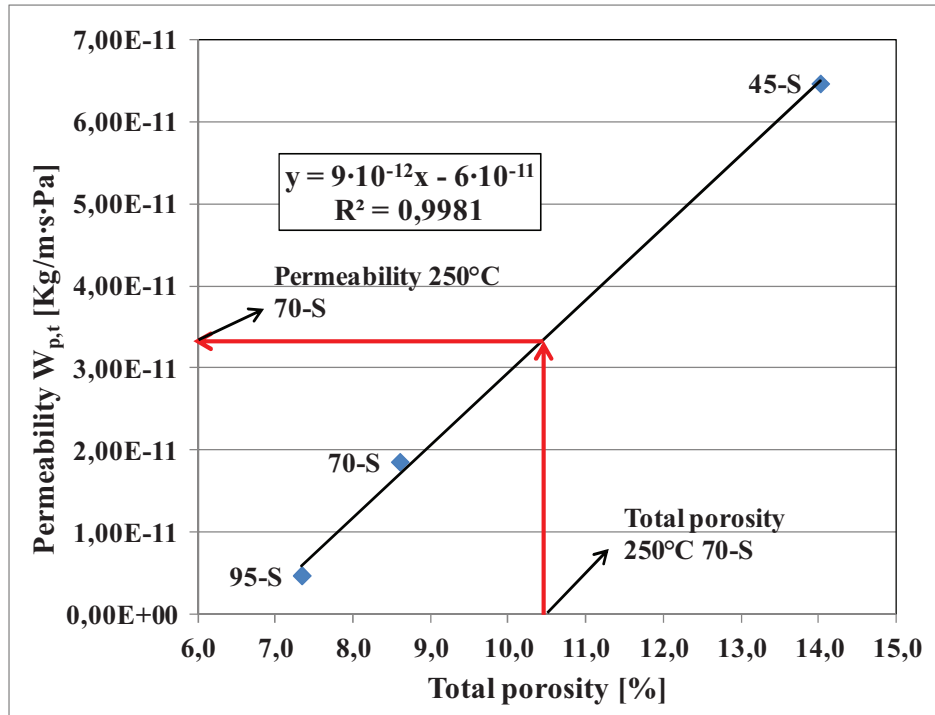


Figure 147: Permeability versus total porosity for different concrete grades at 20°C.

Another important point to be investigated is finding the relationships between porosity and temperature ($f_p = f_p [T(t)]$), and between permeability and porosity ($K = K (f_p)$). Once these relationships are known, a numerical model can be defined in order to predict the occurrence of spalling in any concrete mix.

6.3 Spalling due to thermal gradients

Even if quantifying the effect of thermal gradients on spalling was not among the objectives of this experimental work, some considerations can be made on this issue, as a starting point for further research activities.

If an increase in temperature ΔT is imposed to concrete in a time interval Δt , the higher the thermal diffusivity, the deeper the material layer which is interested by thermal gradients and is at risk of spalling. If the thermal diffusivity is low, the depth of the material interested by the thermal gradients is reduced. It is worth nothing that a low diffusivity values implies also a delay of the thermal wave inside the elements with beneficial effects in terms of protection of the reinforcement.

Being aggregate nature among the most influential parameters affecting thermal diffusivity, the volume of concrete subjected to spalling strongly depends on aggregate nature and on the ensuing thermal gradients.

7. CONCLUDING REMARKS

7. CONCLUDING REMARKS

The present work is focused on the study of the thermal behaviour of eleven concrete mixes (one NSC and ten HPC) with the main objective of investigating the relationships between the intrinsic damage and the mechanical properties, as well as the thermo-mechanical damage deriving from vapour pressure build-ups.

The experimental campaign was preceded by an extensive bibliographic research.

From this review, some important information was drawn.

Regarding the study of intrinsic damage, it was found that:

- Cement pastes, when exposed to high temperature and/or fire, are subjected to chemical transformations, each of them occurring in a specific temperature range. They have an impact on the total porosity and on its distribution, and this effect becomes more relevant as temperature increases. Concerning the thermal stability of aggregates, it appears that the higher the material heterogeneity the more distributed are the microcracks induced by thermal exposure;
- The duration of heating markedly influences the conversion degree of the thermal degradation reactions, with marked effects on the intrinsic damage. In particular, when heating rate increases, the temperature corresponding to the complete decomposition of hydrated phases increases as well. Moreover, it has been observed that, at constant temperature value, the higher the heating rate, the lower the degree of hydrates conversion and the slower the development of the capillary porosity.

Concerning concrete mechanical damage, from the literature and from the results of a companion project on concrete heat-induced mechanical decay, the following information can be drawn:

- The higher the temperature, the higher the decay of the mechanical properties; in particular, the decay of the elastic modulus seems to be more affected by thermal exposure in comparison with the compressive strength;
- The heating rate effect on the mechanical parameters appears consistent with the effect on the dehydration of hydrated phases. At a given temperature, the lower the heating rate, the higher the conversion degree of dehydration reactions, the lower the compressive strength;
- Regarding explosive spalling, numerical analysis shows that under fast heating conditions, the thermal stresses induced by temperature gradients play a critical role in controlling

7. CONCLUDING REMARKS

explosive spalling, while under slow heating, the damage is mainly caused by the stresses induced by vapour pressure. In this context, the permeability becomes the key parameter in vapour transport phenomena influencing pressure build-ups, while thermal diffusivity controls heat transport through the concrete, which causes the thermal gradients, and consequently the thermal stresses. This means that knowing the permeability and the diffusivity is the key factor in understanding explosive spalling.

On the basis of these considerations, the experimental campaign has been planned in order to investigate the microstructural and mechanical properties of concrete, before and after heating.

The **microstructural** (chemo-physical) **results** give the following indications:

- The X-Ray Diffraction and Thermogravimetric Analysis confirm the chemical evolution of the main hydrated constituents of the cementitious matrix, under increasing temperature, as well as the transformations concerning the aggregates;
- Scanning Electron Microscopy observations allow monitor crack pattern evolution for increasing exposure to high temperature. Cracking usually started at the aggregate-cement paste interface, propagated into the cement matrix and finally bridged the aggregates. In the case of basalt concrete, this evolution was strongly limited, even after exposure to 750°C, and only few thin cracks were observed. In calcareous and silico-calcareous concretes, cracks are wider and more diffused. Moreover, the behaviour of calcareous concrete is worse than that of silico-calcareous concrete.
- The Mercury Intrusion Porosimetry tests indicate that the higher the maximum temperature, the higher the total porosity; moreover, pore-radius peaks move towards coarser pores, as temperature increases. The distributions become more enlarged and new peaks appear for larger pore diameters (macropores). In the concrete mixes containing polymeric fibers, after heating to 250 and 500°C, some peaks appear in the zone of macropores, as a consequence of melting/degradation of PP fibers.

The **mechanical results** give the following indications:

- The compressive strength and elastic modulus exhibit a downward trend at increasing temperature, confirming the values found by other Researchers. In particular, the lowest-grade silico-calcareous mix turns to be the less affected than the other silico-calcareous concretes, in terms of compressive strength and elastic modulus. Basalt aggregate

7. CONCLUDING REMARKS

guarantees the best residual (normalized) properties compared to calcareous and silico-calcareous aggregates.

- Concerning the σ - ε curve, the highest-grade mix exhibits the highest stiffness up to 250°C, while the intermediate basalt concrete becomes the stiffest at higher T; the latter, at and above 250°C, exhibits the highest residual compressive strength, followed by the highest-grade concrete. Moreover, in the same thermal conditions, the intermediate calcareous mix appears to be the most heat-damaged, especially in terms of compressive strength and elastic modulus.
- The measurements of pore pressure (P_{lim}) according to the specific test procedure developed at the Politecnico di Milano highlight that the higher the concrete grade, the higher the pore pressure inside the material. Moreover, for intermediate concrete grades, calcareous aggregate yields a much lower pore pressure, than either basalt or silico-calcareous aggregates. It is also observed that both PP fibers types are very effective in reducing pore pressure, but monofilament ones are slightly better, regardless of their content.
- The thermal diffusivity depends on concrete grade and aggregate mineralogical nature. In particular, the higher the compactness of concrete, the higher its thermal diffusivity. The aggregate type plays a substantial role up to 300°C, with basalt concrete exhibiting the lowest diffusivity.

At the end of the experimental campaign, the link between the microstructural results and the mechanical response after heating can be established by cross-examining the results. The following considerations can be made:

- It was observed that P_{lim} exhibits a typical exponential decay at increasing total porosity, after thermal exposure (similar behaviour was mentioned above for compressive strength). The Mercury Intrusion Porosimetry results allows justify the exponential decay law by identifying a critical range of pore radius responsible for the sizable differences in P_{lim} of mixes having almost the same total porosity, after heating, but different compressive strength.
- Coupling Mercury Intrusion Porosimetry and Scanning Electron Microscopy results allows identify the appearance of microcracks, whose size is similar to that of macro pores ($>10\mu\text{m}$). From these observations, basalt concrete exhibits less microcracking compared with silico-calcareous and calcareous concretes, after thermal exposure, as already

7. CONCLUDING REMARKS

mentioned. This microstructural behavior is in some way reflected by the different post-peak behaviors of the σ - ε curves. In fact, Mercury Intrusion Porosimetry and Scanning Electron Microscopy observations indicate that after exposure at 500°C, basalt concrete is affected by very thin microcracks, this being associated with the steeper post-peak branch than in both silico-calcareous and calcareous concretes.

- Concerning spalling-related phenomena, results are used to determine the water released into the pore system and the moisture specific volume (V_{sp}). In this way the pressure $P_w(T)$ values corresponding to the measured temperatures T_{lim} are identified in Clapeyron's plane (P - V_{sp}). A satisfactory agreement is found between the experimental values (P_{lim} and T_{lim}) and those obtainable from Clapeyron's plane. Through this procedure, once the relationships P_{lim} - f_p and V_{sp} - f_p are known, it is possible to identify the thermodynamic state (P_w, T, V_{sp}) of the moisture at any given temperature. These considerations concern a "frozen" situation at a given temperature, without exchanges of mass and energy with the external environment.
- In a real case, in presence of in-time temperature changes and one or more faces of the concrete unit volume exposed to the external environment, it is possible to give to the interface a nonzero value of permeability. A mass balance can be established considering the water content change in the inner concrete volume and the water transported to the exterior, allowing identify a condition of potential risk;
- A spalling sensitivity index has been defined as local (referred to unit control concrete volume $V_{o,c}$), risk of failure $S_{s,o}$. It is expressed as the ratio between the $P_w(T)$, that is the pressure value of the liquid+vapour mixture identified in the Clapeyron's plane in correspondence of specific volume V_{sp} , and P_{lim} , that is the pressure (experimental) value at which the material is affected by failure. If $S_{s,o} \geq 1$, the system is not able to sustain the $P_w(T)$ at a specific temperature exposure, thus failure occurs, while if $S_{s,o} < 1$, the system is in a "safe" condition.

8. OUTLOOK

8. OUTLOOK

In order to extend our knowledge on spalling as a complex coupled phenomenon and to find solutions to reduce its occurrence in cementitious composites, further studies should be carried out on pressure build-ups and thermal stresses.

Regarding the first phenomenon, understanding and modeling moisture transport requires more information on concrete permeability at high temperature. Then, the next phase may consist in defining a robust and suitable parameter concerning concrete risk of explosive spalling.

Concerning the thermal stresses, a quantification of their effect on concrete should be performed taking into account the experimentally-measured thermal diffusivity.

The knowledge ensuing from the mentioned studies may markedly contribute to the development of more heat-resistant concrete mixes with reduced or nonzero spalling.

References

References

ACI 216-1.07 (2007), *Code requirements for determining fire resistance of concrete and masonry construction assemblies*. Report by Joint ACI/TMS Committee 216, 32.

Alonso C., Fernandez L., Dehydration and rehydration processes of cement paste exposed to high temperature environments, *Journal of Material Science* 39 (2004) 3015-3024.

Alonso M.C., Flor-Laguna V., Sanchez M., Microstructural response of polypropylene fibres at high temperature to protect concrete from spalling, 3th International Workshop on Concrete Spalling due to Fire Exposure, Paris, France, 25-27 September, 2013.

Anderberg Y., Spalling phenomena of HPC, *Proceedings of International Workshop on Fire Performance of High-Strength Concrete*, NIST, L.T. Phan, N.J. Carino, D. Duthinh, E. Garboczi (Eds.), NIST, Gaithersburg, MD, USA, 13-14 February, 69-73, 1997.

Atkins P., de Paula J., *Atkin's Physical Chemistry*, Eighth Edition, W.H. Freeman and Company, New York, 2006.

Bayasi Z., McIntyre M., Application of Fibrillated Polypropilene Fibers for Restraint of Plastic Shrinkage Cracking in Silica Fume Concrete, *Materials Journal*, 99 (4), 337-344, 2002.

Bazant, Z. P., Analysis of pore pressure, thermal stress and fracture in rapidly heated concrete, *Proceedings of International Workshop on Fire Performance of High-Strength Concrete*, NIST, Gaithersburg, MD, 13-14 February 1997, 155-164.

Bazant, Z. P. and Kaplan, *Concrete at High Temperatures: Material Properties and Mathematical Models*, Longman Group Ltd, England (1996).

Beitel J.J., Iwankiw, N. R., *Historical Survey of Multi-Story Building Collapses Due to Fire*, Document published by Hughes Associates, 2010.

References

- Bentz, D.P., Fiber percolation and spalling of high performance concrete, *ACI Material Journal*, 351–359, 2000.
- Bhargava P., Sharma U.K., Kaushik S.K., Compressive Stress-Strain Behavior of Small Scale Steel Fibre Reinforced High Strength Concrete Cylinders, *Journal of Advanced Concrete Technology*, 4 (1), 109-121, 2006.
- Biot M.A., General theory of three-dimensional consolidation, *Journal of Applied Physics*, Vol. 12, N. 2, pp. 155-164, 1941.
- Bošnjak J., Ožbolt J., Sharma A., Periškić, Permeability of concrete at high temperature and modeling of explosive spalling, VIII International Conference on Fracture Mechanics of Concrete and Concrete Structures (FramCoS-8), Toledo, Spain, 10-14 March, 2013.
- Brushlinsky N. N., Hall J.R., Sokolov S.V., Wagner P., World Fire Statistic, CTIF International Association of Fire and Rescue Services, Report N. 17, 2012.
- Buchanan A., *Structural Design for Fire Safety*, John Wiley & Sons, LTD, 2001.
- Castellote M., Alonso C., Andrade C., Turrillas X., Campo J., Composition and microstructural changes of cement pastes upon heating, as studied by neutron diffraction, *Cement and Concrete Research* 34 (2004) 1633–1644.
- Chan Y.N., Luo X., Sun W., Compressive strength and pore structure of high-performance concrete after exposure to high temperature up to 800°C, *Cement and Concrete Research* 30 (2000) 247–251.
- Chang Y.F., Chen Y.H., Sheu M.S., Yao G.C., Residual stress–strain relationship for concrete after exposure to high temperatures, *Cement and Concrete Research* 36 (2006) 1999–2005.

References

Cheng F., Kodur V.K.R., Wang T., Stress-strain curves for high strength concrete at elevated temperatures, *Journal of Materials in Civil Engineering*, v. 16, no. 1, January/February 2004, pp. 84-94.

Coussy O., *Poromechanics*, John Wiley & Sons Ltd, England (2004).

Crispino E., Studies on the Technology of Concretes Under Thermal Conditions, Paper SP-34-25 in *Concrete for Nuclear Reactors*, pp. 443-479, American Concrete Institute, Farmington Hills, Michigan, 1972.

Collepari M., *Scienza e Tecnologia del Calcestruzzo*, Third Edition, Hoepli, 1991.

DeBrujin G., Skeates C., Greenaway R., Harrison D., Parris M., James S., Mueller F., Ray S., Riding M., Temple L., Wutherich K., High Pressure, High Temperature Technologies, Oilfield Review, Schlumberger, 2008.

Dias W.P.S, Khoury G.A. and Sullivan P.J.E., Mechanical Properties of Hardened Cement Paste Exposed to Temperatures up to 700°C (1292 F), *ACI materials Journal*, Vol. 87, N. 2, March-April 1990.

Etherington H., *Nuclear Engineering Handbook*, McGraw-Hill, New York, 109–111, 1958.

European Thematic Networks of Fire in Tunnels, *Fire in Tunnels General Report*, 2005.

Felicetti R., Gambarova P.G., Effects of High Temperature on the Residual Compressive Strength of High-Strength Siliceous Concretes, *ACI Materials Journal*, V. 95, No. 4, July-August 1998.

Felicetti R., Gambarova P.G., Heat in concrete: Special issues in materials testing, *Studies and Reseraches*, Volume 24 (2003), Graduate School F.lli Pesenti, Politecnico di Milano, Starrylink Editor.

References

Felicetti R., Lo Monte F., Concrete spalling: Interaction between tensile behaviour and pore pressure during heating, 3th International Workshop on Concrete Spalling due to Fire Exposure, Paris, France, 25-27 September, 2013.

Felicetti R., Lo Monte F., Pimienta P., The influence of pore pressure on the apparent tensile strength of concrete, 7th International Conference on Structures in Fire (SiF), Zurich, Switzerland, 6-8 June, 2012.

Fletcher I.A., Welch S., Torero J.L., Carvel R.O., Usmani A., Behaviour of concrete structures in fire, *Thermal Science*, Vol. 11 (2007) No. 2, pp. 37-52.

Gallé C., Pin M, Ranc G., Rodrigues S., Effect of the heating rate on residual thermo-hydro-mechanical properties of a high-strength concrete in the context of nuclear waste storage, Transactions of the 17th International Conference on Structural Mechanics in Reactor Technology (SMiRT 17) Prague, Czech Republic, August 17 –22, 2003.

Georgieva V., Vlaev L. and Gyurova K, Non-Isothermal Degradation Kinetics of CaCO₃ from Different Origin, Hindawi Publishing Corporation, *Journal of Chemistry* Volume 2013, Article ID 872981, 12 pages.

Giussani F, Mola F., Durable concrete pavements: The reconstruction of runway head 36R of Milano Linate International Airport, *Construction and Building Materials* 34 (2012) 352–361.

Glasstone S., Sesonske A., *Nuclear Reactor Engineering*, D. Van Nostrand, Princeton, New Jersey, pp. 614–615, 1967.

Guerrini G.L., Gambarova P.G., Rosati G., Microstructure of High-Strength Concrete Subjected to High Temperature, Workshop “Fire Design of Concrete Structures: What now? What next?” Milan University of Technology, Milan, Italy, December 2-3, 2004.

Harmathy T.Z., *Fire Safety Design & Concrete*, Longman Scientific & Technical, Essex, England, 1993.

References

Iverson B., Maxson J., Bour D., Strength Retrogression in cements under high-temperature conditions, Thirty-Fifth Workshop on Geothermal Reservoir Engineering Stanford University, Stanford, California, February 1-3, 2010.

Ju J.W., Zang Y., Axisymmetric thermomechanical constitutive and damage modeling for airfield concrete pavement under transient high temperature, *Mechanics of Materials* 29 (1998) 307-323

Kalifa P., Chenè G., Gallè C., High-temperature behaviour of HPC with polypropylene fibres From spalling to microstructure, *Cement and Concrete Research* 31 (2001) 1487–1499.

Kalifa P., Menneteau F.D., Quenard D., Spalling and pore pressure in HPC at high temperature, *Cement and Concrete Research* 30 (2000) 1915-1927.

Kassir M.K., Bandyopadhyay K.K., Reich M., Thermal degradation of concrete in the temperature range from ambient to 315°C (600°F), Engineering Research and Application Division, Department of Advanced Technology, Brookhaven National laboratory, Associated Universities, INC., Upton, New York 11973—5000, October 1996.

Khoury G.A., Compressive strength of concrete at high temperatures: a reassessment, *Magazine of Concrete Research*, 1992, V. 44, No. 161, pp. 291-309.

Khoury G.A., Effect of fire on concrete and concrete structures, *Progress in Structural Engineering and Materials*, 2000 (2) 429-447.

Khoury G.A., Polypropylene Fibres in Heated Concrete. Part 2: Pressure Relief Mechanisms and Modelling Criteria, *Magazine of Concrete Research*, 60 (3), 189–204, 2008.

Khoury G.A., Sullivan P.J.E., Grainger B.N., Radial temperature distributions within solid concrete cylinders under transient thermal states, *Magazine of Concrete Research* 36, 1984, 146-156.

Massazza F., Pezzuoli M., Cement paste-quartz bond in autoclaved concretes, *Proceedings of the 7th International Congress on the Chemistry of Cement (ICCC)*, Paris, 1980.

References

- Mazars, J., Pyaudier-Cabot, G., Continuum damage theory-application to concrete, *Journal of Engineering Mechanics*, ASCE, Vol. 115(2), 1989, p. 345-365,
- Mehta P.K. and Monteiro P.J.M., *Concrete – Microstructure, Properties, and Materials*, McGraw Hill, New York, New York, 2006.
- Mendes A., Sanjayan J. and Collins F., Phase transformations and mechanical strength of OPC/Slag pastes submitted to high temperatures, *Materials and Structures* (2008) 41:345–350.
- Mindeguia J.C., Pimienta P., Hager I., Carré H., Influence of water content on gas pore pressure in concretes at high temperature, 2nd International RILEM Workshop on Concrete Spalling due to Fire Exposure 5-7 October 2011, Delft, The Netherlands.
- Mindeguia J.C., Pimienta P., Noumowè A., Kanema M., Temperature, pore pressure and mass variation of concrete subjected to high temperature – Experimental and numerical discussion on spalling risk, *Cement and Concrete Research* 40 (2010) 477-487.
- Moran M.J., Shapiro H.N., *Fundamentals of Engineering Thermodynamics*, John Wiley & Sons, Ltd, England (2008).
- Morsy M.M., Shebl S.S. and Rashad A.M., Effect of fire on microstructure and mechanical properties of blended cement pastes containing metakaolin and silica fume, *Asian Journal of Civil Engineering (Building and Housing)*, Vol. 9, N. 2 (2008) pp. 93-105.
- Naus D.J., T A Compilation of Elevated Temperature Concrete Material Property Data and Information for Use in Assessments of Nuclear Power Plant Reinforced Concrete Structures, Office of Nuclear Regulatory Research, 2010.
- Niry R., Beaucour A.-L., Hebert R., Noumowé A., Ledésert B., Bodet R., Thermal stability of different siliceous and calcareous aggregates subjected to high temperature, 3rd International Workshop on Concrete Spalling due to Fire Exposure, Paris, France, 25-27 September, 2013.

References

Noumowe A., Mechanical properties and microstructure of high strength concrete containing polypropylene fibres exposed to temperatures up to 200°C, *Cement and Concrete Research* 35 (2005) 2192 – 2198.

Noumowé, N.A., "Effet de hautes températures sur le béton. Cas particulier du béton à hautes performances", Ph.D.- Thesis, INSA Lyon, France, 1995.

Nuovo Colombo, *Manuale dell'Ingegnere*, 83th Edition, Volume 1, Ulrico Hoepli Milano Editor, 1997.

Orosz Á, Effect of temperature upon reinforced concrete cooling towers, Department of Reinforced Concrete Structures, Technical University, Budapest, 1980.

Ožbolt J., Bošnjak J., Modelling explosive spalling and stress induced thermal strains of HPC exposed to high temperature, 3th International Workshop on Concrete Spalling due to Fire Exposure, Paris, France, 25-27 September, 2013.

Peng G., Huang Z., Change in microstructure of hardened cement paste subjected to elevated temperatures, *Construction and Building Materials* 22 (2008) 593–599.

Phan L.T., Carino N.J., Review of mechanical properties of HSC at elevated temperature, *Journal of Materials in Civil Engineering* (1998) 58.

Piasta J., Sawicz Z., Rudzinski L., Changes in the structure of hardened cement paste due to high temperature, *materials and Constructions*, 17 (1984) 291.

Pistol K., Weise F., Meng B., Schneider U., The Mode of Action of Polypropylene Fibres in High Performance Concrete at High Temperatures, Proceedings of 2nd International RILEM Workshop on Concrete Spalling due to Fire Exposure, E.A.B. Koenders, F. Dehn (Eds.), Delft, The Netherlands, 5-7 October, 289-296, 2011.

References

- Poon C., Azhar S., Anson M., Wong Y., Comparison of the strength and durability performance of normal- and high-strength pozzolanic concretes at elevated temperatures, *Cement and Concrete Research* 31 (2001) 1291–1300.
- Poon C.S., Shui Z.H., Lam L., Compressive behavior of fiber reinforced high-performance concrete subjected to elevated temperatures, *Cement and Concrete Research* 34 (2004) 2215–2222.
- Pourchez J., Valdivieso F., Grosseau P., Guyonnet R., Guilhot B., Kinetic modelling of the thermal decomposition of ettringite into metaettringite, *Cement and Concrete Research* 36 (2006) 2054–2060.
- Rashad A.M., Zeedan R.S., A preliminary study of blended pastes of cement and quartz powder under the effect of elevated temperature, *Construction and Building Materials* 29 (2012) 672–681.
- Savva A., Manita P., Sideris K.K., Influence of elevated temperatures on the mechanical properties of blended cement concretes prepared with limestone and siliceous aggregates, *Cement & Concrete Composites* 27 (2005) 239–248.
- Schaube F., Koch L., Worner A. and Muller-Steinhagen H., A thermodynamic and kinetic study of the de- and rehydration of $\text{Ca}(\text{OH})_2$ at high H_2O partial pressures for thermo-chemical heat storage, *Thermochimica Acta* 538 (2012) 9–20.
- Schneider U., Permeability of High Performance Concrete at Elevated Temperatures, 6th International Conference on Structures in Fire (SiF), East Lansing, Michigan, USA 2-4 June, 2010.
- Shaw S., Henderson C.M.B., Komarschek B.U., Dehydration/recrystallization mechanisms, energetics, and kinetics of hydrated calcium silicate minerals: an in situ TGA/DSC and synchrotron radiation SAXS/WAXS study, *Chemical Geology* 167, 2000, 141–159.
- Siddique R., Noumowe A.N., An Overview of the Properties of High-strength Concrete Subjected to Elevated Temperatures, *Indoor and Built Environment* 2010; 19; 6; 612-622.
- Verstraete J., Approche multi-technique et multi-échelle d'étude des propriétés structurales des matériaux hétérogènes, Thèse de l'Université de Haute Alsace, 2005.

References

Tennis P.D., Jennings H.M., A model for two types of calcium silicate hydrate in the microstructure of Portland cement pastes, *Cement and Concrete Research* 30 (2000) 855-863.

Tognon G.P., Ursella P., Coppetti G., Bond strength in very high strength concrete, *Proceedings of the 7th International Congress on the Chemistry of Cement (ICCC)*, Paris, 1980.

Ulm, F.J., Coussy, O., Bazant, Z. P., The 'Chunnel' fire. I: chemoplastic softening in rapidly heated concrete, *Journal of Engineering Mechanics*, Vol. 125(3), 1999a, p. 272-282.

Ulm, F.J., Acker, P., Levy, M., The 'chunnel' fire. II: analysis of concrete damage, *Journal of Engineering Mechanics*, Vol. 125(3), 1999b, p. 283-289.

Verstraete J., Approche multi-technique et multi-échelle d'étude des propriétés structurales des matériaux hétérogènes, *These de l'Université de Haute Alsace*, 2005.

Xing Z., Beaucour A-L., Hébert R., Noumowe A., Ledesert B., Influence of the nature of aggregates on the behaviour of concrete subjected to elevated temperature, *Cement and Concrete Research* 41 (2011) 392–402.

Xing Z., Hébert R., Beaucour A.-L., Ledésert B., Noumowé A., Linder N., Influence of aggregate's nature on their instability at elevated temperature, *2nd International RILEM Workshop on Concrete Spalling due to Fire Exposure*, Delft, The Netherlands, 5-7 October 2011.

Zang J., Weissinger E. A., Peethamparan S., Scherer G.W., Early hydration and setting of oil well cement, *Cement and Concrete Research* 40 (2010) 1023–1033.

Zelić J., Rušić D., Krstulović R., Kinetic analysis of thermal decomposition of Ca(OH)_2 formed during hydration of commercial Portland cement by DSC, *Journal of Thermal Analysis and Calorimetry*, Vol. 67 (2002) 613-622.

References

Zhang Q., Ye G., Microstructure Analysis of Heated Portland Cement Paste, *Procedia Engineering* 14 (2011) 830-836.

Zhao, J., Fire-Induced Spalling Modeling of High-Performance Concrete, PhD Thesis, TU Delft, The Netherlands, 2012.

Annex A

Annex A

N	Country	Cost in portion of GDP (%)					$\sum_{i=1}^5 C_i$	Expenditure / Losses (C3 + C4 + C5)/ (C1+C2)
		Direct losses	Indirect losses	Cost of fire service	Fire protection in buildings	Fire insurance administration		
		C ₁	C ₂	C ₃	C ₄	C ₅		
N	Страна	Стоимость в долях ВВП (%)					$\sum_{i=1}^5 C_i$	Затраты / Потери (C3 + C4 + C5)/ (C1+C2)
		Прямой ущерб	Косвен. ущерб	Содержание пожарной охраны	ППЗ зданий	Страхованье		
		C ₁	C ₂	C ₃	C ₄	C ₅		
N	Staat	Kosten in BSP-Anteilen (%)					$\sum_{i=1}^5 C_i$	Ausgaben / Verluste (C3 + C4 + C5)/ (C1+C2)
		Direkter Schaden	Indirekter Schaden	Unterhalt Feuerwehren	VB in Gebäuden	Feuerversicherung		
		C ₁	C ₂	C ₃	C ₄	C ₅		
1	Czechia	0,08	0,005 (2001)	-	0,19	-	-	-
2	Denmark	0,20	0,029 (1994)	0,07	0,26	0,09	0,649	1,83
3	Finland	0,17	0,010	0,20	-	0,03	-	-
4	France	0,20	0,010 (2006)	-	0,18	0,07	-	-
5	Germany	0,13	0,016	-	-	0,04	-	-
6	Italy	0,17	0,014 (1994)	-	0,35	0,05	-	-
7	Japan	0,12	0,006	0,30	0,14	0,09	0,656	4,21
8	New Zealand	0,11	0,007 (2004)	0,16	0,23	0,08	0,587	4,02
9	Norway (2003-2005)	0,22	0,002	0,11 (2005)	0,36 (2005)	0,10 (2005)	0,792	2,57
10	Poland	0,09	-	0,16	-	-	-	-
11	Singapore*	0,05	-	0,03	0,39	0,02	0,502	7,10
12	Slovenia (2002-2004)	0,07	0,021	0,05 (2003)	0,16	0,06	0,361	2,97
13	Sweden	0,17	0,008	0,13	0,19	0,05	0,548	2,08
14	UK	0,13	0,010	0,21	0,22	0,10	0,670	3,79
15	USA	0,11	0,007	0,27	0,41	0,12	0,917	6,84
16	Netherlands	0,16	0,027 (1996)	0,19	0,31	-	-	-
17	Australia	0,08	-	0,16	0,35	-	-	-
18	Spain	0,08	-	-	-	-	-	-
	Avg./Сред./Mittel.	0,13	0,010	0,17	0,26	0,07	0,638	3,55

* - Estimation under average meaning C₂ / Оценка при среднем значении C₂ / Wert C₂ geschätzt.

Figure A1: Economic-statistical evaluation of "costs" of fire (average for 2006-2008 years).

Annex A

N	Country	Population, thous. inh.	Number of fire deaths					Average number		
			2006	2007	2008	2009	2010	per year	per 100 thous.inh.	per 100 fires
	Страна	Население, тыс. чел.	Число погибших					Среднее число		
Staat	Einwohner in 1.000	2006	2007	2008	2009	2010	je Jahr	je 100.000 Einw.	je 100 Brände	
1	USA	311 537	3 245	3430	3320	3010	3 120	3 225	1,04	0,22
2	Russia	141 900	17 223	16066	15165	13946	13061	15 092	10,64	7,53
3	Japan	128 056	1 509	1455	1452	-	-	1 472	1,15	-
4	Vietnam	86 000	53	50	-	62	60	56	0,07	2,51
5	Germany	82 218	424	346	398	-	-	389	0,47	0,20
6	France	65 027	341	378	402	394	438	391	0,60	0,12
7	UK*	60 776	504	443	453	416	388	441	0,73	0,12
8	Italy	58 500	112	67	80	109	74	88	0,15	0,04
9	Spain	47 021	245	2325	270	196	192	646	1,37	0,56
10	Ukraine	45 871	4 035	4005	3896	3209	2819	3 593	7,83	3,12
11	Poland	38 167	608	605	574	584	525	579	1,52	1,13
12	Malaysia	24500	71	80	-	-	-	76	0,31	0,05
13	Romania	21 504	220	252	225	234	247	236	1,10	1,20
14	Netherland	16 306	80	-	68	-	-	74	0,45	0,47
15	Kazachstan	15 819	667	602	501	558	528	571	3,61	1,21
16	Greece	11 237	72	70	63	55	-	65	0,58	0,35
17	Portugal	11 000	65	75	-	0	0	35	0,32	0,10
18	Czechia	10 517	150	130	142	-	131	138	1,31	0,37
19	Hungary	9 999	154	133	140	125	112	133	1,33	0,66
20	Belarus	9 500	1 149	1084	1064	-	1120	1 104	11,62	5,01
21	Sweden	9 341	83	96	115	124	-	105	1,12	1,07
22	Austria	8 388	33	-	50	36	39	40	0,47	0,14
23	Switzerland	7 786	21	-	-	-	0	11	0,13	0,03
24	Serbia	7 566	89	86	93	86	81	87	1,15	0,32
25	Bulgaria	7 364	96	105	112	122	79	103	1,40	0,68
26	Denmark	5 500	71	-	90	71	74	77	1,39	0,24
27	Slovakia	5 435	49	53	68	56	41	53	0,98	0,29
28	Finland	5 375	119	84	-	107	80	98	1,81	0,84
29	Norway	4 858	62	74	-	-	65	67	1,38	0,43
30	Croatia	4 290	33	68	37	28	26	38	0,90	1,04
31	New Zealand	4 271	25	33	34	36	34	32	0,76	0,66
32	Singapore	4250	3	4	0	0	0	1	0,03	-
33	Ireland	4 109	42	41	35	-	38	39	0,95	0,31
34	Lithuania	3 245	307	297	270	203	233	262	8,07	3,73
35	Latvia	2 230	235	207	163	145	144	179	8,02	0,79
36	Slovenia	2 057	7	-	19	-	16	14	0,68	0,04
37	Estonia	1 340	164	134	89	63	69	104	7,75	0,60
38	Cyprus	839	-	0	0	3	6	2	0,27	0,04
Total/Итого/Gesamt:		1 283 699	32 366	32 878	29 388	23 978	23 840	29 715	2,31	0,91

* - data of 2009-2010 year for Great Britain

Figure A2: Trends in fire deaths in the countries of the world in 2006-2010.

Annex A

N	Country	Population, thous. inh.	Number of fire injuries					Average number	
			2007	2008	2009	2010	per year	per 100 thous.inh.	per 100 fires
	Страна	Население, тыс. чел.	Число травмированных					Среднее число	
			2007	2008	2009	2010	в год	на 100 тыс.чел.	на 100 пожаров
	Staat	Einwohner in 1.000	Anzahl der Brandverletzten					Mittelwert	
			2007	2008	2009	2010	je Jahr	je 100.000 Einw.	je 100 Brände
1	USA	311 537	17675	16705	17050	17720	17 143	5,50	1,17
2	Russia	141 900	13688	12887	13269	13117	13 281	9,36	6,63
3	France	65 027	12439	14159	13637	13513	13 412	20,62	3,99
4	UK	60 776	13200	12200	-	-	12 700	20,90	3,55
5	Italy	58 500	375	299	85	101	253	0,43	0,11
6	Ukraine	45 871	-	1817	-	-	1 817	3,96	1,58
7	Poland	38 155	-	3383	-	-	3 383	8,87	6,61
8	Malaysia	24 500	67	-	-	-	77	0,31	0,05
9	Romania	21 504	381	499	563	442	481	2,24	2,46
10	Netherland	16 306	-	843	-	-	843	5,17	5,32
11	Greece	11 237	146	118	40	-	101	0,90	0,54
12	Portugal	11 000	-	8	106	250	57	0,52	0,15
13	Czechia	10 517	1023	1109	980	1060	1 037	9,86	3,83
14	Hungary	9 999	583	492	609	455	561	5,61	2,81
15	Belarus	9 500	382	-	473	481	428	4,50	1,94
16	Sweden	9 341	1352	1158	1235	-	1 248	13,36	12,74
17	Austria	8 338	106	-	-	-	106	1,27	0,37
18	Serbia	7 566	316	307	262	311	295	3,90	3,45
19	Bulgaria	7 364	306	320	298	292	308	4,18	2,04
20	Slovakia	5 435	234	232	245	244	237	4,36	1,29
21	Finland	5 375	563	-	729	639	646	12,02	5,57
22	Croatia	4 290	147	98	99	92	115	2,67	3,09
23	New Zealand	4 271	371	361	380	276	371	8,68	7,54
24	Singapore	4 250	96	122	127	143	103	2,42	-
25	Lithuania	3 245	270	242	211	215	241	7,43	3,43
26	Latvia	2 230	271	245	194	242	237	10,61	1,05
27	Estonia	1 340	133	102	110	102	115	8,58	0,67
28	Cyprus	839	0	-	32	20	16	1,91	0,09
Total/Итого/Gesamt:		900 213	64 124	67 706	50 734	49 715	69 612	7,73	2,13

Figure A3: Trends in fire injuries in the countries of the world in 2007-2010.

Annex B

Annex B

Concrete mixes thermograms obtained by TGA, determined after all the exposure temperatures.

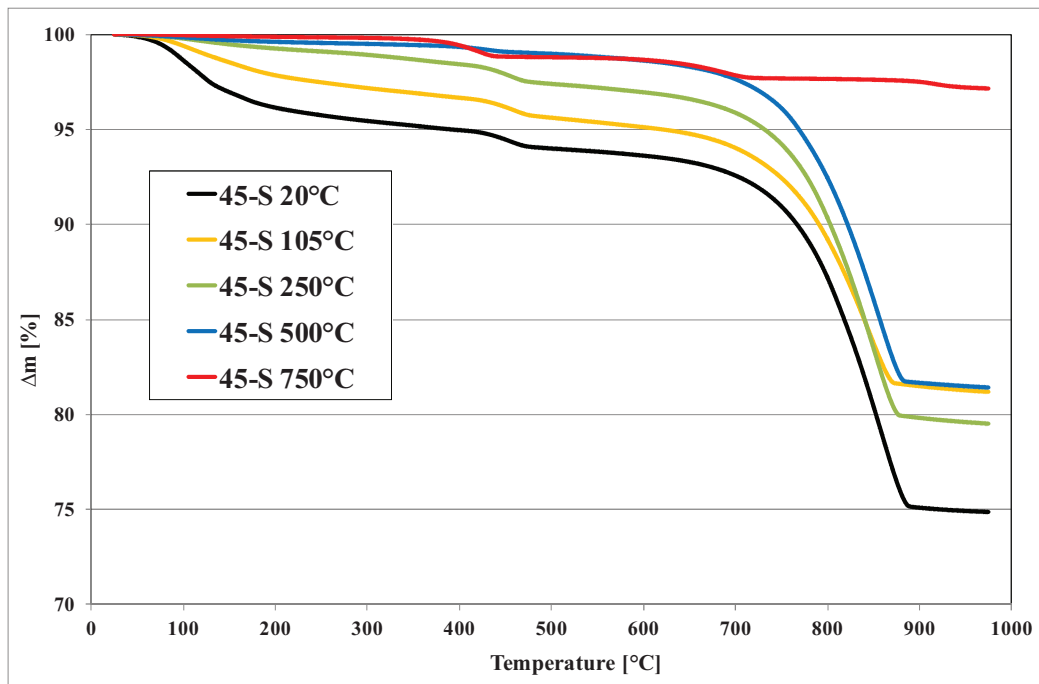


Figure B1: TGA experimental trends for 45-S after all exposure temperatures.

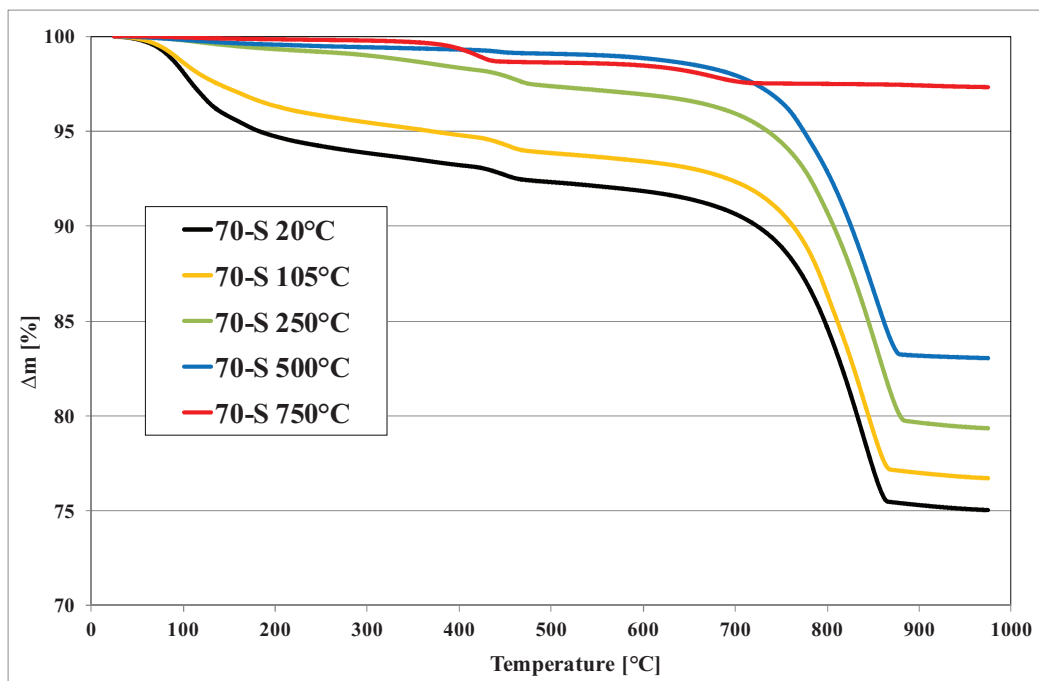


Figure B2: TGA experimental trends for 70-S after all exposure temperatures.

Annex B

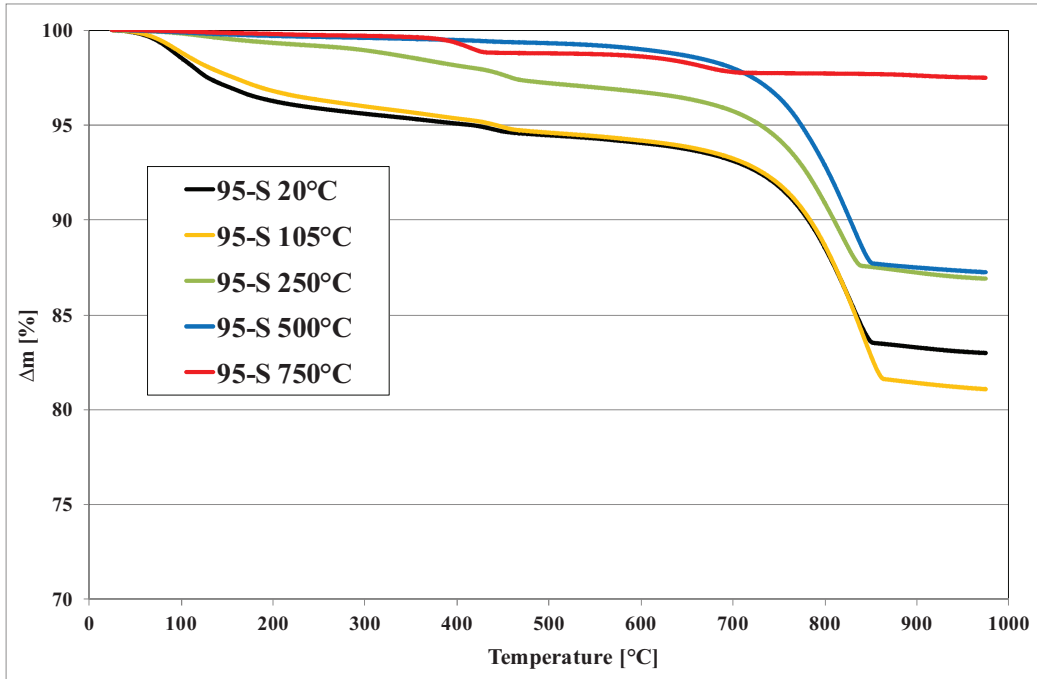


Figure B3: TGA experimental trends for 95-S after all exposure temperatures.

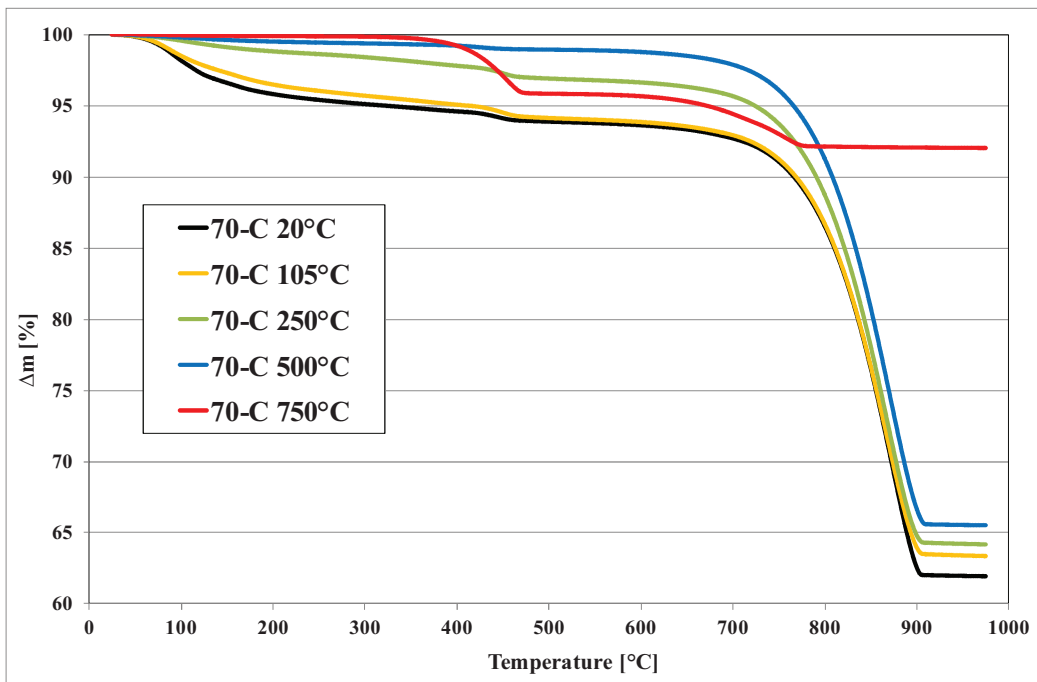


Figure B4: TGA experimental trends for 70-C after all exposure temperatures.

Annex B

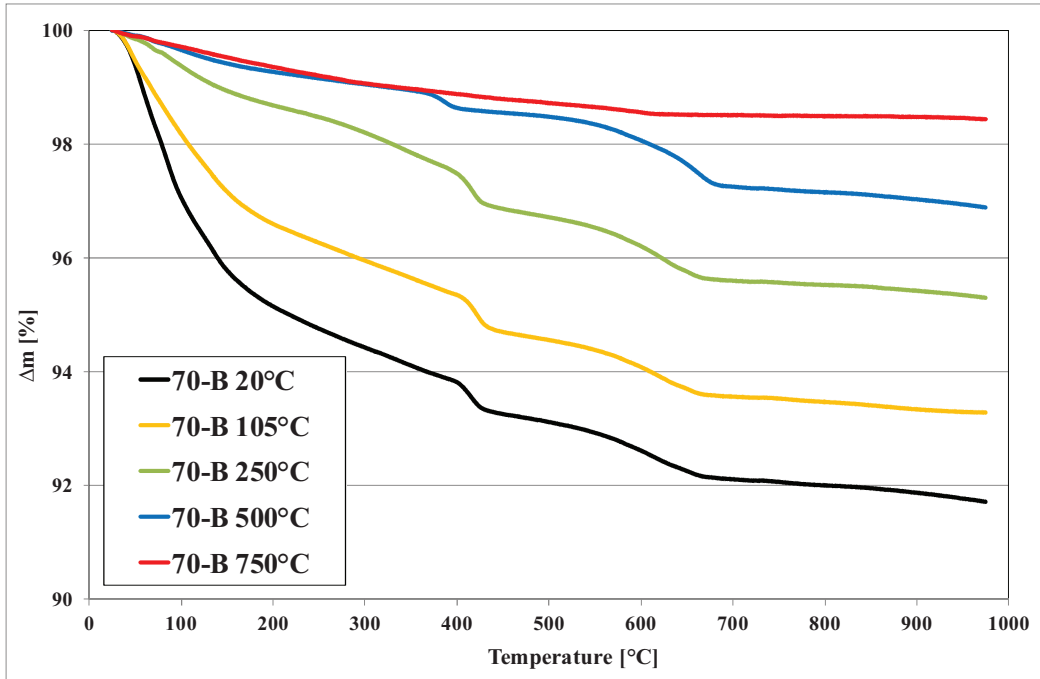


Figure B5: TGA experimental trends for 70-B after all exposure temperatures.

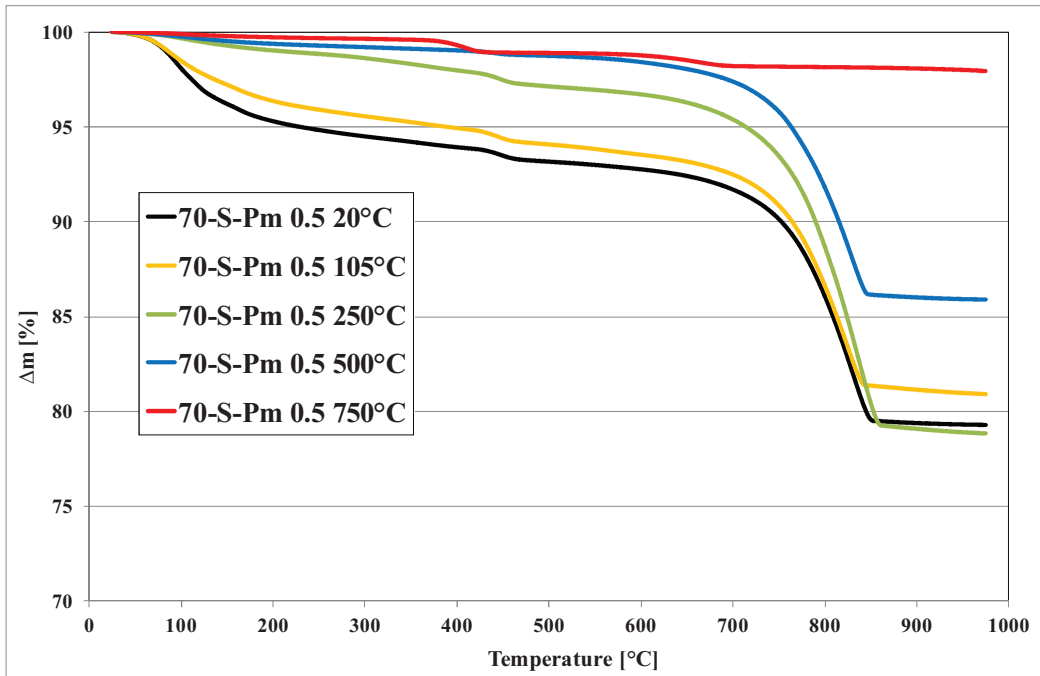


Figure B6: TGA experimental trends for 70-S-Pm 0.5 after all exposure temperatures.

Annex B

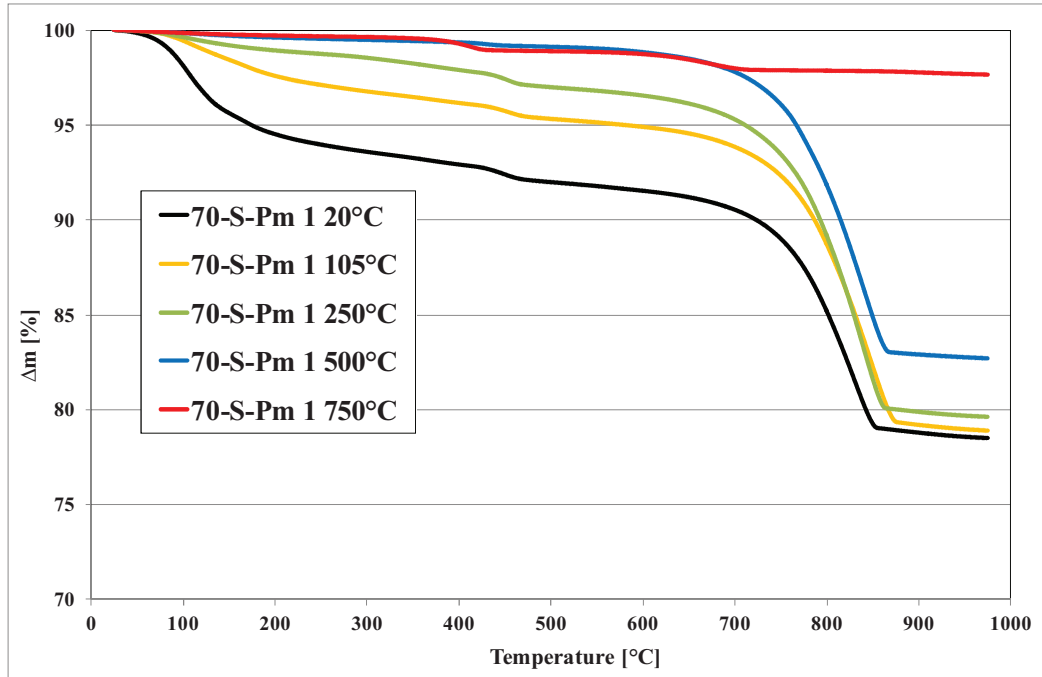


Figure B7: TGA experimental trends for 70-S-Pm 1 after all exposure temperatures.

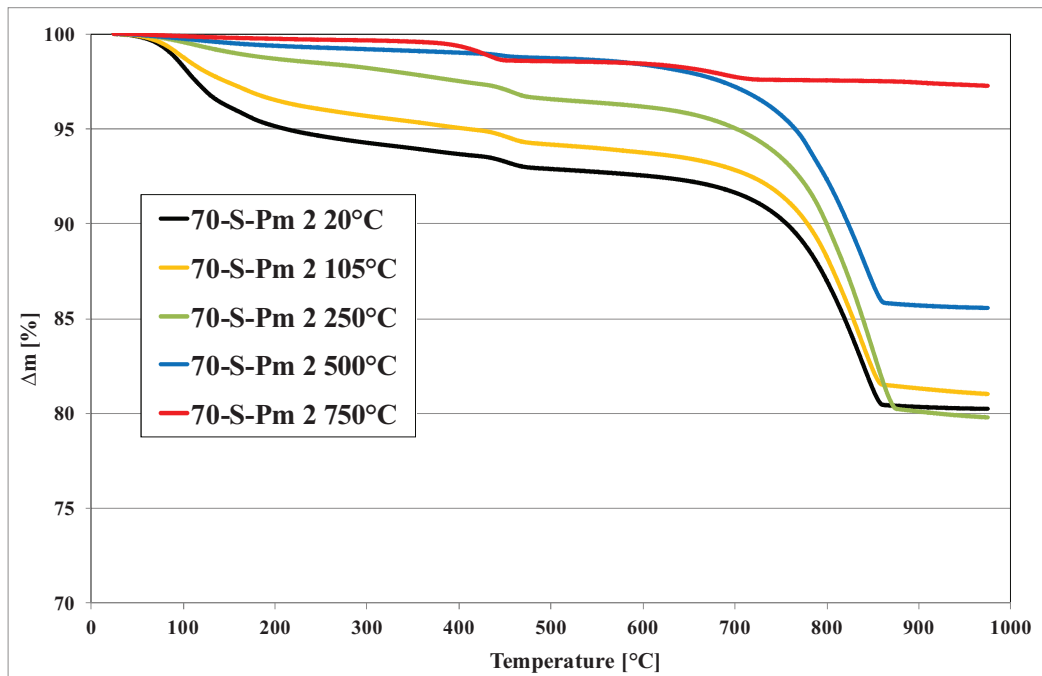


Figure B8: TGA experimental trends for 70-S-Pm 2 after all exposure temperatures.

Annex B

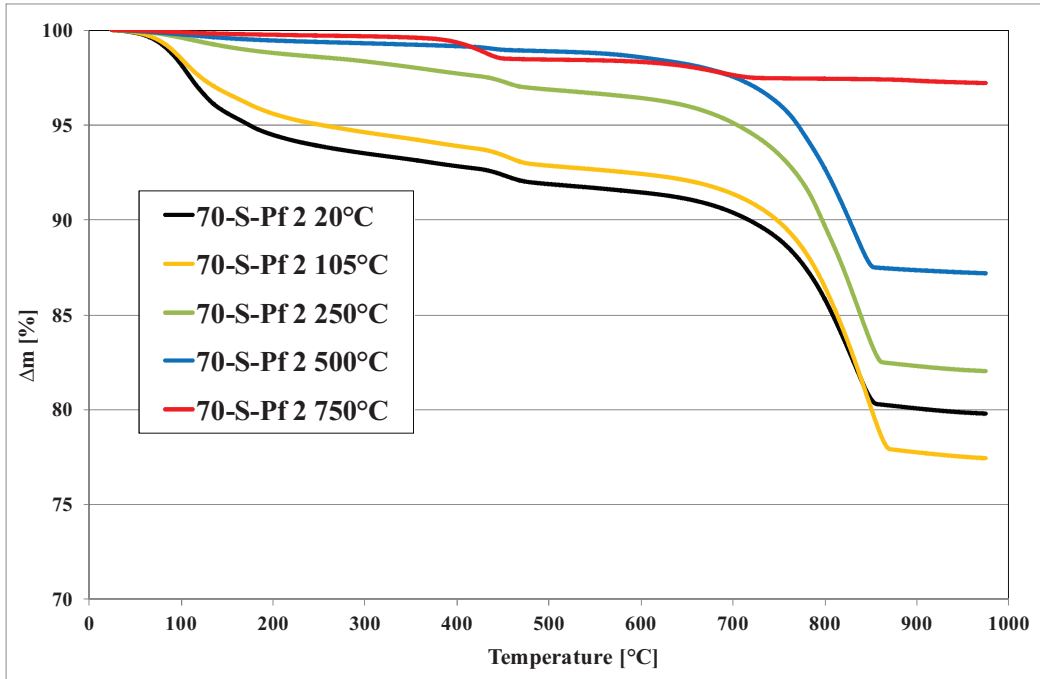


Figure B9: TGA experimental trends for 70-S-Pf 2 after all exposure temperatures.

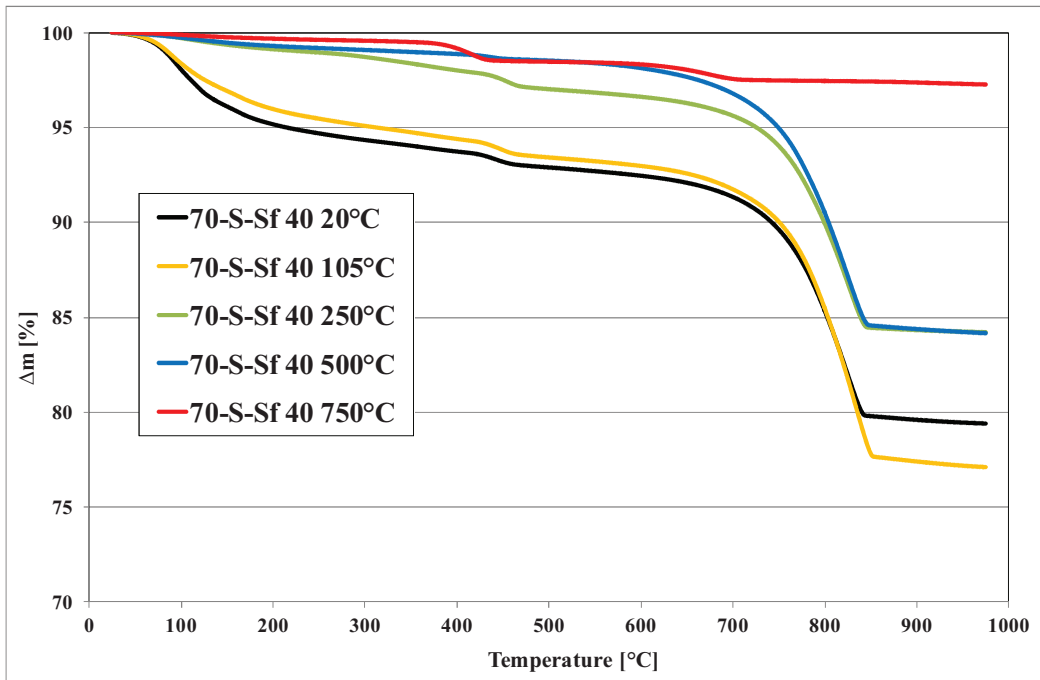


Figure B10: TGA experimental trends for 70-S-Sf 40 after all exposure temperatures.

Annex B

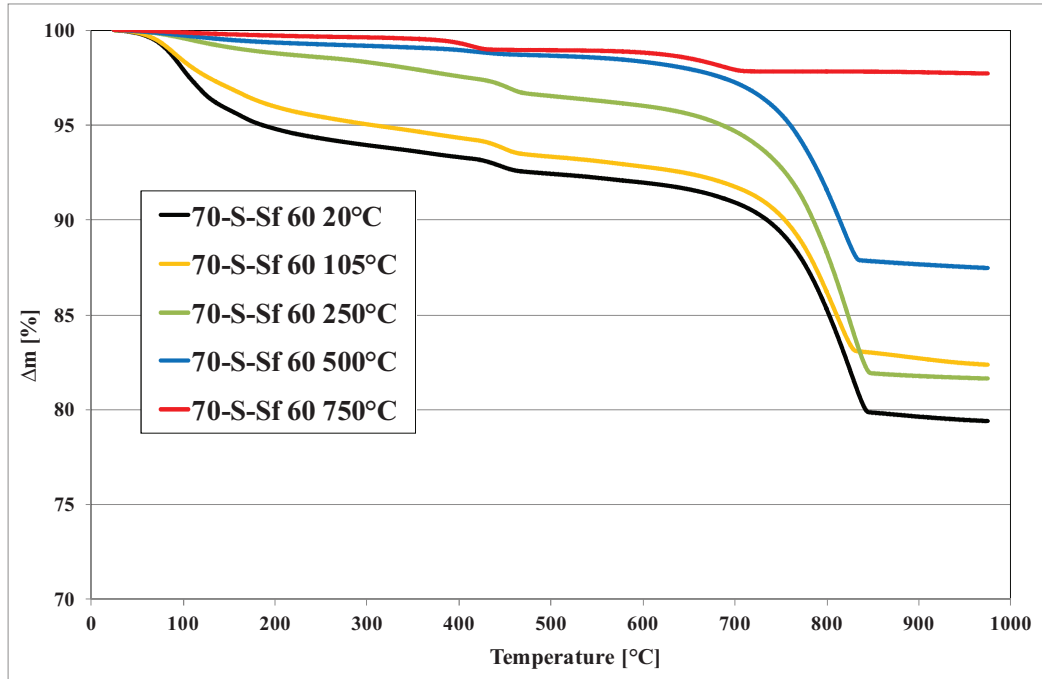


Figure B11: TGA experimental trends for 70-S-Sf 60 after all exposure temperatures.

Annex C

Concrete mixes XRD patterns determined after all the exposure temperatures.

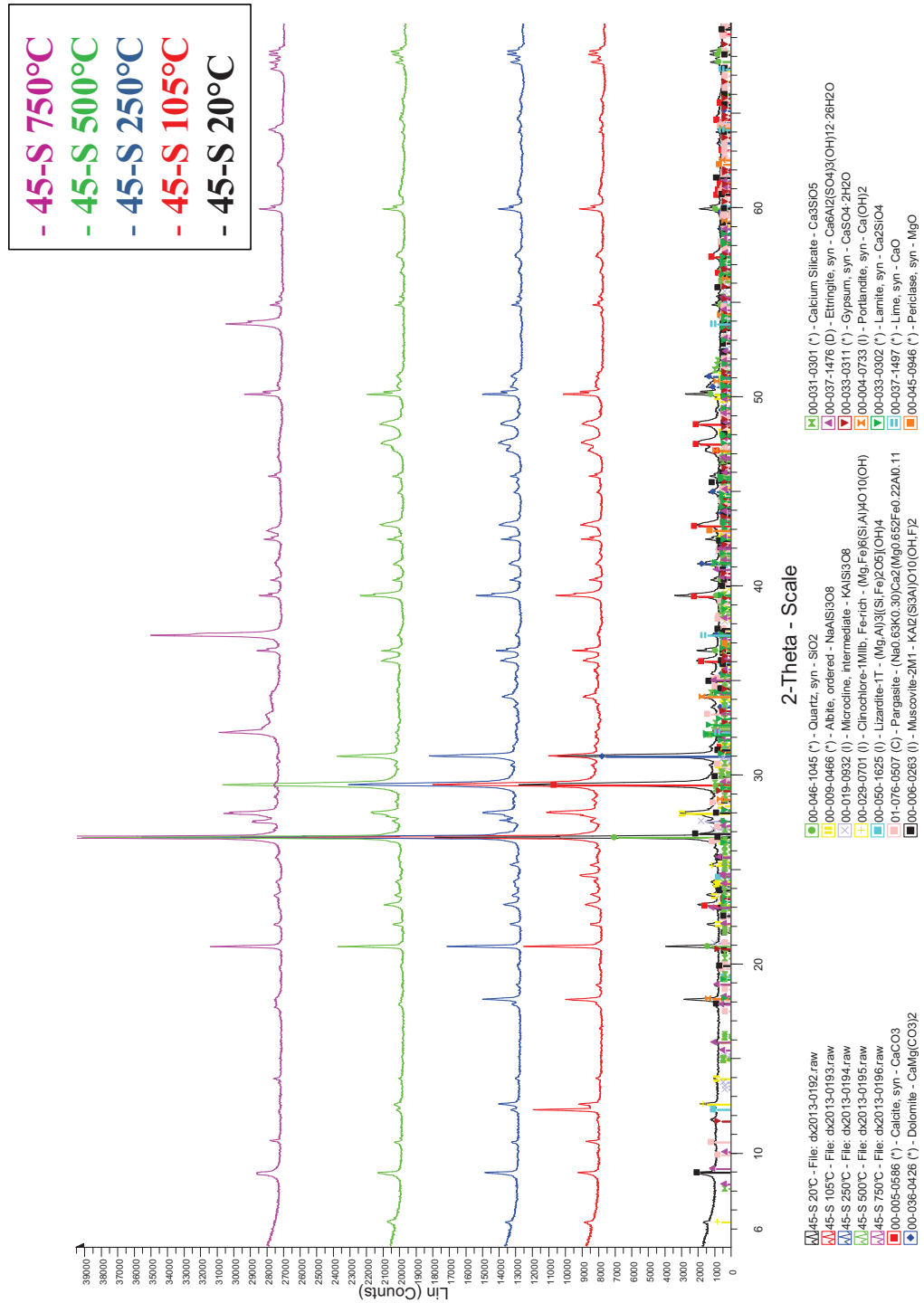


Figure C1: XRD patterns for 45-S after all exposure temperatures.

Annex C

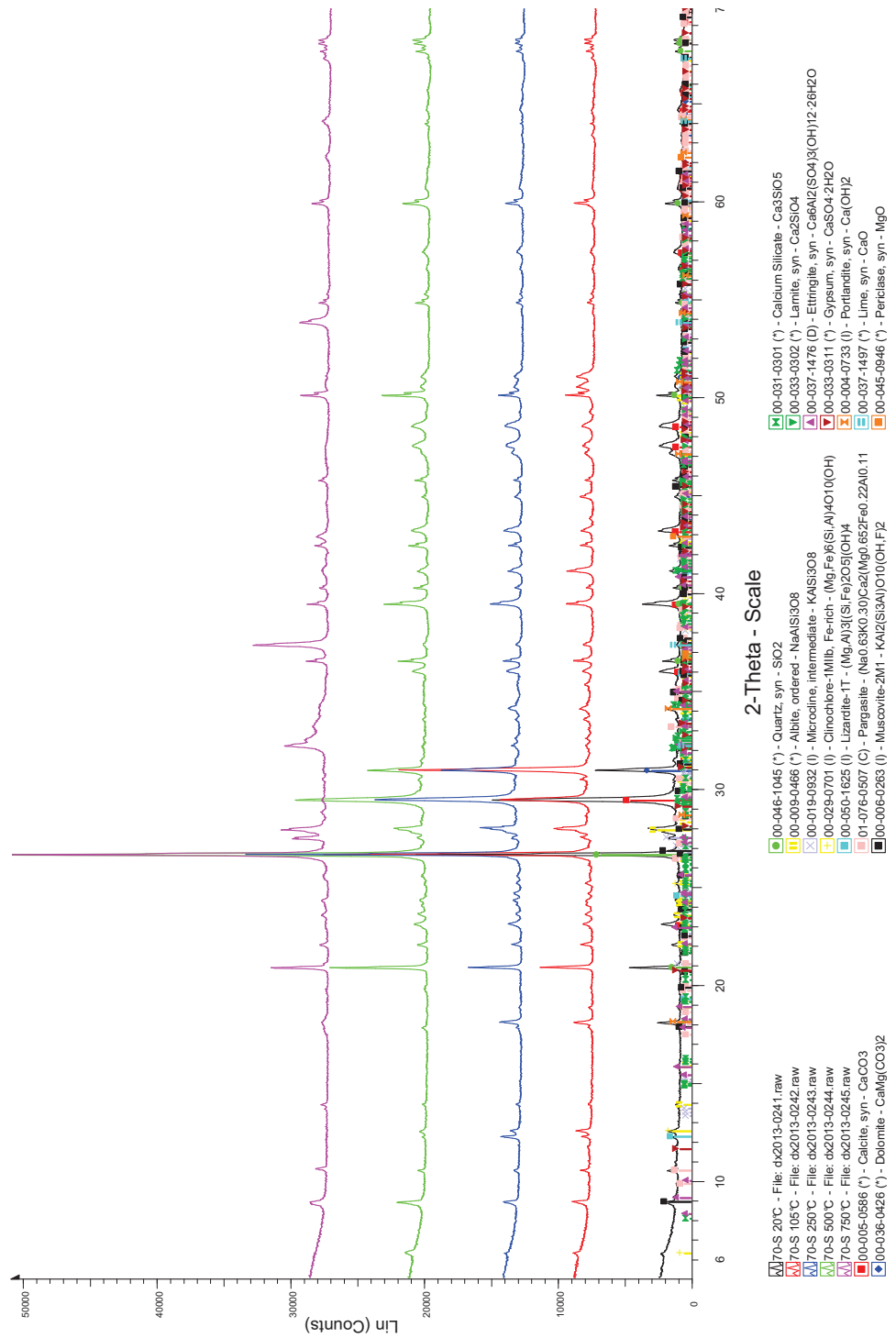


Figure C2: XRD patterns for 70-S after all exposure temperatures.

Annex C

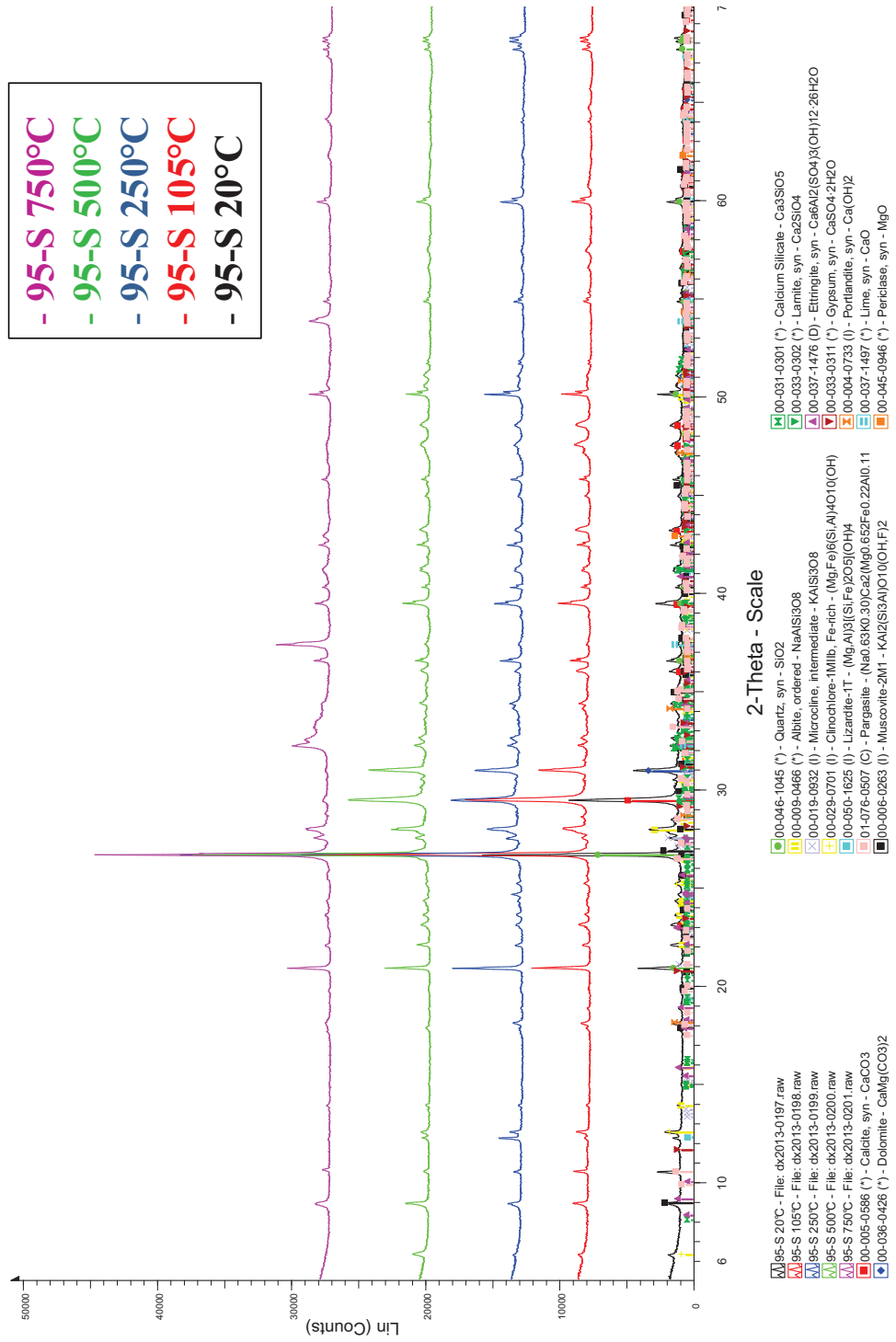


Figure C3: XRD patterns for 95-S after all exposure temperatures.

Annex C

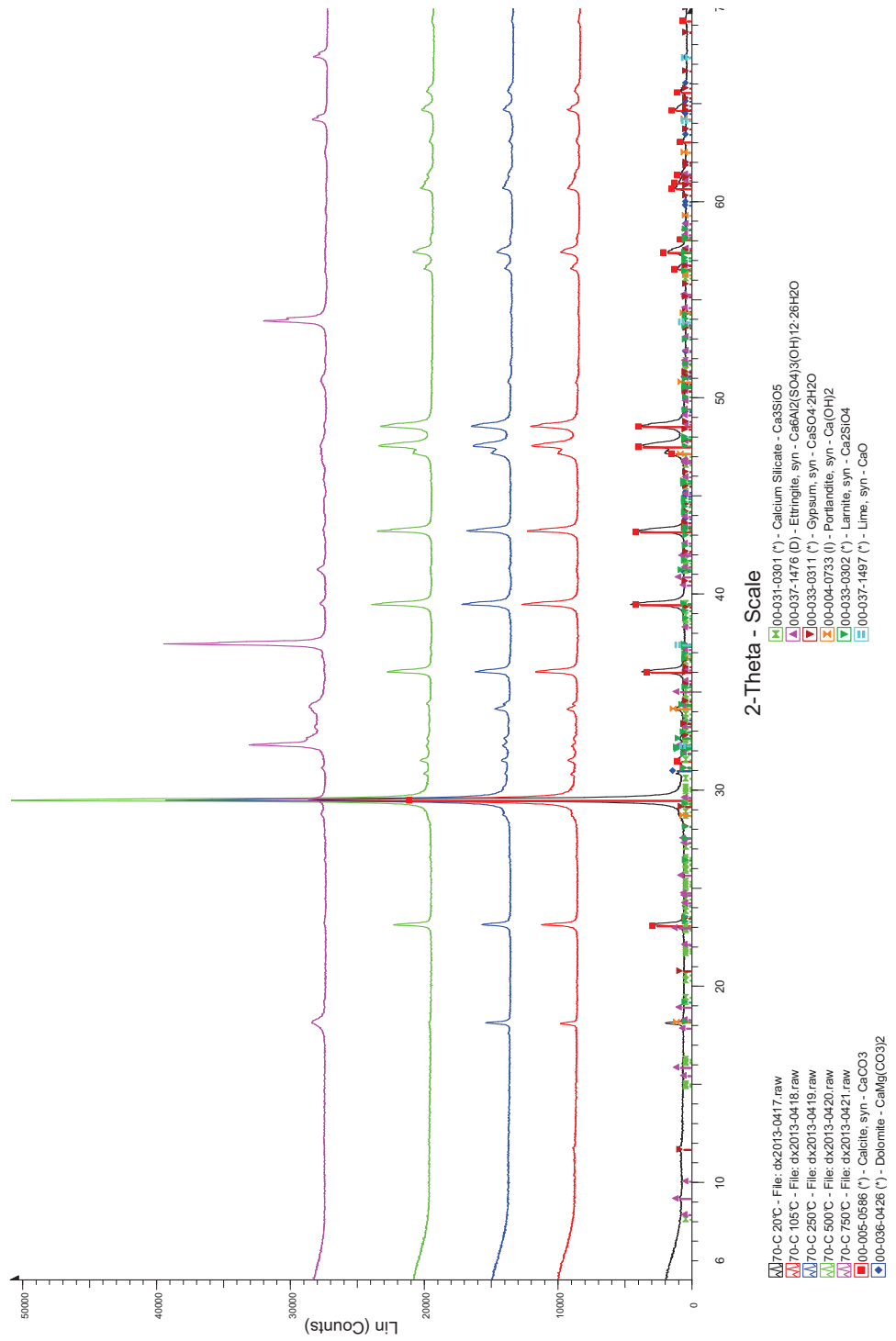


Figure C4: XRD patterns for 70-C after all exposure temperatures.

Annex C

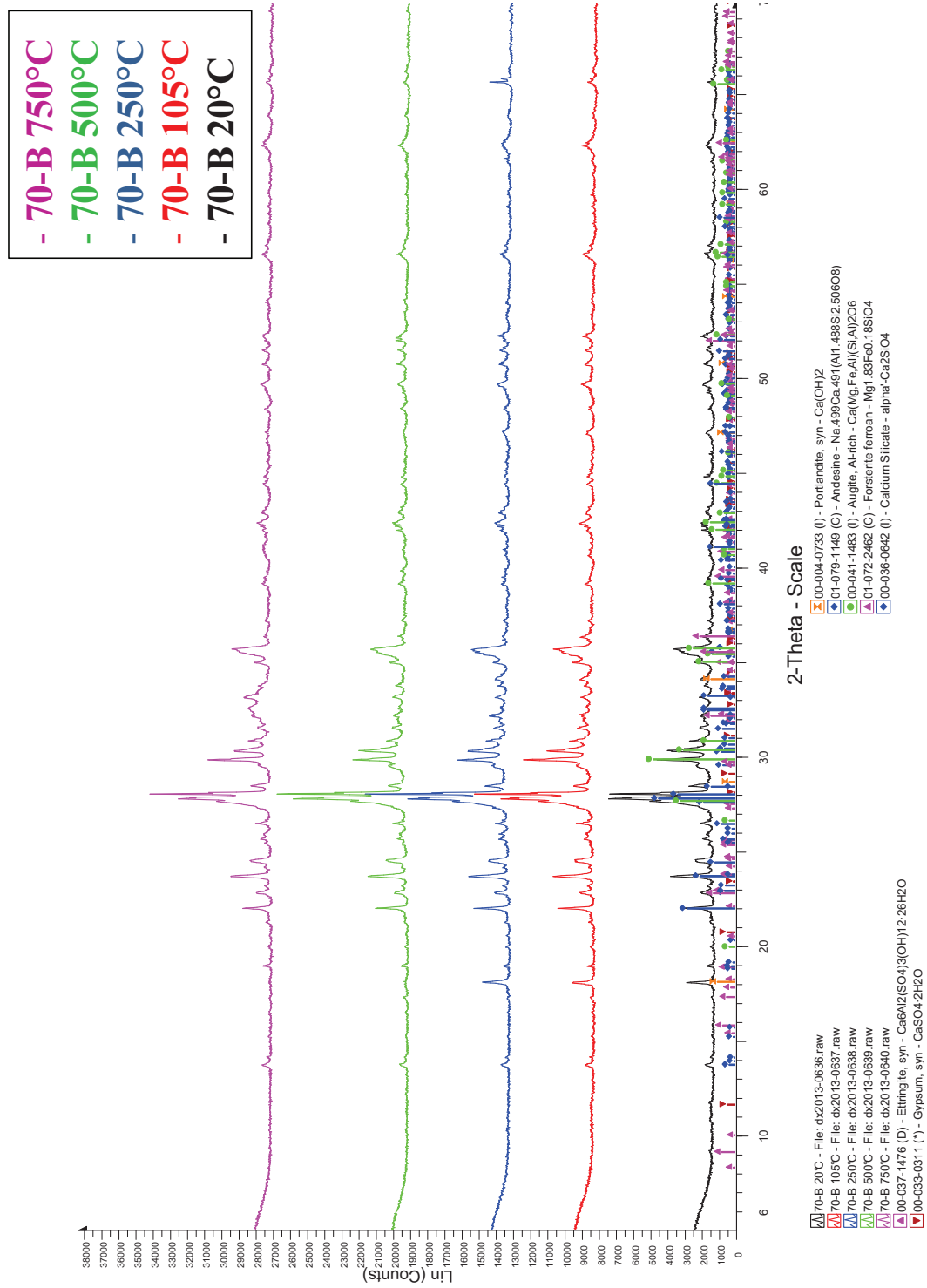


Figure C5: XRD patterns for 70-B after all exposure temperatures.

Annex C

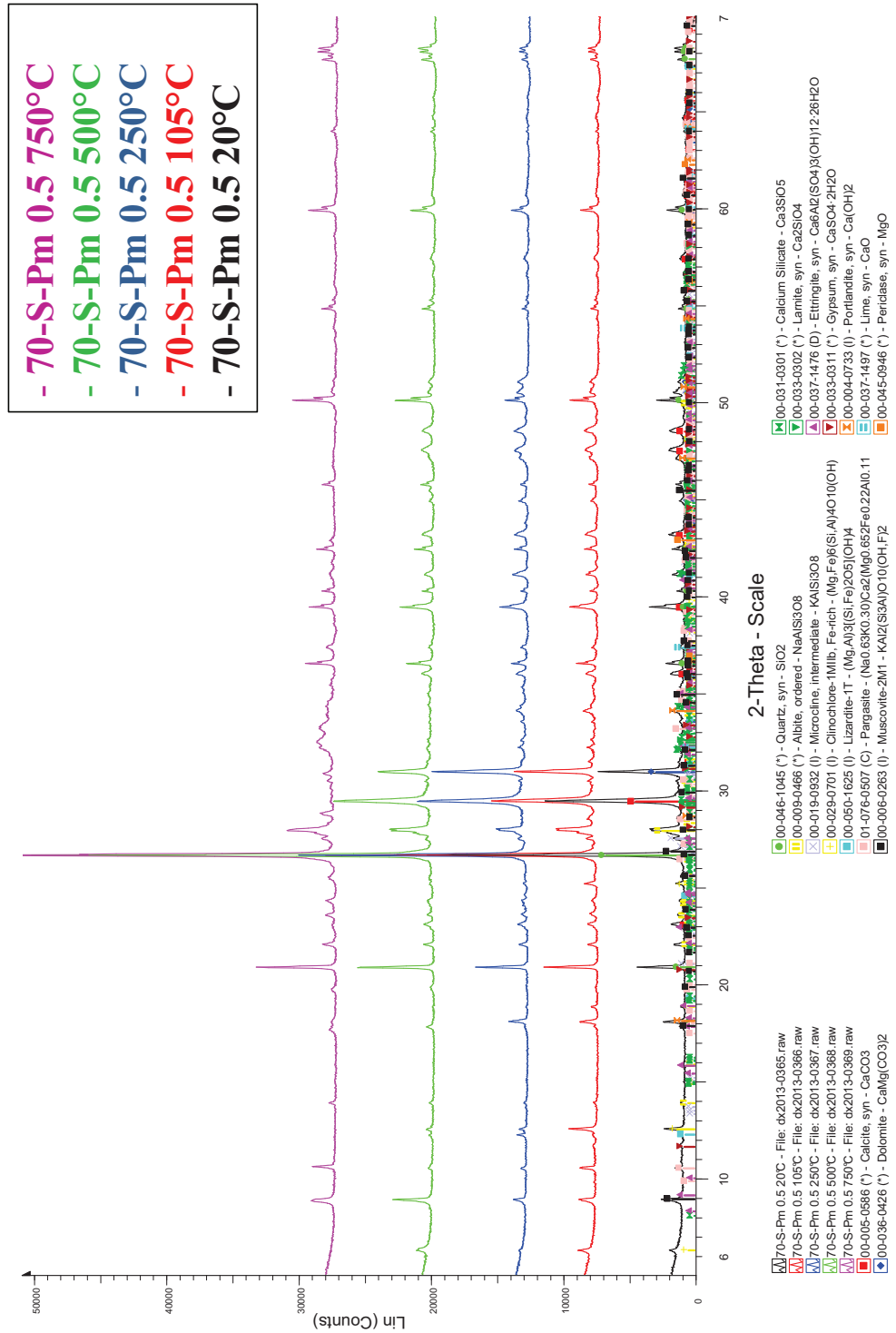


Figure C6: XRD patterns for 70-S-Pm 0.5 after all exposure temperatures.

Annex C

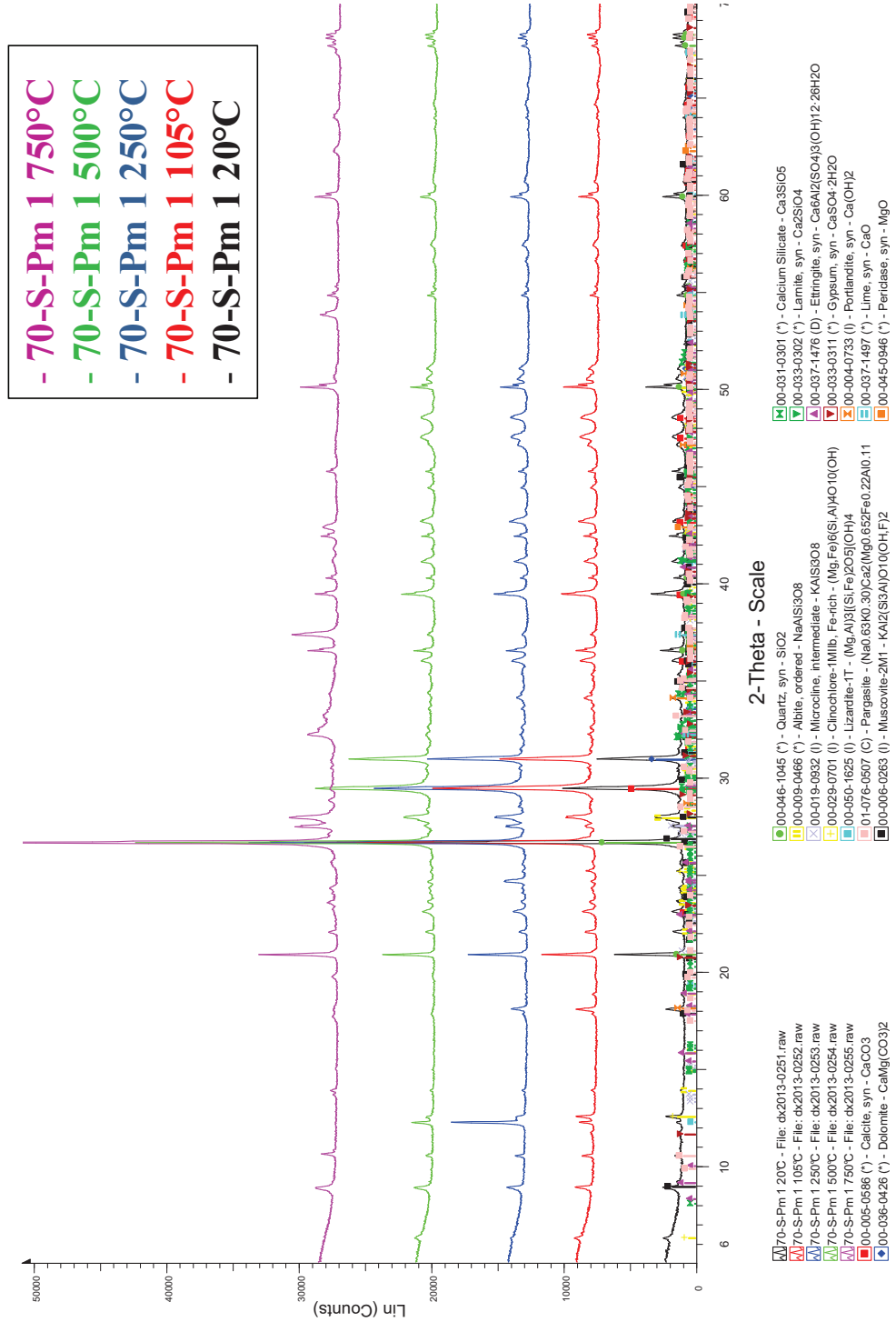


Figure C7: XRD patterns for 70-S-Pm 1 after all exposure temperatures.

Annex C

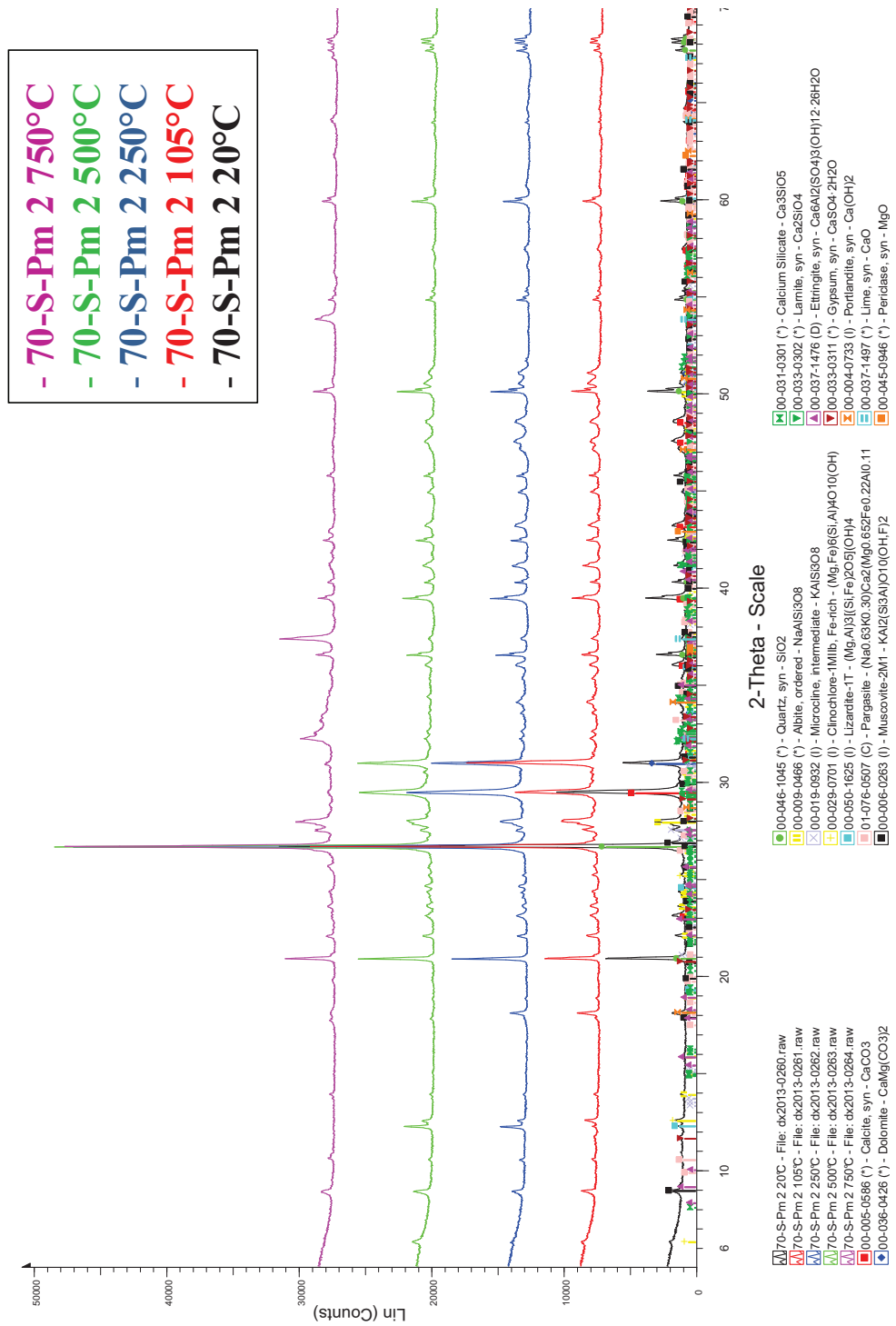


Figure C8: XRD patterns for 70-S-Pm 2 after all exposure temperatures.

Annex C

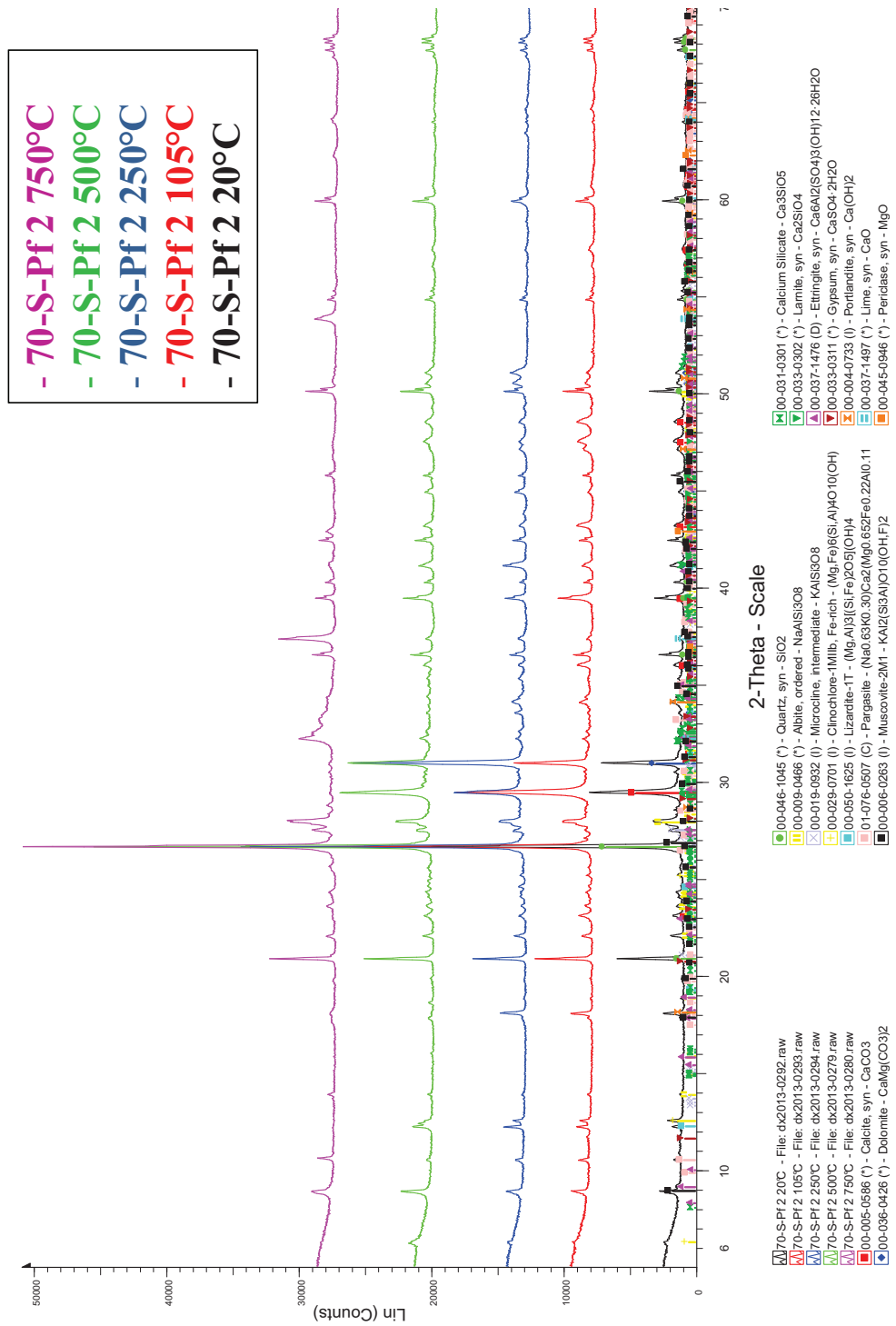


Figure C9: XRD patterns for 70-S-Pf 2 after all exposure temperatures.

Annex C

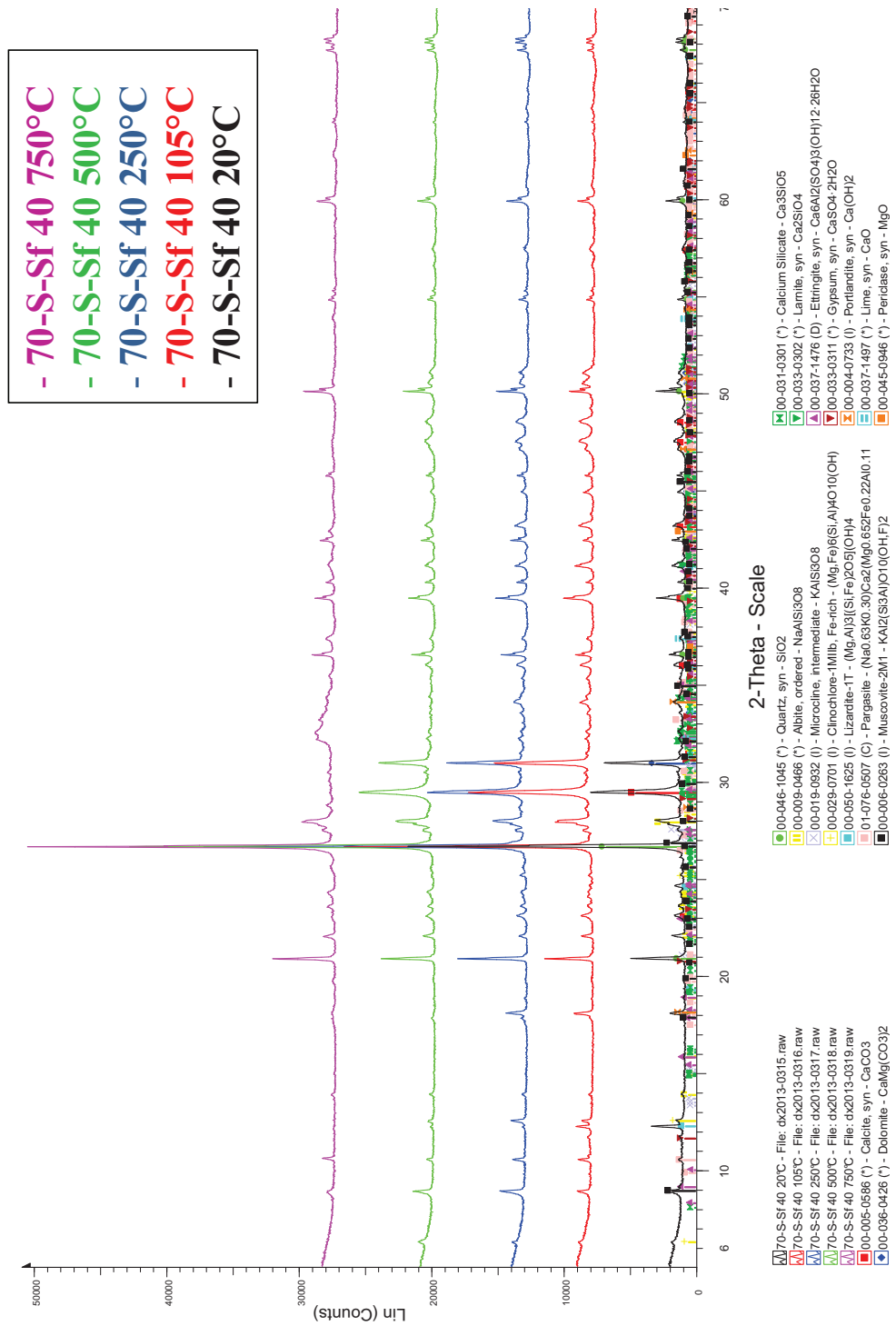


Figure C10: XRD patterns for 70-S-Sf 40 after all exposure temperatures.

Annex C

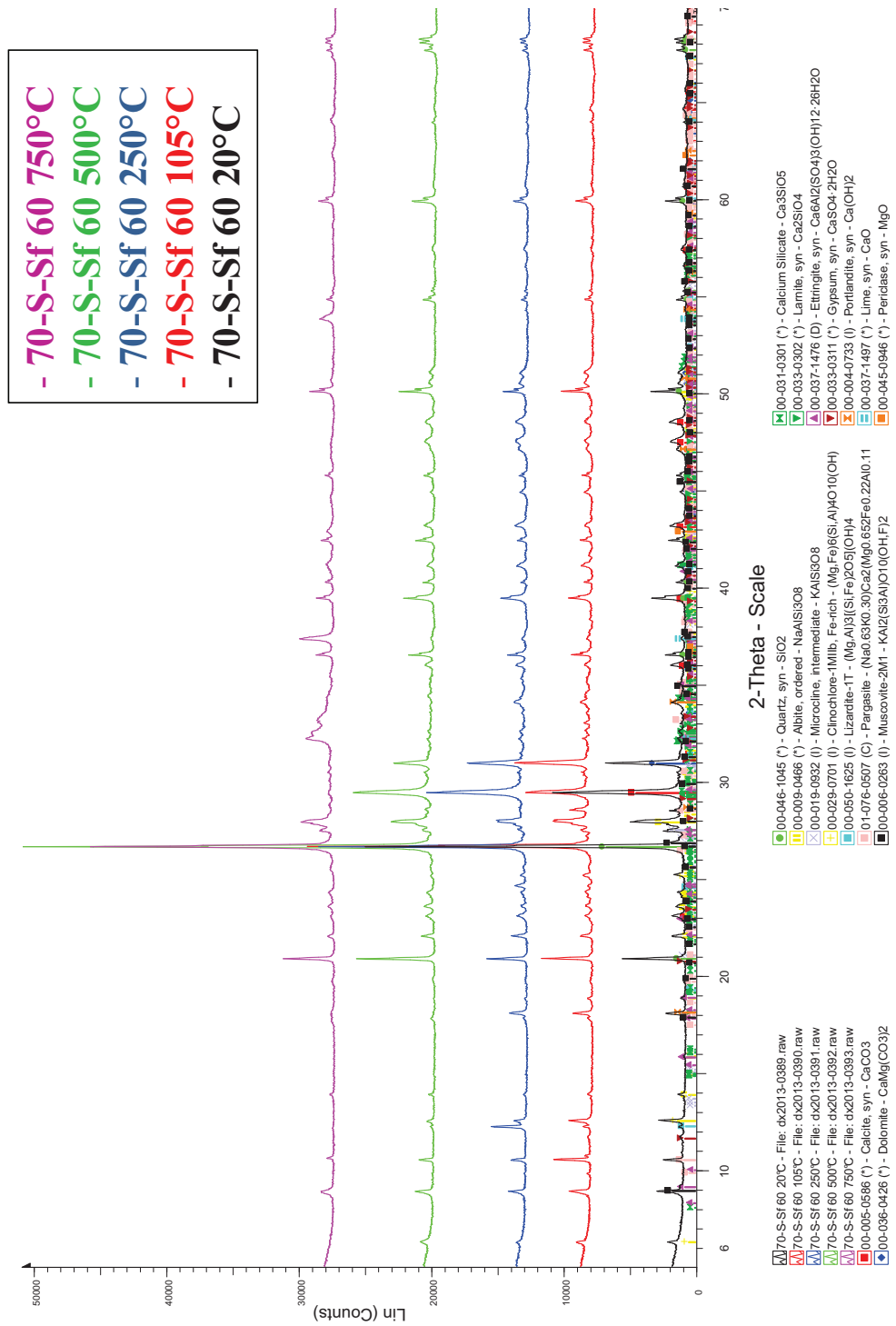


Figure C11: XRD patterns for 70-S-Sf 60 after all exposure temperatures.

Annex D

Concrete mixes cumulative and differential distributions, obtained by MIP, determined after all the exposure temperatures.

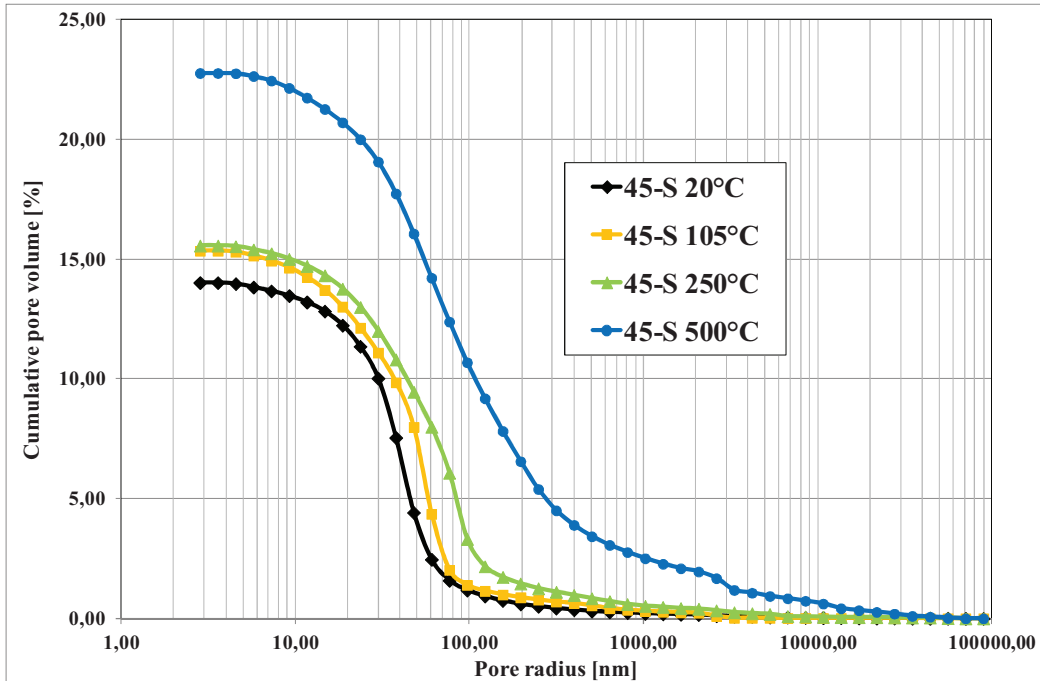


Figure D1: MIP cumulative distributions for 45-S in residual conditions.

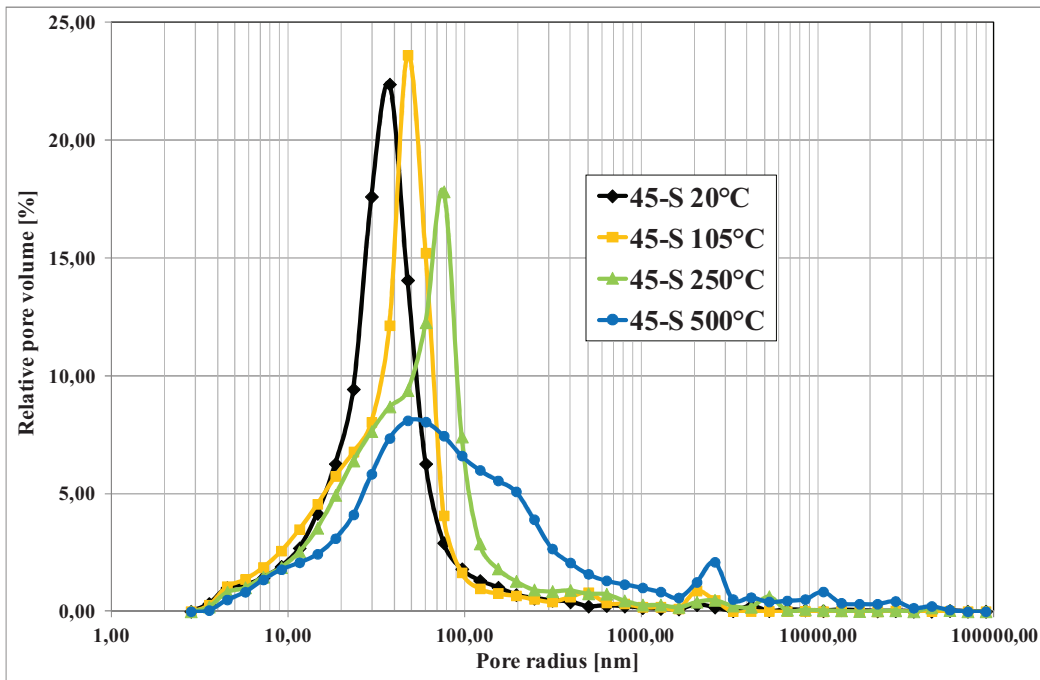


Figure D2: MIP differential distributions for 45-S in residual conditions.

Annex D

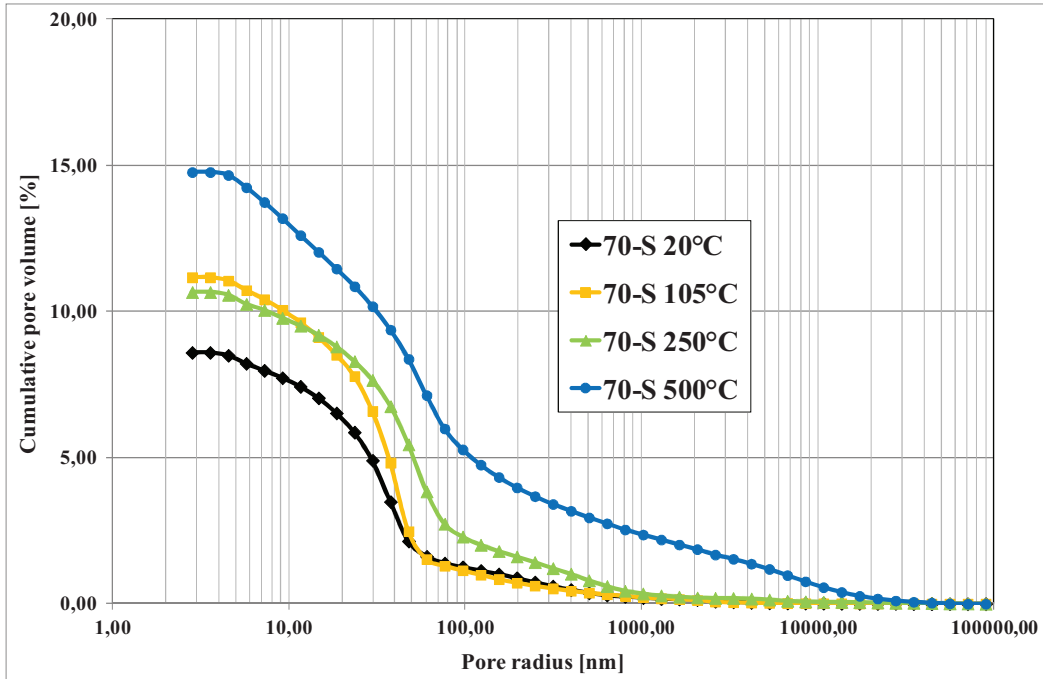


Figure D3: MIP cumulative distributions for 70-S in residual conditions.

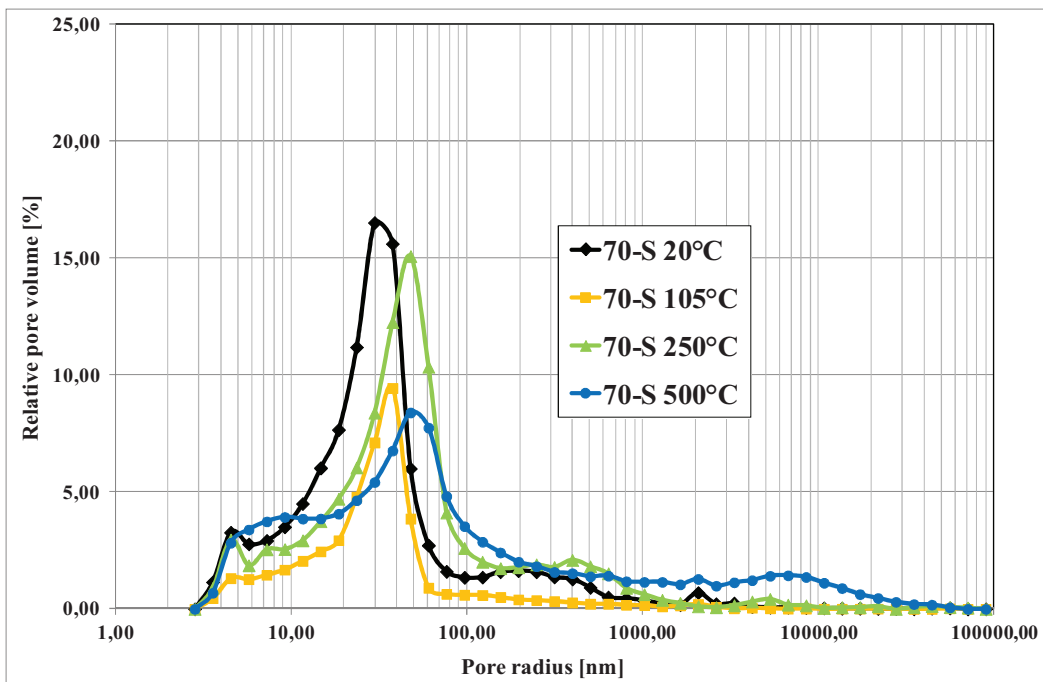


Figure D4: MIP differential distributions for 70-S in residual conditions.

Annex D

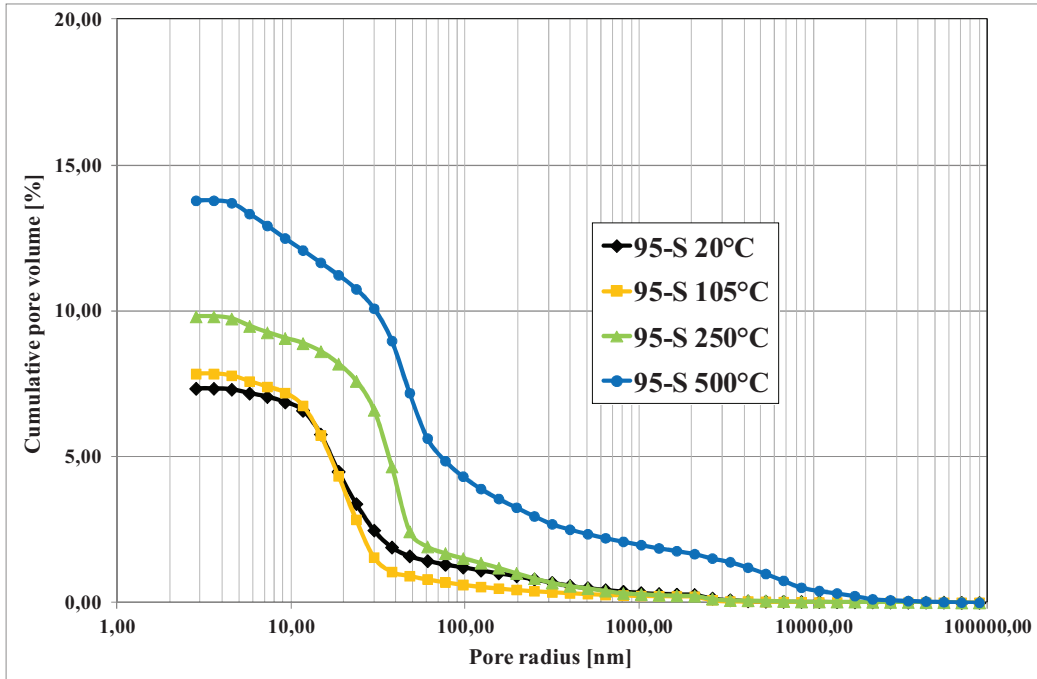


Figure D5: MIP cumulative distributions for 95-S in residual conditions.

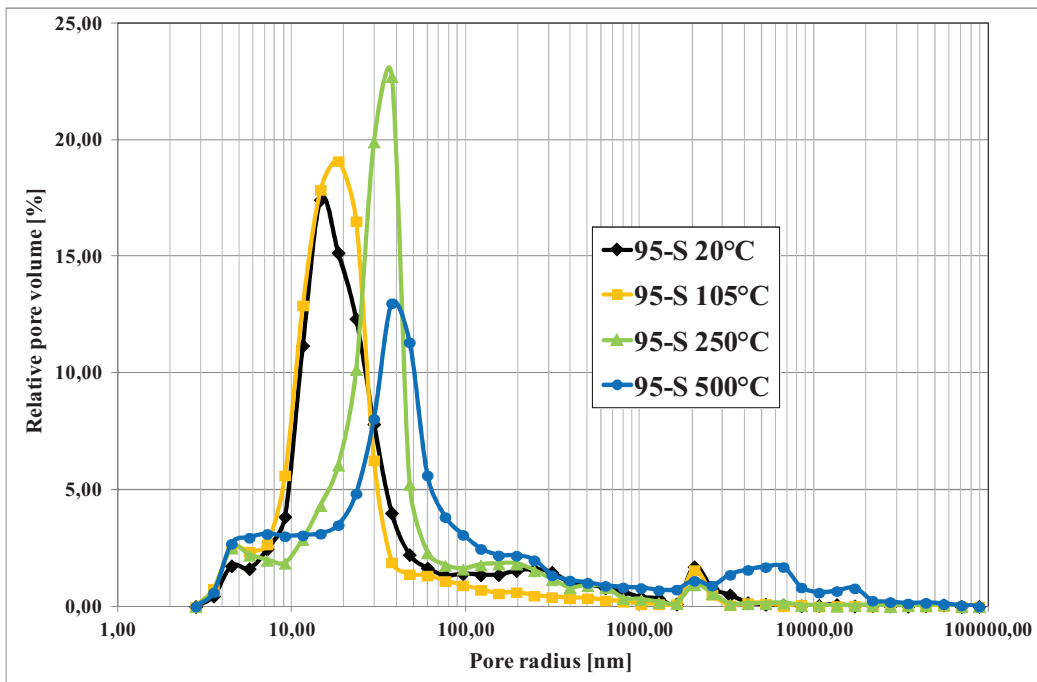


Figure D6: MIP differential distributions for 95-S in residual conditions.

Annex D

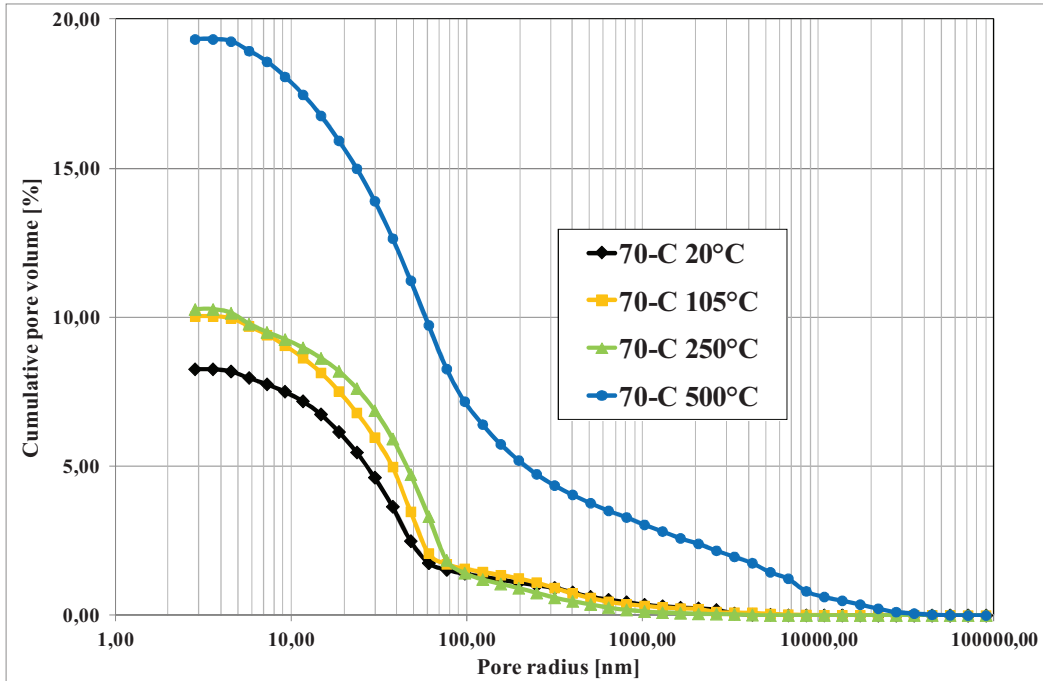


Figure D7: MIP cumulative distributions for 70-C in residual conditions.

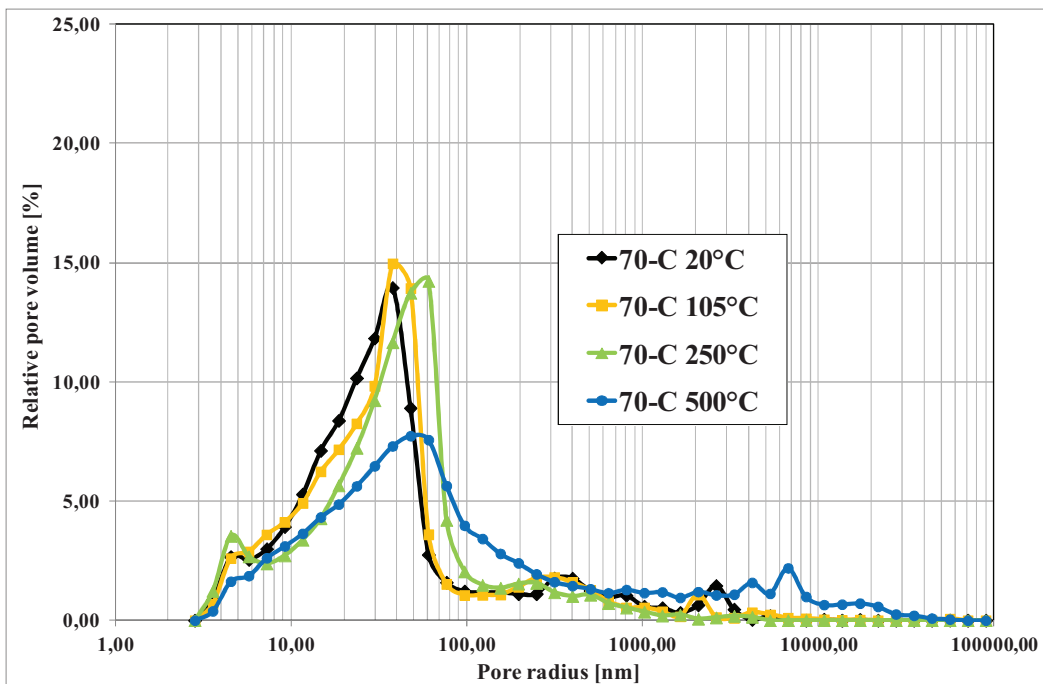


Figure D8: MIP differential distributions for 70-C in residual conditions.

Annex D

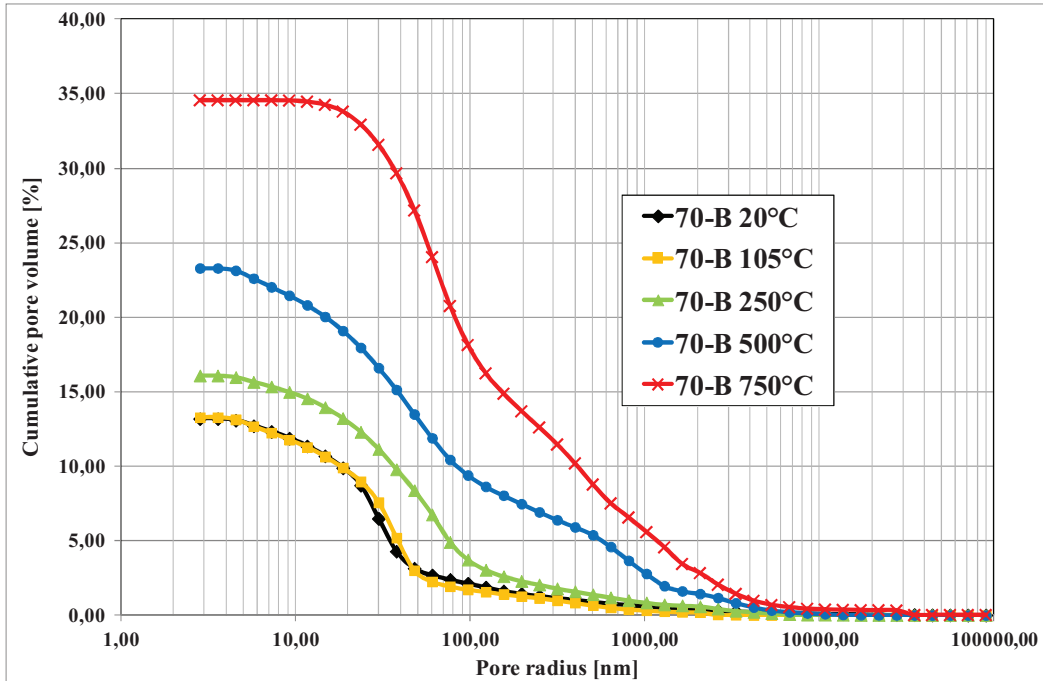


Figure D9: MIP cumulative distributions for 70-B in residual conditions.

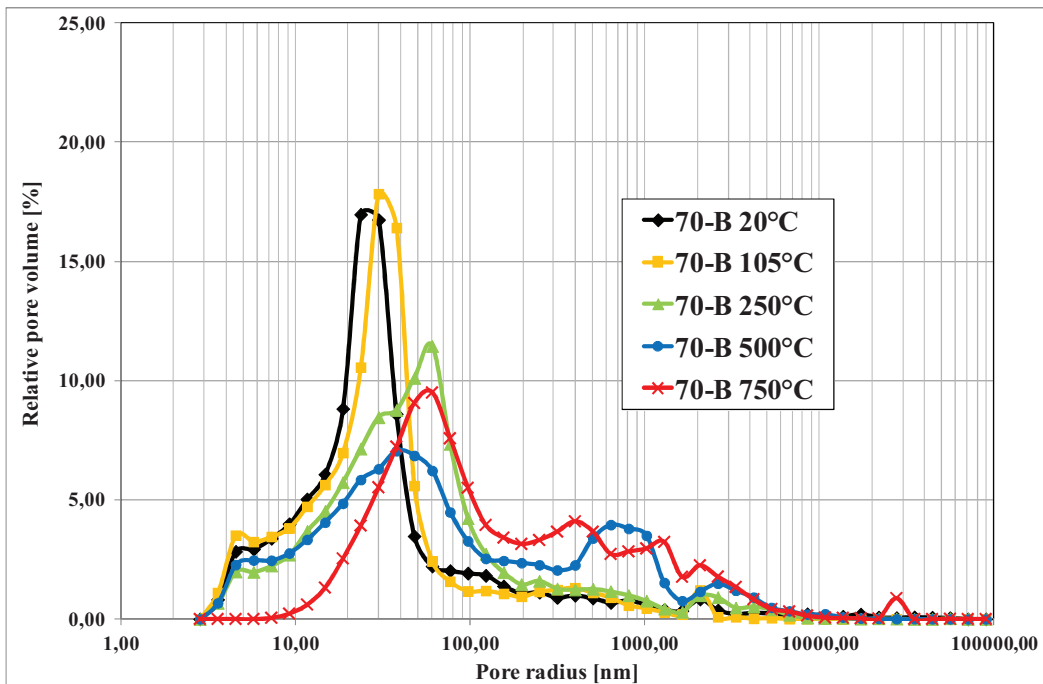


Figure D10: MIP differential distributions for 70-B in residual conditions.

Annex D

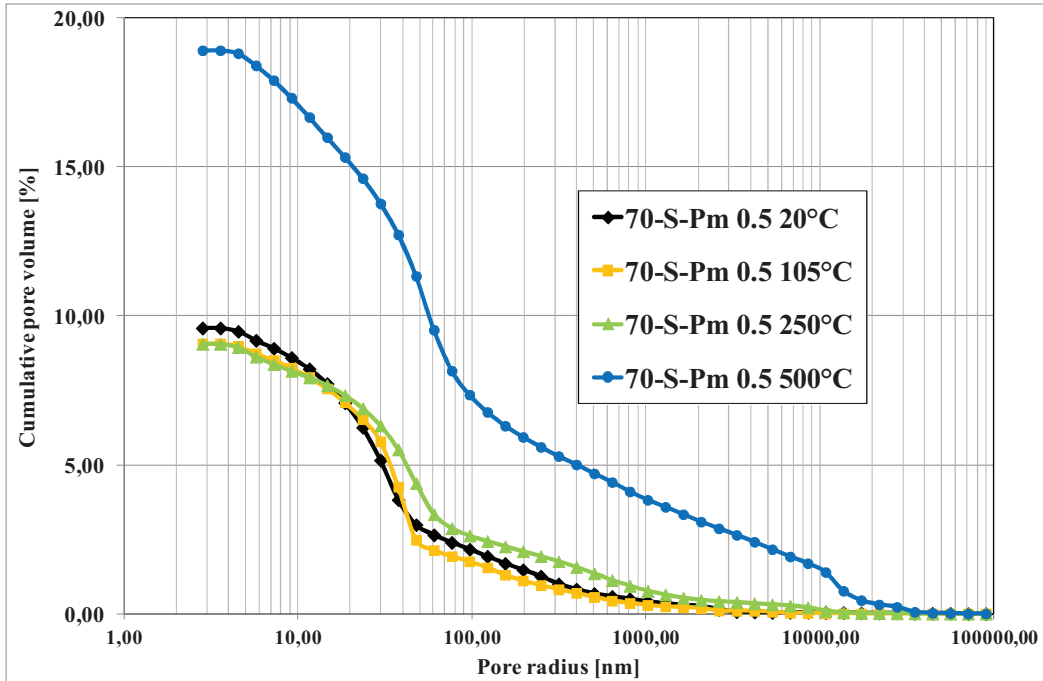


Figure D11: MIP cumulative distributions for 70-S-Pm 0.5 in residual conditions.

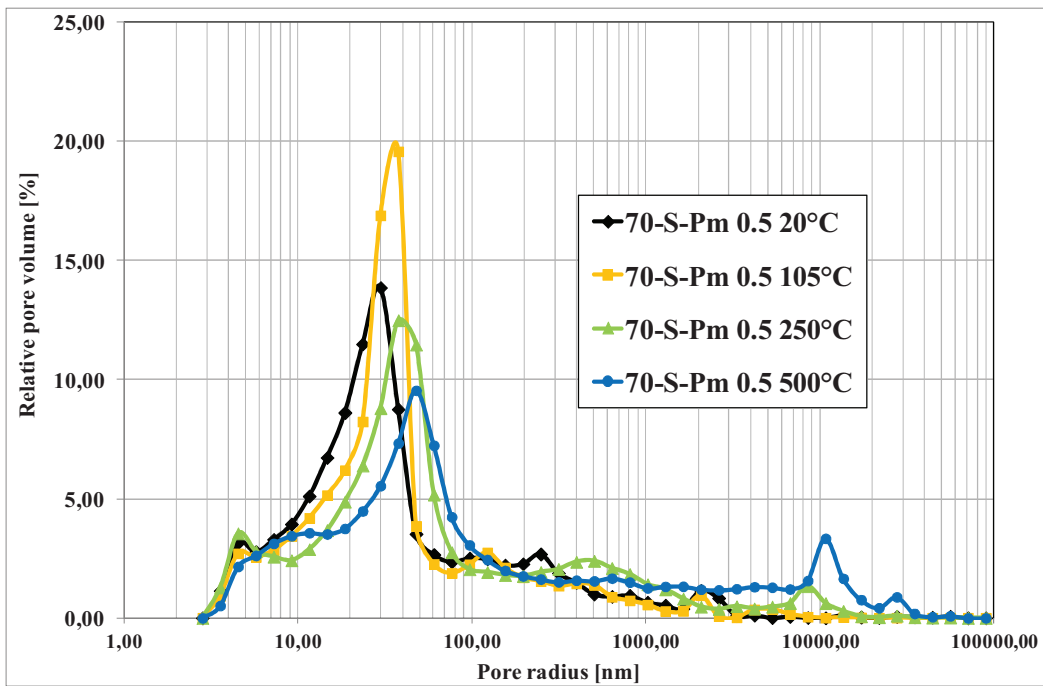


Figure D12: MIP differential distributions for 70-S-Pm 0.5 in residual conditions.

Annex D

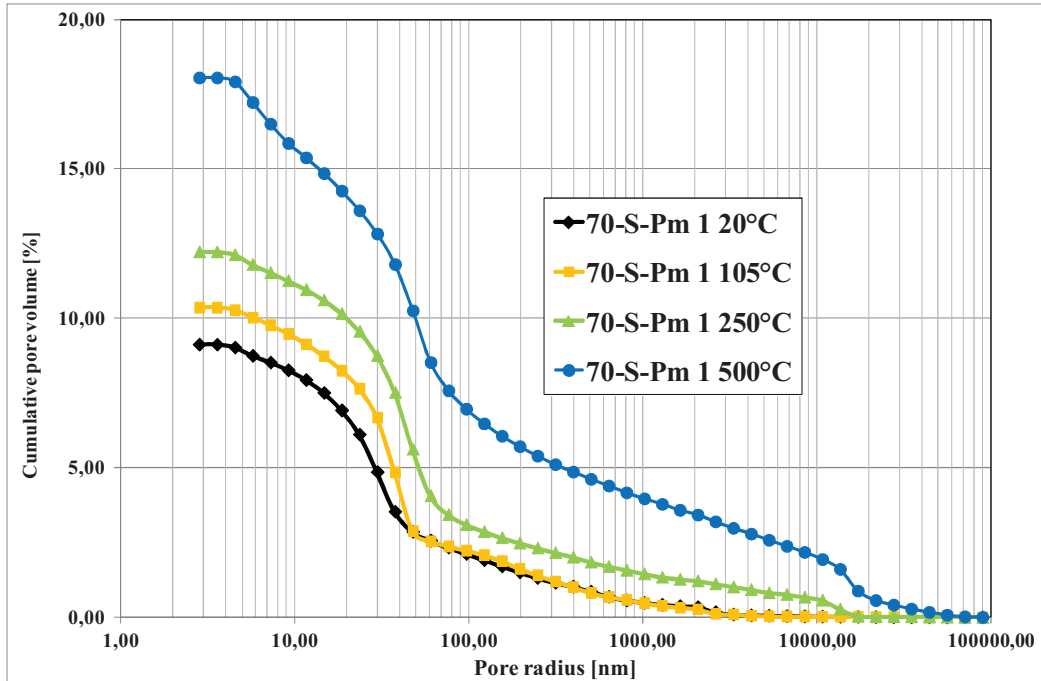


Figure D13: MIP cumulative distributions for 70-S-Pm 1 in residual conditions.

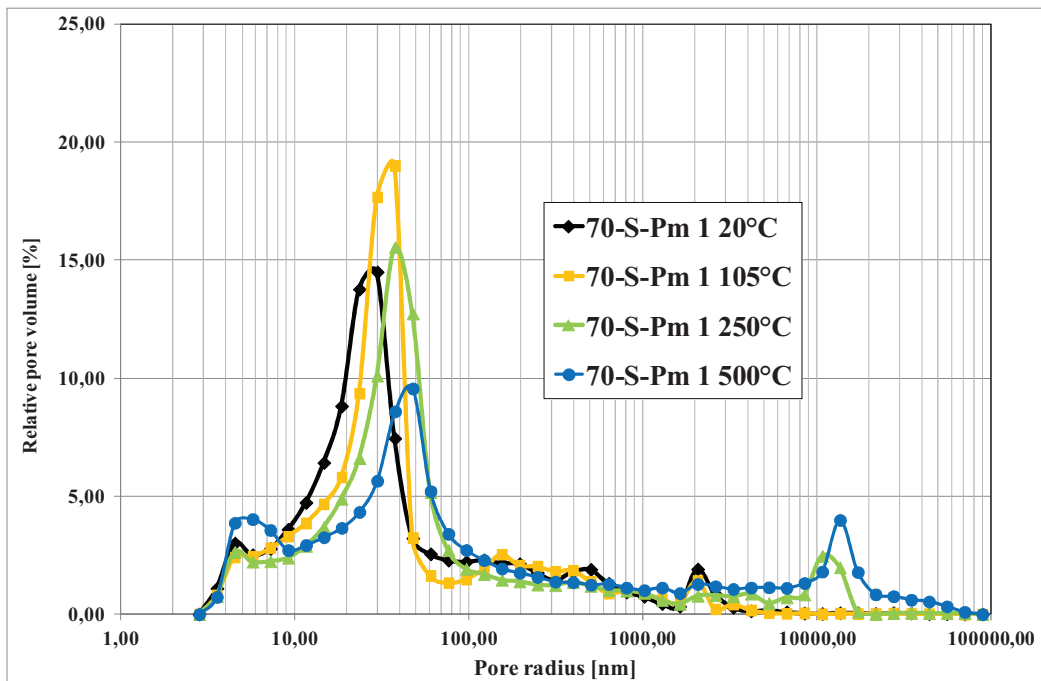


Figure D14: MIP differential distributions for 70-S-Pm 1 in residual conditions.

Annex D

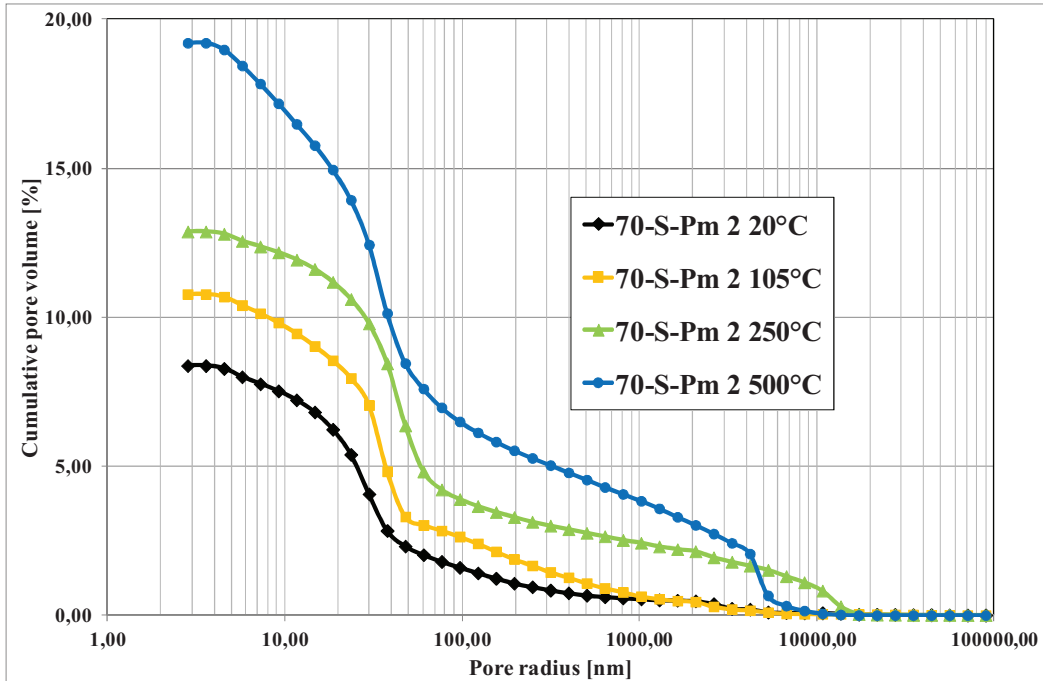


Figure D15: MIP cumulative distributions for 70-S-Pm 2 in residual conditions.

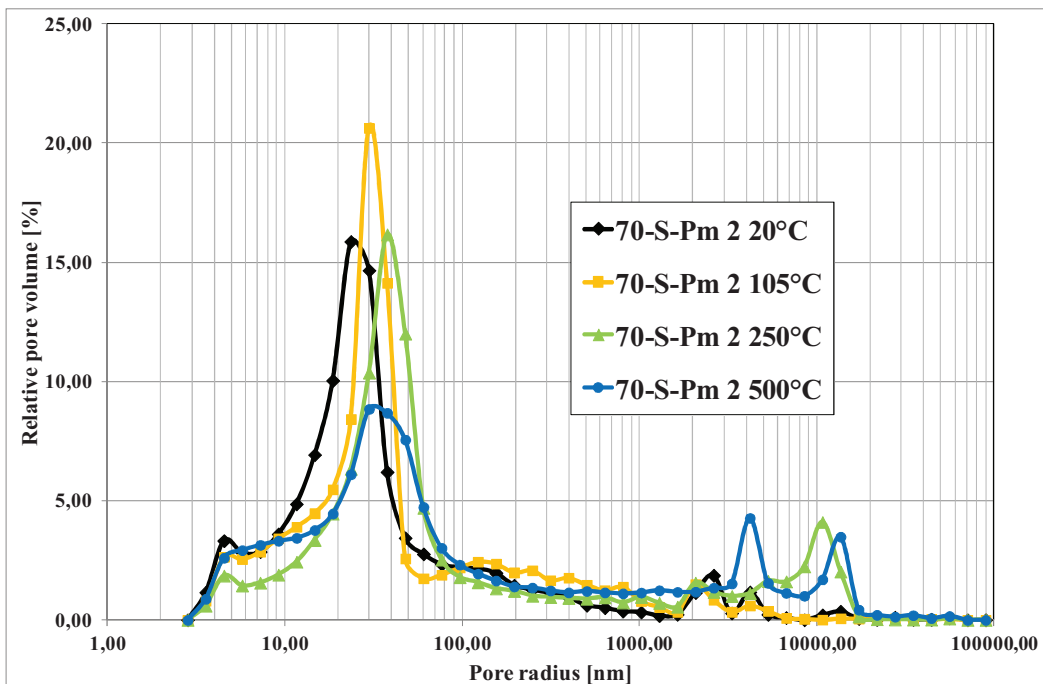


Figure D16: MIP differential distributions for 70-S-Pm 2 in residual conditions.

Annex D

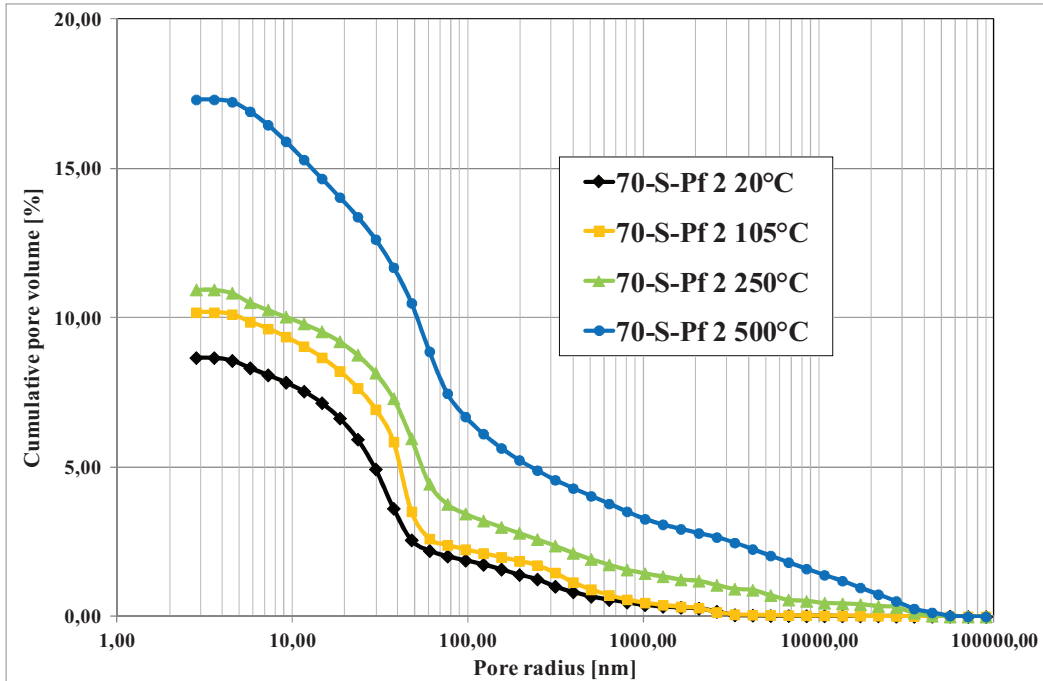


Figure D17: MIP cumulative distributions for 70-S-Pf 2 in residual conditions.

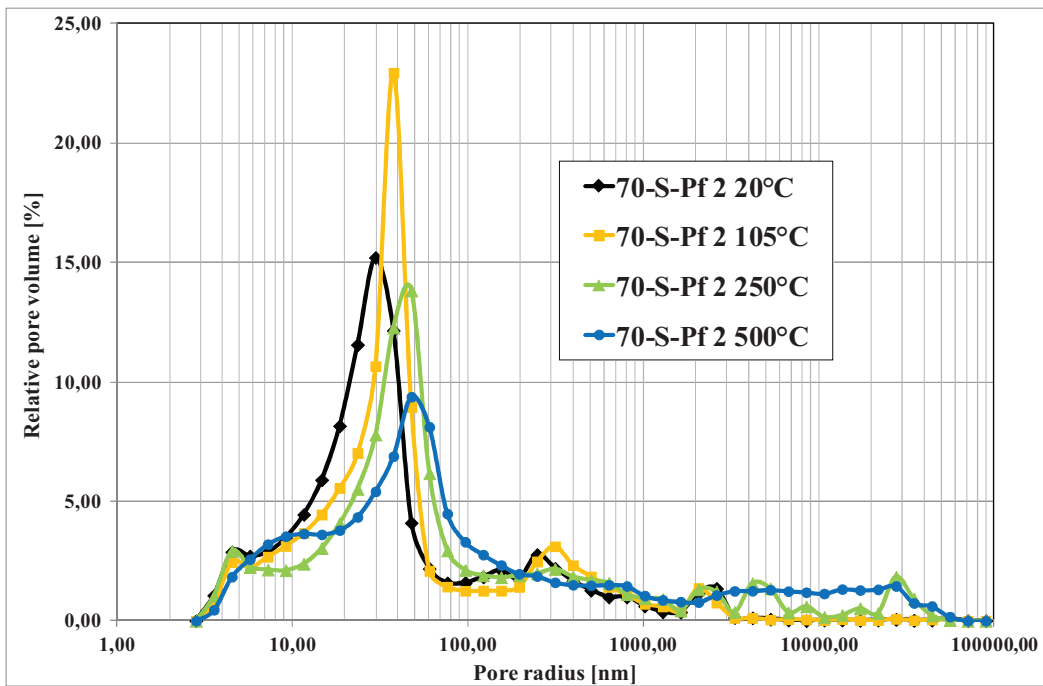


Figure D18: MIP differential distributions for 70-S-Pf 2 in residual conditions.

Annex D

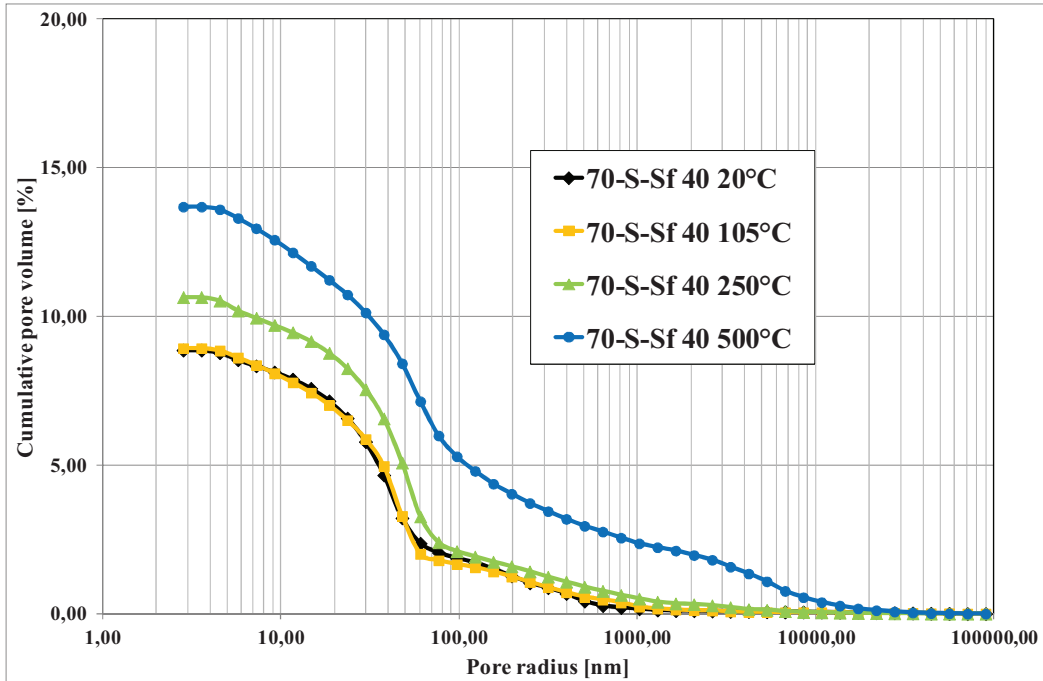


Figure D19: MIP cumulative distributions for 70-S-Sf 40 in residual conditions.

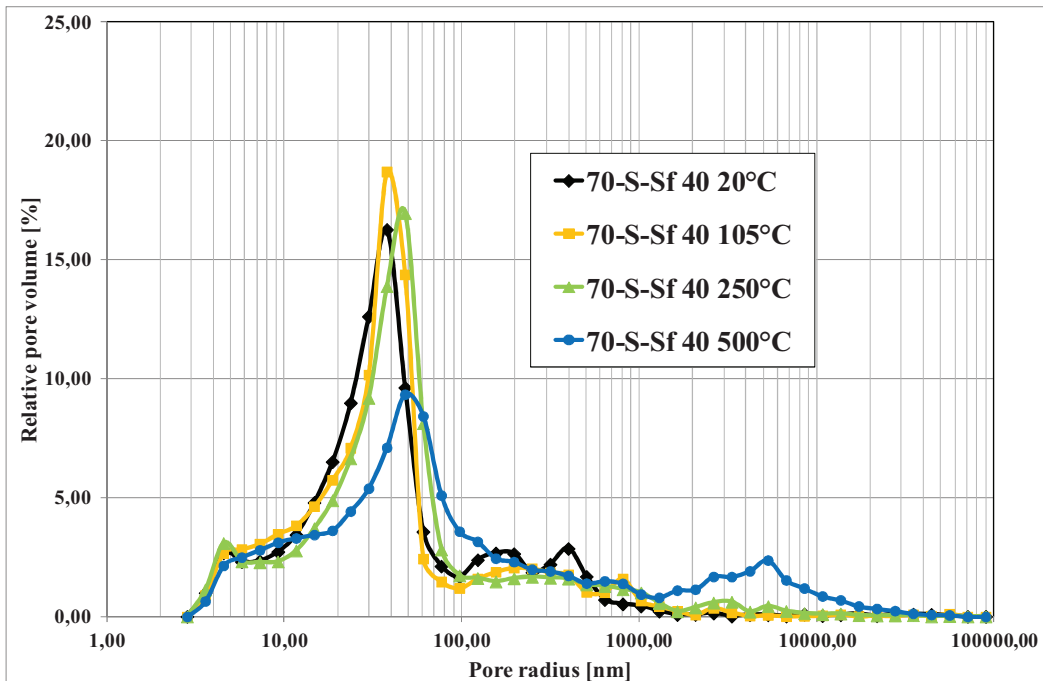


Figure D20: MIP differential distributions for 70-S-Sf 40 in residual conditions.

Annex D

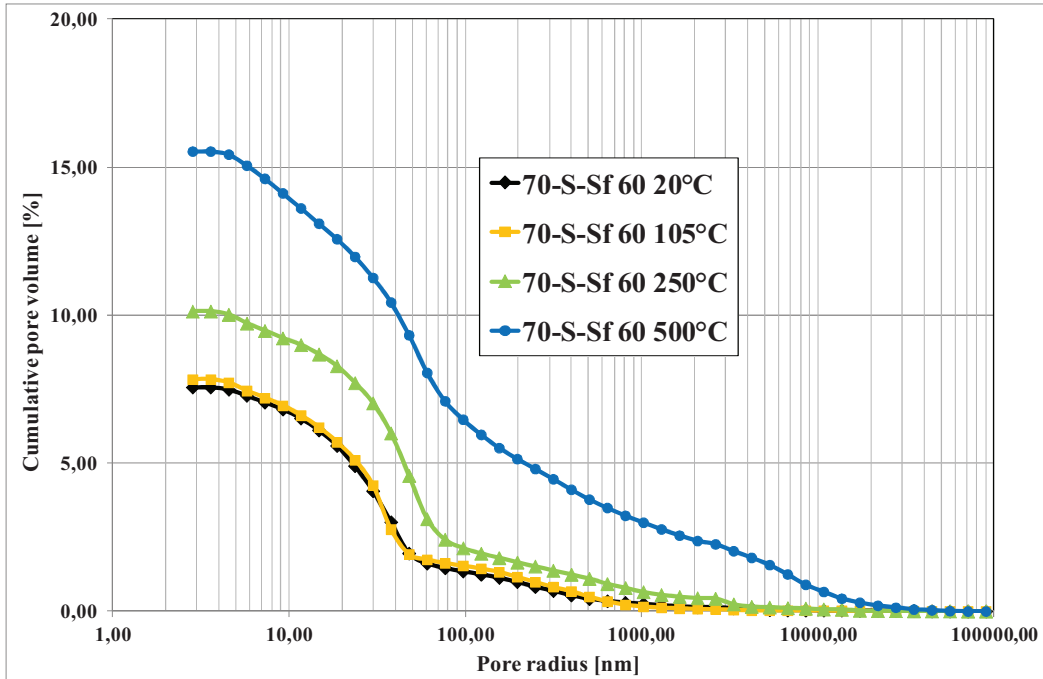


Figure D21: MIP cumulative distributions for 70-S-Sf 60 in residual conditions.

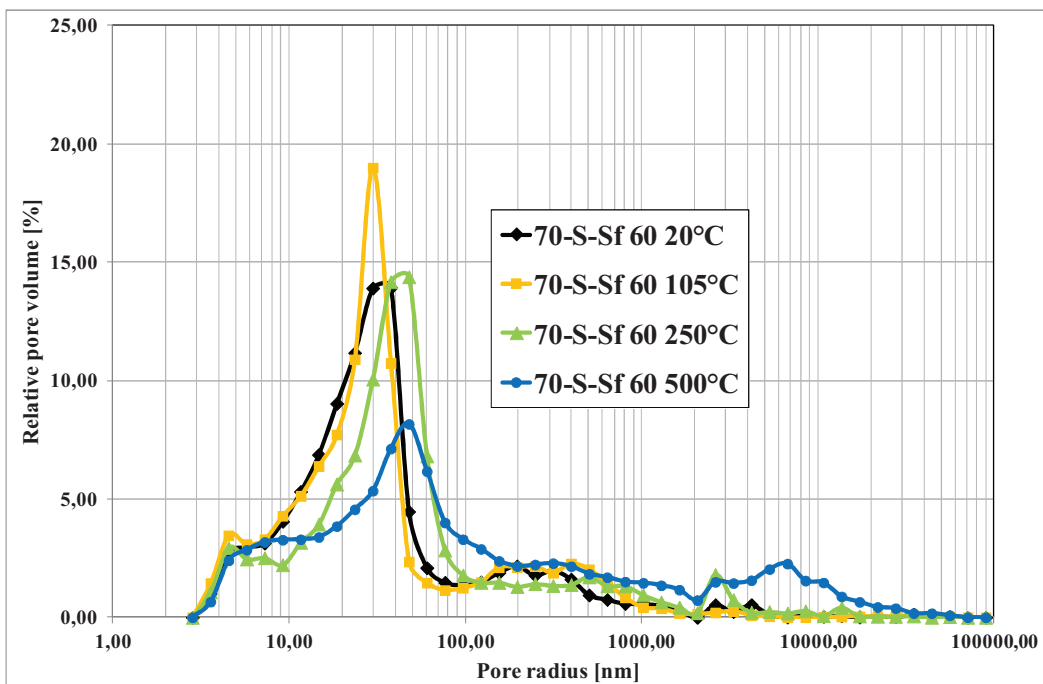


Figure D22: MIP differential distributions for 70-S-Sf 60 in residual conditions.

Annex E

Annex E

Concretes images obtained by SEM, determined after all the exposure temperatures.

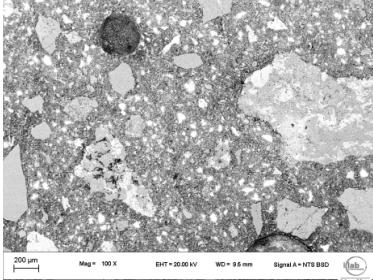
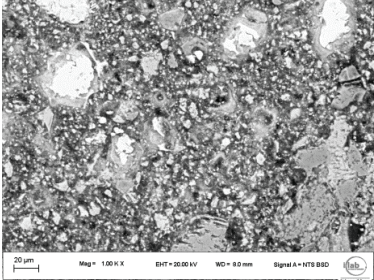
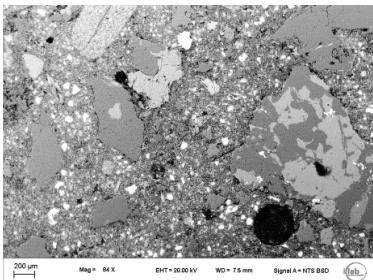
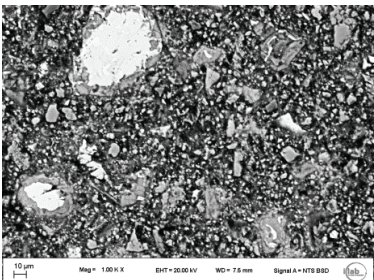
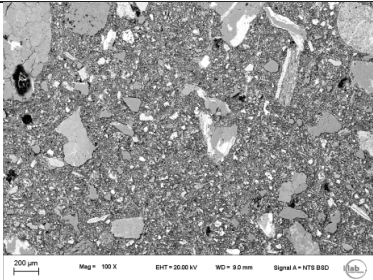
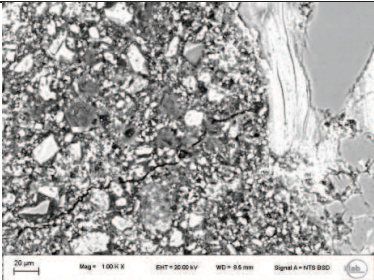
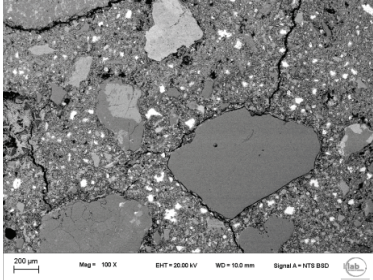
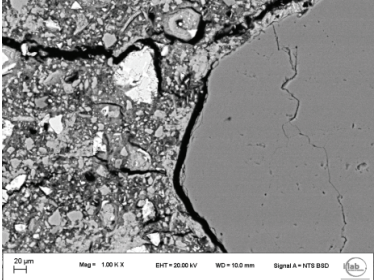
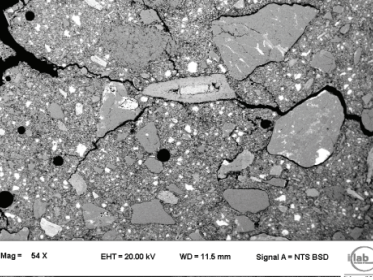
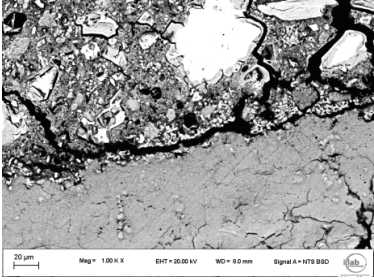
Mix	45-S 100X	45-S 1000X
20°C		
105°C		
250°C		
500°C		
750°C		

Figure E1: SEM images 45-S at 100X and 1000X magnitude after all exposure temperatures.

Annex E

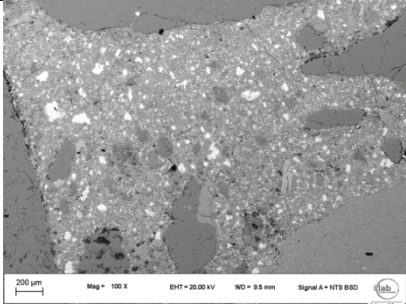
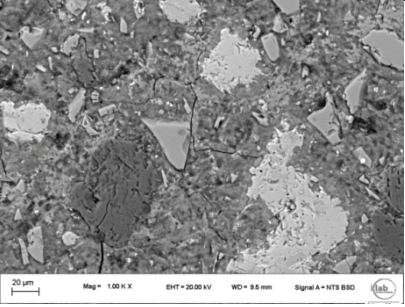
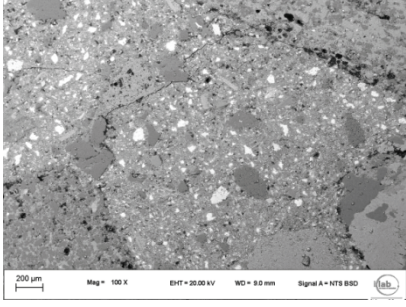
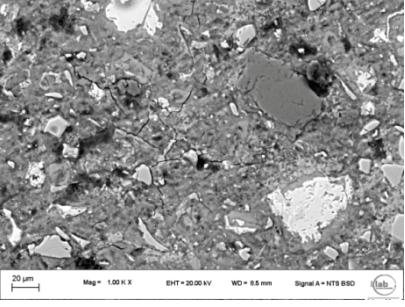
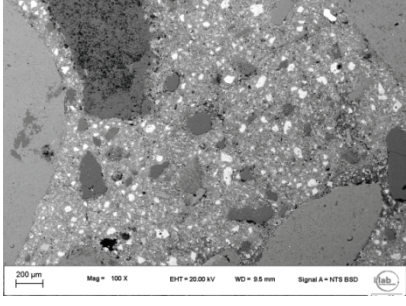
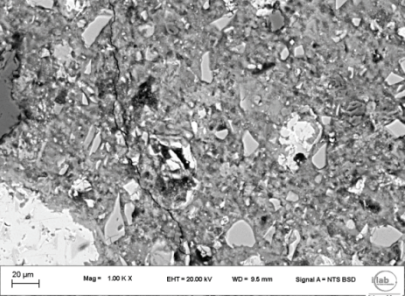
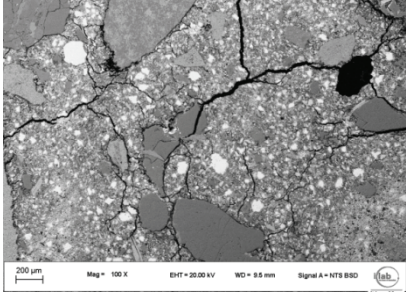
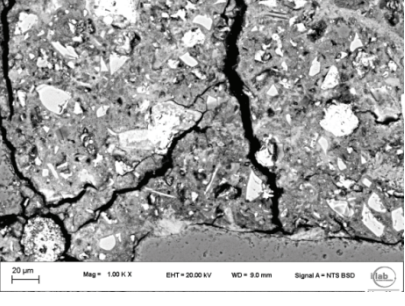
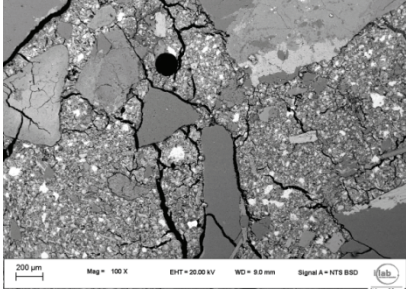
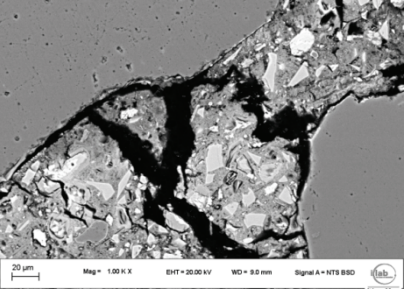
Mix	70-S images 100X	70-S images 1000X
20°C		
105°C		
250°C		
500°C		
750°C		

Figure E2: SEM images 70-S at 100X and 1000X magnitude after all exposure temperatures.

Annex E

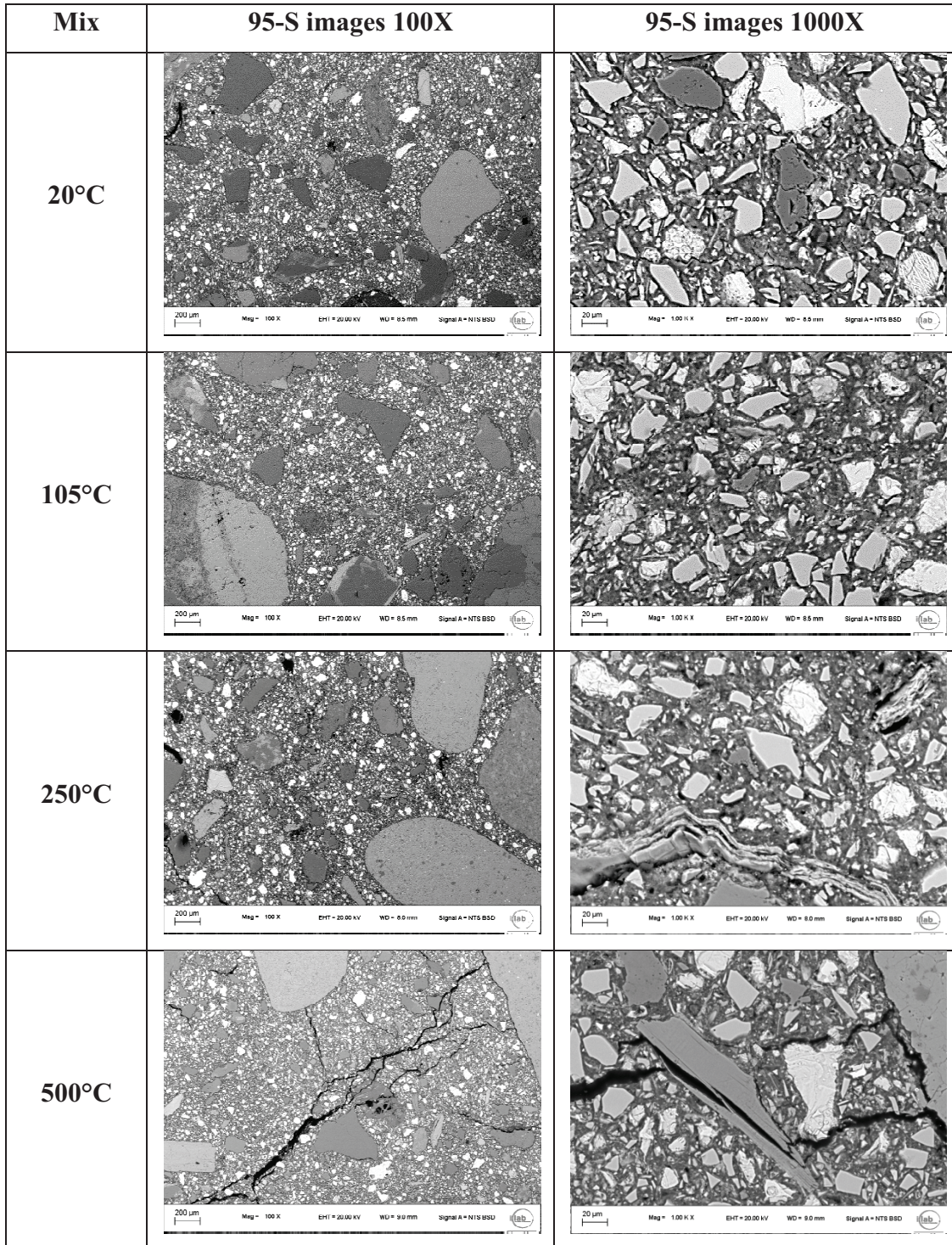


Figure E3: SEM images 95-S at 100X and 1000X magnitude after all exposure temperatures.

Annex E

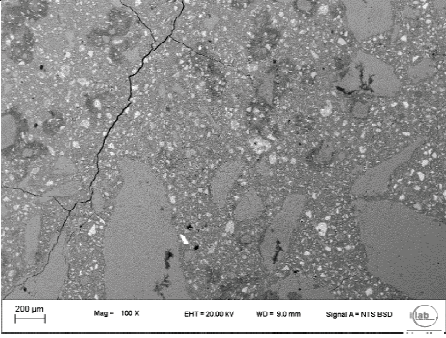
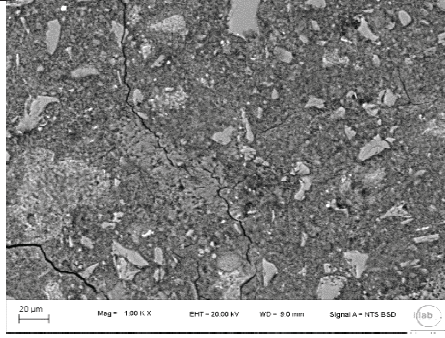
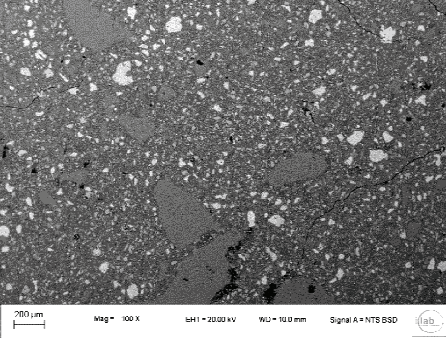
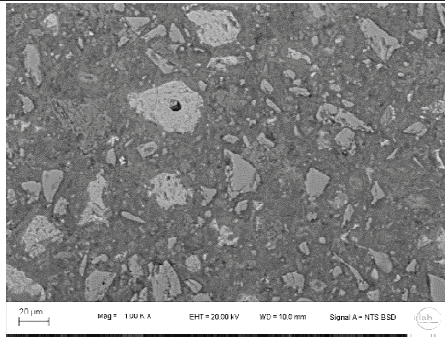
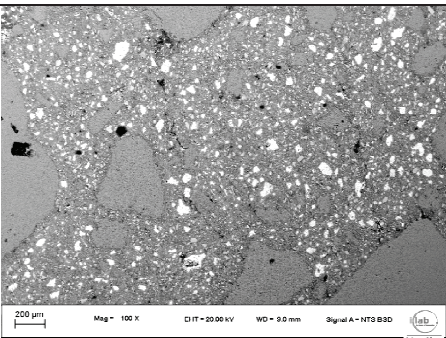
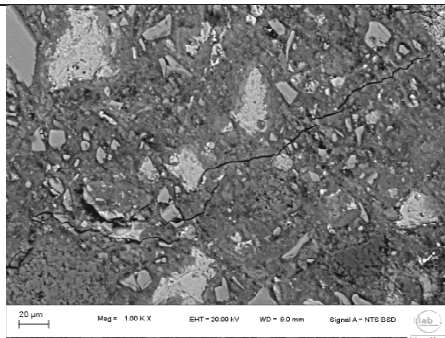
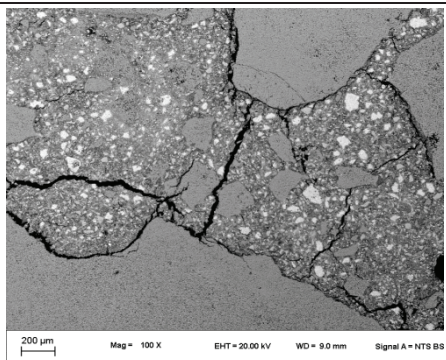
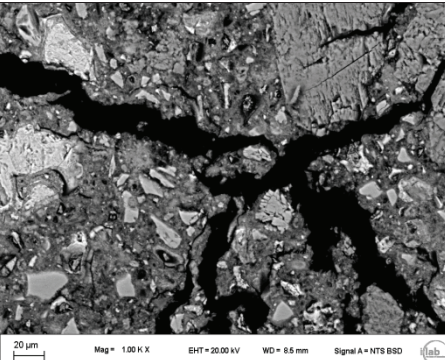
Mix	70-C images 100X	70-C images 1000X
20°C		
105°C		
250°C		
500°C		

Figure E4: SEM images 70-C at 100X and 1000X magnitude after all exposure temperatures.

Annex E

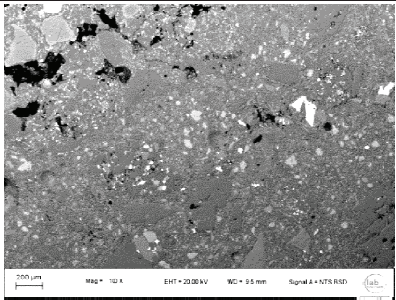
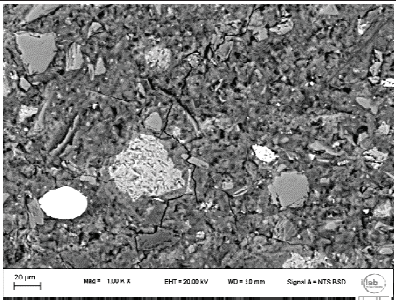
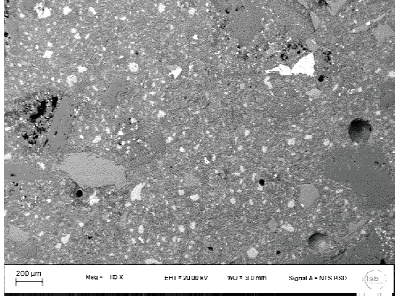
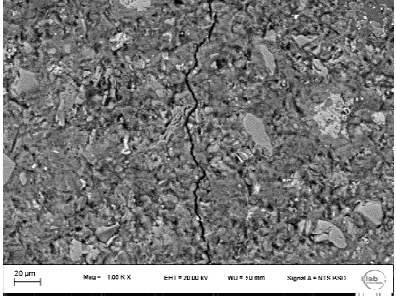
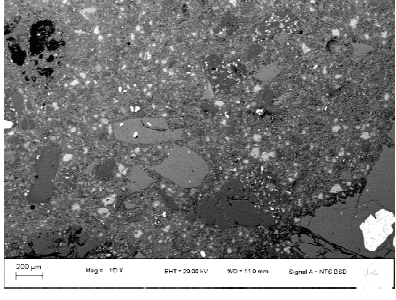
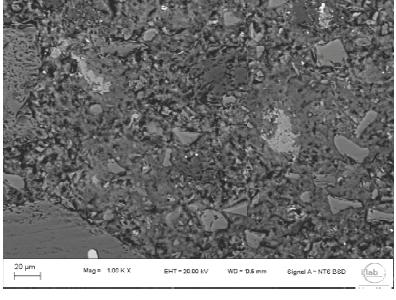
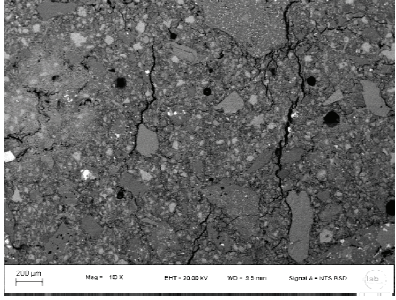
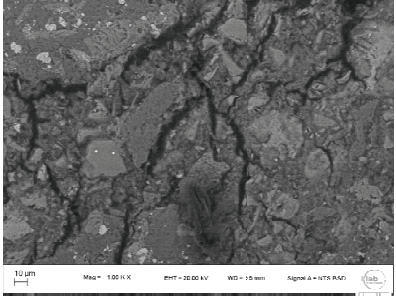
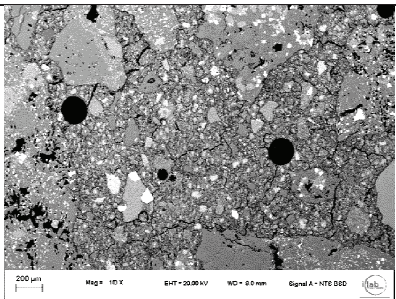
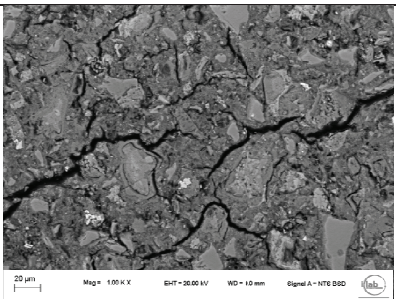
Mix	70-B images 100X	70-B images 1000X
20°C		
105°C		
250°C		
500°C		
750°C		

Figure E5: SEM images 70-B at 100X and 1000X magnitude after all exposure temperatures.

Annex E

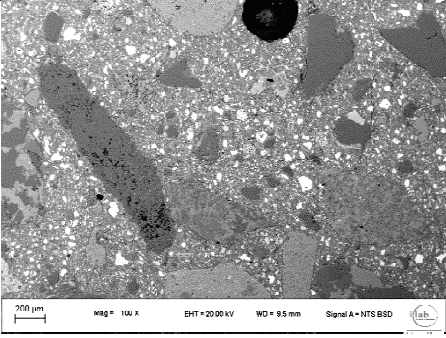
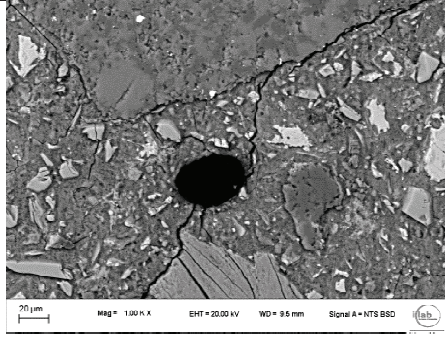
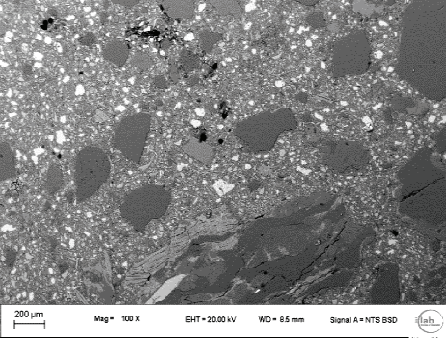
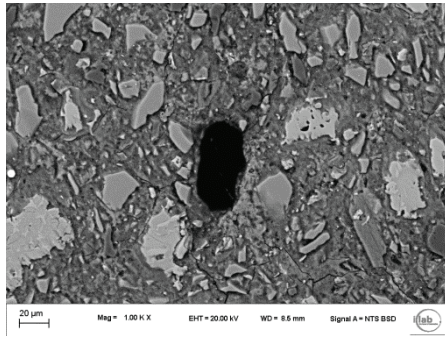
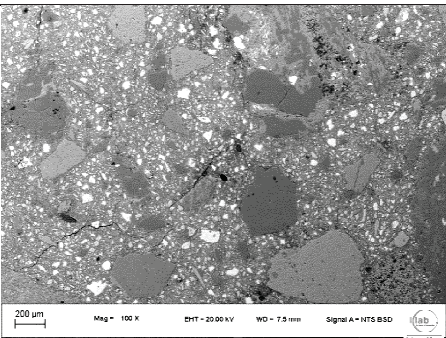
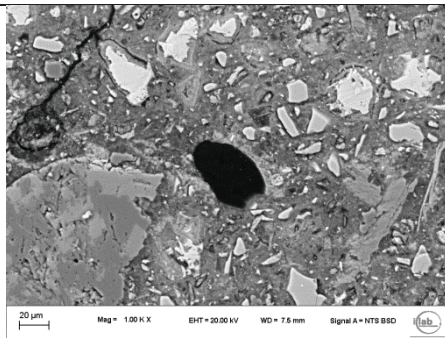
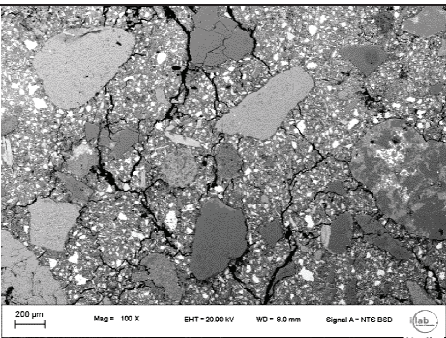
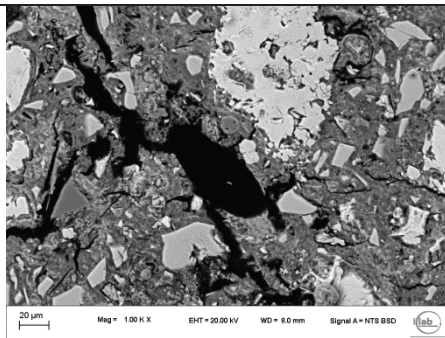
Mix	70-S-Pm 0.5 images 100X	70-S-Pm 0.5 images 1000X
20°C		
105°C		
250°C		
500°C		

Figure E6: SEM images 70-S-Pm 0.5 at 100X and 1000X magnitude after all exposure temperatures.

Annex E

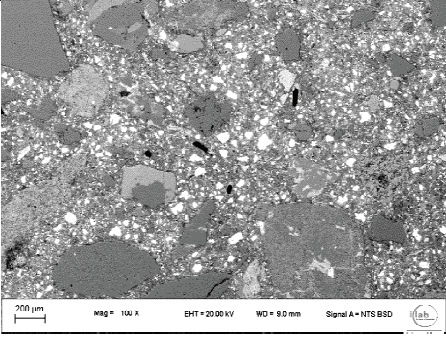
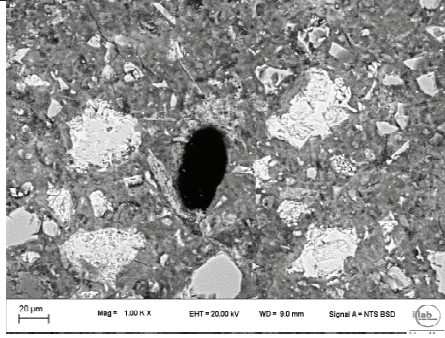
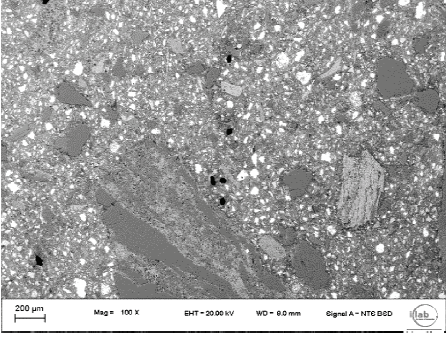
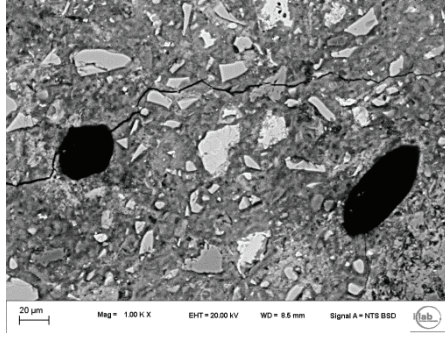
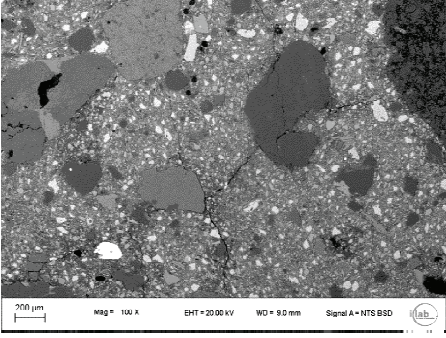
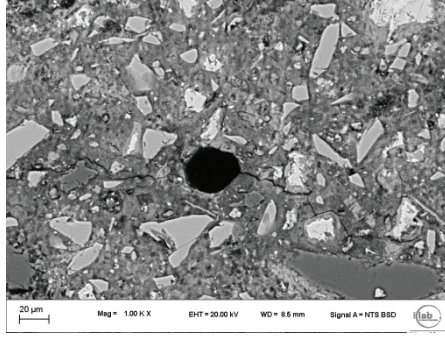
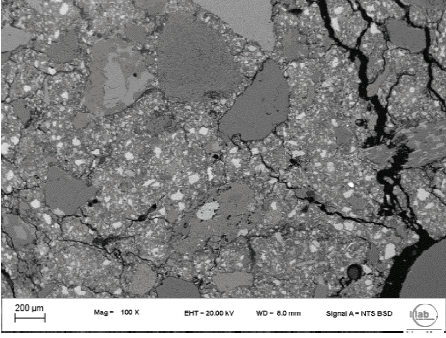
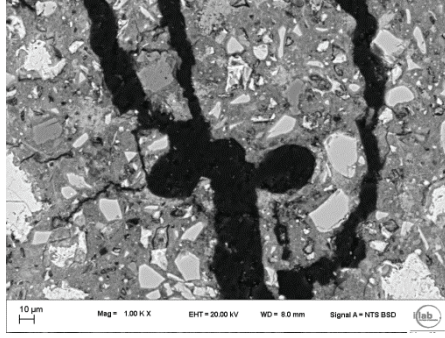
Mix	70-S-Pm 1 images 100X	70-S-Pm 1 images 1000X
20°C		
105°C		
250°C		
500°C		

Figure E7: SEM images 70-S-Pm 1 at 100X and 1000X magnitude after all exposure temperatures.

Annex E

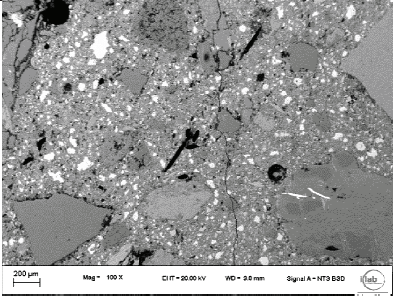
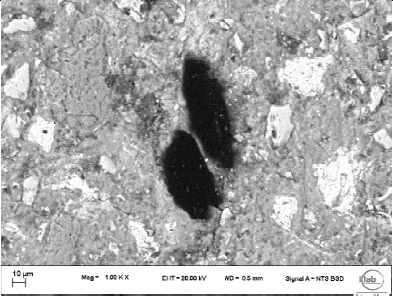
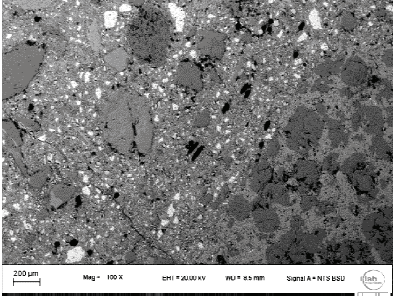
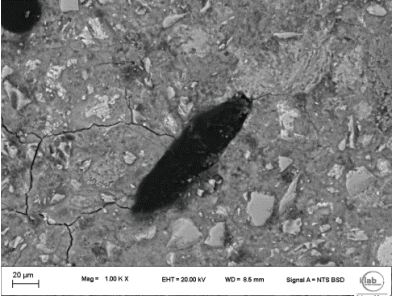
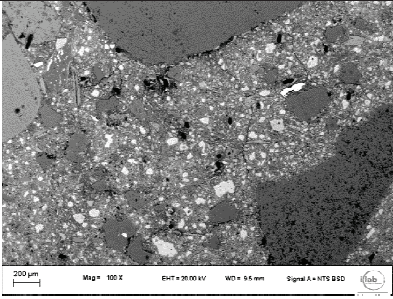
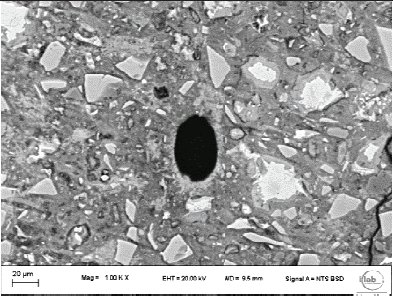
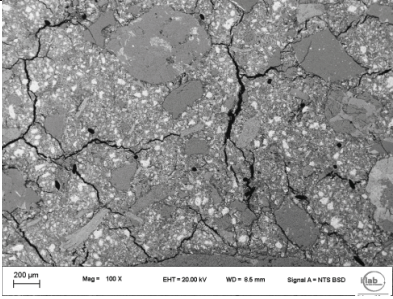
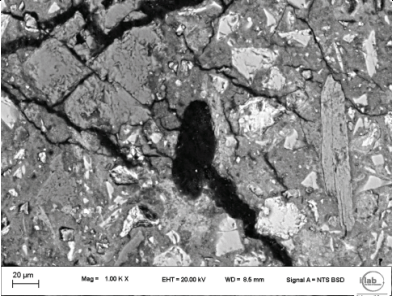
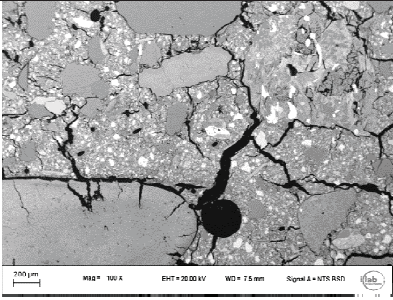
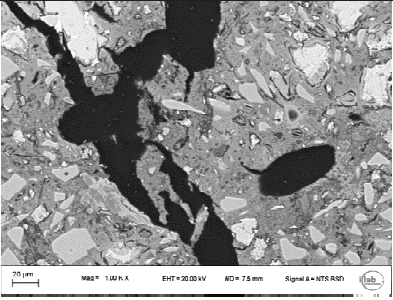
Mix	70-S-Pm 2 images 100X	70-S-Pm 2 images 1000X
20°C		
105°C		
250°C		
500°C		
750°C		

Figure E8: SEM images 70-S-Pm 2 at 100X and 1000X magnitude after all exposure temperatures.

Annex E

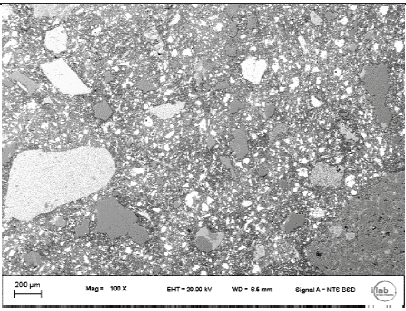
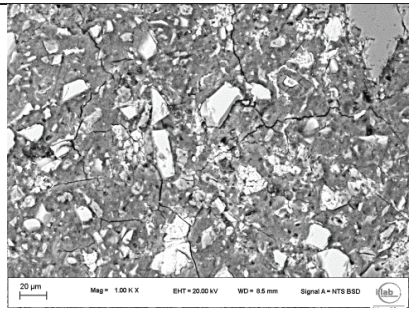
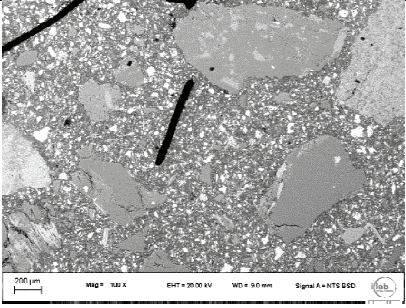
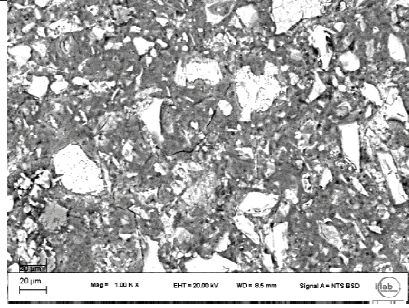
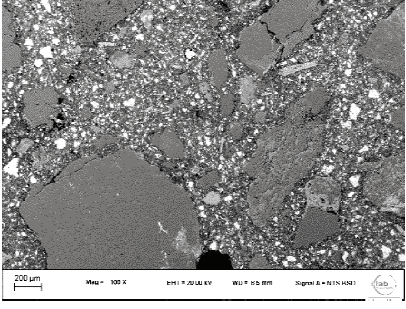
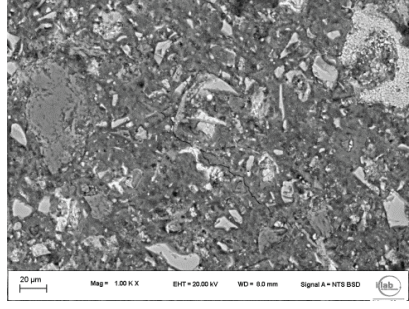
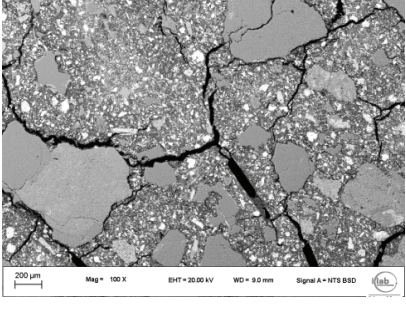
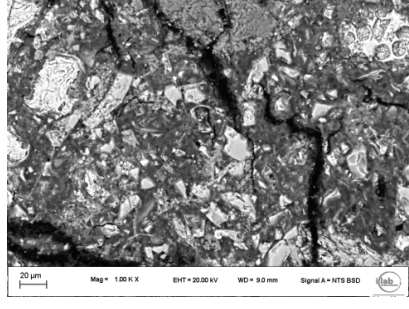
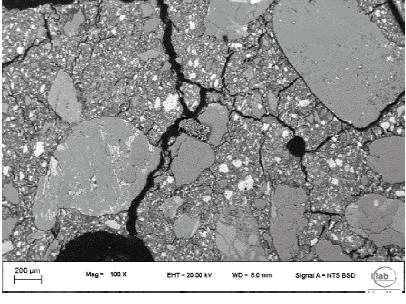
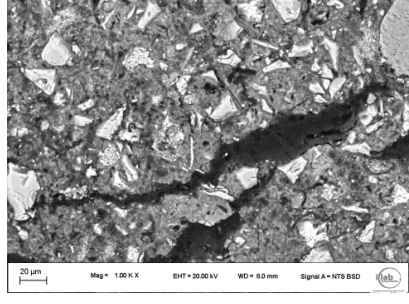
Mix	70-S-Pf 2 images 100X	70-S-Pf 2 images 1000X
20°C		
105°C		
250°C		
500°C		
750°C		

Figure E9: SEM images 70-S-Pf 2 at 100X and 1000X magnitude after all exposure temperatures.

Annex E

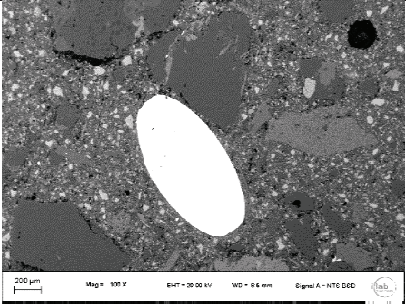
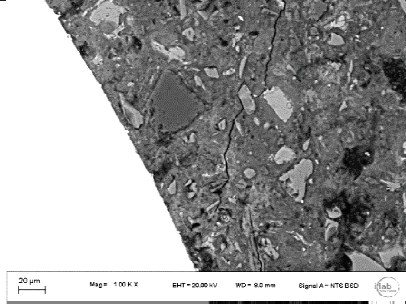
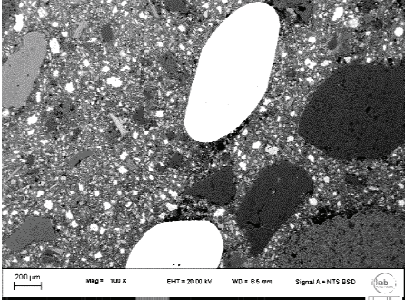
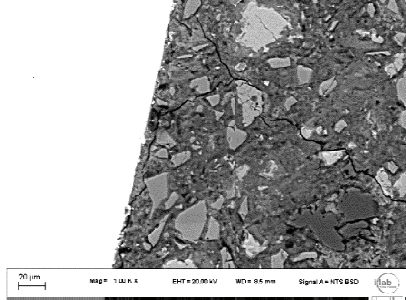
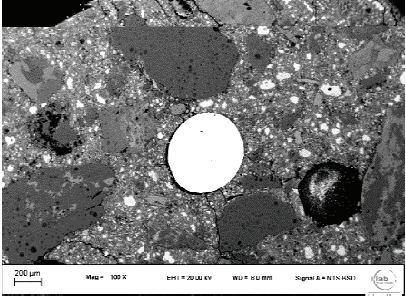
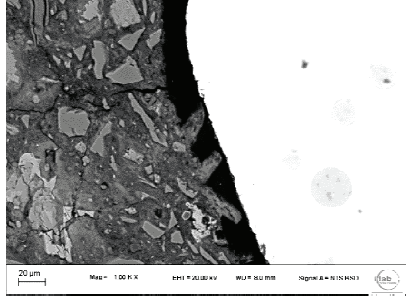
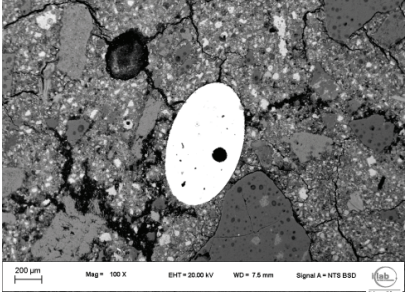
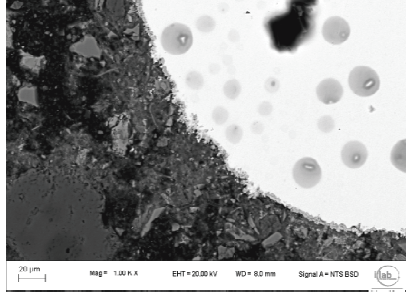
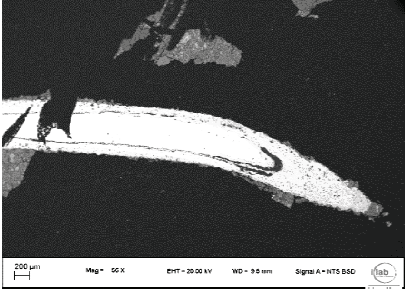
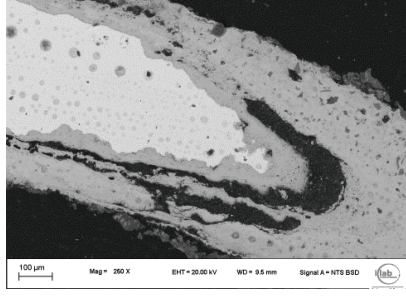
Mix	70-S-Sf 40 images 100X	70-S-Sf 40 images 1000X
20°C	 <p>200 μm Mag = 100 X EHT = 20.00 kV WD = 6.6 mm Signal A = HTS B50</p>	 <p>20 μm Mag = 1.00 K X EHT = 20.00 kV WD = 8.0 mm Signal A = HTS B50</p>
105°C	 <p>200 μm Mag = 100 X EHT = 20.00 kV WD = 6.6 mm Signal A = HTS B50</p>	 <p>20 μm Mag = 1.00 K X EHT = 20.00 kV WD = 8.0 mm Signal A = HTS B50</p>
250°C	 <p>200 μm Mag = 100 X EHT = 20.00 kV WD = 6.6 mm Signal A = HTS B50</p>	 <p>20 μm Mag = 1.00 K X EHT = 20.00 kV WD = 8.0 mm Signal A = HTS B50</p>
500°C	 <p>200 μm Mag = 100 X EHT = 20.00 kV WD = 7.6 mm Signal A = HTS B50</p>	 <p>20 μm Mag = 1.00 K X EHT = 20.00 kV WD = 8.0 mm Signal A = HTS B50</p>
750°C	 <p>200 μm Mag = 50 X EHT = 20.00 kV WD = 9.6 mm Signal A = HTS B50</p>	 <p>100 μm Mag = 200 X EHT = 20.00 kV WD = 9.6 mm Signal A = HTS B50</p>

Figure E10: SEM images 70-S-Sf 40 at 100X and 1000X magnitude after all exposure temperatures.

Annex E

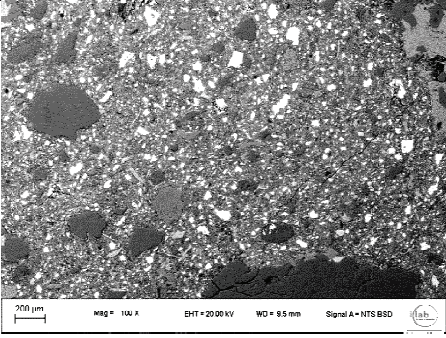
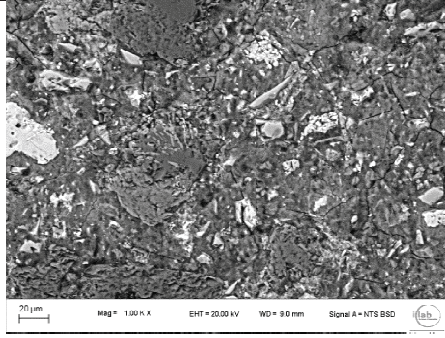
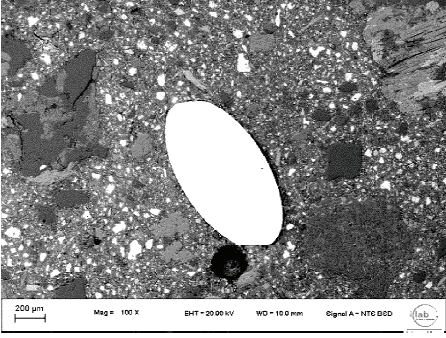
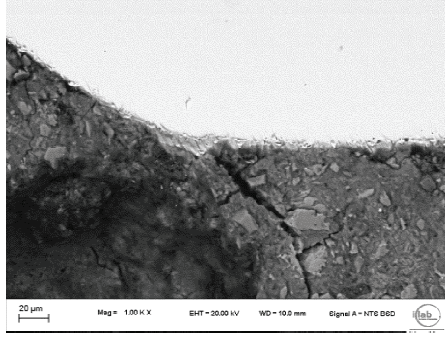
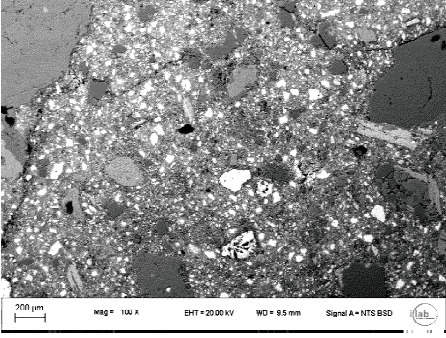
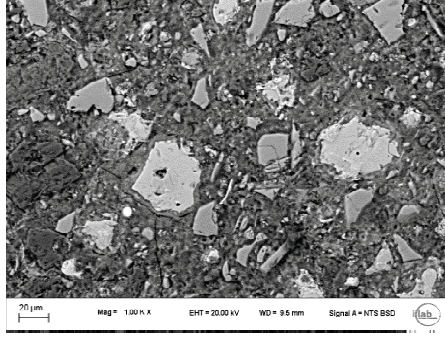
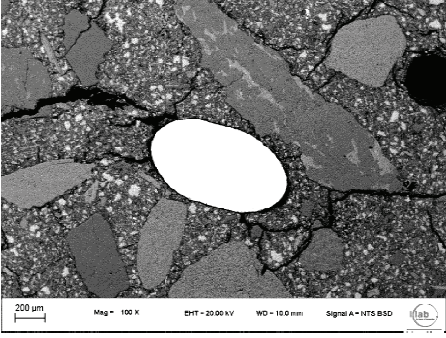
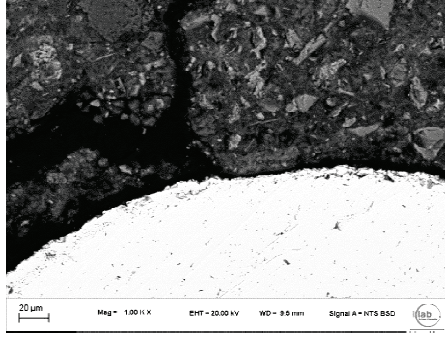
Mix	70-S-Sf 60 images 100X	70-S-Sf 60 images 1000X
20°C		
105°C		
250°C		
500°C		

Figure E11: SEM images 70-S-Sf 60 at 100X and 1000X magnitude after all exposure temperatures.